

# Positioning of Droplets in Inhomogeneous Fluids

## DISSERTATION

zur Erlangung des akademischen Grades

Doctor rerum naturalium  
(Dr. rer. nat.)

vorgelegt

dem Bereich Mathematik und Naturwissenschaften  
der Technischen Universität Dresden

von

M. Sc. Samuel Krüger  
geboren am 11. August 1987 in Erfurt



**TECHNISCHE  
UNIVERSITÄT  
DRESDEN**



Diese Dissertation wurde in der Zeit von April 2013 bis September 2018 am Leibniz-Institut für Polymerforschung und am Max-Planck-Institut für Physik komplexer Systeme angefertigt.

---

*eingereicht am 2. Oktober 2018*

*Eröffnung des Promotionsverfahrens am 15. Oktober 2018*

*verteidigt am 5. Februar 2019*

*Erster Gutachter Prof. Jens-Uwe Sommer*

*Zweiter Gutachter Prof. Frank Jülicher*

# Acknowledgements

Many people had direct or indirect influence on this work. I received support from very different angles and I am very thankful for this. It is not possible for me to thank everybody by name but this shall not diminish my gratitude to them who are not named.

First and foremost I would like to thank my supervisors Frank Jülicher and Jens-Uwe Sommer for many discussions and advises about this project and their guidance through the process of completing these studies. I would also like to thank Christoph Weber for plenty of deep scientific and technical discussions as well as dialogue and advice about the process of completing these studies. A very important forum for detailed discussions about employed approaches and obtained results was the droplet meeting. I would like to thank the members of the droplet meeting group Omar Adame Arana, Tyler Harmon, Hui-Shun Kuan, Jakob Löber, Patrick McCall, Florian Oltsch, Suropriya Saha, and Rabea Seyboldt. I would like to thank colleagues and former colleagues from the Leibniz-Institut für Polymerforschung, namely Ron Dockhorn, Hauke Rabbel, and Martin Wengenmayer especially for rich discussion about Monte-Carlo simulations and simulation-related problems in general. I would also like to thank my former colleagues from the Max-Planck-Institut für Physik komplexer Systeme Gary Klindt, Wolfram Pönisch, and Andre Scholich for several fruitful and rich after-lunch discussions as well as discussions in general. From the chemical information processing path of the center for advancing electronics Dresden I would like to thank Andreas Richter and Martin Elstner for discussions about experimental studies of the predicted effects and preliminary experiments.

I would like to thank Ulrike Burkert and Nicole Krause for their continuous support regarding administrative and organization questions and problems.

Last but certainly not least I would like to thank my parents and grandparents, my brothers and my sister for their various support.

*Dresden, September 2018*

S. K.



# Abstract

A central task of biological cells is the spatial control of their functions. One fundamental approach to achieve this is the formation of liquid compartments by phase separation, which leads directly to a spatially differentiated cell. One prominent example of spatial organization of the cell is the one cell stage embryo of the roundworm *C. elegans*. In this embryo, droplet-like structures, the P granules, are formed. The position of these compartments is controlled by protein gradients. As a result, all P granules are positioned at one side of the cell and the cell divides asymmetrically. Motivated by this observation also technological applications can be imagined. Droplets show an important role in microfluidics, because they provide a different chemical environment compared to their surrounding fluid. A positioning mechanism like in the biological cell can e.g. provide a sorting tool for droplets.

To investigate this positioning of droplets, we model this system as a ternary liquid containing two demixing components and one regulating component that mixes with the other two. The regulating component establishes a gradient through the system. Two different ways of generating this gradient are considered: The origin of the gradient is either an external potential that effects only the regulator, or boundary conditions on the regulator flux that lead to a pumping of regulator material from one side of the system to the other. We use lattice based Monte-Carlo simulation to find and evaluate the stable states of the model. In the case of a system in equilibrium, we also give a mean-field formulation employing the Flory-Huggins free energy.

This mean-field approach reveals a first order phase transition between a droplet positioned at low regulator concentration and a droplet positioned at high regulator concentration. The phase separation is controlled by the interaction parameters. The stability of the respective solutions is also observed in the simulation. Furthermore, the simulation shows, that the non-equilibrium case is surprisingly closely related to the equilibrium situation.



# Zusammenfassung

Die räumliche Organisation der zellulären Funktionen stellt eine wichtige Aufgabe für die biologische Zelle dar. Diese Organisation kann durch eine Kompartimentierung der Zelle durch Phasenseparation erreicht werden. Ein häufig verwendetes Modellsystem, das einen solchen Mechanismus aufweist, ist der Embryo des Fadenwurms *C. elegans* kurz vor dessen erster Zellteilung. In diesem Embryo werden tropfenartige Strukturen, sogenannte P granules, ausgebildet. Die Position dieser Tropfen wird durch einen Konzentrationsgradienten des Proteins Mex-5 beeinflusst. Dies führt dazu, dass sich alle Tropfen an einer Seite der Zelle befinden, wenn sich diese asymmetrisch teilt. Ein solcher Prozess der Tropfenpositionierung motiviert auch technische Anwendungen. Tropfen spielen eine wichtige Rolle in der Mikrofluidik, da sie eine definiert chemische Umgebung darstellen, die von der umgebenden Fluidphase verschieden ist. Ein Mechanismus, ähnlich dem in der biologischen Zelle, kann eine Möglichkeit darstellen, um Tropfen zu sortieren oder zu positionieren.

Um die Ursachen der Tropfenpositionierung zu untersuchen, nutzen wir ein ternäres Minimalsystem des flüssigen Systems: Zwei nicht mischbare Komponenten, welche die zwei Phasen ausbilden, und eine Regulatorkomponente, die sich mit den anderen Komponenten mischt. Die Regulatorkomponente bildet einen Konzentrationsgradienten aus. Wir betrachten zwei Möglichkeiten diesen Konzentrationsgradienten zu erzeugen. Die Ursache dieses Gradienten kann entweder ein externes Potenzial sein, das nur Regulatorpartikel beeinflusst, oder Randbedingungen bezüglich des Regulatorflusses. Wir nutzen Monte-Carlo Simulationen, um die stationären Zustände des Systems zu bestimmen und zu untersuchen. Außerdem stellen wir eine Meanfield Beschreibung für das System im Gleichgewicht vor, welche auf der Flory-Huggins Theorie basiert.

Der Meanfield Ansatz zeigt einen neuen Phasenübergang zwischen einem Tropfen, der bei minimaler Regulatorkonzentration positioniert ist und einem Tropfen, der bei maximaler Regulatorkonzentration positioniert ist. Dieser Phasenübergang kann durch die energetischen Wechselwirkungen des Regulators mit den anderen Komponenten gesteuert werden. Die Stabilität der entsprechenden Lösungen kann auch in der Simulation gezeigt werden. Außerdem zeigt die Simulation, dass sich das Nicht-Gleichgewichtssystem und das Gleichgewichtssystem sehr ähnlich bezüglich der stationären Zustände verhält.



# Contents

<b>Acknowledgements</b>	<b>i</b>
<b>Abstract (English/Deutsch)</b>	<b>iii</b>
<b>List of Figures</b>	<b>xi</b>
<b>List of Symbols</b>	<b>xiii</b>
<b>1 Introduction</b>	<b>1</b>
1.1 Motivation of this Thesis . . . . .	1
1.2 Phase Separation in Multicomponent Fluids . . . . .	2
1.2.1 Phase Separation in Thermodynamic Equilibrium . . . . .	2
1.2.2 Equilibrium States of Inhomogeneous Systems . . . . .	5
1.2.3 Molecular Simulation of Liquids . . . . .	10
1.3 Spatial Organization of the Cell Through Phase Separation . . . . .	13
1.3.1 Droplet-like Units in the Biological Cell . . . . .	13
1.3.2 Phase Separation in a Polarized Biological Cell . . . . .	14
1.4 Droplet Positioning in Engineering Science . . . . .	19
1.5 Central Questions Adressed in this Thesis . . . . .	21
<b>2 Phase Separation in the Presence of Concentration Gradients in and out of Equilibrium</b>	<b>23</b>
2.1 Flory-Huggins Theory of Phase Separation in Homogeneous Systems . . . . .	23
2.2 Equilibrium Concentration Gradients in External Fields . . . . .	28
2.3 Concentration Gradients Maintained by Nonequilibrium Conditions . . . . .	29
2.4 Gedankenexperiment on the Concentration Gradient in a Phase Separating System . . . . .	31
<b>3 Mean-Field Theory for the Spatial Regulation of Phase Separation in Equilibrium</b>	<b>33</b>
3.1 Minimization of the Mean-Field Free Energy of the Inhomogeneous System . . . . .	33
3.2 Results of the Mean-Field Calculation . . . . .	36
3.2.1 Defining an Order Parameter to Characterize the Correlation of Volume Fraction Fields . . . . .	36
3.2.2 Classification of the Observed Steady States . . . . .	38
3.2.3 Influence of the Interfacial Width . . . . .	39
3.2.4 Transition of Equilibrium Solutions . . . . .	40
3.2.5 Phase Diagram of the Mean-Field Model . . . . .	43
3.3 Droplet in an Periodic Regulator Distribution . . . . .	46

3.4	Analytical Prediction of the Phase Transition in a Limiting Case . . . . .	49
<b>4</b>	<b>Spatial Regulation of Phase Separation on a Lattice with Fluctuations</b>	<b>55</b>
4.1	Implementation of the Ternary Liquid Model in a Monte Carlo Simulation . . . . .	55
4.1.1	Lattice Based Monte Carlo Simulation . . . . .	55
4.1.2	Umbrella Integration . . . . .	57
4.1.3	Definition of Boundary Conditions and Maintaining a Concentration Gradient . . . . .	59
4.2	Equilibrium System without Regulator Gradient . . . . .	61
4.3	Equilibrium System: Regulator Gradient by External Potential . . . . .	63
4.3.1	Characterization of States . . . . .	64
4.3.2	Phase Transition between Equilibrium States . . . . .	66
4.3.3	Regulator Distribution in the Droplet Phases and its Environment . . . . .	69
4.3.4	Transition States and Signature of the Phase Transition . . . . .	71
4.4	Non-Equilibrium System: Regulator Gradient by Diffusion . . . . .	72
4.4.1	Non Equilibrium System with Exchange Dynamics . . . . .	72
4.4.2	Non Equilibrium System with Constrained Exchange Dynamics . . . . .	75
<b>5</b>	<b>Conclusions and Outlook</b>	<b>79</b>
5.1	Summary of the Physical Behavior of the Inhomogeneous System . . . . .	79
5.2	Outlook and Discussion of an Proposed Experimental Realization . . . . .	81
<b>A</b>	<b>Mean Field</b>	<b>85</b>
A.1	Exchange Chemical Potential in a Lattice Model . . . . .	85
A.2	Derivation of the Flory-Huggins Free Energy of Mixing from Principles of Statistical Physics . . . . .	86
A.2.1	Binary System . . . . .	86
A.2.2	Ternary System . . . . .	88
A.3	Relation Between the Interfacial Parameter and the Flory-Huggins Interaction Parameter for a Three Component System . . . . .	93
A.4	First Order Form of the Euler-Lagrange equation . . . . .	95
A.5	Normalization of the Order Parameters . . . . .	96
A.6	Influence of the Shape of the Regulator Gradient on the Transition Point . . . . .	98
A.7	Regulator Peak at the Droplet Interface . . . . .	99
A.8	Hysteresis of the Order Parameter . . . . .	103
A.9	Ensemble with Constant Regulator Distribution . . . . .	104
A.9.1	Conditions for the Stationary Points of the Free Energy . . . . .	104
A.9.2	Linear Regulator Profile . . . . .	106
A.9.3	Periodic Regulator Profile . . . . .	107
<b>B</b>	<b>Simulation</b>	<b>111</b>
B.1	Computation of the Energy Difference between Succeeding Configurations . . . . .	111
B.2	Monte Carlo Simulation without Regulator Gradient - Growth dynamics . . . . .	114
B.3	Calculation of the Eccentricity from Configuration Data . . . . .	115
B.4	Mastercurve of the Regulator Flux through Boundary Conditions . . . . .	117
B.5	Positioning of Droplets with Immobile Regulator Particles . . . . .	119
	<b>Bibliography</b>	<b>129</b>

Versicherung	131
--------------	-----



# List of Figures

1.1	Membraneless organelles of a cell. . . . .	2
1.2	Free energy for $T < T_c$ and $T > T_c$ . . . . .	3
1.3	Schematic two component phase diagram. . . . .	4
1.4	Procedure of a MC simulation and a MD simulation. . . . .	11
1.5	Droplet positioning in the <i>C. elegans</i> embryo. . . . .	16
1.6	Onset model by Brangwynne. . . . .	17
1.7	Onset model by Gharakhani. . . . .	18
1.8	Ternary model by Lee. . . . .	19
2.1	Sketch of a 2D cut through the 3D lattice. . . . .	24
2.2	Mixed state and state of pure components. . . . .	25
2.3	Generic free energy of a binary system and Maxwell construction. . . . .	27
2.4	Regulator gradient in an external potential $U_R$ . . . . .	29
2.5	Spatial effects in a inhomogeneous ternary liquid system. . . . .	32
3.1	Possible types of equilibrium states. . . . .	39
3.2	Kink of the free energy. . . . .	42
3.3	Behavior of the order parameters $\rho_{BR}$ , $\rho_{AR}$ and $\rho_{AB}$ . . . . .	43
3.4	Relations between the order parameters. . . . .	44
3.5	Phase diagram of the ternary system with regulator gradient. . . . .	45
3.6	Triple points. . . . .	46
3.7	Stationary profiles of a droplet in a periodic potential $U_R$ . . . . .	47
3.8	Kink of the free energy and jump of the order parameter $\rho_{BR}$ of a droplet in a periodic potential $U_R$ . . . . .	48
3.9	Phase diagram of a droplet in a periodic potential $U_R$ . . . . .	48
3.10	Profiles of $\phi_R$ and $\phi_A$ obtained by free energy minimization and the corre- sponding analytic ansatz. . . . .	49
3.11	Comparison of the analytical and numerical free energy difference $\Delta F$ . . . . .	52
3.12	Analytic phase diagram and jump of the order parameter $\rho_{BR}$ . . . . .	53
4.1	Pumping of the regulator. . . . .	61
4.2	Regulator profiles from external potential or flux boundary conditions. . . . .	61
4.3	Phase diagram of a two component system. . . . .	62
4.4	Phase diagrams without imposed regulator gradient. . . . .	63
4.5	Anti-correlated and correlated states from Monte-Carlo simulation. . . . .	65
4.6	Phase diagram of the ternary equilibrium system. . . . .	67
4.7	Drift velocity to equilibrium in external potential . . . . .	68
4.8	Accumulation of regulator inside a droplet. . . . .	69

## List of Figures

---

4.9	Regulator distribution inside and outside an equilibrium droplet. . . . .	70
4.10	Free energy profile from simulation. . . . .	73
4.11	Fluxes in a diffusion generated regulator gradient (exchange dynamics). . .	74
4.12	Phase diagram and drift velocity of a droplet in a regulator gradient generated by diffusion (exchange dynamics). . . . .	75
4.13	Fluxes in system with a diffusion generated regulator gradient (constrained Kawasaki dynamics). . . . .	76
4.14	Phase diagram and drift velocities of the system with a flux generated regulator gradient (constrained Kawasaki dynamics). . . . .	77
5.1	Sketch of a microfluidic realization . . . . .	82
A.1	Normalization of the order parameters. . . . .	96
A.2	Dependency of the transition on $\bar{\phi}_A$ . . . . .	98
A.3	Two example profiles of regulator peaks . . . . .	100
A.4	Peak height and area for different $\kappa$ -parameters . . . . .	100
A.5	Energetic dependency of the peak height. . . . .	101
A.6	Free energy for different peak heights. . . . .	102
A.7	Hysteresis of the order parameter. . . . .	104
A.8	Profiles with constant regulator distribution . . . . .	107
A.9	Kink of the free energy with constant regulator distribution . . . . .	108
A.10	Difference of the free energy with constant regulator distribution . . . . .	109
A.11	Order parameter with constant regulator distribution . . . . .	109
A.12	Profiles with constant periodic regulator distribution . . . . .	110
A.13	Free energy and order parameter with constant periodic regulator distribution	110
B.1	Snapshots of droplet growth . . . . .	114
B.2	Characteristic length during the droplet growth. . . . .	115
B.3	Relative Fluxes . . . . .	118
B.4	Transition point in a simulation with immobile regulator particles. . . . .	119

# List of Symbols

In the following description and text, we use the term free energy as a short form for the Helmholtz free energy. If we consider the Gibbs free energy, we name it explicitly. In some cases, one symbol has different meanings depending on context. The different meanings are separated by ";".

$a$	lattice constant; long axis of a fitted ellipse
$a_i$	measure of the importance of $P_i^{\text{bias,sim}}$ for the computation of $F(\gamma)$
$A$	parameter of the periodic potential determining its amplitude; general observable; parameter for adjusting the rate of the diffusion of $R$ -particles through the wall
$b$	short axis of a fitted ellipse
$c_R^i$	concentration of $R$ -particles in phase $i$
$C_i$	integration constant
$D_i$	diffusion coefficient of particles of component $i$
$e$	eccentricity
$E$	internal energy
$E_{\text{mix}}$	internal energy of a mixed system
$E_{\text{pure}}$	internal energy of a pure system
$f$	degrees of freedom, free energy density
$f_0$	Flory-Huggins free energy density of a homogeneous system
$f_{\text{FH}}$	Flory-Huggins free energy density
$F$	free energy
$F_S$	free energy contribution containing entropic terms
$F_U$	free energy contribution containing the external potential term
$F_\chi$	free energy contribution containing particle interaction terms
$F^l$	free energy corresponding to the anti-correlated branch of solutions
$F^r$	free energy corresponding to the correlated branch of solutions
$F_{\text{bulk}}$	free energy of the bulk region of the system
$F_{\text{bulk}}^{\text{cons}}$	free energy of the bulk region of the system considering constraints
$F_{\text{hom}}$	free energy of the homogeneous system
$F_{\text{MF}}^{\text{pure}}$	mean field free energy of the pure system
$F_{\text{mix}}$	free energy of a mixed system
$F_{\text{pure}}$	free energy of a pure system
$g$	Gibbs free energy density
$g_i(\phi_i)$	constraint function regarding $\phi_i$
$G$	Gibbs free energy
$\mathcal{G}(m)$	multiplicative contribution to $\Delta F$ containing only parameters of the ansatz profiles of the analytic model

## List of Symbols

---

$\vec{h}$	vector of the contributions of the Euler-Lagrange equations that contain no spatial derivatives
$H$	hamiltonian
$H_g$	grand canonical hamiltonian
$H^{\text{pure}}$	hamiltonian of the pure system
$H_{\text{MF}}$	mean field hamiltonian
$H_{\text{MF}}^{\text{pure}}$	mean field hamiltonian of the pure system
$j_{\text{bc}}$	flux through boundary
$j_i$	flux of particles of component $i$
$j_{ij}^i$	partial flux defined as the flux of $i$ -particles because of $ij$ -exchanges on the lattice
$J_{ij}$	diagonalized interaction parameter
$J_{ij}^{\alpha\beta}$	interactions between $\alpha$ - and $\beta$ -particle at the lattice sites $i$ and $j$
$k_B$	Boltzmann constant
$L$	spatial system size
$m$	slope of the linear $R$ -profile
$m_0$	offset of the linear $R$ -profile
$m_i^{\text{drop},x}$	$i$ 'th moment of the distribution of $A$ -particles in the droplet in $x$ -direction
$M$	number of components; matrix of the gradient coefficients
$n$	number of simulation steps
$N$	total number of particles
$N_{\text{drop}}$	combined number of $A$ - and $R$ -particles in the droplet
$N_i$	number of particles of component $i$
$N_i^{\text{in}}$	number of $i$ -particles inside the droplet
$N_i^{\text{out}}$	number of $i$ -particles outside the droplet
$\mathcal{N}_{ij}$	normalization of the order parameter $\rho_{ij}$
$p$	partition coefficient of $R$ -particles between an $A$ -enriched and an $A$ -depleted phase
$p_A$	acceptance probability in the Metropolis algorithm
$p_i(\gamma)$	weights of the different windows for the umbrella sampling generated by the different bias potentials
$P$	number of coexisting phases
$P(r)$	probability distribution of the configurations $r$
$P(\gamma)$	temporal average of the distribution of configurations constrained to the reaction coordinate $\gamma$
$P^{\text{bias,sim}}(\gamma)$	temporal average of the biased distribution of configurations in the simulation constrained on the reaction coordinate $\gamma$
$P^{\text{sim}}(\gamma)$	temporal average of the distribution of configurations in the simulation constrained on the reaction coordinate $\gamma$
$P_{\text{drop}}^{\phi}(x)$	distribution of particles that are part of the droplet in $x$ -direction
$P_i^{\alpha}$	occupation operator of species $\alpha$ in a ternary system
$V$	total volume of the system
$Q(N, V, T)$	canonical partition function
$Q(\gamma)$	canonical partition function constrained to the reaction coordinate $\gamma$
$Q_i^{\text{bias}}(\gamma)$	biased canonical partition function constrained to the reaction coordinate $\gamma$
$r$	general spatial coordinate; radial spatial coordinate

---

$r_{\text{com}}$	position of the center of mass of the droplet
$R$	radius in the respective context
$R_g$	radius of gyration
$s$	parameter of the external potential $U_R$ determining its slope
$s_i$	occupation operator of component $i$ in a binary system
$S$	entropy
$S_{\text{mix}}$	entropy of a mixed system
$S_{\text{pure}}$	entropy of a pure system
$t$	time
$T$	thermodynamic temperature
$T_c$	critical temperature
$T_w$	wetting temperature
$U_i$	relative external potential effecting component $i$
$U_i^{\text{bias}}$	bias potential for the umbrella sampling
$w_i$	effective interaction of $A$ - or $B$ -particles with the wall
$W$	number of micro states
$W_i$	wall potential
$W_{\text{mix}}$	number of micro states of a mixed system
$W_{\text{pure}}$	number of micro states of a pure system
$x$	normalized spatial coordinate $x = \hat{x}/L$
$x_{\text{com}}$	$x$ -position of the center of mass of the biggest cluster
$\hat{x}$	spatial coordinate
$Z_{\text{MF}}^{\text{pure}}$	mean field canonical partition sum of the pure system
$Z_{g,\text{MF}}$	mean field grand canonical partition sum
$Z_{g,\text{MF}}^1$	mean field one particle grand canonical partition sum
$\alpha$	volume fraction of phase $a$ with respect to the total volume; parameter of the bias potential $U_i^{\text{bias}}$ describing its strength
$\beta$	inverse temperature $\beta = (k_B T)^{-1}$
$\gamma$	reaction coordinate
$\bar{\gamma}, \bar{\gamma}(r)$	value of the reaction coordinate for a given configuration $r$
$\gamma_i$	minimum of the harmonic bias potential $U_i^{\text{bias}}$
$\bar{\gamma}_i^{\text{bias,sim}}$	mean of $P_i^{\text{bias,sim}}$ from simulation assuming a Gaussian distribution
$\delta(x)$	delta distribution
$\delta_{ij}$	Kronecker symbol
$\delta\phi_i$	functional derivative with respect to $\phi_i$
$\Delta$	Laplace operator
$\Delta_i$	one of the two independent occupation operators of the ternary system applied on lattice site $i$
$\Delta F$	difference between the free energy branches, $\Delta F = F^l - F^r$
$\Delta\rho_{ij}$	jump of the order parameter at the transition line
$\epsilon_{ij}$	microscopic interaction parameters
$\epsilon_l$	width of the $A$ -rich phase for the anti-correlated solution
$\epsilon_r$	width of the $A$ -rich phase for the correlated solution
$\zeta$	coordination number of the lattice
$\Theta(x)$	Heaviside step function

## List of Symbols

---

$\Theta_i$	one of the two independent occupation operators of the ternary system applied on lattice site $i$
$\kappa_i$	gradient coefficients
$\lambda_i$	Lagrange multiplier corresponding to constrain function $g_i(\phi_i)$
$\mu_i$	relative chemical potential of component $i$
$\tilde{\mu}_i$	chemical potential of component $i$
$\nu_i$	molecular volume of component $i$
$\xi$	random unit vector
$\rho_{ij}$	order parameter describing the correlation between the fields $\phi_i$ and $\phi_j$
$\rho_{ij}^l$	order parameter of the anti-correlated branch of solutions
$\rho_{ij}^r$	order parameter of the correlated branch of solutions
$\left(\sigma_i^{\text{bias,sim}}\right)^2$	variance of $P_i^{\text{bias,sim}}$ from simulation assuming a Gaussian distribution
$\sigma_{i,\text{max}}^2$	maximum variance of a step profile given the average volume fraction $\bar{\phi}_i$
$\vec{\phi}''$	vector of the second spatial derivatives of the volume fractions
$\phi_{A,\text{in}}$	volume fraction of $A$ in the $A$ -rich phase
$\phi_{A,\text{out}}$	volume fraction of $A$ in the $A$ -depleted phase
$\phi_{A,\text{out,bin}}$	volume fraction of $A$ in the $A$ -depleted phase of the binary $AB$ -system
$\phi_i$	volume fraction of component $i$
$\bar{\phi}_i$	average volume fraction of component $i$
$\phi_i^c$	critical volume fraction of component $i$
$\phi_i^l$	volume fraction profile of a anti-correlated solution
$\phi_i^r$	volume fraction profile of a correlated solution
$\phi_R^{\text{in}}$	volume fraction of $R$ inside droplets
$\phi_R^{\text{out}}$	volume fraction of $R$ outside droplets
$\chi_{ij}$	Flory-Huggins parameter describing the interaction between component $i$ and $j$
$\chi_{ij}^*$	value of the Flory-Huggins parameter $\chi_{ij}$ at a phase transition
$\omega$	number of state variables of a system not describing its composition; parameter of the periodic potential describing its phase shift
$\Omega$	grand canonical potential
$\Omega_{\text{MF}}$	mean field grand canonical potential

# 1 Introduction

## 1.1 Motivation of this Thesis

Living cells are of enormous physical and chemical complexity. Multiple chemical species and chemical reactions have to be organized in time and space. A very broad but important question is how these order can be established and maintained to ensure a functional cell. Fig 1.1 gives an impression of the complex spatial structure of an animal cell. Of important role are the organelles [116]. These are distinct regions (compartments) of the cell that have specific functions [116]. Two general types of organelles can be identified regarding their structure [116]. There are organelles that are separated from the cytoplasm by a membrane or membrane-less organelles. The membrane-less organelles behave like a phase separated liquid system.

An additional level of cell organization is the polarization of the cell, which leads to an ordering of compartments [13]. We will illustrate this with the example of the fertilized egg cell of the roundworm *C. elegans*. During its development, the cells have to differentiate. At an early stage, this is achieved by asymmetric cell division in the young embryo [15]. Membrane-less organelles, the P granules are formed in the cell [71]. Before cell division, they are positioned at one side of the cell, the created daughter cells are different. The cells with P granules form the germ line of the growing organism, the cells without P granules are its somatic cells [15].

Motivated by this process, we are interested in describing and understanding droplet positioning in liquid systems. We give a short introduction to equilibrium phase separation in liquid systems (section 1.2.1). This phase separation is the origin of droplet formation considered in this thesis. Even in the introduced biological system, the formation of membrane-less organelles can be fairly understood with this concept [116]. If thermodynamic arguments are used to investigate these questions it is important that they are capable of take spatial information into account. To this end we give a short introduction to density functional theory (see section 1.2.2). This is an powerful tool for investigating the thermodynamic properties of inhomogeneous systems [180, 127]. Later, in chapter 3 we will use density functional theory to describe the positioning of droplets in a inhomogeneous model system. We also give a short introduction to molecular simulations as an alternative approach to investigate inhomogeneous liquid systems. This points to chapter 4, where we employ lattice based Monte-Carlo simulation as an additional method to study the positioning of droplets.

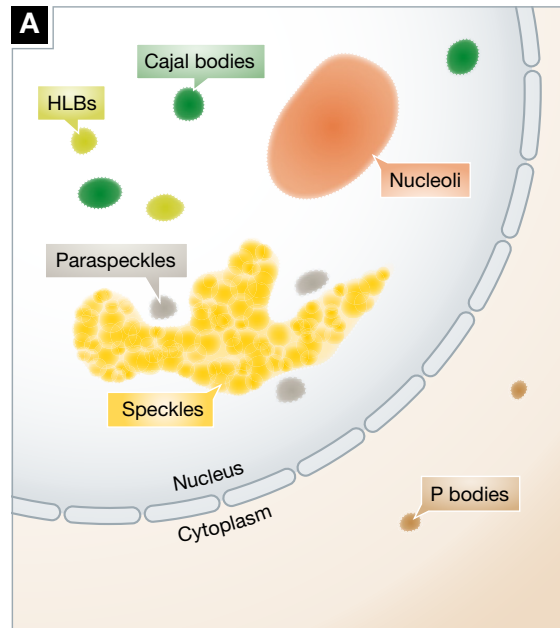


Figure 1.1 – Nucleus of an animal cell with surrounding cytoplasm. The shown organelles are membraneless organelles [29] (Permission for republishing in this thesis granted by John Wiley and Sons).

After the introduction of these concepts, we give a short overview about droplet positioning in biology and engineering. To this end, we have a closer look at membrane-less organelles as an example for liquid-liquid phase separation in the cell (section 1.3.1). The actual droplet positioning is shown in section 1.3.2, where cell polarization is introduced focusing on the *C. elegans* embryo. In section 1.4, we give an overview about droplet positioning in engineering. We close this chapter by emphasizing three central questions of this thesis (section 1.5).

## 1.2 Phase Separation in Multicomponent Fluids

### 1.2.1 Phase Separation in Thermodynamic Equilibrium

In equilibrium, the behavior of the system is described by a thermodynamic potential. Here, we choose the Helmholtz free energy considering a canonical ensemble.<sup>1</sup> The free energy  $F(\{N_i\}, V, T)$  is dependent on the state variables thermodynamic temperature  $T$ , total volume  $V$  and particle numbers  $N_i$ . In this section we will consider homogeneous systems only. For them it is sufficient to discuss the free energy density  $f(\{\bar{\phi}_i\}) = F/V$ , which is dependent on the total temperature and the average volume fractions  $\bar{\phi}_i = N_i\nu_i/V$ . The parameter  $\nu_i$  is the molecular volume of particles of type  $i$ . The choice of using the volume fraction to describe the composition of the system is arbitrary, it is also possible to use other properties to describe its composition, e.g. concentration. For simplicity, we will discuss this free energy density for a two-component system. The system is incompressible and its composition is sufficiently determined by one volume fraction  $\bar{\phi}$ , because  $1 = \sum_i \bar{\phi}_i$  has to be fulfilled for these type of systems.

<sup>1</sup>We will use the short term free energy for the Helmholtz free energy.

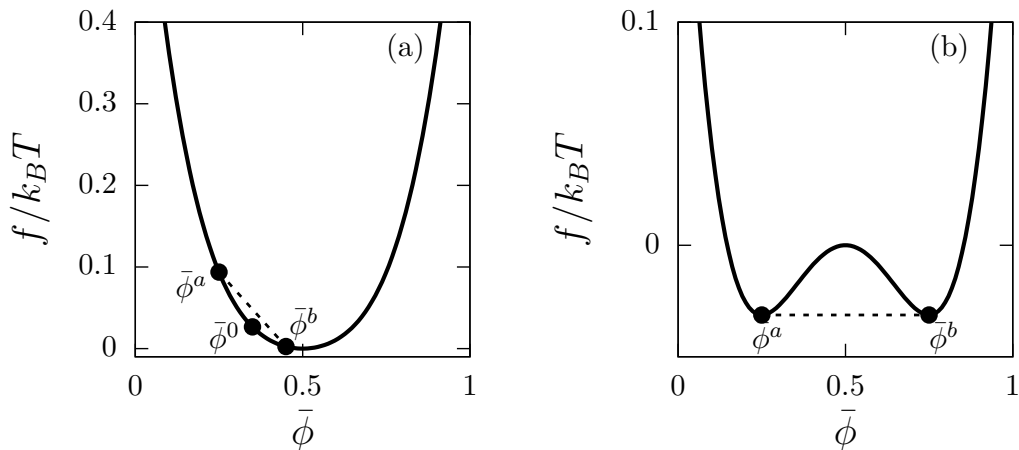


Figure 1.2 – Ginzburg-Landau free energy density. (a)  $T > T_c$ . The free energy is convex for the whole interval  $0 < \bar{\phi} < 1$ . If the system decomposes into the phases  $\bar{\phi}^a$  and  $\bar{\phi}^b$ , the free energy of the total system is increased (dashed line). (b)  $T < T_c$ . Inside the region  $\bar{\phi}^a < \bar{\phi} < \bar{\phi}^b$ , the total free energy of the system is decreased if the system decomposes into the phases  $\bar{\phi}^a$  and  $\bar{\phi}^b$ . Outside this region the not separated system is stable.

A generic form of the free energy which is capable of illustrating important behavior of the system is the fourth order polynomial

$$\beta f = a(\bar{\phi} - \bar{\phi}_c)^2 + \frac{b}{2}(\bar{\phi} - \bar{\phi}_c)^4. \quad (1.1)$$

This is a Taylor expansion around the critical point of the system characterized by the critical temperature  $T_c$  and the critical volume fraction  $\bar{\phi}_c$  [57]. We can distinguish two different scenarios of the system.

In the first scenario  $T > T_c$ . Considering eq. (1.1) that means that  $a > 0$  and  $b > 0$ . This scenario is illustrated in fig. 1.2(a). Now, the free energy density is convex for all volume fractions  $\bar{\phi}$ . That means that if the system would separate in the two phases  $\bar{\phi}^a$  and  $\bar{\phi}^b$ , the free energy of the system would increase (see fig. 1.2(a)). Thus, the one phase state of the system characterized with  $\bar{\phi}^0$  is stable. The system is stable for each average volume fraction  $\bar{\phi}$ ,  $\partial^2 f / \partial \bar{\phi}^2 < 0$  for all  $\bar{\phi}$ .

In the second scenario, illustrated in fig. 1.2(b), the temperature is lower than the critical temperature ( $T < T_c$ ). Now, the parameters are  $a < 0$  and  $b > 0$ . In this scenario it exists a region between  $\bar{\phi}^a$  and  $\bar{\phi}^b$ , where the system can decrease its free energy by separating into the two phases  $\bar{\phi}^a$  and  $\bar{\phi}^b$  (see fig. 1.2(b)). The composition of these two phases are  $\bar{\phi}^{a,b} = \bar{\phi}_c \pm a/b$ . Outside this region, for  $\bar{\phi} < \bar{\phi}^a$  and  $\bar{\phi} > \bar{\phi}^b$ , the one phase system is stable. We discuss the calculation of  $\bar{\phi}^a$  and  $\bar{\phi}^b$  in section 2.1.

If the behavior of the free energy is known for a system, the phase diagram of the system can be predicted from that free energy. We consider both components to be chemically inert, so that no chemical reaction is performing in this system. A typical phase diagram of this passive system is shown in Fig. 1.3. As mentioned before, we use  $\bar{\phi}_i$  to describe the average volume fraction of component  $i$  in the system. The parameter  $\beta$  is the inverse temperature  $1/k_B T$ . If the system is homogeneous like considered in this section, the average volume fraction is equal to the local volume fraction  $\phi_i$ . In an incompressible fluid of  $M$  components, the total volume is given by the sum of the volumes of all particles

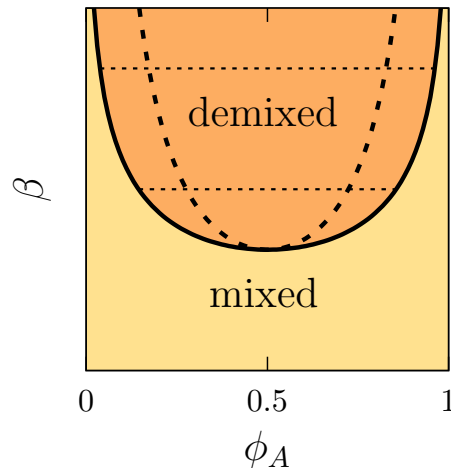


Figure 1.3 – Phase diagram of a two component liquid system of the components A and B in the  $\beta - \phi_A$  plane. The light color indicates the mixed region, the demixed region is highlighted by the shadowed area. The solid black line at the border of the shaded region is the binodal line. The spinodal line is represented by the curved dashed line in the demixed region. Two representative tie lines are indicated by the horizontal dashed lines. We did not use a quantitative measure for the  $\beta$ -axis, because that is also dependent on the particle interactions.

$V = \sum_{i=1}^M N_i \nu_i$  and the molecular volumes  $\nu_i$  are constant parameters.

The phase diagram of the two component system shows two different regions in its phase space (see fig. 1.3). In the brighter region, the mixture of the components is stable. In the shaded area, the system separates in an  $A$ -rich phase  $a$  and a  $B$ -rich phase  $b$ . The connecting line between these two particular phases is called tie-line (horizontal dashed lines). In the considered simple system, these tie-lines are horizontal lines that connect two points of the binodal line. The two connected points are coexistent in thermal equilibrium. The solid thick line shows the binodal line of the phase diagram. If two different volume fractions coexist in thermal equilibrium, both have to be element of the binodal line. Together, binodal line and the tie-lines determine the possible coexistent volume fractions sufficiently.

The curved dashed line of the phase diagram is the spinodal line. In the area between the spinodal line, the system demixes spontaneously into the two phases. This process is called spinodal decomposition. Typical examples are found in [25, 24, 115]. In the region between the binodal line and the spinodal line a different mechanism of separation is observed. Now, the droplet phase is formed by nucleation and growth.<sup>2</sup> As the name suggests, small droplets are nucleated at the beginning of this process. Afterwards these small nuclei grow and merge [45].

The spinodal and binodal line touch exactly at one point, which is the critical point at the critical temperature  $T_c$  and the critical volume fraction  $\phi_A^c$ . At this point, the two phases have the same composition and can not be distinguished. If the particles of type  $A$  and  $B$  are chemically stable for sufficient high temperatures, the liquid system generally mixes, because the entropy of the system overwhelms the particle interactions. This is the common behavior of a liquid mixture. For special chemical structures, it is also possible to

<sup>2</sup>The system forms droplets on the onset of the phase separation. It is possible, that no drops are existent once the system is equilibrated.

induce mixing by decreasing the temperature, like it is observed for PEG [141]. This effect is generally observed, if the solvent is able to bind to the respective component. These two effects are known as LCST and the UCST [91]. UCST means the upper critical solution temperature. This is the standard scenario of a phase diagram like mentioned above. For high temperatures, the entropic contribution dominates the free energy of the system and the components mix. Some systems show a LCST, a lower critical solution temperature, like the PEG example. There a specific interaction leads to a stronger interaction between the particles for higher temperatures, the components demix. In general this LCST occurs in addition to the UCST.

In general, two properties can have significant influence on the shape of the binodal and spinodal line. The first important property is the interaction between the present particles. Repulsive net-interactions between the components favor demixing, and lead to an increased demixed region of the phase diagram [47]. As a second point the influence of the particle size should be mentioned. This is well investigated especially for phase separating polymers. There, increasing the chain length leads to a reduced entropic contribution and to a favored demixed state [47]. In fact, these influences are much more complex and can also lead to qualitative different shapes of the phase diagram like mentioned for PEG, but here we restricted ourselves to these two fundamental aspects. The discussion of the phase transition is extended in chapter 2.

The complexity of the phase diagram can be strongly increased by adding more components to the system. The possible number of coexisting phases can be determined using the Gibbs phase rule

$$f = M - P + \omega, \tag{1.2}$$

where  $M$  is the number of components,  $P$  is the number of coexisting phases,  $\omega$  is the number of state variables, which do not describe the composition of the system, and  $f$  is the number of the degrees of freedom. Here, this quantity is defined by the number of state variables, which can be varied without changing the number of coexisting phases. Most commonly,  $\omega = 2$  for fluid systems when temperature and pressure dependencies are discussed. This rule gives an impression how complexity increases if more components are added successively to the system.

### 1.2.2 Equilibrium States of Inhomogeneous Systems

#### Concepts of the Density Functional Theory and Examples

In section 1.2.1 we discussed the equilibrium states of a homogeneous system. We considered only systems, in which the volume fraction is constant in space. Even the simple example of the phase separation of a binary liquid system shows, that the system is not homogeneous because multiple phases are present. With the homogeneous approach we were able to predict the phase behavior of the system. Technically, we investigated the mixed homogeneous state and tested, if this state becomes not stable. Now, if we are interested in the properties of the separated state, we need a technique, which allows us to investigate the separated inhomogeneous state directly. To this end, we can employ the classical density functional theory (classical DFT), which will be introduced in this section.

Historically, this technique was firstly formulated and established for the investigation of the

ground state of the electron gas by Hohenberg and Kohn [73] in 1964. Later, this approach was generalized for systems of nonzero temperature [112]. The pragmatic implementation of this theory by Kohn and Sham [89] finally allowed this technique to be the established powerful approach in computational chemistry.

From a mathematical point of view, the electronic DFT is closely related to the classical DFT with the difference that the electronic DFT considers densities of electrons where the classical DFT considers densities of atoms or coarse grained particles which correspond to parts of larger molecules [180]. This difference also leads to neglecting quantum mechanical effects in the classical DFT. The literature uses the same acronym for both types of density functional theories.

The classical DFT is based on the theorem, that for an open system characterized by its temperature  $T$ , total volume  $V$  and chemical potentials  $\mu_i$  of all present species, the underlying external potential of each component  $U_i(r)$  is uniquely defined by the equilibrium density  $\rho(r)$  [73, 180].<sup>3</sup> Another result of this theorem is, that a Helmholtz energy  $F[\{\rho_i(r)\}]$  can be defined which is a functional of the densities of the present particles and independent of the external potential [73, 180]. The expression  $\{\rho_i\}$  indicates that the Helmholtz energy is a functional of all particle densities corresponding to the involved particle types  $i$ . In the literature this Helmholtz energy is also denoted as the intrinsic Helmholtz energy to point out its independence from the external potentials [180]. The central property and the independent variable of the free energy functionals is the particle density  $\rho_i(r)$ .<sup>4</sup> Because we will consider the volume fraction in this thesis, we will also use the volume fraction in this introduction instead of the particle density. These two components are coupled by the particle volume  $\nu_i$  with  $\phi_i = \nu_i \rho_i$ . This volume fraction can be obtained from the particle configuration

$$\phi_i(r) = \nu_i \left\langle \sum_{N_i} \delta r_j \right\rangle. \quad (1.3)$$

The positions  $r_j$  are the positions of particles of type  $i$  and  $\delta$  means the delta distribution. The volume fraction is obtained by calculating the ensemble average of the sum over all  $N_i$  positions of particles of type  $i$ . Later, we will use the short form  $\phi_i$  for the volume fraction.<sup>5</sup>

According to the second law of thermodynamics, the grand canonical ensemble has to be in a minimum in equilibrium for the considered grand canonical ensemble. This grand canonical ensemble can be written as a functional of the volume fractions [180].

$$\Omega[\{\phi_i\}] = F[\{\phi_i\}] + \sum_i \int \phi_i (U_i(r) - \mu_i) dr. \quad (1.4)$$

We consider the grand canonical potential because we have considered a grand canonical ensemble at the beginning. In general, we have to formulate the corresponding thermodynamic potential to the considered ensemble and minimize this potential to obtain the respective equilibrium state. If a canonical ensemble is considered which is characterized by

---

<sup>3</sup>Here, we are considering the density  $\rho$ , because it is the classical property considered by cited literature.

<sup>4</sup>Here we consider only densities of particles that consist of exactly one particle. It is also possible to extend this formalism to a molecular density (see [180]). In that case a multidimensional vector  $\mathbf{R}$  has to be considered instead of the spatial vector  $r$ . The vector  $\mathbf{R}$  contains the information of the position of all particles of the molecule.

<sup>5</sup>Alternatively to DFT it is also possible to determine the equilibrium properties from the particle configurations. This can be done by employing Monte-Carlo simulation (see section 4.1.1)

a constant temperature, total volume and particle numbers, the free energy is minimized directly. The different thermodynamic potentials can be transformed into each other by Legendre transformation. The minimization of the grand canonical potential leads to the variational equations

$$0 = \frac{\delta F[\{\phi_i\}]}{\delta \phi_i} + U_i(r) - \mu_i. \quad (1.5)$$

Eq. (1.5) can be solved if the expression of the free energy is known. The solutions of this equation are the equilibrium volume fraction profiles of  $\phi_i$ . If the equilibrium profiles are known, the thermodynamic properties of the system can be computed employing methods of statistical mechanic [67]. In general, the exact form of the free energy is not known but approximated by physical models of the real system. We give three historic examples of free energy functionals of different systems, which shall give an impression what different kind of systems can be investigated with this approach. After that, we give a short systematic overview of approximating the free energy functional.

Before the systematic introduction of the DFT by Hohenberg and Kohn, a variational approach was already used by van der Waals to investigate the surface tension and the structure of the vapor-liquid interface in 1893 [168]. There he uses a second order gradient expansion of the free energy to describe the phase separated system. The free energy model was

$$F = \int f(\phi(r))dr + \kappa \int (\nabla\phi(r))^2 dr. \quad (1.6)$$

The investigated system consists of one component in a constant total volume and temperature [168]. The vapor (V) state of this component is in equilibrium with its liquid (L) state, the state can be described by one density profile. The parameter  $\kappa$  is a constant that can be related to the inverse temperature  $\beta$  and the direct correlation function  $c(r, \bar{\phi})$  containing the average volume fraction  $\bar{\phi} = (\phi_V + \phi_L)/2$  [168, 180].<sup>6</sup> The original work of van der Waals was not extremely visible at this time, which led to the reinvention of this method by Landau and Lifshitz in 1935 investigating the boundary of magnetic domains [97]. Later, Cahn and Hilliard established a related theory in 1958 to understand the vapor-liquid and liquid-liquid interface [26].

The last example considered isotropic particles only. The variation approach is also capable of investigating ensembles of anisotropic particles. This was originally done by Onsager in 1949 [126]. In that article he described the isotropic-nematic transition of lyotropic liquid crystals. In that case, the volume fraction  $\phi(r, \omega)$  is a function of the center of mass of the particles and the orientation angle of the molecules.<sup>7</sup> Onsager computed the lowest-order expansion of the free energy with respect to the now anisotropic density profile, which gives

$$F = \int \frac{\phi(r, \omega)}{\nu} \left( \ln \frac{\phi(r, \omega)}{\nu} - 1 \right) dr d\omega - \frac{1}{2\beta} \int dr_1 d\omega_1 \int \frac{\phi(r_1, \omega_1)\phi(r_2, \omega_2)}{\nu^2} e^{-\beta u(r_1 - r_2, \omega_1, \omega_2)} dr_2 d\omega_2. \quad (1.7)$$

---

<sup>6</sup>The direct correlation function is defined as the second functional derivative of the excess free energy [180].

<sup>7</sup>A more strict approach is to introduce the more general molecular density and expand this molecular density in terms of the center of mass of the particles and the orientation angle of the molecules [180].

In that formulation,  $u(r_1 - r_2, \omega_1, \omega_2)$  is the pair potential between two liquid crystal particles. The first integral can be identified as the ideal contribution of the free energy. The second integral considers the particle interaction and is derived as a virial expansion of the free energy up to the second order. This procedure is closely related to the derivation of the free energy of a not ideal gas.

The DFT was firstly used as a general methodology for a classical system by Ebner, Saam and Stroud in 1976 [40]. In their original work, they investigated the interfacial properties of a Lennard-Jones fluid. Their approach is related to the work of van der Waals, because the free energy functional is also obtained from a gradient expansion. The obtained free energy of the Lennard-Jones fluid is

$$F = \int f(\phi) dr + \frac{1}{4\beta} \int c(|r_1 - r_2|, \bar{\phi}) \left( \frac{\phi(r_1) - \phi(r_2)}{\nu} \right)^2 dr_1 dr_2. \quad (1.8)$$

The function  $c$  is again the direct correlation function. Now, the volume fraction  $\bar{\phi} = (\phi(r_1) + \phi(r_2))/2$  is the average volume fraction considering the spatial positions  $r_1$  and  $r_2$ . They also compared their results with respect to the surface tension and the binodal line of the phase diagram with experimental data for liquid argon, which shows good agreement.

### Modeling the Free Energy Functional

In this section, we present a short overview about the possible approaches of modeling the free energy functional. In section 1.2.2 we have already mentioned that the free energy functional is of special importance for the DFT method. If the functional form of the free energy is known, the density profiles can be obtained by minimizing this functional or the functional of a related thermodynamic potential dependent on the considered ensemble. We will present three methods of modeling this functional: the square gradient approximation, the excess free energy and the weighted density approximation.

The square gradient method is a phenomenological approach to solve a problem that raises for free energy functionals that depend only locally on the volume fraction. In that case the interfacial width vanishes, which is not consistent with experiments [145]. One of the simplest solutions is to expand the free energy functional in terms of the gradient of the volume fraction. If this expansion is truncated after the lowest order, the square gradient approximation is obtained [127]. The expression of the functional is the same as van der Waals derived shown in eq. (1.6) [168]. The minimization of this type of free energy functional gives a second order differential equation [44].

It is also possible to construct the free energy functional by perturbation around a known state with a known free energy. The free energy functional is then the sum of the ideal gas contribution, which is exactly known, and an excess term [180, 127]. The excess term is then expanded around the reference state of the uniform liquid [127]. The ideal gas contribution is

$$F^{\text{id}} = \frac{1}{\beta} \sum_i \int \frac{\phi_i}{\nu_i} \left( \ln \frac{\phi_i}{\nu_i} - 1 \right) dr. \quad (1.9)$$

Because we are considering a series expansion of a real system around the state of an ideal gas, we can use  $\phi_i/\nu_i$  to estimate the corresponding particle density of the ideal gas. The lowest order not vanishing term of the expansion of the excess free energy contains the

direct correlation function, which is related to the structure factor of the fluid [127]. This is also the reason for the appearance of this property in some of the previous examples. The dependence on this direct correlation function allows to construct the perturbative excess free energy from experimental data or independent theoretical investigations [127]. In general, multiple types of particle interactions influence the excess term of the free energy. The most commonly considered interactions are short range repulsion, van der Waals attraction, weak association, electrostatics and correlation attributed to chain connectivity [180].

The short range repulsion is commonly modeled as a hard sphere potential. There exist multiple analytic theories that describe the thermodynamic properties of a hard sphere fluid. The first established theories are the scaled particle theory [134], the Percus-Yevick theory [133] and the Boublik–Mansoori–Carnahan–Starling–Leland theory [14, 107]. From that basis, different DFT methods have been published to investigate an inhomogeneous system of hard spheres [180]. Here, we will only mention the fundamental measure theory by Rosenfeld, which is a self consistent theory [137]. The important feature of this method is that it is based physical and mathematical principles. Most other DFT on hard sphere systems employ the empiric weighted density approximation [180]. The fundamental measure theory can be applied to simple hard sphere liquids, polydisperse hard sphere liquids, fluid and solid phases, and not spherical particles as liquid crystals [138].

Van der Waals interactions are the commonly used interactions to describe non bound interactions [180]. Most DFT methods that consider van der Waals interactions employ the mean field approximation to evaluate them [180]. In the best scenario, these methods are semiquantitative [180]. Tang and Wu published an improved approach for the attractive excess free energy [159]

$$F_{\text{att}}^{\text{ex}} = F_{\text{att}}^{\text{ex}}(\{\bar{\phi}_i\}) + \sum_i \mu_i^{\text{att}} \int \Delta\phi_i dr - \frac{1}{2\beta} \sum_{i,j} \int \int c_{ij}^{\text{att}}(|r-r'|) \Delta\phi_i \Delta\phi_j dr dr'. \quad (1.10)$$

The term  $F_{\text{att}}^{\text{ex}}(\{\bar{\phi}_i\})$  is the attractive excess free energy of the reference fluid, the volume fraction  $\bar{\phi}_i$  are the average densities of the components  $i$ . This approach needs the excess chemical potential  $\mu_i^{\text{att}}$  and the direct correlation function  $c_{ij}^{\text{att}}$  as an input [180]. Commonly, the expressions of the excess chemical potential and the direct correlation functions are obtained from the first order mean-spherical approximation [180, 158]. It has been shown that this procedure is in very good agreement with the results obtained from simulation of simple systems like Lennard-Jones fluids and coarse grained polymers [102].

In the last part of this section we will shortly discuss the weighted density approximation. This is a class of approximations that are an alternative to the perturbation approach [127]. The fundamental idea of this approximations is that the free energy is not evaluated for the local value of the density but for weighted density averaged in a small region around the evaluated point in space [127]. The several weighted density approximations differ in the choice of the introduced weight function [127]. All approximations have to fulfill the condition that the second derivative of the excess free energy gives the direct correlation function [127, 32, 36]. These methods were successfully employed, e.g. to calculate the interface of liquids [31] and investigate the freezing of liquids [33].

### 1.2.3 Molecular Simulation of Liquids

In addition to the presented mean-field and density functional methods, liquid systems can also be investigated with molecular simulations. In molecular simulations the liquid system is modeled on particle level and the thermodynamic properties are computed with the temporal or ensemble averages of the simulated configurations [164]. We will consider two types of simulation in this section, the Monte-Carlo method and the molecular dynamics method. The Monte-Carlo method will be used in our studies to investigate the positioning of droplets (see chapter 4). Nevertheless, we include the molecular dynamics method because it is the alternative very popular and powerful method to simulate liquid systems. One important choice is the considered ensemble. The choice of the ensemble is determined by compared experiments or the application of the simulation. The ensemble is determined by which properties are fixed and the considered probability density of the states of the system [111]. The not fixed properties fluctuate and their average can be computed as a result of the simulation. The canonical ensemble is defined by constant particle number, total volume and thermodynamic temperature. If the pressure is fixed instead of the total volume, the ensemble is isothermal-isobaric. Both ensembles are mostly used to investigate phase properties [164]. For the investigation of adsorption isotherms and selectivities, the grand canonical ensemble is most commonly used. In that ensemble the chemical potentials, the total volume and the thermodynamic temperature are fixed. The Gibbs ensemble gives good results if phase transitions are simulated [131]. In that ensemble the total system is divided in multiple simulation boxes, each box contains one phase. The fixed variables can be particle number, total volume and temperature (Gibbs ensemble with imposed global volume) or particle number, pressure and temperature (Gibbs ensemble with imposed global pressure). Now, the total volume is the combined volume of all simulation boxes and the particle number is the combined particle number of all boxes. In addition to change the configuration of one box during a simulation step, the particles can also move from one box to another during simulation to sample the Gibbs Ensemble. The micro-canonical ensemble with fixed particle number, total volume and energy is of conceptual importance for molecular dynamics simulations [164].

In this section, we consider mostly continuous simulation models, where the spatial coordinate is continuous. This makes it easier to consider and introduce Monte-Carlo and molecular dynamics simulations in a combined section. Nevertheless, it is also possible to propose a lattice model of a liquid system for Monte-Carlo simulations [68, 113]. In this thesis we use such a lattice model to investigate the positioning of droplets (see section 4.1.1).

In this section, we consider only particles with no internal degrees of freedom. The second important feature of the model is the choice of the interactions between the particles. Very often the interaction  $U$  between two particles is modeled as the sum of the dispersion-repulsion interaction  $U_{ij}^{\text{d-r}}$ , the electrostatic interaction  $U_{ij}^{\text{el}}$  and polar interaction  $U_{ij}^{\text{pol}}$  [136]. The interaction between two particles is than  $U_{ij} = U_{ij}^{\text{d-r}} + U_{ij}^{\text{el}} + U_{ij}^{\text{pol}}$ . The total potential energy of the system is the sum of the pair interactions. The dispersion-repulsion interaction is important for weakly polar particles and commonly modeled by the Lennard-Jones potential [100]

$$U_{ij}^{\text{d-r}} = 4\epsilon_{ij} \left( \left( \frac{\sigma_{ij}}{r_{ij}} \right)^{12} - \left( \frac{\sigma_{ij}}{r_{ij}} \right)^6 \right). \quad (1.11)$$

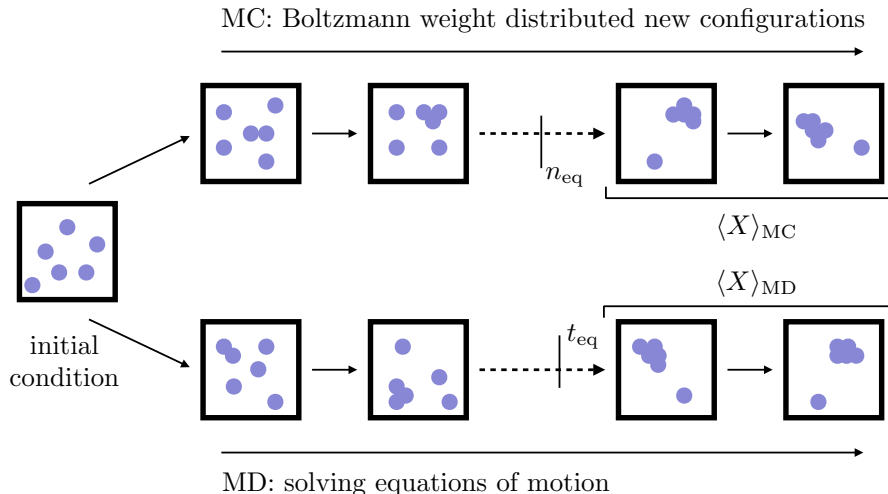


Figure 1.4 – A scheme of the generation of new configurations in Monte-Carlo (MC) simulations and molecular dynamics (MD) simulations. The initial conditions can be equal. The system is equilibrated after the time  $t_{\text{eq}}$  in the MD simulation or after  $n_{\text{eq}}$  steps in the MC simulation. The resulting equilibrium average of property  $X$  has to be equal for both methods. This sketch is adapted from [164].

The electrostatic interactions are computed from the Coulomb potential [164]. The polar interaction is influenced by the molecular polarizability, which can be obtained from experiment [164].

Very generic interactions are often used in lattice simulations [68, 113]. There the interaction between two particles is characterized by a parameter that is dependent on the distance on the lattice. Very often only nearest neighbor interactions are considered.

In the last part of this section we want to give an overview about important principles of Monte-Carlo simulations and molecular dynamics simulations.

#### *Monte-Carlo (MC) simulation*

To sample the probability density of the considered ensemble it is sufficient to maintain detailed balance during the simulation [164]<sup>8</sup>

$$P_i w_{ij} = P_j w_{ji} \quad (1.12)$$

$P_i$  is the probability of configuration  $i$  and  $w_{ij}$  is the transition probability from configuration  $i$  to configuration  $j$ . The probability of a configuration is proportional to its Boltzmann weight  $P_i \propto e^{-\beta E_i}$ , where  $E_i$  is the energy of configuration  $i$ .

The transition probability during a Monte-Carlo move is constructed so that detailed balance is maintained. One example of such a transition probability is found in the Metropolis algorithm [113]

$$w_{ij} = \min \left( 1, \frac{P_j}{P_i} \right). \quad (1.13)$$

<sup>8</sup>A more detailed discussion is given in chapter 4

If a canonical ensemble is considered, this transition probability is

$$w_{ij} = \min(1, e^{-\beta\Delta E}) \quad (1.14)$$

<sup>9</sup> The equilibrium value of a property  $X$  of a simulated system are obtained by computing the ensemble average over equilibrated configurations

$$\langle X \rangle_{\text{MC}} = \frac{1}{n - n_{\text{eq}}} \sum_{i=n_{\text{eq}}}^n X_i. \quad (1.15)$$

Here,  $X_i$  is the value of property  $X$  for configuration  $i$ . The number of configurations is  $n$ , the system is in equilibrium after  $n_{\text{eq}}$  configurations.

### *Molecular dynamics (MD) simulation*

Commonly, molecular dynamics simulations consider classical dynamics of the particles [164]. This assumption is well justified, if the de Broglie wavelength is much smaller than the average distance between two particles  $\Lambda_t \ll (V/N)^{1/3}$  [164]. The considered classical system can be described by the hamiltonian  $H(\{r_i\}, \{p_i\})$  in terms of the particle coordinates  $\{r_i\}$  and particle momenta  $\{p_i\}$ .

$$H(\{r_i\}, \{p_i\}) = \sum_i \frac{p_i^2}{2m_i} + U(\{r_i\}). \quad (1.16)$$

The first term is the kinetic energy of translation,  $m_i$  is the mass of particle  $i$ . The second term is the potential energy of the system. We neglect other contributions to the kinetic energy, like rotational energy, because we consider only simple particles with no internal degrees of freedom. With the hamiltonian eq (1.16), we obtain the Hamilton equations of motion

$$\frac{dr_i}{dt} = \frac{\partial H}{\partial p_i} = \frac{p_i}{m_i}, \quad (1.17)$$

$$\frac{dp_i}{dt} = -\frac{\partial H}{\partial r_i} = -\nabla_{r_i} U(\{r_i\}). \quad (1.18)$$

During the simulation these equations of motions are integrated using finite difference methods as the Verlet algorithms [171] or the Gear predictor-corrector algorithms [23]. These algorithms can be implemented in the micocanonical ensemble and also the other ensembles [164].

If molecular dynamics simulations are used, it is important to note, that the equations of motion sample the microcanonical ensemble. Other ensembles can be investigated by introducing a coupling with a heat bath or a pressure bath [121, 74], applying the Gauss constraint principle [43], or by rescaling of the velocities and/or particles [164].

The equilibrium value of a properties  $X$  in the considered ensemble are computed using the time average over equilibrated configurations

$$\langle X \rangle_{\text{MD}} = \frac{1}{t - t_{\text{eq}}} \int_{t_{\text{eq}}}^t X(t') dt'. \quad (1.19)$$

---

<sup>9</sup>In chapter 4, we use the more technical name acceptance probability  $p_A$  for the transition probability  $w_{ij}$

The time  $t_{\text{eq}}$  is the time after which the system is equilibrated. For ergodic systems in equilibrium this average is equal to the ensemble average obtained from the Monte-Carlo simulation  $\langle X \rangle_{\text{MC}} = \langle X \rangle_{\text{MD}}$ .

## 1.3 Spatial Organization of the Cell Through Phase Separation

### 1.3.1 Droplet-like Units in the Biological Cell

To ensure the complex functionality of a living cell, the cell has to be able to organize its components spatially and timely, respectively. One way of establishing spatial structures is the formation of compartments within the cell by liquid-liquid phase separation [116]. Membrane-less organelles are a typical example of these kind of structures. The membrane-less organelles can be found both in the nucleus and in the cytoplasm [116]. Examples of these objects in the nucleus are nucleoli, paraspackles, nuclear spackles, and Cajal bodies [116]. These organelles perform different tasks in the cell. In eukaryotic cells nucleoli are places of ribosome biogenesis besides the cytoplasm [69].<sup>10</sup> The function of paraspeckles and nuclear speckles can be summarized under control of gene expression [96, 152, 48, 49]. Until now, the role of the Cajal bodies is not fully understood [116]. What is known is that the Cajal bodies contribute to the regulation of small nuclear ribonucleo proteins (snRNPs) [28].<sup>11</sup>

Important examples of membrane-less organelles in the cytoplasm are P bodies, stress granules and germ granules [116].<sup>12</sup> The functions of the organelles are very different. The P bodies take part in mRNA transport, modification and translation [78]. Stress granules are membrane-less organelles that are formed in response of stress signals [5] and disassemble if the stress signal is removed [80]. Germ granules define the germ line of an organism during its development [172]. The P granules mentioned in the introductory sentences of this chapter are part of this class of organelles.

The formation of the organelles leads to a 10 to 100 fold higher concentration of certain proteins and nucleic acids inside the organelles compared to their fluid environment [101, 122]. This concentrated phase can be either be liquid-like [101, 122] or gel-like [84, 51]. These two situations can be differentiated experimentally by applying a shear stress on the surface of the organelle. In such a scenario gels show no flux under steady state conditions [84, 51, 95]. Other organelles are identified as liquid-like by investigating their viscoelastic properties [15, 101, 182, 41]. Furthermore, photobleaching experiments show a very fast exchange of molecules inside the liquid-like organelles with the surrounding phase [132, 117, 101, 21, 182].

After describing the existence of liquid-like objects in the cell we want to give a summary of the microscopic origin of these phase separations. In biology, two processes are important for triggering phase separation: (i) The interactions between the components can be changed, e.g. by phosphorylation [174], or (ii) its composition is adjusted, leading to the formation of macromolecular complexes [9, 21, 104, 117, 147, 175, 182]. It has been shown

---

<sup>10</sup>Ribosomes are organelles important for protein synthesis [153]

<sup>11</sup>snRNPs are proteins which build up larger structures used for splicing in the nuclear speckles.

<sup>12</sup>We want to point out that P bodies and the P granules mentioned in the introducing sentences of this chapter are different types of organelles. P granules are the germ granules of *C. elegans*, P bodies are a type of RNA granules which are contained in all cells.

that heterogeneous interactions, the interactions between different types of molecules, are essential for the phase separations involved in organelle formation [19, 174, 3, 163, 63]. Furthermore, the phase separation is strongly supported by multivalent features of the employed interactions [116]. The structural origin of this multivalent character is the repetitive use of folded domains, which are able to interact with other molecules, and low complexity disordered segments in the protein structure [116].<sup>13</sup> The flexibility of the disordered segments are necessary for the uncoupled binding events observed in liquid-like organelles [101]. This observation also explains why the disordered regions are overrepresented in proteins which are essential for the formation of liquid-like organelles [116]. According to these findings, the formation of membrane-less organelles can be regarded as an example of case (ii) of phase separation in biological systems. Regarding the detailed nucleation of the droplet-like structures in cells, the current understanding is that specific protein-nucleic acid or protein-protein interactions initiate the droplet formation by creating a micro-environment for the phase separation of other components [116]. The specific interactions are mostly electrostatic interactions or aromatic interactions. A current opinion is, that the variable contribution of the intermolecular interactions determines the selective accumulation of specific proteins in the organelles [116].

Analyzing the composition of the membrane-less organelles it has been revealed that most proteins are shared between different types of organelles [116]. On the other side, each organelle contains a specific type of RNA, which is essential for the organelle's identity [116]. It has been also shown that the disruption of the RNA transcription causes a re-localization of the proteins in different proteins, which makes the RNA essential for defining the protein composition of the organelles [148, 4]. In general, two functional types of components are present in organelles. i) Multivalent components which are essential for the phase separation. ii) components that are recruited by the intermolecular interactions [116].

### 1.3.2 Phase Separation in a Polarized Biological Cell

In the section 1.3.1 we presented examples of phase separation in biological cells. To be more specific, the biological examples are not homogeneous in general, but the presented arguments consider their formation as phase separation in homogeneous systems. In this section we will also consider the inhomogeneous character of a biological cell. To this end, we give a short introduction to cell polarity and discuss phase separation in a polarized environment considering the example of the one cell stage embryo of *C. elegans*.

Processes of generating an inhomogeneous environment in biological cells can be summarized as cell polarity [13, 39]. In general, cell polarity can be defined as a structurally and functionally asymmetric organization of the cell [13]. The field of cell polarity is very broad and contains multiple different mechanisms. Following Bornens' Review, two categories of cell polarity can be described [13]. In the first category, examples of cell polarity caused by intrinsic asymmetry of cell compartments can be found. In the second category, the cell polarity is generated by connecting compartmental polarities. Examples for the intrinsic asymmetry of cell compartments are the plasma membrane [6, 139], the actin [169, 167, 114] and tubulin cytoskeleton [79, 81, 120], the centriole or basal body organelle [7], and endomembranes [105]. The plasma membrane is composed of different types of

---

<sup>13</sup>Low complexity disordered segments are a special kind of intrinsically disordered protein regions, which show a bias to a small set of amino acids [116].

### 1.3. Spatial Organization of the Cell Through Phase Separation

---

lipids [13]. Under certain circumstances, these lipids can segregate and spatial asymmetry can be observed [13]. The actin and the tubulin assembly is caused by a head-to-tail polymerization leading to polarized structures [13]. Centrioles are intrinsically asymmetric, they possess proximo-distal and circumferential asymmetry [13]. The endomembrane system is build up by an intrinsically orientated array of membrane-bound organelles [13]. Examples of the second category of cell polarity, the connection of compartmental polarities, can be found in the cell cortex [108, 128, 178], the centrosome and microtubule-cortex connection [30], the centrosome-nucleus connection [106], and the golgi and the nucleus-centrosome connection [18]. The cell cortex is defined as the plasma membrane and the underlying associate proteins, e.g. cytoskeletal proteins [13]. In lower eukaryotes, the polar structure of the cortex is generated by the lateral connection of a microtubuli network with the plasma membrane [13]. The centrosome is an organelle, which has an approximately central position in the most animal cells [13]. It acts as the main microtubule organizing center. Its position is maintained by nucleation and anchoring of microtubuli [13]. By reorganizing its position, the centrosome can be part of polarization processes [13]. The centrosome and the nucleus maintain a strong connection in animal cells [13]. One function of this connection is the positioning of the nucleus [13]. The interaction of the golgi apparatus with the nucleus-centrosome connection can influence the position of the golgi apparatus [13].

This thesis is motivated by the cell polarity of the fertilized egg-cell of *C. elegans* before the first cell division [15, 71, 155]. With respect to the previously introduced classes of examples, this cell polarity is caused by the centrosome and microtubule-cortex connection. The interaction of the sperm centrosome and the cortex triggers the reorganization of the egg-cell and creates the polarity along the antero-posterior axis [30].

It has been observed, that between the fertilization and the first cell division, P granules are formed in the one cell stage embryo and collected on one side of the cell [155]. P Granules are non-membrane-bound compartments and consist of many proteins and RNA. Thus, they are of the same class as nucleoli [16], Cajal bodies [156] and stress granules [179].<sup>14</sup> P granules are liquid-like objects, which contain proteins and RNA. They are called liquid-like, because these compartments are not enclosed by a membrane and show typical droplet like behavior like wetting surfaces and the ability to fuse [15]. An important protein of this mixture is PGL-3. It is responsible for the phase separation forming the P granules [166]. Biologically, the P granules determine the germ lineage of the organism. Cells, which contain P granules are part of this germ line and form sperm cells or oocytes. Cells without the P granules differentiate into the somatic tissue [165]. It was currently claimed, that P granules are essential for the epigenetic inheritance of *C. elegans* [173]. In the later germ line development, two proteins segregate from the P granules forming Z granules.<sup>15</sup> In the adult worm, the P granules, Z granules and a third type of liquid droplets called *Mutator* foci form tri-condensate assemblages, the PZM granules. These structures are involved in controlling the transgenerational epigenetic inheritance [173]. A fertilized cell with P granules is shown in Fig. 1.5. Before the first cell division, the P granules are collected at the posterior side of the cell, which leads to an asymmetric cell division. This step is essential to obtain cell differentiation. After the forth cell division, the cells divide symmetrically to increase the number of cells [71]. The origin of this polarity of

---

<sup>14</sup>An introduction of this type of compartments was given in section 1.3.1. At this point we will repeat the important features of the P granules.

<sup>15</sup>The nomenclature of these structures is taken from [173]

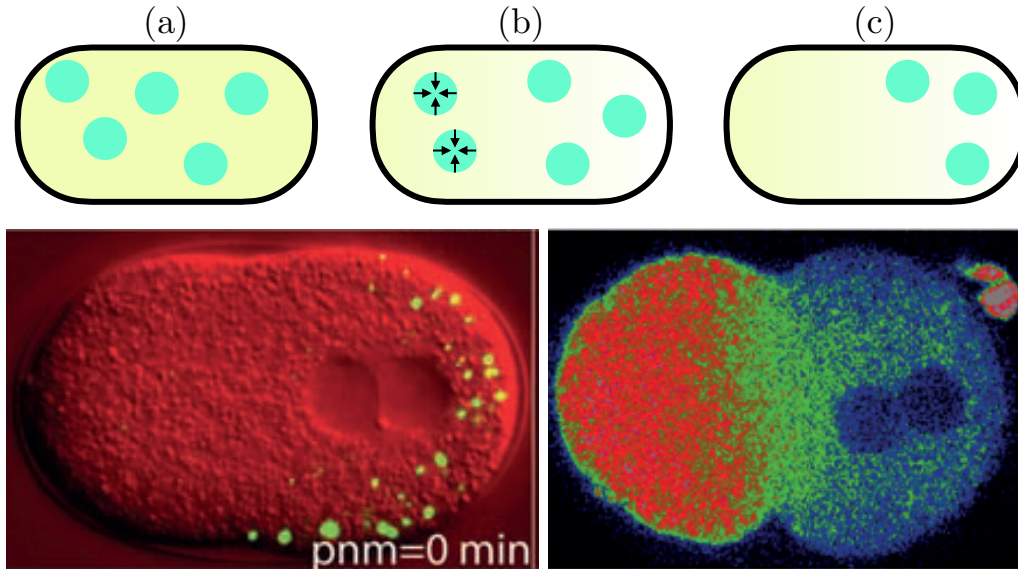


Figure 1.5 – (top) Generic sketch of the positioning of the P granules. Initially, the P granules (circles) are distributed homogeneously through the cell (a). After the creation of the Mex-5 gradient (background color gradient), the P granules dissolve at high Mex-5 concentrations and are stable at low Mex-5 concentration (b). This process leads to the polarization of the *C. elegans* embryo (c). (bottom left) P granules (green) are collected at the posterior side of the one cell stage embryo [15] (Permission for republishing in this thesis granted by the American Association for the Advancement of Science). (bottom right) The fluorescence intensity of the Mex-5 protein is plotted as a rainbow color code from blue (low concentrations) to red (high concentrations). The protein Mex-5 establishes a spatial gradient in the one cell stage embryo, where it is highly concentrated at the anterior side and low concentrated at the posterior side [59] (Permission for republishing in this thesis granted by Cell Press).

the cell is the fertilization itself, where one side is determined by the entrance of the sperm cell [30]. The penetration of the membrane of the egg cell leads to a different distribution of the membrane-bound PAR-proteins at the anterior and the posterior side of the cell [61, 72]. With this distinguishable functionalization of the membrane, proteins in the cytoplasm can be activated or deactivated differently on both sides of the cell. This mechanism generates a concentration gradient of the RNA-binding proteins MEX-5 and MEX-6 in the cytoplasm [35, 59, 129, 146, 160]. Mex-5 shows an approximately constant gradient in the cell [59]. These gradients are essential for segregating the P granules [15, 35, 53, 59, 146, 160]. At the anterior side, Mex-5 is highly concentrated, at the posterior side low concentrated. There are predictions that local concentrations of a chemical agent can regulate position dependent phase separation [15, 56, 98].

The first physical models that explained the positioning of P granules were onset models which studied the onset of symmetry breaking of the *C. elegans* embryo [15, 56]. They used spatial binary models considering that the P granule material is described by the volume fraction  $\phi$  and the remaining cytoplasm is described by the volume fraction  $1 - \phi$ . The models are based on the spatial dependence of the saturation volume fraction  $\phi_{\text{sat}}$ . The saturation volume fraction  $\phi_{\text{sat}}$  is the volume fraction value that has to be locally reached to observe droplet formation.

Brangwynne’s model is shown in fig. 1.6. He proposed a generic model that assumes that

### 1.3. Spatial Organization of the Cell Through Phase Separation

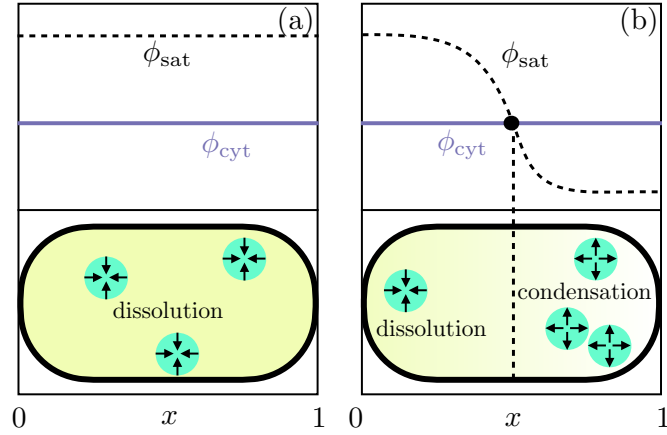


Figure 1.6 – (a) In the unpolarized cell, the saturation volume fraction of the droplet forming material  $\phi_{sat}$  is much higher than the volume fraction present in the cytoplasm  $\phi_{cyt}$ . The P granules are dissolving in the whole cell. (b) The polarization of the cell leads to a not constant saturation volume fraction along the anterior-posterior axis of the cell. If the onset volume fraction  $\phi_{cyt}$  is lower than the saturation volume fraction, dissolution of the P granules is observed in that region. Vice versa, if  $\phi_{cyt}$  is higher than  $\phi_{sat}$ , condensation of P granules is observed. This sketch is adapted from [15].

the saturation volume fraction  $\phi_{sat}$  is constant in the unpolarized cell. The volume fraction of the P granule material in the cytoplasm  $\phi_{cyt}$  is also constant in the unpolarized cell but much lower than the saturation volume fraction  $\phi_{sat}$ . This leads to dissolution of the P granules in the unpolarized cell. The second central assumption of this model is that the symmetry breaking leads to a not constant distribution of the saturation volume fraction  $\phi_{sat}$ . Now, two qualitatively different regions can be identified in the cell. Near the anterior side ( $x = 0$ ) of the cell, the onset volume fraction of the P granule material  $\phi_{cyt}$  is smaller than the saturation volume fraction  $\phi_{sat}$ . In that region dissolution of the P granules is observed. Near the posterior side ( $x = 1$ ) of the cell, the onset volume fraction  $\phi_{cyt}$  is higher than the saturation volume fraction  $\phi_{sat}$ . There, a condensation of P granules can be observed [15]. This model gives no detailed explanation of maintaining the gradient of  $\phi_{sat}$  and does not consider steady states of the system. Nevertheless, it is not clear, if the steady states are the essential features for the biological mechanism of droplet formation.

The model proposed by Gharakhani is based on the onset model proposed by Brangwynne. Gharakhani's model is sketched in fig. 1.7. He explains the spatial dependence of the separation volume fraction with the spatial dependence of the Flory-Huggins interaction parameter  $\chi = \chi(x)$ . At this point it is temporarily sufficient to interpret the Flory-Huggins interaction parameter as a binary interaction parameter between the P granule material and the solvent material. This interpretation is not exact, the Flory-Huggins interaction parameter is discussed in more detail in section 2.1. The idea of a spatial dependent Flory-Huggins parameter is based on a proposed influence of the Mex-5 protein on the self-interaction of the P granule material. A high concentration of Mex-5 leads to a weak interaction between the P granule particles and thus a dissolution of the P granules. Vice versa, a low concentration of Mex-5 induces a strong attractive interaction between the P granule particles and P granules are formed. To map this dependence, the Flory-Huggins interaction parameter  $\chi(x)$  is modeled as a linear increasing function along the anterior-posterior axis of the cell. This assumption of a spatial dependent Flory-Huggins

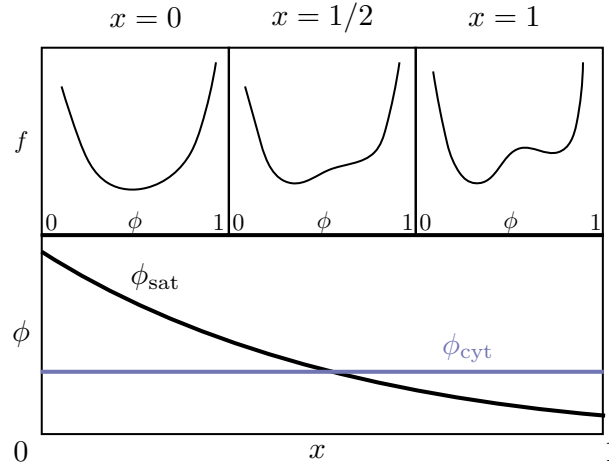


Figure 1.7 – In this model, the Flory-Huggins interaction parameter is linearly dependent on  $x$ ,  $\chi = \chi(x)$ . The evolution of the free energy density in space is sketched in the top row. This spacial dependence of the free energy leads to spatial dependence of the saturation volume fraction  $\phi_{\text{sat}}$ . Droplet growth is observed for  $\phi_{\text{cyt}} > \phi_{\text{sat}}$ . The droplets dissolve if  $\phi_{\text{cyt}} < \phi_{\text{sat}}$ . This sketch is adapted from [56].

interaction parameter leads directly to a spatial dependence of the free energy density  $f$ , which allows the calculation of the spatial profile of the saturation volume fraction  $\phi_{\text{sat}}$ . As a central result Gharakhani also obtains one region of the cell, where P granule dissolution is observed and one region where condensation of P granules is observed [56].

Lee proposed thermodynamic arguments employing a ternary liquid system considering the P granule material described by  $\phi_A$ , the regulator Mex-5 described by  $\phi_R$  and the remaining cytoplasm. His arguments use the two phase phase diagram of this ternary system shown in fig. 1.8. He proposed that the anterior-posterior axis can be modeled as a linear path in the ternary phase diagram in good approximation.<sup>16</sup> For the unpolarized cell, this path lies entirely in the demixed region of the phase diagram.<sup>17</sup> For the polarized cell, this path starts in the mixed region for the anterior side of the cell, crosses the binodal line at one point and thus ends in the demixed region for the posterior side of the cell. The use of thermodynamic arguments leads to a strong qualitative change of the spatially observed droplet formation even for weak imposed Mex-5 gradients [98].

The biological mechanism is not only based on liquid-liquid phase transition [17]. A detailed explanation of the positioning of droplets in the *C. elegans* embryo considering a maintained Mex-5 gradient is given in [143]. This explanation is based on the interaction between the protein PGL-3, mRNA (both are essential components of P granules) and the protein Mex-5. They present recent experiments that show, that mRNA binds PGL-3 in absence of Mex-5, which leads to a locally increased concentration of the protein PGL-3 and thus to phase separation [143]. In presence of Mex-5, mRNA is more likely to bind to MEX-5 and the droplet formation is inhibited. The combination of the different binding constants and the spatial gradient of Mex-5 leads to the positioning of the P granules in

<sup>16</sup>To elaborate this more, it is not important for this model that the path is linear. It seems to be sufficient if the path crosses the binodal line at exactly one point.

<sup>17</sup>The models of Brangwynne and Gharakhani consider a dissolution of the unpolarized cell, while Lee's model considers the presence of droplets in the unpolarized cell. This is most likely explained by different interpretation of the available data or different referred experiments. Nevertheless, this is not a serious problem for the presented models because they can be easily adapted for the respective other case.

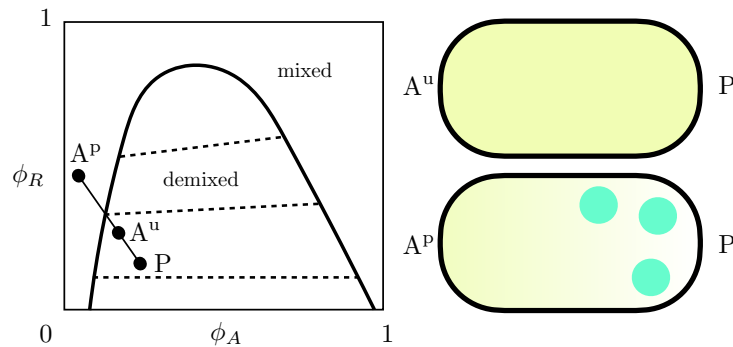


Figure 1.8 – This model considers a ternary liquid system of the P granule forming material  $A$ , the regulator Mex-5  $R$  and the cytoplasm. The interactions are chosen so that two phases can be present in the ternary liquid system. (left) The phase diagram of the ternary liquid system. The solid black line is the binodal line that separates the mixed region from the demixed region. The dashed lines are the tie lines that connect coexisting points in the phase diagram. (top right) The model proposes that the volume fraction of the regulator  $\phi_R$  lies in the demixed region for the whole cell.  $A^u$  indicates the anterior side of the unpolarized cell and  $P$  the posterior side. (bottom right) In the polarized cell the volume fraction of the regulator  $\phi_R$  reaches from the mixed region of the phase diagram to the demixed region. Mixing is observed near the anterior side of the polarized cell ( $A^P$ ), demixing at the posterior side ( $P$ ).

the polarized cell [143].

In this thesis, we call Mex-5 a regulator, because it controls the liquid-liquid phase transition of the system. The term regulator will be used in general for components that effects the phase separation of a liquid system. The presented biological effect is our motivation to investigate positioning of droplets in a generic three component liquid system. Because of this generic nature of this effect, it is also suitable to mention possible technical application of the positioning of droplets.

## 1.4 Droplet Positioning in Engineering Science

Besides biology, droplet positioning is also important for technical applications. In this section, we will give a short overview about microfluidic applications that involve droplets and consider some chosen examples. The focus will be on microfluidic systems because their small characteristic length scale is favorable for the generally long timescales of phase separation and diffusion. Furthermore, microfluidic systems are a very commonly used tool to applicate liquid systems. In the second part of this section, we give a short overview about the methods of droplet sorting as an example of droplet positioning in technical applications.

Microfluidic systems are considered to be one possibility of non electronic information processing [42]. This type information processing is based on chemical information or different states of the microfluidic system [42]. These processes are summarized as wet computing [42]. The advantage of such solutions is that the microfluidic system does not need a electronic periphery to process information, this task can be performed intrinsically. A common example of information processing on microfluidic devices are lab-on-a-chip systems for medical analytics [62, 88]. These lab-on-a-chip systems are microfluidic systems

in which the fluid sample is carried through some predefined tests [62, 88]. It is one way to automate standard procedures in analytics.

Another application of droplets in microfluidic systems is the possibility to run chemical reactions inside them [151]. There are two major reasons to perform reactions inside droplets. They can work as microreactors where reactions are performed with very small amount of educts. This is important, if the reagents are expensive or only available in limited amount [77, 177, 176]. They can also be used to realize compartmentized reaction conditions [38]. The applied chemical reactions can be broadly structured into two fields: biological chemistry and synthesis. Examples for biology related reactions in droplets are the analysis of DNA [22], protein crystallization [66, 65, 64] and enzyme kinetics, especially for the directed evolution of proteins [1, 37]. An example topic for synthesis inside droplets, which is not related to biology, is the synthesis of organic molecules. It is possible to perform simple one step reactions like the bromination of alkenes inside droplets [34] or more complex reactions like the formation of monomeric and novolak azo dyes in two steps [60]. Beside this organic reactions, droplets can also be used to synthesize mono disperse nanoparticles, e. g. silica gel particles [86], or microparticles with a controlled morphology, e. g. uniform capsules [157]. If it is possible to control the position of these microreactors, it would be possible to spatially control the chemical reaction.

In the last paragraphs we showed some examples of microfluidic applications that could profit from a possible droplet positioning. An actual example of droplet positioning in microfluidic devices is the sorting of droplets [144]. The techniques of droplet sorting can be broadly classified into active, passive and combined methods [144]. We have to mention, that in this section these terms are used according to their definition in Sajeesh's review [144]. The active and passive processes of droplet sorting should not be confused with the physical terms and is not related to active and passive systems in physics. Here, an active method is characterized sufficiently by the presence of an external field in which the droplets are sorted [144]. A passive method does not have this external field, it employs interactions between the particles, the structure of the microchannel or the flowfield [144]. In general active methods show a higher relative efficiency and throughput but can be problematic to apply because of the additional energy input to the system [144]. In that case passive methods can be chosen. Combined methods improve the efficiency or throughput of passive methods by applying also an external field [144]. Examples for passive methods are the pinched flow fractionation [124] or filtration [58].

The separation of droplets because of their movement on a surface with a hydrophobicity gradient can be regarded as an example for the active type of droplet sorting, because a hydrophobicity field is applied [76, 170]. The hydrophobicity gradients on the surface can be established by grafting mixed brushes on that surface [76]. The droplet moves to the preferred region of hydrophobicity. Other active methods are Dielectrophoresis [54, 52] and magnetic methods [27, 130].

Inspired by the *C. elegans* system presented in section 1.3.2, the droplets could be sorted qualitatively into one group of droplets, that moves to low regulator concentration and one group, which moves to higher regulator concentration. Also a quantitative sorting can be imagined. Here we propose, that it is somehow possible to build a chamber of a microfluidic device, that acts as a channel in which the droplets are moved by convection orthogonal to the gradient. If the droplets have the same velocity component in the direction of convection, after a given time they end up at different positions along the gradient. This positions can depend on different properties of the droplet like interaction

between regulator and droplet, size of the droplet or its mass. But with an adjusted assay, especially in preparing the set of droplets, a detailed sorting can be possible. Such a sorting protocol would be closely related to the method of chromatography [110].

## 1.5 Central Questions Adressed in this Thesis

Motivated by the asymmetric cell division of the *C. elegans* embryo, we have introduced a three component liquid system, where one of the components forms droplets in a solvent. A third component effects this phase separation and is called the regulator. Although the biological mechanism is understood [143], we aim to investigate this simplified system on a more general level to reveal fundamental physical principles of the phase transition in an inhomogeneous environment. To this end the following questions are focussed in this thesis:

1. *In *C. elegans*' one cell stage embryo a gradient of a chemical component regulates the positioning of the *P* granules at one side of the cell. Treating the multicomponent cytoplasm as a one component solvent we can ask for the distribution of the chemical components in the system. This is closely related to the question for a minimal model of the liquid system, that still shows the localization of droplets.*
2. *Are there stationary positions of droplets and what is the influence of the energetic interactions to these positioning? Do droplets prefer regions of high regulator concentration (correlated) or low regulator concentration (anti-correlated)? If such a stationery position exists, there are at least two qualitatively different possible dynamics of the droplet to reach this position. The droplet can simply drift to the stable position or it can dissolve and reassemble at the stationary positions. Can these dynamics be reproduced in the model and what determines the observed dynamics?*
3. *It is possible to investigate equilibrium models or non equilibrium models of the system with a regulator gradient. What are the differences or similarities of the results from these models regarding the droplet positioning?*

The positioning of droplets is of general interest. Besides of biology, this is an important tool in engineering and life science. We will comment on the potential contribution to this aspect in the outlook chapter 5 of this thesis.



## 2 Phase Separation in the Presence of Concentration Gradients in and out of Equilibrium

In this chapter we introduce a local equilibrium mean field description of the liquid system based on the Flory-Huggins theory [47, 75]. We will also describe how a concentration gradient of one component can be generated and maintained in such an equilibrium system. Furthermore, we will discuss the possibilities of maintaining a concentration gradient in non-equilibrium systems. We will close this chapter with a gedankenexperiment about how these concentration gradient can influence the phase separation of the system.

### 2.1 Flory-Huggins Theory of Phase Separation in Homogeneous Systems

In this section we discuss a local equilibrium description of a homogeneous three component liquid system. To this end we give an introduction to the Flory-Huggins theory for simple particles on a lattice and derive the free energy of this system. Here, simple particles mean that all types of particles have the same size.

The Gibbs free energy of the ternary system is  $G(N_A, N_B, N_R, T, P)$ , where the variable  $N_i$  describes the number of particles of component  $i$ . As mentioned in section 1.2.1, we can use Legendre transformation to obtain other thermodynamic potentials. The free energy is  $F(N_A, N_B, N_R, T, V) = G - PV$ .<sup>1</sup> We have to consider that only incompressible liquid systems are studied in this thesis. In that case we have to be careful which thermodynamic potential we choose. The reason for this is that the total volume  $V$  is determined by the sum of the volumes of the particles  $V = \nu_A N_A + \nu_B N_B + \nu_R N_R$ . All molecular volumes  $\nu_i$  are regarded as constant parameters describing the volume of one particle of type  $i$ . The state variable  $V$  is no longer independent from the composition state variables  $N_i$ . This do not change anything for the thermodynamic potential  $G$  because it is dependent on the pressure  $P$  and not the total volume. But if we consider  $F$ , we have to consider the additional constraint between  $V$  and  $N_i$  and the free energy  $F(N_A, N_B, N_R, T, V)$  is dependent on one less variable. The choice of  $N_A$  and  $N_R$  as the independent variables is arbitrary, each possible choice is physically equivalent. In this section, we will derive the free energy  $F$  of the homogeneous liquid system to introduce the Flory-Huggins theory. With that choice we also do not have to discuss and to define the pressure in the lattice model. Furthermore, we will use the volume fractions  $\phi_i = \nu_i N_i / V$  as the intensive variables to

---

<sup>1</sup>In this thesis, we use the short term free energy for the Helmholtz free energy. If other types of free energies are used, they will be explicitly named.

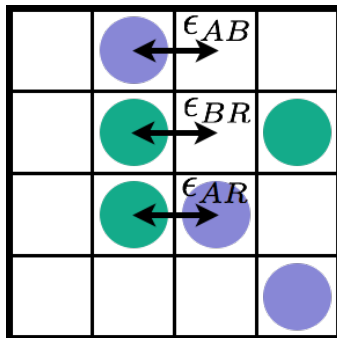


Figure 2.1 – 2D cut through the lattice model of the liquid system. The component  $B$  is represented as vacancies. The energetic cross interactions are labeled in this sketch, the self interactions are omitted.

describe the composition of the ternary system. These volume fractions are also constrained to  $1 = \phi_A + \phi_B + \phi_R$ .

We use a lattice model to describe the liquid system. The lattice is incompressible and completely filled with the three types of particles. There are no vacancies because that would introduce a fourth identity of the lattice sites. Each lattice site is occupied by exactly one particle. In the case of the completely filled lattice, the total volume of the system is given by the particle numbers and the lattice constant  $a$ , because each particle volume  $\nu_i$  is now  $a^3$ .

One way of computing the corresponding free energy is to determine the partition sum of this system using a mean field approximation of the lattice model to derive the free energy from it. This calculation is presented in appendix A.2 for a binary system and a ternary system. Here, in this introduction, we follow a simple derivation as presented in Rubinstein's book [140]. For that derivation we choose to consider a simple cubic lattice (fig. 2.1). The choice of the lattice is arbitrary and will only change the value of one parameter in the free energy. One lattice site has the volume  $\nu = a^3$ . We assume that this volume of the lattice sites is equal to the volume of the particles  $\nu_A = \nu_B = \nu_R = \nu$ . At this point, it would also be possible to derive the more general case in which particles can occupy more than one lattice site. This more general case was considered in the original work of Flory and Huggins [47, 75]. If such polymer-like particles are considered the following calculation, especially the calculation of the entropy, would become significantly more comprehensive. Because we will only consider particles with equal molecular volume  $\nu$  in this thesis, we decided to present the simplified case of one lattice site per particle in this introduction.

In the spirit of the Flory-Huggins theory we chose the state of the pure components as the reference state. The obtained free energy will thus describe the change of the free energy if these pure components are mixed. This argument is sketched in fig. 2.2. The three independent lattices of pure components of the initial system are combined to a completely filled lattice containing the three components, which is the mixed system. For that reason the Flory-Huggins free energy is also called the free energy of mixing. This free energy of mixing is defined as the free energy difference

$$F_{FH} = E_{\text{mix}} - E_{\text{pure}} - T(S_{\text{mix}} - S_{\text{pure}}). \quad (2.1)$$

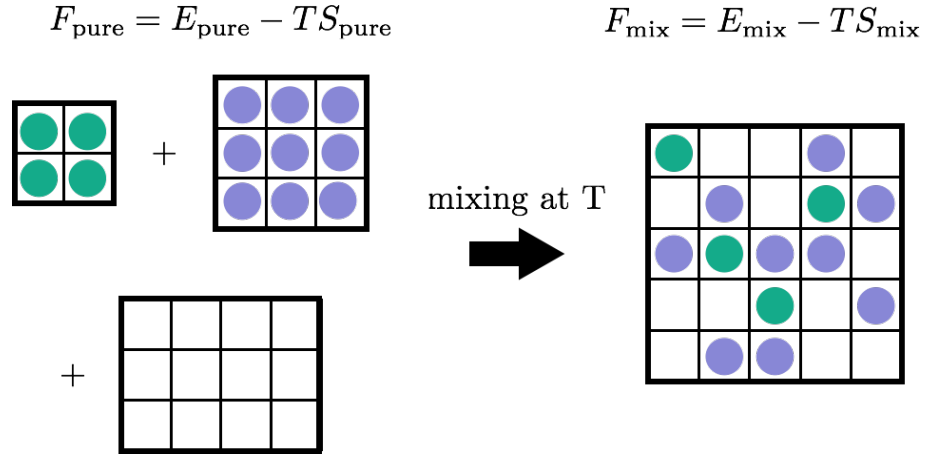


Figure 2.2 – Sketch of the state of the three pure substances (left side of the arrow) and the state of the mixture of these components (right side of the arrow). The free energy of mixing  $F_{FH}$  describes the free energy difference between these two states in the labeled direction.

We will discuss the difference of the entropy of the two states  $S_{\text{mix}} - S_{\text{pure}}$  and the difference of the internal energy of these states  $E_{\text{mix}} - E_{\text{pure}}$  separately. The entropy is given by Boltzmann's formula  $S = k_B \ln W$ , where  $W$  is the number of possible microstates of the system corresponding to a given macrostate. In the lattice model the microstates are specific configurations of particles on the lattice. The macrostates are determined by fixing the values of the state variables like the numbers of particles  $N_i$  and the lattice size  $N$ . Because we have exactly as many particles as lattice sites, we obtain  $W_{\text{mix}} = N!$  for the mixed state. The state of the pure substances consists of three lattices, where each lattice contains only one type of particles (see fig. 2.2). These lattices are also completely filled. For each separate lattice, the number of microstates is  $W_{i,\text{pure}} = N_i!$ . Because these three lattices are independent, the total number of microstates is the product of the number of microstates of the three lattices  $W_{\text{pure}} = N_A!N_R!(N - N_A - N_R)!$ . Applying Stirling's approximation  $\ln N! \approx N \ln N - N$ , the entropy of mixing is

$$S = N_A \ln \phi_A + N_R \ln \phi_R + (N - N_A - N_R) \ln (1 - \phi_A - \phi_R). \quad (2.2)$$

To calculate the internal energy, a mean field approximation is used. In this approximation, the composition of the environment of one particle is approximated by the averaged volume fractions of the three components. Because of this assumption, each lattice site can be considered separately. The internal energy of the total system is then given by the sum of the energy of all lattice sites. Furthermore, we consider only nearest neighbor interactions. The energy of a lattice site occupied by a particle of type  $i$  in the surrounding mean field is  $E_{i,\text{mix}}^{(1)} = \sum_{j=\{A,B,R\}} \epsilon_{i,j} \zeta \phi_j$ . The interaction energy of two adjacent particles  $i$  and  $j$  is given by  $\epsilon_{ij}$  (see fig. 2.1). The parameter  $\zeta$  is the coordination number and gives the number of nearest neighbors on the chosen lattice. In the case of the simple cubic lattice,

## Chapter 2. Phase Separation in the Presence of Concentration Gradients in and out of Equilibrium

---

$\zeta = 6$ . In the mean field approach, the probability of finding a particle of type  $j$  in an adjacent lattice site is equal to the average volume fraction of this component  $\phi_j$ . With this argument, the energy of the mixed state is given by  $E_{\text{mix}} = \frac{\zeta}{2} \sum_{i,j=\{A,B,R\}} \epsilon_{ij} N_i \phi_j$ . The energy of the pure state is  $E_{\text{pure}} = \frac{\zeta}{2} \sum_{i=\{A,B,R\}} \epsilon_{ii} N_i$ . Now, we introduce a new interaction parameter, the Flory-Huggins parameter, as

$$\chi_{ij} = \frac{\beta\zeta}{2} (2\epsilon_{ij} - \epsilon_{ii} - \epsilon_{jj}). \quad (2.3)$$

This Flory-Huggins interaction parameter  $\chi_{ij}$  can be interpreted as the energy change of separating two adjacent particles of type  $i$  in an environment composed only of particles of type  $j$  on the lattice. Using this parameter, the change of the internal energy of mixing is

$$\beta E = \chi_{AR} N_A \phi_R + \chi_{AB} N_A (1 - \phi_A - \phi_B) + \chi_{RB} N_R (1 - \phi_A - \phi_R). \quad (2.4)$$

The homogeneous free energy density is simply calculated by  $f_0 = F_{FH}/(N\nu)$  and has the form

$$\begin{aligned} \beta\nu f_0 = & \phi_A \ln \phi_A + \phi_R \ln \phi_R + (1 - \phi_A - \phi_R) \ln(1 - \phi_A - \phi_R) \\ & + \chi_{AB} \phi_A \phi_B + \chi_{AR} \phi_A \phi_R + \chi_{BR} \phi_B \phi_R. \end{aligned} \quad (2.5)$$

The choice of the lattice effects only the Flory-Huggins interaction parameter, because only this includes the coordination number  $\zeta$  of the lattice.

With this free energy of mixing we can calculate the equilibrium phase diagram of the system using the convex hull method. This is an geometrical method constructing the minimal convex free energy of the system. The idea is that the free energy has to be a convex function. The coexisting phases can be obtained from the corresponding convex hull. We sketch this method using a one dimensional free energy describing a binary liquid system. A generic free energy of that system is plotted in fig. 2.3. It is the free energy of the mixed systems. Now, we are asking for the coexisting phases, which are indicated by the points  $(\phi^a, f(\phi^a))$  and  $(\phi^b, f(\phi^b))$ . The condition of equal chemical potentials means, that the slope of the free energy is equal at both points. The free energy density of the phase separated system is  $\alpha f(\phi^a) + (1 - \alpha)f(\phi^b)$ , where  $\alpha$  is the volume of phase  $a$  divided by the total volume of the system. This condition is fulfilled, if both tangent lines are equal. This is known as the common tangent rule or Maxwell construction and is the special case of the convex hull method for one dimensional free energies. For higher dimensions we have to construct common tangent planes or common tangent hyperplanes to get the minimal convex free energy [70].

An essential thermodynamic potential and also a tool for calculating the equilibrium phase diagram of a system is the chemical potential  $\mu_i$  of a component  $i$ . A common definition of the chemical potential is the derivative of the free energy with respect to the particle numbers  $\mu_i = \partial_{N_i} F|_{T,V,N_{j \neq i}}$ . In general, the chemical potential can also be derived from other thermodynamic potentials corresponding to a thermodynamic ensemble. In the thermodynamic limit these definitions lead to the same property. When calculating the chemical potential on a lattice we have to take care from which thermodynamic potential it is derived. If we introduce the chemical potential as  $\mu_i = \partial_{N_i} F|_{T,V,N_{j \neq i}}$ , we have to be careful about the dependencies of the state variables  $V$  and  $N_i$ . It is not trivial to obtain the chemical potentials from the free energy considering an incompressible lattice model.

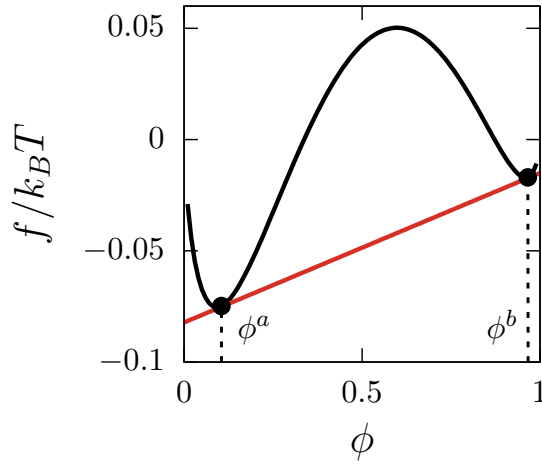


Figure 2.3 – The generic free energy density of a two component system is plotted as a black line. With the common tangent (red line) we obtain the two coexisting phases of composition  $\phi^a$  and  $\phi^b$ .

To define the chemical potential properly in this model, we can employ the Gibbs free energy  $G$ . The Gibbs free energy is related to the free energy by Legendre transformation

$$G(T, P, \{N_i\}) = F + PV. \quad (2.6)$$

All state variables of the thermodynamic potential  $G$  are independent for the lattice model and we can define the chemical potential as

$$\mu_i = \left. \frac{\partial G}{\partial N_i} \right|_{T, P, N_{j \neq i}}. \quad (2.7)$$

To explain the difference between eq. (2.7) and the definition of the chemical potential as derivative of the free energy, we will stress the lattice model once more. If we use the free energy, the chemical potential  $\mu_i$  measures the energy difference of inserting or removing one particle of type  $i$  to or from the lattice by keeping the temperature, the number of the particles of other components and the total volume constant. Constant total volume in the incompressible lattice model means also constant number of lattice sites. Such a property is hard to interpret and very hard to calculate. One solution of this problem is to define relative chemical potentials by defining which particle is removed from the lattice if a particle of type  $i$  is inserted and which particle replaces a removed particle of type  $i$  (mentioned in [142], see appendix A.1). If the Gibbs free energy is used to calculate the chemical potential like in eq. (2.7), it measures the energy difference of adding or removing a particle of type  $i$  by keeping the pressure, the temperature and the particle number of the other components constant. In this ensemble, the volume can change and adding or removing a particle can be done by changing the total number of lattice sites by one. In terms of the Gibbs free energy density  $g = G/V$  and the volume fractions  $\phi_i$ , the chemical

potential of a component in an incompressible lattice model is

$$\frac{\mu_i}{\nu} = g + \frac{\partial g}{\partial \phi_i} - \sum_{k=1}^{M-1} \phi_k \frac{\partial g}{\partial \phi_k}, \quad i < M \quad (2.8)$$

$$\frac{\mu_M}{\nu} = g - \sum_{k=1}^{M-1} \phi_k \frac{\partial g}{\partial \phi_k}. \quad (2.9)$$

This form of the chemical potential can be calculated by using the chain rule  $\partial_{N_i} = \sum_{k=1}^{M-1} \partial_{N_i} \phi_k \partial_{\phi_k}$  as well as the relations  $G = gV$  and  $V = \nu \sum_{j=1}^M N_j$ . The two cases in eq. (2.8) take into account, that  $M$  components are present, but the composition can be described sufficiently by  $M - 1$  volume fractions. This chemical potential can be used to compute the equilibrium phase behavior of the system. Two phases  $a$  and  $b$  coexist in thermodynamic equilibrium if the respective chemical potentials are equal  $\mu_i^a = \mu_i^b$ . Here, we consider a system in which one or two phases can be present. If only these two phases can be formed, we get  $M$  conditions from eq. (2.8). Compared to the  $2M - 2$  independent volume fractions, which are describing the composition of the two phases  $a$  and  $b$ , we have  $M - 2$  degrees of freedom. In the three component system, we can choose one volume fraction arbitrarily and calculate the others using the condition on the chemical potentials. In a binary system, the number of the degrees of freedom is zero, there is only one composition of phase  $a$  and one composition of phase  $b$  (see fig. 2.3). This considerations assume constant temperature and pressure. The number of degrees of freedom will change, if more than two phases can form (see eq. (1.2)). The chemical potentials can be identified as the slopes of the free energy density (compare fig. 2.3). Because of that the two discussed approaches of constructing the equilibrium phase diagram, namely the convex hull method and using the chemical potentials, are related.

## 2.2 Equilibrium Concentration Gradients in External Fields

In section 2.1 we discussed a ternary liquid system in thermodynamic equilibrium. This system was homogeneous. Now, we will introduce inhomogenities to the system by generating a non zero concentration gradient of one component. There are different possibilities for maintaining such a gradient. The first possibility is the use of diffusion, which will be discussed in section 2.3. The gradient is maintained by diffusion fluxes and asymmetric boundary conditions. In that case, the system is no longer in thermodynamic equilibrium because detailed balance is broken at the boundaries.

In this section, we discuss the maintaining of a regulator gradient in thermodynamic equilibrium. To this end, we introduce an external potential  $U_R(x)$ , which effects only the regulator directly. From now on, we call the component corresponding to the imposed concentration gradient regulator. This name is inspired by the asymmetric cell division of the *C. elegans* embryo described in section 1.3.2, where the protein gradient is essential for regulating the phase separation spatially. The spatial coordinate  $x$  is normalized by the system size  $L$ , it is  $x = \hat{x}/L$  with the spatial coordinate  $\hat{x}$  in real units. The free energy density including this external potential is

$$\beta \nu f(x, \phi_A, \phi_R) = \beta \nu f_0(\phi_A, \phi_R) + \beta U_R(x) \phi_R. \quad (2.10)$$

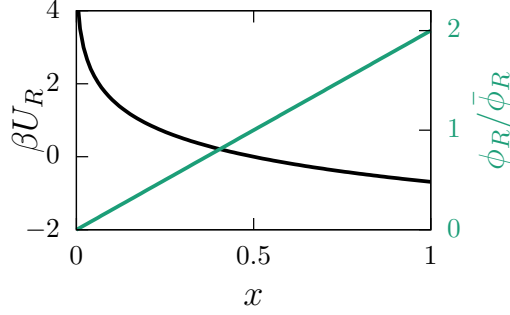


Figure 2.4 – External potential (black) and corresponding regulator distribution (grey) in the Boltzmann limit. The regulator distribution is presented by plotting the probability density of the regulator. The used parameter is  $s = 0.99$ .

This potential introduces a spatial dependence of the free energy density. Now, also the volume fractions are functions of the spatial coordinate  $x$ , it is  $\phi_i = \phi_i(x)$ . The derivation of  $f_0$  (see appendix A.2.2) shows, that the external potential can simply be included in the hamiltonian of the lattice model, so that eq. (2.10) can be derived directly. Now we can choose a certain potential. In this thesis, for the major part of the discussion, a logarithmic potential of the form

$$U_R(x) = -k_B T \ln(1 + s(2x - 1)) \quad (2.11)$$

is used. The parameter  $s$  determines the slope of the potential. The reason for this choice of the external potential is to get an linear regulator profile in the dilute limit. In the dilute limit, the profile can be estimated using the Boltzmann relation  $\phi_{R,\text{diluted}}/\bar{\phi}_R = \exp(-\beta U_R)$ , with the average volume fraction of the regulator  $\bar{\phi}_R$ . This gives the linear profile  $\phi_{R,\text{diluted}} = (2sx - s + 1)\bar{\phi}_R$ . At this point we should shortly discuss the limiting cases of the parameter  $s$ . For  $s = 0$  the potential vanishes. The cases  $s = -1$  and  $s = 1$  are the lower and upper limit of  $s$ . For  $s < -1$ , the argument of the logarithm becomes negative for  $x$  close to 1. In the other case, for  $s > 1$ , the argument of the logarithm becomes negative for  $x$  close to 0. These singularities vanish for  $-1 < s < 1$  and the potential is well defined. We choose the regulator gradient to be positive, so that we can confine the parameter  $s$  in  $0 \leq s < 1$ . This can be done without loss of generality, because a negative  $s$  would simply change the direction of the  $x$ -axis. The shape of the potential and the corresponding regulator profile is shown in fig. 2.4.

### 2.3 Concentration Gradients Maintained by Nonequilibrium Conditions

A regulator gradient can be established without the use of an external potential if a system out of equilibrium is considered. In this section, we set  $U_R$  to zero. Under non equilibrium conditions, the gradient can be created by a diffusion process of the regulator, if the respective boundary conditions are asymmetric. We assume, that the diffusion coefficient of the regulator is independent of the spatial position and the volume fractions of the components. This is valid, if the components are sufficiently diluted. That is the case outside of the droplet. Assuming a constant diffusion coefficient, the steady state regulator

profile is given by

$$\Delta\phi_R = 0, \tag{2.12}$$

where  $\Delta = \partial_x^2 + \partial_y^2 + \partial_z^2$  is the Laplace operator. The solutions of this condition are linear functions, the slopes and offsets are determined by the boundary conditions.

We will discuss three different boundary conditions, which can be used to create a linear regulator profile. We begin with considering constant regulator flux and constant regulator concentration boundary conditions. These are the standard examples for the diffusion process. Then, we introduce a special case of a regulator flux boundary condition, where the flux is dependent on the regulator concentrations at the system boundaries. We will include this special type of boundary condition, because we will use it later in the Monte Carlo simulations (see section 4.1.3). In the first case the volume fraction  $\phi_R$  is fixed at the boundaries. This is related to a constant chemical potential of the regulator at the boundaries. In average this two approaches will lead to the same result, but we have to be careful about the impact of fluctuations. If constant regulator concentration is used, the chemical potential of the regulator at the boundaries will fluctuate. Vice versa, if the chemical potential is chosen to be constant at the boundaries, the regulator concentration fluctuates. In the second case, the regulator gradient at the boundaries  $\partial_x\phi_R$  is given. The physical interpretation of this is a given regulator flux through the boundaries of the system. Because we are working with conserved particle numbers, the fluxes and thus the slope of the regulator profile have to be equal at  $x = 0$  and  $x = 1$ . We can relate this boundary condition to a gradient of the chemical potential of the regulator  $\mu_R$  at the boundaries. This relation is based on the definition of the particle flux  $j_R = -\Gamma_R\partial_x\mu_R$ , with the mobility of the regulator particles  $\Gamma_R$ . At this point we are neglecting possible dependencies of the regulator flux on the gradients of the other chemical potentials, assuming that the Onsager-coefficients of the cross couplings are small compared to  $\Gamma_R$  [125]. The mobility is dependent on the volume fractions, but a priori this dependence is unknown. Considering the Flory-Huggins free energy of mixing without an external potential eq. (2.5), we obtain  $\beta\partial_x\mu_R = 1/\phi_R\partial_x\phi_R$  for the gradient of the chemical potential if the regulator is diluted ( $\phi_R \ll 1$ ). It is known from experiments that the diffusion coefficient is a constant parameter for normal diffusion of diluted components [46]. To this end, the mobility has to be proportional to  $\phi_R$  within the Flory-Huggins model to obtain  $j_R = -D_R\partial_x\phi_R$ . Dependent on the employed representation the regulator flux is proportional to the gradient of the chemical potential or the gradient of the volume fraction of the regulator. Again, we have to be careful about the fluctuations. If a constant flux boundary condition is used, the gradient of the volume fraction and the chemical potential fluctuates. Otherwise, for a constant gradient of the volume fraction or chemical potential at the boundaries, the regulator flux will fluctuate.

The last boundary condition that is shortly discussed in this section is also a type of flux boundary conditions. Now, we introduce a regulator flux at the boundary which is dependent on the local volume fraction of the regulator there. This regulator flux is not constant, but if a steady state is reached, the flux of the regulator has to be equal at both boundaries and constant. This boundary condition is related to the constant flux boundary condition mentioned earlier if the steady state is considered. We will discuss this boundary condition in detail in section 4.1.3 and the appendix B.4. Considering a microscopic model, we can construct such a boundary condition by implementing an semipermeable wall for

the regulator particles at  $x = 0$  and a hard wall at  $x = 1$ . Each regulator particle which leaves the system at  $x = 0$  is immediately inserted at  $x = 1$ . Because the regulator particles move by diffusion, it is more likely that a particle leaves the system, if the local volume fraction at  $x = 0$  is high. With this mechanism, both, the regulator flux and the volume fraction gradient fluctuates. Also the volume fraction at the boundary shows fluctuations. The advantage of this mechanism is to maintain a strictly conserved total particle number on the microscopic level, which leads to a well defined canonical ensemble.

## 2.4 Gedankenexperiment on the Concentration Gradient in a Phase Separating System

Now, that we have introduced a gradient of the regulator, we will discuss the phenomenological effects of this gradient on the phase separating system. A more detailed and quantitative discussion of the inhomogeneous liquid system based on a Flory-Huggins type of free energy will be introduced in chapter 3. Here, we use arguments that are related to the model published in [98]. For the phenomenological gedankenexperiment, we start with the phase diagram of the homogeneous three component liquid system. We consider a two phase system, which means that two of the components segregate and the third component mixes with both phases. The phase diagram is shown in fig. 2.5 and was built using the convex hull method.<sup>2</sup> We choose  $\phi_A$  and  $\phi_R$  as the control parameters. The solid black line indicates the binodal line. The binodal line separates the phase diagram into two regions. In one region, the components  $A$  and  $B$  demix, in the other region a well mixed phase is observed.

We can discuss a spatial coordinate in the phase diagram by considering the regulator gradient. Because we consider a linear gradient, the simplest approach for the spatial inhomogeneous system is to map the  $x$ -coordinate to the different values of  $\phi_R(x)$ . The dark grey line shows a possible path in the phase diagram. We have to mention, that even if we know the exact distribution of the regulator, we do not know the exact response of the  $A$  material to this regulator gradient. That means that we know the  $x$ -parametrization of the  $\phi_R$ -axis but not of the  $\phi_A$ -axis. Because of this, the exact path is not known. We choose a simple straight line as a model path for the following phenomenological discussion. The model of a straight line is a good approximation for the onset of the phase separation. If the system is already separated, this approach will oversimplify the system. This is plausible, because there has to be a jump or jump-like behavior of the  $A$  volume fraction at the  $x$ -value of interface. Nevertheless, we will use this simple approach of a straight line in this discussion, because it is sufficient to visualize some general principles and effects of the inhomogeneous system. If we follow this path, we see that it lies in the mixed region of the phase diagram for high  $x$ -values, which correspond to high  $\phi_R$  (see fig. 2.4). At a certain point  $x_0$  it crosses the binodal line and continues in the demixed region of the phase diagram until it reaches  $x = 0$ . This simple example shows that the inhomogeneities of the system lead to new features of the three component liquid system. In this case the spatial distribution of the regulator results in a spatial controlled phase separation. Like mentioned, this is a simple gedankenexperiment and does not give access to the real distributions of the three components. Furthermore, the real effects can be much more

---

<sup>2</sup>We choose  $\chi_{AB} = 4$  and  $\chi_{AR} = \chi_{BR} = 1$  to build this phase diagram.

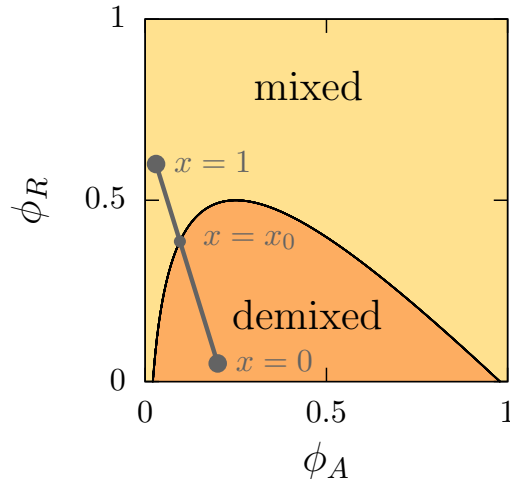


Figure 2.5 – Phase diagram of a three component liquid system. The solid black line indicates the binodal line. The solid grey line indicates a path along the regulator gradient parametrized by the spatial coordinate  $x$ . The exact values of  $\phi_A$  are not known, that line should be regarded as an model path to visualize spatial effects. Following this path, the system is well mixed for high  $x$ , which corresponds to high  $\phi_R$ . At a certain point  $x_0$  the path crosses the binodal line and continues in the demixed region of the phase diagram.

complex as we will see in chapter 3 and chapter 4. In chapter 3 we will introduce the free energy as a functional of the volume fractions  $\phi_A$  and  $\phi_R$  using the Flory-Huggins free energy density. The minimization of this free energy gives access to the actual equilibrium states of the mean-field model of the system. Furthermore, we will present Monte Carlo simulations in chapter 4, which are applied to equilibrium systems and non-equilibrium systems. To this end, we will employ the different ways of generating a regulator gradient, namely the external potential method and diffusion method.

# 3 Mean-Field Theory for the Spatial Regulation of Phase Separation in Equilibrium

In this chapter we will introduce a one-dimensional mean field model of the ternary liquid system in equilibrium. The results of this approach reveal, that two steady states of droplets are possible if a linear regulator distribution is maintained. The droplet can either be localized at high regulator concentration or at low regulator concentration. The transition between these two states is identified as a discontinuous phase transition.

## 3.1 Minimization of the Mean-Field Free Energy of the Inhomogeneous System

In this section, we describe an inhomogeneous liquid system of three components and compute its equilibrium state. Therefore, we start with the Flory-Huggins free energy density, which now has a spatial dependence [47, 75]

$$\begin{aligned}
 \beta \nu f(x) = & \phi_A \ln \phi_A + \phi_R \ln \phi_R + (1 - \phi_A - \phi_R) \ln(1 - \phi_A - \phi_R) \\
 & + \chi_{AB} \phi_A \phi_B + \chi_{AR} \phi_A \phi_R + \chi_{BR} \phi_B \phi_R \\
 & + U_R(x) \phi_R + \frac{\kappa_A}{2} (\partial_x \phi_A)^2 + \frac{\kappa_R}{2} (\partial_x \phi_R)^2 + \frac{\kappa}{2} \partial_x \phi_A \partial_x \phi_R, \\
 U_R(x) = & - \ln(1 + s(2x - 1)).
 \end{aligned} \tag{3.1}$$

The used spatial coordinate  $x$  is scaled by the system size  $L$  with  $x = \hat{x}/L$ , where  $\hat{x}$  is the not scaled Cartesian coordinate. The first line in eq. (3.1) contains the entropic contributions to the free energy, which have a logarithmic form. The second line shows bilinear terms, which are obtained from the binary particle interactions. In this mean field model, the strength of this interaction is linearly dependent on the volume fractions of both interacting components. The strength of the interactions between component  $i$  and  $j$  are given by the Flory-Huggins interaction parameters  $\chi_{ij}$ . These contributions were already introduced in section 2.1 (see eq. (2.3)). In the case of an inhomogeneous system all volume fractions are fields  $\phi_i = \phi_i(x)$ . Because we are interested in finding the equilibrium states of the mean-field description, we use the external potential  $U_R$  to generate the regulator gradient. Here, we use the potential introduced in eq. (2.11) if no other potential is explicitly defined. Now, we introduce also gradient terms in the spatial dependent free energy density. The three gradient terms act as an energetic penalty for large gradients. The dependency of the free energy on the gradient terms is obtained from

the gradient expansion of the free energy [180, 168]. Because of symmetry arguments we consider only even terms in this expansion. The expansion is truncated after the quadratic term. The complete quadratic term is  $\tilde{\kappa}_A/2(\partial_x\phi_A)^2 + \tilde{\kappa}_B/2(\partial_x\phi_B)^2 + \tilde{\kappa}_R/2(\partial_x\phi_R)^2 + \tilde{\kappa}_{AB}/2\partial_x\phi_A\partial_x\phi_B + \tilde{\kappa}_{AR}/2\partial_x\phi_A\partial_x\phi_R + \tilde{\kappa}_{BR}/2\partial_x\phi_B\partial_x\phi_R$ . Applying  $\phi_B = 1 - \phi_A - \phi_R$  to the gradient terms leads to the gradient terms included in eq. (3.1). With respect to the gradient expansion we are considering effective coefficient in this model. The constant  $1/\sqrt{\kappa_i}$  can be identified as a characteristic length scale of the interface of a droplet of component  $i$ . Eq. (3.1) can also be obtained by computing the continuum limit of the introduced lattice model. This derivation is presented in [142] for a binary liquid system. Based on this, the corresponding derivation for a three component system is presented in appendix A.3. We will discuss the effect of the interfacial width and the choice of the  $\kappa_i$  parameters in section 3.2.3.

The free energy of the bulk region of the system is given by the integral of the free energy density over the system size <sup>1</sup>

$$F_{\text{bulk}}[\phi_A, \phi_R] = \int_0^1 f dx. \quad (3.2)$$

Furthermore, we consider particle conservation of all three types of particles. Because the composition is described by only two independent numbers of particles (we choose  $N_A$  and  $N_R$ ), we can define two constraints on the corresponding volume fractions

$$\bar{\phi}_i = \int_0^1 \phi_i dx, \quad (3.3)$$

where  $\bar{\phi}_i$  is the average volume fraction of component  $i$ . The index  $i$  can be either  $A$  or  $R$ . This choice is arbitrary, every combination of two components can be chosen. This integral gives exactly the average volume fraction because we chose the system size to be 1. The constrained free energy is

$$F_{\text{bulk}}^{\text{cons}}[\phi_R, \phi_A] = \int_0^1 \left( f + \sum_i \lambda_i (\phi_i - \bar{\phi}_i) \right) dx, \quad (3.4)$$

with each Lagrange multiplier  $\lambda_i$  corresponding to the respective constrain on  $\phi_i$ .

At the boundaries, we introduce a short ranged potential  $W_i(x)$ . This potential controls the wetting behavior of component  $i$  and is determined by the interaction between the particles of component  $i$  and the wall particles. We choose that the wall at  $x = 0$  and  $x = 1$  is of the same type. The wall potential can be written as

$$W_i = w_i (\phi_i(0) + \phi_i(1)). \quad (3.5)$$

The parameters  $w_i$  are effective interaction parameters of  $A$ - and  $R$ -particles with the wall. They are related to the molecular interaction strength  $\hat{w}_i$  of a particle with the wall by  $w_i = \hat{w}_i - \hat{w}_B$ . The origin of these effective parameters is again the dependence of the volume fractions  $1 = \phi_A + \phi_B + \phi_R$ . We consider the case of equal interactions at both walls, so that it is sufficient to use one interaction parameter  $w_i$  for each of the independent fields to describe the boundaries. A negative  $w_i$  means, that the wall is attractive to component  $i$ , in this case wetting at the boundary is expected. A positive  $w_i$  corresponds

---

<sup>1</sup>Here, the bulk region of the system means the system without the boundaries.

### 3.1. Minimization of the Mean-Field Free Energy of the Inhomogeneous System

---

to a repulsive wall interaction regarding component  $i$  and we expect weaker wetting at the boundary. The total free energy of the system is the sum of the constrained bulk free energy eq. (3.4) and the boundary interactions eq. (3.5)

$$F[\phi_A, \phi_R] = F_{\text{bulk}}^{\text{cons}} + \sum_{i=A,R} W_i. \quad (3.6)$$

At this point, we neglect constant contributions, which appear because of the use of the effective wall interactions  $w_i$ . This constant offset has no influence on the physics of the system.

To obtain the equilibrium states, the total free energy eq. (3.6) is minimized. To this end, we compute the first functional derivatives of the free energy functional with respect to the independent volume fraction fields  $\phi_A$  and  $\phi_R$ . The equilibrium states are stationary points of the free energy functional. As a necessary condition, the first functional derivatives have to vanish.<sup>2</sup>

$$\begin{aligned} 0 &= \delta_{\phi_i} F[\phi_A, \phi_R] \\ &= \int_0^1 \left( \frac{\partial f_0}{\partial \phi_i} + U_R \delta_{iR} + \lambda_i \right) \delta \phi_i dx \\ &\quad + w_i (\delta \phi_i|_{x=0} + \delta \phi_i|_{x=1}) + \int_0^1 \left( \kappa_i \partial_x \phi_i + \frac{\kappa}{2} \partial_x \phi_j \right) \delta (\partial_x \phi_i) dx \\ &= \int_0^1 \left( \frac{\partial f_0}{\partial \phi_i} + U_R \delta_{iR} + \lambda_i - \kappa_i \partial_x^2 \phi_i - \frac{\kappa}{2} \partial_x^2 \phi_j \right) \delta \phi_i dx \\ &\quad + \left( w_i + \kappa_i \partial_x \phi_i|_{x=1} + \frac{\kappa}{2} \partial_x \phi_j|_{x=1} \right) \delta \phi_i|_{x=1} \\ &\quad + \left( w_i - \kappa_i \partial_x \phi_i|_{x=0} - \frac{\kappa}{2} \partial_x \phi_j|_{x=0} \right) \delta \phi_i|_{x=0}. \end{aligned} \quad (3.7)$$

The term  $f_0$  is the free energy density without the external potential and the gradient terms. It has the same form as  $f_0$  introduced in section 2.1 as the homogeneous free energy density (see eq. (2.5)). The difference is that the volume fractions have to be interpreted as volume fraction fields, here. The last two lines of eq. (3.7) are the result of the partial integration of the functional derivative. Because there are two independent volume fraction fields, we have to minimize the free energy functional with respect to these two arguments. We get two first functional derivatives, which is indicated by the index  $i$ , that can be either  $A$  or  $R$ . The index  $j$  is the corresponding component  $R$  or  $A$ . The variation of the fields  $\delta \phi_i$  occurs in the integral kernel and the boundary term as a factor. Because the variation  $\delta \phi_i$  is of arbitrary value, the functional derivatives only vanish if both brackets, the bracket in the integral kernel and in the boundary terms, are zero.<sup>3</sup> With this argument, we get the Euler-Lagrange equations from the integral kernel and the boundary conditions of the system from the boundary term. Considering  $i = A, R$  the two Euler-Lagrange equations are

$$0 = \frac{\partial f_0}{\partial \phi_i} + U_R \delta_{iR} + \lambda_i - \kappa_i \partial_x^2 \phi_i - \frac{\kappa}{2} \partial_x^2 \phi_j. \quad (3.8)$$

---

<sup>2</sup>Besides the minima, this condition also accounts for maxima and saddle points.

<sup>3</sup>The characterization as arbitrary is slightly sloppy at this point, because  $\delta \phi_i$  has to be consistent with the constraints eq. (3.3).

The solutions also have to solve the four boundary conditions

$$\begin{aligned} 0 &= w_i - \kappa_i \partial_x \phi_i|_{x=0} - \frac{\kappa}{2} \partial_x \phi_j|_{x=0} \\ 0 &= w_i + \kappa_i \partial_x \phi_i|_{x=1} + \frac{\kappa}{2} \partial_x \phi_j|_{x=1}. \end{aligned} \quad (3.9)$$

These type of boundary conditions, which are directly derived from the minimization condition considering an arbitrary variation  $\delta\phi_i$  are called the natural boundary conditions of the problem [55].<sup>4</sup> If we are neglecting the cross term  $\kappa$  for a moment, a closer look at the boundary conditions shows that for an attractive  $w_i < 0$ , the gradient of the field  $\phi_i$  has to be negative at  $x = 0$ , because  $\kappa_i$  is always positive.<sup>5</sup> This leads to a local accumulation of component  $i$  near the left boundary. This is referred to as a wetting boundary condition. The term non wetting boundary condition is used for  $w_i > 0$ . In our studies, we will always use  $w_i = 0$ . The equilibrium density profiles of the components  $A$  and  $R$  are the solutions of the second order boundary value problem eqs. (3.8, 3.9).

The system of differential equations can be diagonalized to separate the second derivatives of the volume fraction fields. This procedure also helps the numerical treatment. To sketch the diagonalization, we use the matrix form of this system of equations.

$$\begin{aligned} M \vec{\phi}'' &= \vec{h} \\ \begin{bmatrix} \kappa_A & \frac{\kappa}{2} \\ \frac{\kappa}{2} & \kappa_R \end{bmatrix} \begin{bmatrix} \partial_x^2 \phi_A \\ \partial_x^2 \phi_R \end{bmatrix} &= \begin{bmatrix} \frac{\partial f_0}{\partial \phi_A} + \lambda_A \\ \frac{\partial f_0}{\partial \phi_R} + U_R + \lambda_R \end{bmatrix} \\ \vec{\phi}'' &= M^{-1} \vec{h}, \\ \text{with } M^{-1} &= \frac{1}{\det M} \begin{bmatrix} \kappa_R & -\frac{\kappa}{2} \\ -\frac{\kappa}{2} & \kappa_A \end{bmatrix} \end{aligned} \quad (3.10)$$

The matrix  $M^{-1}$  is the inverse matrix to the coefficient matrix  $M$ , the product  $M^{-1}M$  gives the  $2 \times 2$  unit matrix. In appendix A.4, we show how this system of differential equations can be reformulated as a first order boundary value problem. The first order problem will be used for the numerical solution.

## 3.2 Results of the Mean-Field Calculation

### 3.2.1 Defining an Order Parameter to Characterize the Correlation of Volume Fraction Fields

Most of the numerical studies in this thesis investigate the influence of the Flory-Huggins interaction parameters. The Flory-Huggins interaction parameters are considered as the control parameters of our studies. For each of this interaction parameter, we define an order parameter as the derivative of the total free energy of the system with respect to a

---

<sup>4</sup>If we have information about the variation  $\delta\phi_i$  at the boundary,  $\delta\phi_i$  can vanish there. In that case, we obtain the essential boundary conditions from this information and the brackets are arbitrary. In section 3.3 a periodic external potential is used and essential boundary conditions are obtained.

<sup>5</sup>The parameters  $\kappa_A$  and  $\kappa_R$  have to be positive as a necessary condition for the existence of stable solutions [55].

control parameter.

$$\rho_{ij} = \frac{1}{\mathcal{N}_{ij}} \frac{\partial (F - F_{\text{hom}})}{\partial \chi_{ij}}. \quad (3.11)$$

Here, we subtract the free energy of a corresponding homogeneous reference system  $F_{\text{hom}} = F(\bar{\phi}_A, \bar{\phi}_B)$ . The homogeneous reference system has the same average volume fractions as the inhomogeneous system. This subtraction causes a constant shift to the order parameter, but does not influence the physics in any sense. We include the shift so that the order parameter can be negative or positive. The parameter  $\mathcal{N}_{ij}$  is the normalization of the corresponding order parameter. This normalization will be discussed in detail in appendix A.5. This procedure defines three order parameters corresponding to the three Flory-Huggins parameters of this model (see eq. (3.1)). By applying the definition of the order parameter eq. (3.11) to the free energy eq. (3.6), the order parameter can be computed using the equilibrium profiles of the respective components

$$\rho_{ij} = \frac{1}{\mathcal{N}_{ij}} \int_0^1 (\phi_i \phi_j - \bar{\phi}_i \bar{\phi}_j) dx. \quad (3.12)$$

The obtained structure is similar to the structure of the covariance used in mathematical statistics. Stressing this similarity, the averages of the volume fractions or products of volume fractions in eq. (3.12) correspond to the average of the random variables and product of random variables in the definition of the covariance [135].<sup>6</sup> Constructing this form is also one reason for including the homogeneous free energy  $F_{\text{hom}}$  in the definition of the order parameter eq. (3.11). Motivated by this similarity to the covariance, we can define three classes of states, depending on the sign of the order parameter. A negative order parameter  $\rho_{ij}$  describes an anti-correlation between the distributions of the two components  $i$  and  $j$ . In this case, we find high concentrations of  $i$  in regions, where the concentration of  $j$  is low. In the same way, we can interpret positive order parameters as a correlation between the respective distributions. In that case, the concentration of component  $i$  and  $j$  are high or low in the same regions. The narrow case of a vanishing order parameter indicates a not correlated system.

The absolute value of the not normalized order parameter is mainly influenced by the average volume fractions of the components. To change this, the normalization of the order parameter is introduced. From the field of mathematical statistics we know, that a covariance can be normalized by the variances. This method cause not beneficial behavior of the order parameter for our studies. The classical correlation factor, which is defined as the covariance normalized by the variances, are +1 or -1 if one random variable is linearly dependent on the other. If we would use this method for the volume fractions in the liquid system, we would observe, that the order parameter is +1 or -1, if the components are mixed, because in that case there is no jump of the volume fractions involved and the volume fractions are approximately linearly dependent on each other. Because we are particularly interested in the droplet states, we introduce a normalization that focus on these phase separated states rather than the mixed states. We call a state a droplet state, if the system separates into a  $A$ -rich phase and a  $B$ -rich phase. To focus on the droplet states we use the maximum variance of the distributions instead of the variance. This maximum variance corresponds to a phase separated state. Because the maximum

---

<sup>6</sup>Given the random variables  $X$  and  $Y$ , the covariance is defined as  $Cov(X, Y) = \langle (X - \langle X \rangle)(Y - \langle Y \rangle) \rangle$ .

variances are always higher than the respective actual variances the order parameter is still confined between  $-1$  and  $+1$ . The volume fraction profiles of the reference state of maximal or minimal order parameter are step functions. Each component can jump independently from 0 to 1. The position of the jump is determined by the respective average volume fraction. Obviously, this is not possible in the physical system because of the constraints on the volume fractions, but constructs the system with the strongest separation as the reference system for the normalized order parameter. The detailed calculation of the maximal variance is shown in appendix A.5. The obtained normalization is

$$\mathcal{N}_{ij} = \sqrt{\bar{\phi}_i (1 - \bar{\phi}_i) \bar{\phi}_j (1 - \bar{\phi}_j)}. \quad (3.13)$$

Now, if the order parameters of two configurations are compared, the configuration with the higher absolute value of the order parameter is more similar to a step-like distribution. Because of this property of the introduced order parameter, the parameter can be used to highlight the correlated or anti-correlated droplet states, which would not be possible with the conventional normalization using the variance.

### 3.2.2 Classification of the Observed Steady States

In this section, we give a short overview about possible equilibrium states of the ternary liquid system. We will also introduce a classification of the equilibrium states. The first criterion of classification is if the system is phase separated in an  $A$ -rich phase and an  $A$ -depleted phase or if it is well mixed. Now, we have to consider that the system is spatial inhomogeneous by construction. A major difference compared to the discussion in section 2.1 is that an external potential is present and influences the distribution of the regulator directly. Because of the inhomogeneous distribution of the regulator, the  $A$ -material is also not homogeneously distributed in the most cases. In general, three coexisting phases are possible in a ternary liquid system. In this thesis we consider only states with two coexisting phases or mixed states. This can be achieved by the choice of the values of the interaction parameters. Considering only two coexisting phases also means that one of the components has no tendency to separate into a separate phase. Here we choose the regulator to be mixed with all the other components.

The second criterion of classification is the correlation between the different volume fraction profiles. Here, we call a configuration correlated, if the volume fraction fields of the regulator and component  $A$  are correlated like sketched in fig. 3.1 (top left). The order parameter  $\rho_{AR}$  is positive in that case. For an anti-correlated configuration, the order parameter  $\rho_{AR}$  is negative, and the volume fraction fields of the regulator and component  $A$  are anti-correlated. Such a state is sketched in fig. 3.1 (top right).

The different combinations of the introduced classification criteria is shown in fig. 3.1. This classification covers all types of steady states we will find in the mean field model. Even though this classification is introduced for the equilibrium states, we will later see, that it can be also applied to the non equilibrium system.

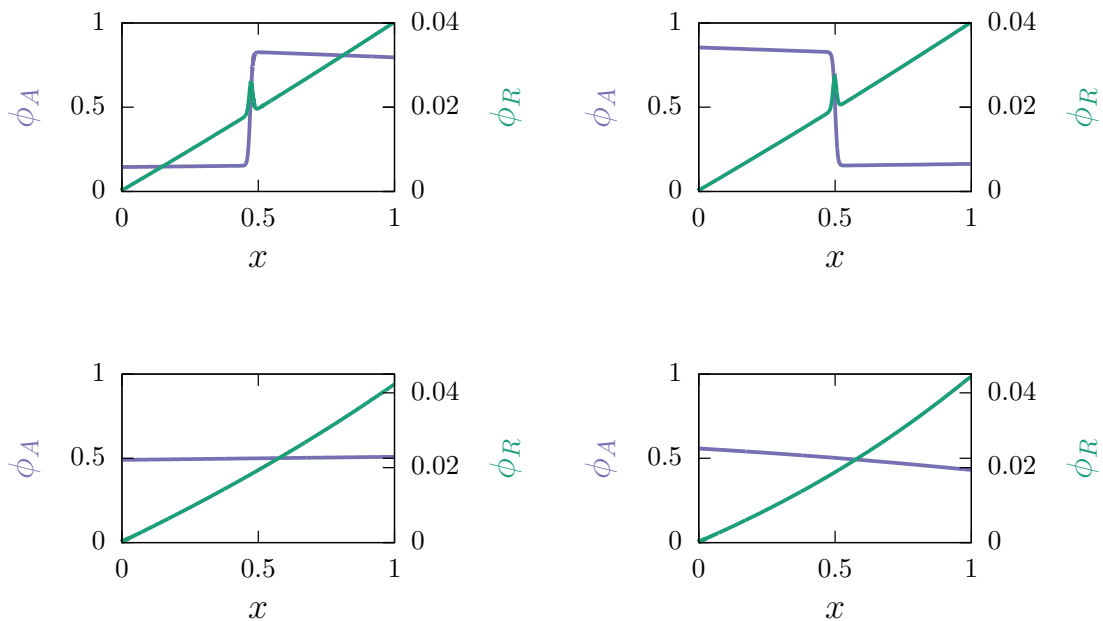


Figure 3.1 – Possible equilibrium states for a three component system, which can separate into two phases: (top left) correlated two phase state, (top right) anti-correlated two phase state, (bottom left) correlated one phase state, (bottom right) anti-correlated one phase state.

### 3.2.3 Influence of the Interfacial Width

The thickness of the interface is influenced by the interaction parameters and the  $\kappa_i$ -parameters. In this chapter, we discuss the choice of the values of  $\kappa_i$ .

We start with discussing  $\kappa_A$ , which is the parameter corresponding to the separating component. We will consider  $\kappa_A$  as a constant parameter independent of the values of interaction parameters. This follows the logic of the gradient expansion of the free energy. If the gradient terms are obtained from the continuum limit of the lattice model presented in [142], it is also possible to derive a relation between the  $\kappa_i$  parameters and the Flory-Huggins parameters. For the  $\kappa$ -parameters, the relations  $\kappa_i = \chi_{iB}/a$  and  $\kappa = (\chi_{AR} - \chi_{AB} - \chi_{RB})/a$  are obtained. The parameter  $a$  is the lattice constant. A more detailed derivation of these relations is presented in appendix A.3. This relation can not be applied, if negative Flory-Huggins parameters are considered. The conditions  $\kappa_A > 0$  and  $\kappa_R > 0$  are necessary to find local minima of the free energy functional eq. 3.6 [55]. Because we will consider negative  $\chi_{BR}$ , which would lead to negative  $\kappa_R$ , this relation can not be used for at least  $\kappa_R$ . To be consistent, we decided to use only constant  $\kappa_i$  in our model.<sup>7</sup> This choice has only a very minor effect on the presented results. Both models lead to a very similar interfacial width (not shown). Based on this result, the choice between these two models should not have a significant effect on the resulting profiles.

The second interfacial parameter we discuss is  $\kappa_R$ . We choose a constant positive value for this parameter. In general, we choose  $\kappa_R$  to be of the same order of magnitude as  $\kappa_A$ , so that they would establish similar interfacial width in the case of phase separation.

<sup>7</sup>The problem of negative Flory-Huggins parameters is not discussed in [142] because Safran considers only a binary system. For binary systems phase separation occurs only for positive Flory-Huggins parameters.

Because we are only considering systems in which the regulator does not segregate, an interface between regulator and solvent material would only be observed if there is a strong accumulation or depletion of regulator material inside the droplet. The value of  $\kappa_R$  has a major effect on two features of the regulator profile considering small interactions between the regulator and the droplet material. It influences the characteristic length scale of a transition region near the boundary. This transition region is the region of the volume fraction profile where the bulk behavior of the profile and the behavior induced by the boundary conditions compete. The regulator distribution in the bulk is governed by the external potential. At the boundaries, the regulator profile has a certain slope, which is determined by the boundary conditions and independent of the external potential. The transition between these limits occurs in the transition region. If very small  $\kappa_R$  are chosen, like in our studies, that region is very small compared to the system size  $L$ . Our solutions show a transition regions smaller than  $L/100$ . If large values of  $\kappa_R$  are chosen, the boundary conditions cause a significant nonlinear contribution to the regulator profile in the bulk due to the extension of the transition region.

All three  $\kappa$ -parameters influence the peak of the regulator profile at the droplet interface. The peak is also visible in the top row of fig. 3.1.<sup>8</sup> Here, we characterize the peak by its area, which is a measure for the amount of regulator material stored in the peak, and the peak height, which can be identified as the regulator concentration at the droplet interface. The peak area becomes zero if the  $\kappa$ -parameters are zero. Interestingly, even if the peak area vanishes, a quasi constant peak height is observed. The behavior of the peak area is majorly governed by controlling the size of the droplet interface.

In the previous discussion, we considered weak interactions between the droplet material and the regulator. If we consider strong interactions, the characteristic length of the droplet interface is still given by  $\kappa_A$ , because  $A$  is the segregating material. Furthermore, the regulator accumulates inside the droplet in the case attractive interactions or outside the droplet in the case repulsive interactions. Considering the regulator profile, there exists an interface between high concentrated regulator region and a low concentrated regulator region. For small  $\kappa_R$  in the order of  $\kappa_A$ , this interface matches with the droplet interface, which is favored in this model, because the interfacial width should be given by the properties of the phase separating material. High  $\kappa_R$  would introduce a significantly different additional characteristic length, which can have influence on the droplet interface. The last interfacial parameter we discuss is the parameter of the cross term  $\kappa$ . In general, this parameter causes similar effects as  $\kappa_R$  to the regulator profile. Furthermore, this term influences the profiles at the boundary of the system, because it appears in the boundary conditions on  $\phi_R$  and  $\phi_A$  (see eq. (3.9)). Here, we will consider values of  $\kappa$ , which are equal to the value of  $\kappa_R$ , which leads to comparable characteristic length. The parameter  $\kappa$  has only very minor effects on quantitative and qualitative studies considered in this thesis. This justifies the arbitrary choice of  $\kappa$ .

#### 3.2.4 Transition of Equilibrium Solutions

In this subsection, we present the main results of the numerical studies about the transition between the correlated and the anti-correlated configuration. A system is called correlated, if the order parameter  $\rho_{AR}$  is positive and it is called anti-correlated, if this order parameter

---

<sup>8</sup>The behavior and the origin of this peak is discussed in more detail in appendix A.7.

is negative. This definition is very general and can be applied on systems which are in the mixed state or in the demixed state. Nevertheless, we will start our investigation considering a system in the demixed region of the phase diagram. After discussing this case, we will comment on systems in the mixed state. We choose  $\chi_{BR}$  as the control parameter in the presented studies. The choice between  $\chi_{BR}$  or  $\chi_{AR}$  as a control parameter is arbitrary. The interaction parameter  $\chi_{AB}$  determines if the system is mixed or demixed. We solved the Euler-Lagrange equations eq. 3.8 numerically for different values of  $\chi_{BR}$ . For each value of this parameter, we find two coexisting solutions, a stable and a metastable one. Here, we call one branch metastable, because we expect a metastable branch in the case of a discontinuous phase transition. However, we did not compute or discuss the second variation of this problem and thus we are not sure of the size of the metastable region. It can even be that the metastable regions shrinks to one point, the transition point, and the remaining part of that branch is not stable.<sup>9</sup> Technically, we use two initial guess for the solver, one guess corresponds to a correlated droplet, one to a anti-correlated droplet. For each guess the numerical solver gives the respective correlated or anti-correlated solution (see fig. 3.1) if such a solution exists. Then, the control parameter is changed by a small value and the corresponding numerical solutions for the new control parameter is computed. The previous solution for the old control parameter is always used iteratively as the initial guess for the numeric solver. We use Matlab's inbuilt solver `bvp4c`, which is a finite difference method using a collocation formula [87]. For each solution, we can calculate the free energy using the functional eq. (3.2). The free energies of the correlated and the anti-correlated branch are plotted in fig. 3.2. The state with the lowest free energy corresponds to the equilibrium solution at the respective  $\chi_{BR}$ -value.

The stability changes dependent on  $\chi_{BR}$ . For low  $\chi_{BR}$ , the anti-correlated state is stable, for high  $\chi_{BR}$  the correlated state. If we follow the lowest free energy solution, which we have already introduced as the equilibrium solution, we observe a kink of the free energy at the point, where the two branches of the free energy intersect. This kink indicates a first order phase transition between the anti-correlated and the correlated state. The metastable solutions, which are plotted as dashed lines in fig. 3.2, indicate an extended hysteresis loop. We propose a very large hysteresis loop, because we were not able to find the points, where the metastable solutions stop to exist. A more detailed discussion of this hysteresis is presented in appendix A.8. We were not able to find the unstable solution, which would be the transition state of this phase transition. The knowledge of it is needed to complete the Gibbs loop.

Using eq. (3.13/), we calculate the order parameters  $\rho_{ij}$  for each solution in dependence of the control parameter. The calculated order parameters are obtained from the same data as the free energy. The order parameters are plotted in fig. 3.3. At first, we shortly discuss  $\rho_{BR}$ . This parameter is proportional to the derivative of the free energy plotted in fig. 3.2 with respect to the control parameter  $\chi_{BR}$  (see eq. (3.12)). The two plotted lines are the order parameter of the anti-correlated solution and of the correlated solution. In this thesis correlation and anti-correlation is defined with respect to the fields of the droplet material  $A$  and the regulator  $R$ . This definition implies, that the order parameter  $\rho_{BR}$  is negative for the correlated solution and positive for the anti-correlated solution. If we follow the

---

<sup>9</sup>Nevertheless, we can exclude the existence of local maxima, because the system fulfills Laplace's necessary condition  $\kappa_i > 0$  for finding minima or saddle points [55]. We also did preliminary dynamic studies of this system employing a Cahn-Hilliard model. Their results (not shown) are consistent with the interpretation that the branch of higher free energy corresponds to a metastable solution.

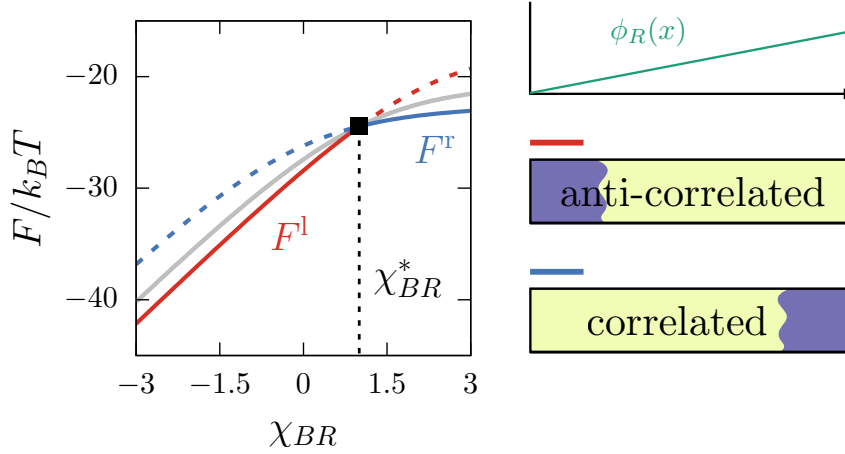


Figure 3.2 – This plot shows the free energy branches  $F^r$  of the correlated (blue) and  $F^l$  of the anti-coorelated (red) solutions. Solid lines indicate stable solutions, dashed lines indicate metastable solutions. The intersection of the two free energy curves, which is equivalent to a kink in the free energy of the stable solution indicates a first order phase transition. The chosen parameters are  $\chi_{AB} = 4$ ,  $\chi_{AR} = 1$ ,  $\bar{\phi}_A = 0.5$ ,  $\bar{\phi}_R = 0.02$ ,  $\kappa_R/L^2 = 7.63 \cdot 10^{-5}$ ,  $\kappa_A/L^2 = 6.10 \cdot 10^{-5}$ ,  $\kappa/L^2 = 6.10 \cdot 10^{-5}$  and  $Ls = 0.99$ .<sup>10</sup>

path of lowest free energy, we observe a jump of the order parameter at the same point as we observed the kink of the lowest free energy. We call this point the transition point  $\chi_{BR}^*$ . This result is the expected behavior for a first order phase transition and consistent with the previously presented result of the behavior of the free energy considering the definition of the order parameter eq. (3.12). Because of this relation the results of the order parameter study and the free energy study are not independent. The two studies can be considered as two alternative representations of the discontinuous phase transition. The order parameter  $\rho_{AR}$  shows a similar behavior as the the order parameter  $\rho_{BR}$ . It also shows a jump at the transition point from negative values for the anti-correlated region to positive values for the correlated region. In the case  $\bar{\phi}_A = 0.5$  shown in fig. 3.3, it behaves approximately like the negative of the order parameter  $\rho_{BR}$ . The remaining order parameter  $\rho_{AB}$  behaves differently. The branch of the equilibrium value of this order parameter has a kink at the transition point. We observe the kink of this order parameter only for the limit case  $\bar{\phi}_A = 0.5$ . This behavior is caused by the symmetry of this case. In general, this order parameter also shows a jump at the transition point, but this jump does not lead to a different sign of the order parameter and is significantly smaller than the jump of  $\rho_{AR}$  or  $\rho_{BR}$ .

To discuss the relations between the order parameters, we take a closer look on the not normalized form of the order parameters  $\mathcal{N}_{ij}\rho_{ij}$ . The property  $\mathcal{N}_{ij}$  is the previously introduced normalization of the normalized order parameter  $\rho_{ij}$  (see eq. (3.13) and appendix A.5). The not normalized order parameters are connected by the relations

$$\mathcal{N}_{BR}\rho_{BR} = -\mathcal{N}_{AR}\rho_{AR} - \mathcal{N}_{RR}\rho_{RR} \quad (3.14)$$

$$\mathcal{N}_{AB}\rho_{AB} = -\mathcal{N}_{AR}\rho_{AR} - \mathcal{N}_{AA}\rho_{AA}. \quad (3.15)$$

The parameters  $\rho_{ii}$  are proportional to the variance of the respective volume fraction field  $\phi_i(x)$  and thus always positive. Fig. 3.4 shows these two relations for a numeric example. In the case of a diluted regulator, as considered in this thesis, the parameter  $\rho_{RR}$  is very small.

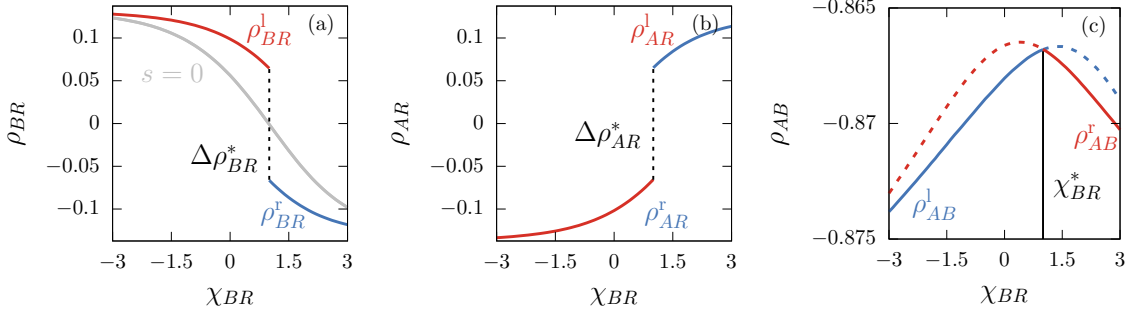


Figure 3.3 – (a) Jump of the order parameter  $\rho_{BR}$ . Here, only the branches of the stable anti-correlated or correlated solution are plotted. The Jump is at the same point as the observed kink of the free energy. (b) Jump of the order parameter  $\rho_{AR}$ . This order parameter is in good approximation the negative of  $\rho_{BR}$ . For better visualization of this similarities, we used the same vertical black line as in (a) to compare the jump. (c) Behavior of the order parameter  $\rho_{AB}$ . Because of the symmetry of the case  $\bar{\phi}_A = 0.5$ , this order parameter shows a kink at the transition point. In the general case, also this order parameter shows a jump. The chosen parameters are  $\chi_{AB} = 4$ ,  $\chi_{AR} = 1$ ,  $\bar{\phi}_A = 0.5$ ,  $\bar{\phi}_R = 0.02$ ,  $\kappa_R/L^2 = 7.63 \cdot 10^{-5}$ ,  $\kappa_A/L^2 = 6.10 \cdot 10^{-5}$ ,  $\kappa/L^2 = 6.10 \cdot 10^{-5}$  and  $Ls = 0.99$ .

Furthermore, this contribution does not change very much between the anti-correlated solution and the correlated solution near the transition point, because there the regulator distribution is linear in very good approximation and the effect of the  $A$ -profile on the regulator distribution is small. This leads to a minor contribution of the parameter  $\rho_{RR}$  to the order parameter  $\rho_{BR}$  and the behavior of  $\rho_{BR}$  is mainly determined by the order parameter  $\rho_{AR}$ . If we consider the relation of order parameter  $\rho_{AB}$ , the parameter  $\rho_{AA}$  can not be neglected. The variance is large for the phase separating component  $A$ . The contribution  $\rho_{AA}$  is also different for the correlated and the anti-correlated state. In general, the value of the parameters  $\rho_{AR}$  and  $\rho_{AA}$  determine the jump of the order parameter  $\rho_{AB}$ . In case of  $\bar{\phi}_A = 0.5$  they can combine to zero and a kink of the order parameter is observed because of the symmetry of the system. If the system is not close to the symmetric case  $\bar{\phi}_A = 0.5$ , the jumps of  $\rho_{AA}$  and  $\rho_{AR}$  are of different height, which results in a jump of the order parameter  $\rho_{AB}$ .

### 3.2.5 Phase Diagram of the Mean-Field Model

Based on our finding of a first order phase transition between the correlated and the anti-correlated state, we are motivated to build phase diagrams of the inhomogeneous system. We consider two dimensional cuts through the high dimensional phase diagram considering the interaction parameters  $\chi_{BR}$  and  $\chi_{AB}$  for chosen values of the average volume fraction  $\bar{\phi}_A$ . The remaining parameters are kept constant for all phase diagrams. Because both parameters  $\chi_{BR}$  and  $\chi_{AR}$  can control the phase transition between the correlated and the anti-correlated state, the choice between them is arbitrary. The interaction parameter  $\chi_{AB}$  is selected to include the transition between phase separation and mixing of the components  $A$  and  $B$  in the phase diagram. The cuts on the  $\bar{\phi}_A$ -axis are shown for  $\bar{\phi}_A = 0.1, 0.5, 0.9$ . The phase diagrams are plotted for the three different average volume fraction in fig. 3.5. The observed phases are the mixed state, the correlated demixed state and the anti-correlated demixed state. The solid dark-grey lines are the transition lines

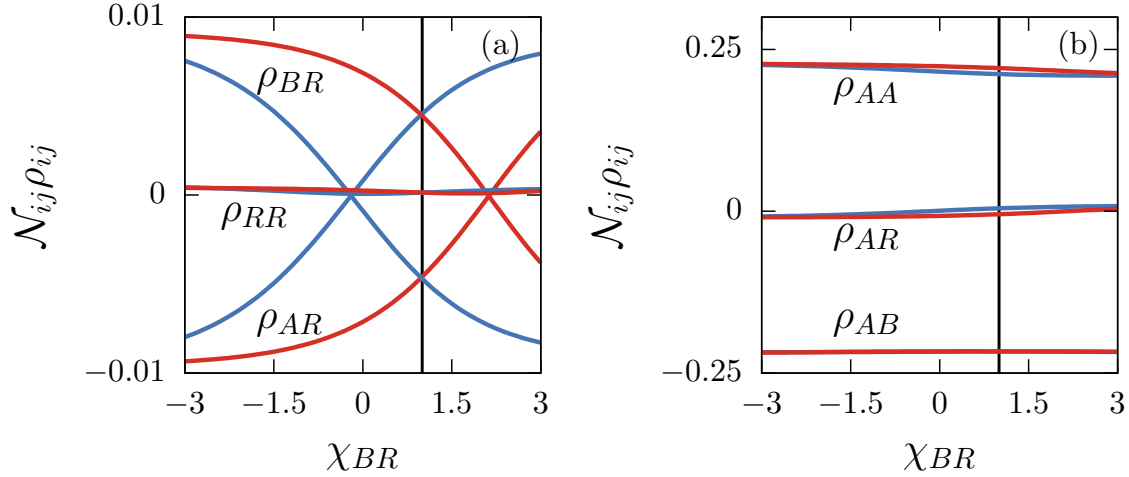


Figure 3.4 – Order parameters and contributions of the order parameters for the correlated state (blue) and the anti-correlated state (red). (a) Plot of the not normalized  $\rho_{BR}$ ,  $\rho_{AR}$  and  $\rho_{RR}$ . The variance of the  $R$ -field is negligible in comparison to the other two parameters, so that  $\mathcal{N}_{BR}\rho_{BR} \approx -\mathcal{N}_{AR}\rho_{AR}$ . (b) Plot of the not normalized  $\rho_{AR}$ ,  $\rho_{AB}$  and  $\rho_{AA}$ . The parameters  $\rho_{BR}$  and  $\rho_{AA}$  have the same absolute value of the jump height at the transition point, but differ in sign. That leads to the cancellation of the jump and the kink of the order parameter  $\rho_{AB}$  at the transition point. The chosen parameters are  $\chi_{AB} = 4$ ,  $\chi_{AR} = 1$ ,  $\bar{\phi}_A = 0.5$ ,  $\bar{\phi}_R = 0.02$ ,  $\kappa_R/L^2 = 7.63 \cdot 10^{-5}$ ,  $\kappa_A/L^2 = 6.10 \cdot 10^{-5}$ ,  $\kappa/L^2 = 6.10 \cdot 10^{-5}$  and  $Ls = 0.99$ .

between the different regions and correspond to a first order phase transition. Here, the transition lines are defined by the existence of a kink of the free energy of the system at the respective value of the control parameter. Technically, this is equivalent to a maximum of the second derivative of the minimum free energy. To calculate the transition lines between the correlated and the anti-correlated states, we used the data and method presented in the previous section 3.2.4. The transition lines between the mixed states and the droplet states are obtained by calculating the free energy  $F(\chi_{AB})$  at constant  $\chi_{BR}$  and identifying the point of maximum second derivative of this free energy. If a kink of the free is observed this definition is identical to finding the kink of the free energy. If the kink is smoothed out in the numeric result like in the case  $\bar{\phi}_A = 0.5$ , this definition can identify an approximate transition line. The color code in the phase diagrams represents the value of the order parameter  $\rho_{BR}$  and indicates the correlated and the anti-correlated solutions.

The phase diagrams presented in fig. 3.5 show a clear trend. In the case of  $\bar{\phi}_A = 0.5$  the transition lines are degenerated to straight lines. This can be explained, because the average volume fraction of component  $A$  is very similar to the critical volume fraction of  $A$  of this system. In a two component system, this critical volume fraction would be exactly 0.5. With the included regulator this value is slightly shifted but still very close to 0.5, because of the strong dilution of the regulator. Close to this volume fraction, we observed a continuous transition from the mixed state to the separated state and vice versa in the numeric results. The transition line is determined by the maximum slope of the free energy curve interpreting the continuous free energy curve as a kink that is numerically smoothed out. This transition line is close to 2, which is consistent with the mean field theory for binary systems, in which the critical Flory-Huggins parameter is exactly 2. The corresponding transition lines for  $\bar{\phi}_A = 0.1$  and  $\bar{\phi}_A = 0.9$  are at higher values as expected

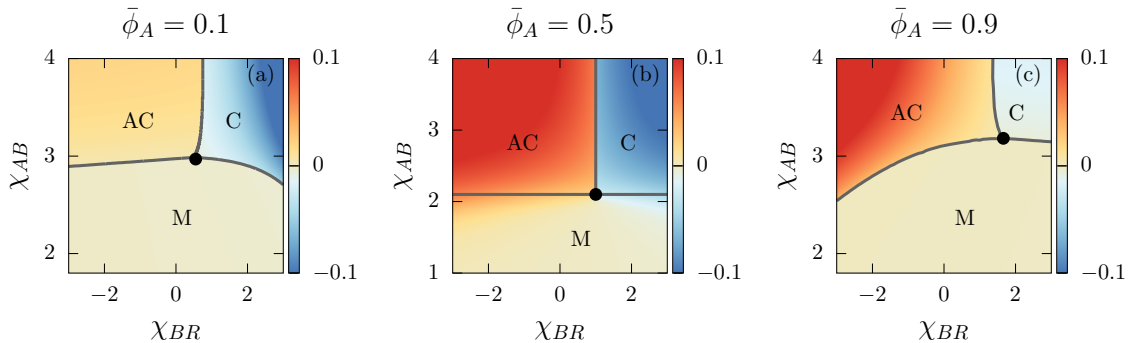


Figure 3.5 – (a) Phase diagram in the  $\chi_{BR}$ - $\chi_{AB}$ -plane for  $\bar{\phi}_A = 0.1$ . The color code represents the value of the order parameter  $\rho_{BR}$ . In this case the transition line between the correlated and the anti-correlated region is bent to the left. (b) Phase diagram for  $\bar{\phi}_A = 0.5$ . Here, the regions of correlated and anti-correlated states are separated by a vertical transition line. We did not observe a kink in the free energy moving from the demixed region to the mixed region at constant  $\chi_{BR}$  because of the quasi critical setting. We used the maximum second derivative of the minimum free energy as approximate transition line. (c) Phase diagram for  $\bar{\phi}_A = 0.9$ . The transition line between the correlated and the anti-correlated region is bent to the right. The black circle indicates the position of the triple point of the phase diagram. The chosen parameters are  $\chi_{AR} = 1$ ,  $\bar{\phi}_R = 0.02$ ,  $\kappa_R/L^2 = 7.63 \cdot 10^{-5}$ ,  $\kappa_A/L^2 = 6.10 \cdot 10^{-5}$ ,  $\kappa/L^2 = 6.10 \cdot 10^{-5}$  and  $L_s = 0.99$ .

and also comparable with the mean field results for the two component system.

Now, we discuss the transition lines separating the correlated and the anti-correlated states. These states are a new feature of the ternary phase diagram and caused by the imposed regulator gradient. The existence of a regulator gradient seems sufficient to observe this phase transition. To stress this point, we have also investigated a system in which the regulator gradient is introduced as a fixed function and no explicit external potential is included. The results obtained from this ensemble are very similar to the system where the regulator gradient is maintained by an external potential (see appendix A.9). Furthermore, the strength of the external potential and thus the regulator gradient has no influence on the observed transition point, it effects only the order parameter difference between the coexisting states (see appendix A.6). These are strong hints, that the existence of the inhomogeneous regulator gradient is sufficient to trigger the correlated-anti-correlated phase transition.<sup>11</sup>

Fig. 3.5 shows, that this transition line is a vertical line close to  $\chi_{BR}^* = \chi_{AR}$  in the case  $\bar{\phi}_A = 0.5$ . For  $\bar{\phi}_A = 0.1$  it is bent to smaller  $\chi_{BR}$  and for  $\bar{\phi}_A = 0.9$  it is bent to higher  $\chi_{BR}$ . Our explanation of this behavior is that for  $\bar{\phi}_A < (1 - \bar{\phi}_R)/2$  component  $B$  has stronger influence, so that a smaller  $\chi_{BR}$  is needed to trigger the transition between the correlated and the anti-correlated state. Otherwise, for  $\bar{\phi}_A > (1 - \bar{\phi}_R)/2$  component  $A$  has stronger influence and a higher  $\chi_{BR}$  is needed. The case  $\bar{\phi}_A = 0.5$  is very close to  $\bar{\phi}_A = (1 - \bar{\phi}_R)/2$  because of the diluted regulator and shows a straight transition line.

The black dots in fig. 3.5 show triple points in the phase diagram. We define a triple point as the intersection point of two transition lines. There, all three equilibrium states have the same total free energy and coexist. The triple points move through the phase space when  $\bar{\phi}_A$  is changed. The trajectory of this movement is shown in fig. 3.6. The movement

<sup>11</sup>Beyond the equilibrium scenario, we find a consistent positioning of droplets in computer simulations of a non-equilibrium system (see section 4.4.)

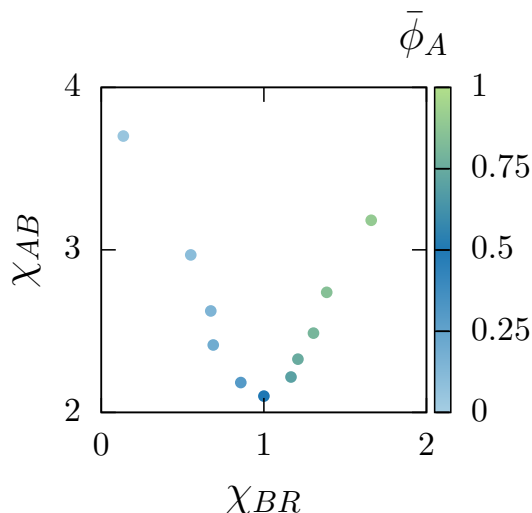


Figure 3.6 – Triple points in the  $\chi_{BR}$ - $\chi_{AB}$ -plane for different  $\bar{\phi}_A$ . The movement of the triple point is determined by the movement of the binodal line between the phase separated state and the mixed states and the bending of the binodal line between correlated and anti-correlated states. The chosen parameters are  $\chi_{AR} = 1$ ,  $\bar{\phi}_R = 0.02$ ,  $\kappa_R/L^2 = 7.63 \cdot 10^{-5}$ ,  $\kappa_A/L^2 = 6.10 \cdot 10^{-5}$ ,  $\kappa/L^2 = 6.10 \cdot 10^{-5}$  and  $Ls = 0.99$ .

is a result of the shift of the transition line between mixed states and droplet states and the different bending of the transition line dividing correlated and anti-correlated states.

### 3.3 Droplet in an Periodic Regulator Distribution

At this point, the origin of the metastable states is still unclear. Because all presented stationary solutions are at the boundary of the system, it is possible that these states are stabilized by the free energy effort needed to create a second interface of the droplet phase. In that scenario, the presented discontinuous phase transition between correlated and anti-correlated states would be closely related to wetting transitions [142, 12]. To this end, we will investigate a liquid system without walls. Such a system is modeled by introducing a periodic external potential. Here, we choose a sinusoidal shape of the external potential

$$U_R(x) = -\ln(1 - A \sin(2\pi(x - \omega))) \quad (3.16)$$

The amplitude  $A$  influences the gradient of the regulator profile by determining the vertical distance between the minimum and the maximum of the regulator distribution. The potential is chosen in this logarithmic form, because a sinusoidal distribution of the regulator is obtained in the limit of diluted regulator. With this potential it is possible to identify correlated states, in which the droplet is located at the maximum of the regulator distribution, and anti-correlated droplet states, where the droplet is placed at the minimum of the regulator distribution.

In the case of a periodic system, periodic boundary conditions for the volume fraction fields  $\phi_A$  and  $\phi_R$  have to be fulfilled. These are essential boundary conditions of the boundary

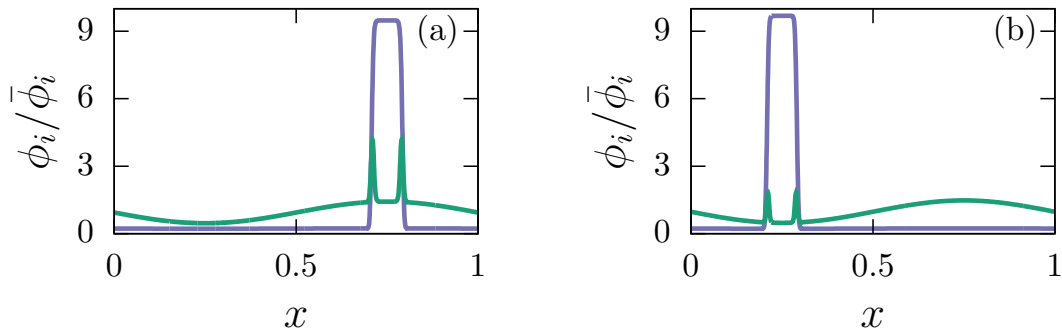


Figure 3.7 – Profiles of the regulator (red) and component  $A$  (blue). (a) In the correlated state, the droplet is placed at the maximum of the regulator profile. (b) In the anti-correlated state, the droplet is placed at the minimum of the regulator profile. The chosen parameters are  $\chi_{AB} = 4$ ,  $\chi_{AR} = 1$ ,  $\chi_{BR} = 1$ ,  $\bar{\phi}_A = 0.1$ ,  $\bar{\phi}_R = 0.02$ ,  $\kappa_R/L^2 = 7.63 \cdot 10^{-5}$ ,  $\kappa_A/L^2 = 6.10 \cdot 10^{-5}$ ,  $\kappa/L^2 = 6.10 \cdot 10^{-5}$  and  $A = 0.5$ .

value problem. The fields should be continuous and differentiable

$$\begin{aligned} 0 &= \phi_i|_{x=0} - \phi_i|_{x=1}, \\ 0 &= \partial_x \phi_i|_{x=0} - \partial_x \phi_i|_{x=1}. \end{aligned} \tag{3.17}$$

With the essential boundary conditions, the boundary terms in eq. (3.7) vanish automatically. The Euler-Lagrange equations do not change, we solve eq. (3.8) with the adapted boundary conditions. Two typical profiles of these states are shown in fig. 3.7.

The total free energy and the order parameters of the system can be computed using the numerically obtained profiles. One exemplary result for the total free energy and the order parameter  $\rho_{BR}$  is shown in fig. 3.8.

In the periodic scenario, we do also observe the kink of the free energy and the jump of the order parameter. This indicates, that the discontinuous phase transition is also present in absence of walls. That means, that the phase transition between the correlated and the anti-correlated states is an intrinsic feature of the spatial inhomogeneous system and is not caused by a wetting mechanism at the system boundaries.

We can build phase diagrams of the system in the same way as we did in subsection 3.2.5 for the not periodic case. The phase diagrams are shown in fig. 3.9.

The phase diagrams look very similar to the corresponding phase diagrams of systems with linear regulator distribution. It is very likely that the major part or the small quantitative differences is simply caused by the different shape of the regulator profile.

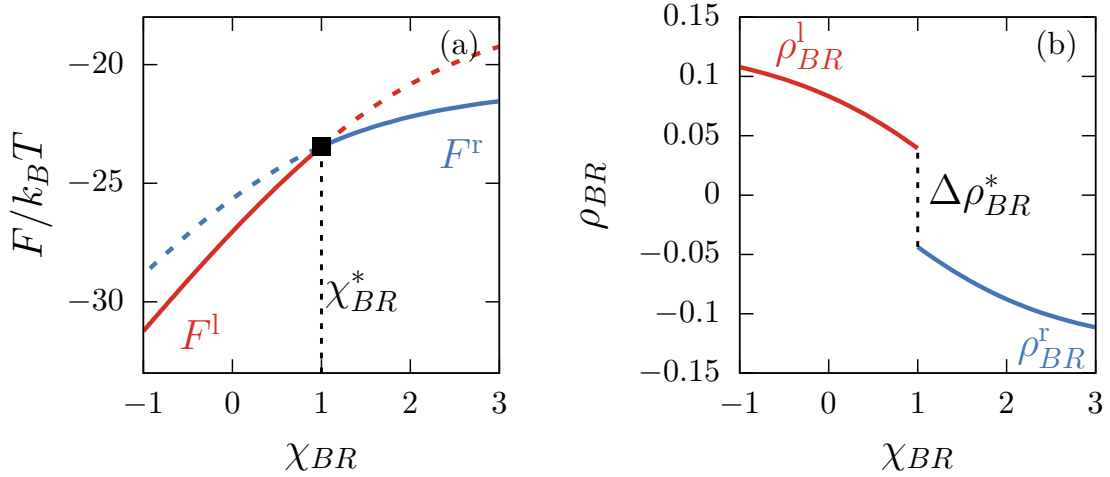


Figure 3.8 – (a) Free energy of the correlated solution (blue) and the anti-correlated solution (red). The branch of the equilibrium solution is shown by a solid line, the metastable solution is indicated by a dashed line. The kink of the free energy of the equilibrium branch indicates a discontinuous phase transition. (b) Order parameter  $\rho_{BR}$  of the correlated solution (blue) and the anti-correlated solution (red). The jump of the order parameter at the transition point is also an indication for a discontinuous phase transition. The chosen parameters are  $\chi_{AB} = 4$ ,  $\chi_{AR} = 1$ ,  $\bar{\phi}_A = 0.5$ ,  $\bar{\phi}_R = 0.02$ ,  $\kappa_R/L^2 = 7.63 \cdot 10^{-5}$ ,  $\kappa_A/L^2 = 6.10 \cdot 10^{-5}$ ,  $\kappa/L^2 = 6.10 \cdot 10^{-5}$  and  $A = 0.5$ .

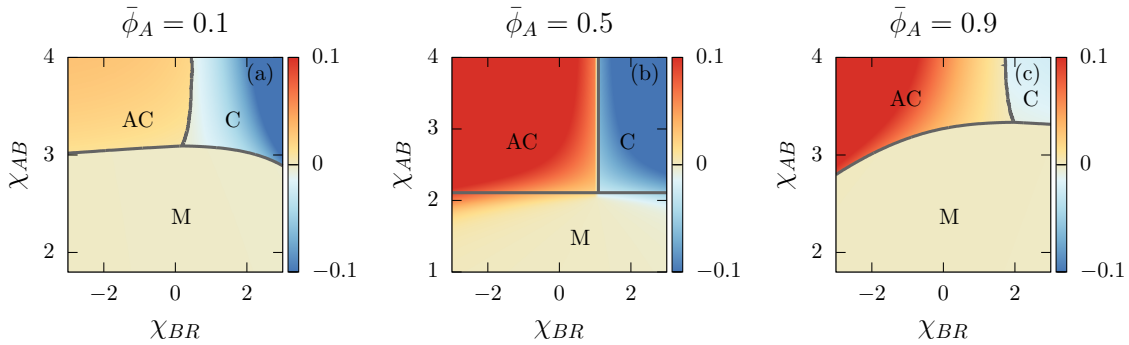


Figure 3.9 – The phase diagram of the ternary liquid system in a periodic external potential  $U_R$  includes the regions of a well mixed system (M), a correlated droplet (C) and a anti-correlated droplet (AC). The dark grey lines show the transition lines of discontinuous phase transitions. The color map indicates the value of the order parameter  $\rho_{BR}$ . (a) Phase diagram for  $\bar{\phi}_A = 0.1$ . (b) Phase diagram for the quasi critical volume fraction  $\bar{\phi}_A = 0.5$ . The transition line between the mixed and the demixed regions is calculated approximately by using the maximum of the second derivative of the minimum free energy as indication of the transition point. (c) Phase diagram for  $\bar{\phi}_A = 0.9$ . The chosen parameters are  $\chi_{AR} = 1$ ,  $\bar{\phi}_R = 0.02$ ,  $\kappa_R/L^2 = 7.63 \cdot 10^{-5}$ ,  $\kappa_A/L^2 = 6.10 \cdot 10^{-5}$ ,  $\kappa/L^2 = 6.10 \cdot 10^{-5}$  and  $A = 0.5$ .

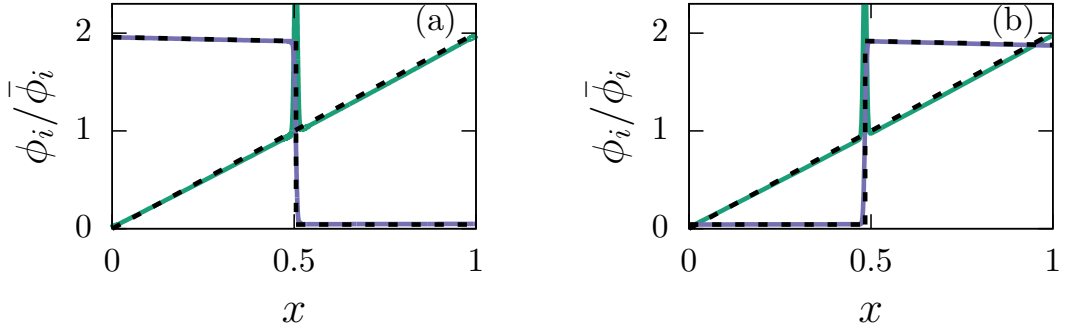


Figure 3.10 – Ansatz of the volume fraction profiles for the analytic model. The ansatzes are shown as a dashed line, the colored solid lines are the volume fraction profiles obtained by solving the Euler-Lagrange equation eq. (3.8). (a) Anti-correlated profile. (b) Correlated profile. The chosen parameters are  $\chi_{AB} = 4$ ,  $\chi_{BR} = 1$ ,  $\chi_{AR} = 1$ ,  $\bar{\phi}_R = 0.02$ ,  $\kappa_R/L^2 = 7.63 \cdot 10^{-5}$ ,  $\kappa_A/L^2 = 6.10 \cdot 10^{-5}$ ,  $\kappa/L^2 = 6.10 \cdot 10^{-5}$  and  $sL = 0.99$ .

### 3.4 Analytical Prediction of the Phase Transition in a Limiting Case

In this section, we will present a simple analytic model of the phase transition between the correlated and the anti-correlated state. We will see, that it is possible to get almost exact results for the binodal line and the jump of the order parameter  $\rho_{BR}$  at this transition for the limiting case  $\bar{\phi}_A = 0.5$ .

The logic of this approach is to define an analytical ansatz for the anti-correlated and the correlated state of the droplet. With these ansatzes, we can compute the free energy and the order parameters of both states directly. Furthermore, we define the phase transition as that point, where the free energies of both states are equal, which corresponds to the intersection of the two branches of the free energy and the resulting kink of the lowest free energy. Fig. 3.10 shows a typical anti-correlated and a typical correlated solution close to the transition line obtained by solving the Euler-Lagrange equation eq. (3.8). The proposed analytic ansatz is compared to this solutions.

Due to the very narrow interfacial width of the droplet we decided to model the profile of component  $A$  by a step function.<sup>12</sup> The profiles obtained by free energy minimization show that the value of the volume fraction of the droplet component is not constant in the two phases, but linear dependent on  $x$  in good approximation. Furthermore, this linear modulation of the profile is negligible in the low concentrated phase. Motivated by this observation we use a constant volume fraction  $\phi_{A,\text{out}} = \phi_{\text{out,bin}}$  to model the environment of the droplet. The value  $\phi_{\text{out,bin}}$  is the volume fraction of  $A$  in the  $A$ -depleted phase obtained from the binary phase diagram of the  $A$ - $B$ -system.<sup>13</sup> This approximation is reasonable because of the dilution of the regulator material. In the high concentrated bulk phase, the

<sup>12</sup>This model can be considered as an effective droplet model (compare [183]).

<sup>13</sup>For the binary  $A$ - $B$ -system, we obtain  $\chi_{BR} = \ln((1 - \phi_{\text{out,bin}})/\phi_{\text{out,bin}})/(1 - 2\phi_{\text{out,bin}})$  from the Flory-Huggins theory.

linear profile is mainly described by the regulator gradient because of excluded volume and can be modeled as  $\phi_{A,\text{in}} = \phi_{\text{in,bin}} - \phi_R(x)$ . The value  $\phi_{\text{in,bin}}$  is the volume fraction of  $A$  in the  $A$ -enriched phase obtained from the binary phase diagram of the  $A$ - $B$ -system. Because of the symmetric shape of the binary phase diagram of equally sized particles, the two volume fractions are related by  $1 = \phi_{\text{out,bin}} + \phi_{\text{in,bin}}$ . The droplet material profile is modeled with a step function. The volume fraction is constant in the low concentrated phase and linear dependent on  $x$  in the high concentrated phase. The respective slope is determined by the regulator gradient. The regulator profile  $\phi_R(x)$  is modeled by a linear function. It is described by the slope  $m$  and the offset  $m_0$ . Using the constraint of particle conservation, it is also possible to use the slope  $m$  and the average volume fraction of the regulator  $\bar{\phi}_R$  to describe the regulator profile. With this argument we find  $m_0 = \bar{\phi}_R - m/2$ . We prefer this form of the regulator profile, because the parameter  $\bar{\phi}_R$  is the natural choice for the considered ensemble. In comparison, the parameter  $m_0$  is more generic. In this approach we are neglecting the peak of the regulator volume fraction at the droplet interface. For  $\kappa_i \rightarrow 0$ , neglecting the peak is well justified, because in this limit the peak area vanishes. Because we are assume an infinitely small interface,  $\kappa_i = 0$  is also the consistent choice for this model.<sup>14</sup> The ansatz profiles are

$$\phi_A^l = (\phi_{A,\text{in}} - \phi_{A,\text{out}}) \Theta(\epsilon_l - x) + \phi_{A,\text{out}}, \quad (3.18)$$

$$\phi_A^r = (\phi_{A,\text{in}} - \phi_{A,\text{out}}) \Theta(\epsilon_r - 1 + x) + \phi_{A,\text{out}}, \quad (3.19)$$

$$\phi_R = mx + m_0, \quad (3.20)$$

$$\phi_{A,\text{in}} = 1 - \phi_{A,\text{out,bin}} - \phi_R, \quad (3.21)$$

$$\phi_{A,\text{out}} = \phi_{A,\text{out,bin}}. \quad (3.22)$$

The corresponding profiles of component  $B$  are obtained from the relation  $\phi_B^{\text{l,r}} = 1 - \phi_A^{\text{l,r}} - \phi_R$ . The domain size of the droplet region is  $\epsilon_r$  for the correlated profile and  $\epsilon_l$  for the anti-correlated profile. These two parameters are determined by the constraints of particle conservation, they read

$$\begin{aligned} \epsilon_{l,r}(m) = & \frac{-2 \mp m + 4\phi_{\text{out,bin}} + 2\bar{\phi}_R}{2m} \\ & + \frac{\sqrt{\pm 8m (\phi_{\text{out,bin}} - \bar{\phi}_A) + (2 \pm m - 4\phi_{\text{out,bin}} - 2\bar{\phi}_R)^2}}{2m}. \end{aligned} \quad (3.23)$$

In the limiting case of vanishing slope  $m$ , both domain sizes become equal  $\epsilon_l(0) = \epsilon_r(0) = (\phi_{\text{out,bin}} - \bar{\phi}_A) / (2\phi_{\text{out,bin}} + \bar{\phi}_R - 1)$ .

With the ansatz eq. (3.18-3.23) we can compute the free energy of the anti-correlated and the correlated state using eq. (3.2). Because we are considering  $\kappa_i = 0$ , the gradient terms in the free energy density vanish (see eq. (3.1)). For the later discussion, we will introduce the different contributions of the total free energy as  $F = F_S + F_\chi + F_U$ , where  $F_S$  describes the entropic part of the total free energy and is the integral of the entropic contributions  $\sum_{i=A,B,R} \phi_i \ln \phi_i$ . The term  $F_\chi$  includes the binary interactions between the components and is the integral  $\sum_i \sum_{j < i} \chi_{ij} \phi_i \phi_j$ . The last term  $F_U$  describes the contribution of the external potential, it integrates the term  $U_R \phi_R$ . The difference  $\Delta F = F^l - F^r$  between the

---

<sup>14</sup>See appendix A.7 for more discussion about the influence of the  $\kappa_i$ -parameters on the peak.

### 3.4. Analytical Prediction of the Phase Transition in a Limiting Case

anti-correlated and the correlated branch of this analytic free energy is

$$\Delta F(m) = \frac{k_B T}{\nu} (\chi_{AR} - \chi_{BR}) \mathcal{G}(m). \quad (3.24)$$

The function  $\mathcal{G}(m)$  depends only on the parameters of the ansatz profiles (see eq. (3.18-3.22))

$$\begin{aligned} \mathcal{G}(m) = & -\frac{1}{4} \left( m^2 + 2\bar{\phi}_R (4\phi_{\text{out,bin}} + 2\bar{\phi}_R - 2) \right) (\epsilon_1 - \epsilon_r) \\ & - m \left( \frac{1}{4} (2 - 4\phi_{\text{out,bin}} - 4\bar{\phi}_R) (\epsilon_1 + \epsilon_r) \right. \\ & + \frac{m}{2} (\epsilon_1^2 - \epsilon_r^2) + \frac{1}{2} (2\phi_{\text{out,bin}} + 2\bar{\phi}_R - 1) (\epsilon_1^2 + \epsilon_r^2) \\ & \left. + \frac{m}{3} (\epsilon_1^3 - \epsilon_r^3) \right). \end{aligned} \quad (3.25)$$

For  $m \rightarrow 0$ , the function  $\mathcal{G}(m)$  vanishes as the domain sizes of the droplet region  $\epsilon_{1,r}(m=0)$  become equal. To leading order in the regulator slope  $m$ ,

$$\mathcal{G}(m) = m(1 - \epsilon) \epsilon (2\phi_{\text{out,bin}} + \bar{\phi}_R - 1) + O(m^2). \quad (3.26)$$

It is  $\epsilon = \epsilon_{1,r}(m=0)$ . The truncated expression eq. 3.26 indicates, that the difference of the domain sizes  $\epsilon_1$  and  $\epsilon_r$  is not essential for the free energy difference. According to eq. 3.25 and eq. 3.26, a vanishing regulator gradient leads to a vanishing free energy difference. The existence of the regulator gradient seems sufficient for obtaining the correlated-anti-correlated phase transition in the analytic model. If a non zero regulator gradient exist, the free energy difference is zero at the transition point

$$\chi_{BR}^* = \chi_{AR}. \quad (3.27)$$

We identify this as the transition point, because the condition  $\Delta F = 0$  gives the position of the kink of the free energy (compare subsection 3.2.4). We can discuss the difference of the free energy branches also with respect to the three contributions introduced earlier. The external potential has no contribution to the free energy difference,  $\Delta F_U = 0$ , because the regulator profiles  $\phi_R^l$  and  $\phi_R^r$  are equal in this approach. The entropic contribution  $\Delta F_S$  also vanishes. This can be understood, because we are only considering excluded volume effects to modulate the volume fraction profiles. This excluded volume effect is implemented in the profile of component  $A$  and  $B$  in a similar way, which leads to the cancellation of this contribution after integrating over the whole system. In this approach, the transition between the correlated and the anti-correlated phase is only effected by the binary interactions between the components. The obtained condition eq. (3.27) is consistent with the phase diagram obtained by free energy minimization for  $\bar{\phi}_A = 0.5$  (see fig. 3.5b). The simple analytical ansatz seems valid for this particular case but has to be refined if other  $\bar{\phi}_A$  are used.

In the case of  $\bar{\phi}_A \approx 0.5$  it is also possible to give a symmetry argument for the condition eq. (3.27). Considering a diluted regulator,  $\bar{\phi}_A \approx \bar{\phi}_B \approx 0.5$ . Now, switching the identity of  $A$  and  $B$  leads to the same free energy density. Thus, in the presence of an external potential affecting only the regulator, the differences in the free energy between the correlated state and the anti-correlated state vanishes for equal interaction parameters with respect to the

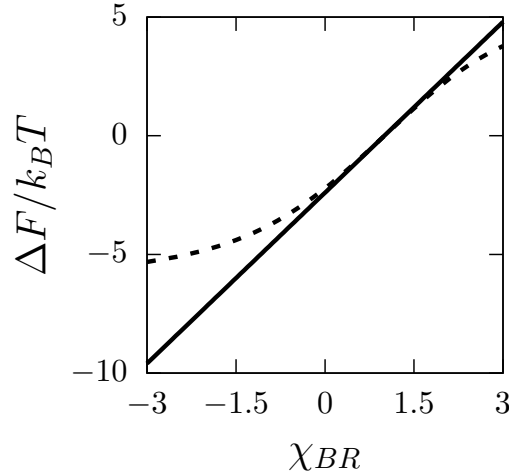


Figure 3.11 – Difference of the free energy between the anti-correlated state ( $F^l$ ) and the correlated state ( $F^r$ ). The solid line shows the result of the analytical model. For comparison, the result obtained by solving eq. (3.8) is included as dashed line. The curves intersect at the transition point  $\chi_{BR}^* = 1$ . The chosen parameter values in the analytic model are  $\chi_{AB} = 4$ ,  $\chi_{AR} = 1$ ,  $\bar{\phi}_A = 0.5$ ,  $\bar{\phi}_R = 0.02$ ,  $\phi_{A,\text{out},\text{bin}} = 0.2332$  and  $m = 1$ . The chosen parameter values for minimizing the mean-field free energy are  $\chi_{AB} = 4$ ,  $\chi_{AR} = 1$ ,  $\bar{\phi}_A = 0.5$ ,  $\bar{\phi}_R = 0.02$ ,  $\kappa_R/L^2 = 7.63 \cdot 10^{-5}$ ,  $\kappa_A/L^2 = 6.10 \cdot 10^{-5}$ ,  $\kappa/L^2 = 6.10 \cdot 10^{-5}$  and  $Ls = 0.99$ .

regulator  $\chi_{AR} = \chi_{BR}$ .

The free energy difference eq. (3.24) is plotted and compared to the free energy difference obtained by free energy minimization in fig. 3.11. The two curves intersect at exactly one point, the transition point  $\chi_{BR}^*$ . According to this graphical result, the analytical model can be identified as the linear approximation of the free energy difference obtained by minimizing the mean-field free energy. In general, the curve obtained by minimization is not linear bends to lower absolute values of the free energy difference compared to the analytic result.<sup>15</sup>

Based on eq. (3.27), we can build a phase diagram of this model. In fig 3.12 we compare this phase diagram with the results of the free energy minimization. We considered the special case  $\phi_A = 0.5$ , because the analytical model is suitable for this scenario.

The second property we want to discuss is the jump of the order parameter at the transition point  $\Delta\rho_{BR}^*$ . Therefore, we employ the definition of the order parameter  $\rho_{BR}$  from eq. (3.12). Thus, we can calculate the order parameter with the ansatz-functions eq. (3.18-3.22) to obtain the value of the order parameter for the two states  $\rho_{BR}^l$  and  $\rho_{BR}^r$ . The jump of the order parameter  $\Delta\rho_{BR}^* = \rho_{BR}^l - \rho_{BR}^r$  is

$$\Delta\rho_{BR}^* = -\frac{k_B T}{\nu} \mathcal{N}_{BR}^{-1} \mathcal{G}(m). \quad (3.28)$$

The difference of the order parameter can also be obtained by computing the derivative of the difference of the free energy eq. (3.24) with respect to  $\chi_{BR}$ . Both ways are equivalent. The profiles of our ansatz are independent of the interaction parameters  $\chi_{ij}$ . That means

---

<sup>15</sup>In appendix A.9, we introduce a model with constant regulator profile instead of an external potential. The results obtained from this ensemble show a very good agreement with the analytical model, because the regulator is always linearly distributed there.

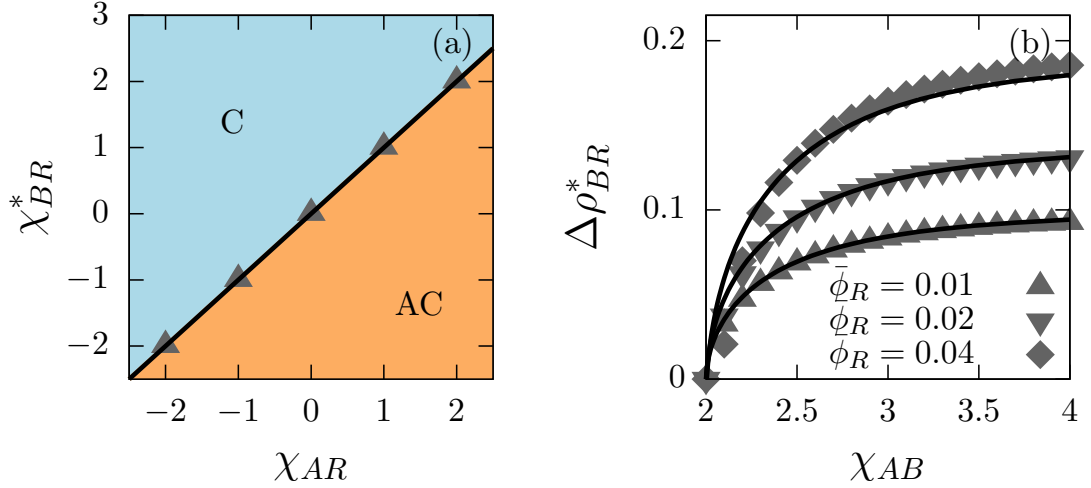


Figure 3.12 – (a) Analytic phase diagram in the  $\chi_{AR}$ - $\chi_{BR}$  space. In this space, the transition line is a linear function given by  $\chi_{BR}^* = \chi_{AR}$ . The two phases are the correlated phase (red) and the anti-correlated phase (blue). The triangles show the results from the free energy minimization. For this plot,  $\chi_{AB} = 4$  and  $\bar{\phi}_R = 0.02$  is used. (b) Jump of the order parameter  $\Delta\rho_{BR}$  along the binodal line between the correlated and the anti-correlated region at  $\chi_{BR} = 1$  for different average volume fractions  $\bar{\phi}_R$ . The symbols indicate the results obtained by minimizing the free energy. Solid lines show the analytic results. The parameters for the analytic curves are  $\bar{\phi}_A = 0.5$ ,  $\phi_{A,\text{out,bin}} = 0.2332$  and  $m = 1$ . The parameters for the points obtained from free energy minimization are  $\bar{\phi}_A = 0.5$ ,  $\kappa_R/L^2 = 7.63 \cdot 10^{-5}$ ,  $\kappa_A/L^2 = 6.10 \cdot 10^{-5}$ ,  $\kappa/L^2 = 6.10 \cdot 10^{-5}$  and  $L_s = 0.99$ .

that the value of the order parameter  $\rho_{BR}$  changes if the anti-correlated state and the correlated state are compared, within one type of state  $\rho_{BR}$  is constant. The same is true for the order parameter  $\rho_{AR}$ . The difference between the value of the anti-correlated state and the correlated state is the jump of the respective order parameter. In fig. 3.12 this jump of the order parameter is shown along the binodal line between the correlated states and the anti-correlated states. In the case of  $\bar{\phi}_A = 0.5$  this means that  $\chi_{BR}$  and  $\chi_{AR}$  are constant and equal. This result also shows very good agreement with the results obtained from free energy minimization. The deviations grow with growing  $\bar{\phi}_R$  because of the increased interaction between the profiles of the  $A$  and the  $R$  component.

A central feature of the ternary inhomogeneous system, the stability of a correlated droplet position or an anti-correlated droplet position can be reproduced with the simple analytic model. Quantitative differences between the analytic model and the minimization of the free energy functional can be mostly explained with the detailed shape of the regulator profile.



# 4 Spatial Regulation of Phase Separation on a Lattice with Fluctuations

In this chapter, lattice based Monte Carlo simulations of the three component liquid system with regulator gradient are presented. We start by discussing the implementation of the physical model in the Monte Carlo simulation. After that, results of an equilibrium system, where the regulator gradient is maintained by an external potential, are presented and compared to the results of the mean field approach discussed in chapter 3. Furthermore, we show results of simulations of non-equilibrium systems, in which the regulator gradient is generated by asymmetric boundary conditions.

## 4.1 Implementation of the Ternary Liquid Model in a Monte Carlo Simulation

The aim of this section is to give a short introduction to the principles of the Monte-Carlo simulations. Furthermore, we introduce a biased sampling technique, a type of Umbrella sampling, which is used in section 4.3.4 to investigate the equilibrium system. At the end of this section we discuss shortly the different types of implemented boundary conditions.

### 4.1.1 Lattice Based Monte Carlo Simulation

In this thesis we use a simplified model of a ternary liquid system that is closely related to the model introduced in chapter 3. To implement this model in the Monte-Carlo simulation, we discretize the volume of the system with a simple cubic lattice. A lattice site can be occupied by an  $A$ -particle, a  $R$ -particle, or can be a vacancy. Vacancies are interpreted as solvent particles ( $B$ -particles) in this model. In this simple model we consider only particles which are occupying exactly one lattice site, we do not consider any type of polymer-like particles. The interaction potential between two particles is also simplified and considers only nearest neighbor interactions between particles. For the simple cubic lattice that means that each particle can interact with up to six adjacent particles. The interaction between two neighboring particles of type  $i$  and  $j$  is described with the constant interaction parameter  $\epsilon_{ij}$ . The parameters  $\epsilon_{ij}$  here have the same meaning as in the mean-field calculation in section 2.1. With these definitions, the properties of one configuration are well described. To perform the particle based simulations we also have to define rules how the particles can move on the lattice and thus generate new configurations. Here, we use

a mechanism known as Kawasaki dynamics [85, 119, 92]. This is an exchange dynamics algorithm. A chosen particle can exchange position with one of the neighboring particles to reach a new position.

Later, we will also use a variation of this dynamics, where the particle can exchange its position only with a neighboring solvent particle, which leads to constrained exchange dynamics. Because this is the only implemented mechanism of generating new configurations, the number of a particular type of particles is kept constant. This is important because we want to consider a canonical ensemble keeping the temperature constant. The volume is kept constant by not changing the total number of lattice sites of the implemented incompressible lattice. The use of the canonical ensemble allows us to use the Flory-Huggins interaction parameters  $\chi_{ij}$  to describe the interactions between the components  $i$  and  $j$  in each step of the simulation (see eq. (2.3)). Because of that feature we have only to consider the three Flory-Huggins interaction parameters of the ternary system instead of the six pair interaction parameters. The calculation of the energetic difference between two configurations is shown in appendix B.1.<sup>1</sup>

We also want to use this section to discuss the Monte-Carlo simulation in more detail. To this end we consider the canonical partition function of the  $N$ -particle system

$$Q(N, V, T) = \int e^{-\beta E(\{r\})} d^N r, \quad (4.1)$$

where  $r$  describes the position in space. Here, we assume that the potential energy is independent of the momenta. In this case the integration over the momenta gives a constant factor and can be absorbed in the normalization. Because of that, it is omitted in further calculations. The free energy of the system can be obtained from the partition function with  $F = -1/\beta \ln Q$ . In equilibrium, the ensemble average of an observable  $A$  can be computed employing the partition function

$$\langle A \rangle = \frac{1}{Q} \int A(\{r\}) e^{-\beta E(\{r\})} d^N r, \quad (4.2)$$

with the Boltzmann-distribution of the configurations

$$P(\{r\}) = \frac{1}{Q} e^{-\beta E(\{r\})}. \quad (4.3)$$

The idea of the algorithm of the Monte-Carlo simulation is to construct a steady state, in which the distribution of states is equal to the Boltzmann distribution  $P(\{r\})$ . This approach is called importance sampling [68, 11, 50]. If such a steady state is generated, the average  $\langle A \rangle$  is obtained from simulation by averaging over each state, that is generated by the simulation in  $n$  steps

$$\langle A \rangle = \lim_{n \rightarrow \infty} \frac{1}{n} \sum_{i=1}^n A(\{r\}). \quad (4.4)$$

The construction of the Boltzmann distributed states is realized in two steps by the Metropolis algorithm [113, 11, 50]. In a first step, a new configuration is generated at random. In the case of molecular simulations, a common way is to select a particle  $i$  at

---

<sup>1</sup>If the ensembles does not strictly conserves particle numbers, the actual pair interactions  $\epsilon_{ij}$  have to be known to describe the energetic difference between two configurations.

random and change its position randomly. We determine the new position of the chosen particle as  $r_i^{\text{new}} = r_i^{\text{old}} + R\xi$ , where  $\xi$  is a random unit vector parallel to a basis vector of the simple cubic lattice and  $R$  is the radius, up to which the position can be changed. In our simulations we use  $R = 1$  and  $\xi$  is a vector in which one randomly chosen component is randomly set to  $+1$  or  $-1$  and the remaining components are 0. The movement of the particle to  $r_i^{\text{new}}$  leads to a positional exchange with the adjacent particle at this position because every lattice site is occupied by exactly one particle in each configuration. This rules of generating a new configuration preserves the particle number. In the second step of the Metropolis algorithm the difference of the potential energy between the two configurations is computed

$$\Delta E \equiv E(\{r\}^{\text{new}}) - E(\{r\}^{\text{old}}). \quad (4.5)$$

The new configuration is accepted with the probability

$$p_A = \min\left(1, e^{-\beta\Delta E}\right). \quad (4.6)$$

If  $\Delta E < 0$ , the new configuration is always accepted. In the case  $\Delta E > 0$ , the new configuration is accepted with a Boltzmann weight. This leads to the Boltzmann distribution in the steady state of the simulation.

#### 4.1.2 Umbrella Integration

The Monte Carlo Simulation, especially the Metropolis algorithm, samples states of global or local minima of the free energy, depending on temperature and fluctuations. The introduced Monte-Carlo method has its limit, if the investigated states are rarely observed. A typical example for rare states are the transition states between two stable or metastable states. In this case the direct sampling can be very resource consuming or quasi impossible. To sample these states of very low probability methods that employ biased sampling are used. Here, we introduce the umbrella sampling, which can be used to explore the free energy landscape between two states in energetic minimum following a certain path through this landscape [162, 93, 82]. The path in the phase space is described by the reaction coordinate  $\gamma$ , which is a scalar parameter.<sup>2</sup> The derivations in this section are taken from Kästner's review [82]. Because we consider only states on the path parametrized by  $\gamma$ , the canonical partition function is constrained.

$$Q(\gamma) = \frac{\int \delta(\tilde{\gamma}(\{r\}) - \gamma) e^{-\beta E(\{r\})} d^N r}{\int e^{-\beta E(\{r\})} d^N r}. \quad (4.7)$$

Here,  $\tilde{\gamma}$  is the value of the defined reaction coordinate for a certain configuration  $\{r\}$  of the system. The free energy along the reaction coordinate reads

$$F(\gamma) = -\frac{1}{\beta} \ln Q(\gamma). \quad (4.8)$$

In the simulation, the whole path can not be sampled directly because of the low probability of the intermediate states. To make the complete path accessible, we introduce a bias

---

<sup>2</sup>In general, the path can also be described by a higher dimensional property [94, 82]. We constrain ourselves to a scalar parameter, because we will use scalar parameters only in our studies.

potential  $U^{\text{bias}}$ . The partition function with the included bias potential is

$$\begin{aligned} Q^{\text{bias}}(\gamma) &= \frac{\int \delta(\tilde{\gamma}(\{r\}) - \gamma) e^{-\beta E(\{r\}) + U^{\text{bias}}(\tilde{\gamma}(\{r\}))} d^N r}{\int e^{-\beta E(\{r\}) + U^{\text{bias}}(\tilde{\gamma}(\{r\}))} d^N r} \\ &= e^{-\beta U^{\text{bias}}(\tilde{\gamma}(\{r\}))} \frac{\int \delta(\tilde{\gamma}(\{r\}) - \gamma) e^{-\beta E(\{r\})} d^N r}{\int e^{-\beta E(\{r\}) + U^{\text{bias}}(\tilde{\gamma}(\{r\}))} d^N r}. \end{aligned} \quad (4.9)$$

We can write the exponential term that contains only the bias potential outside the integral, because of the delta distribution which makes it independent of the positions of the particles. Using eq. (4.7), we can eliminate the delta distribution and get a relation between the unbiased and the biased partition function

$$\begin{aligned} Q(\gamma) &= Q^{\text{bias}}(\gamma) e^{\beta U^{\text{bias}}(\gamma)} \frac{\int e^{-\beta E(\{r\}) + U^{\text{bias}}(\tilde{\gamma}(\{r\}))} d^N r}{\int e^{-\beta E(\{r\})} d^N r} \\ &= Q^{\text{bias}}(\gamma) e^{\beta U^{\text{bias}}(\gamma)} \langle e^{-\beta U^{\text{bias}}(\gamma)} \rangle. \end{aligned} \quad (4.10)$$

The fraction in the first line of eq. (4.10) can be identified as the average used in the second line. With this partition sum, the unbiased free energy can be calculated as

$$F(\gamma) = -\frac{1}{\beta} \ln Q^{\text{bias}}(\gamma) - U^{\text{bias}}(\gamma) + C, \quad (4.11)$$

where  $C$  is the average  $C = -1/\beta \ln \langle e^{-\beta U^{\text{bias}}(\gamma)} \rangle$ . Because of averaging,  $C$  is independent of  $\gamma$  and can be regarded as an unknown constant contribution to the free energy. In general, we can not calculate or measure the partition function  $Q^{\text{bias}}$ . In computer simulation, we can use the identity between the partition function and the temporal average  $P(\gamma)$  in ergodic systems.

$$Q(\gamma) = P(\gamma) \equiv \lim_{t \rightarrow \infty} \frac{1}{t} \sum \delta_{\tilde{\gamma}\gamma} \Delta t. \quad (4.12)$$

We use the discrete formulation of the average, because of the discreteness of the simulation time steps. Furthermore, we observe only discrete values of the reaction coordinate  $\gamma$  in the considered lattice based Monte Carlo simulation. This is the reason for the appearance of the Kronecker symbol in the temporal average. This discrete values of  $\gamma$  do not have to be integers. Technically, we will get an approximation of this average  $P^{\text{sim}}(\gamma)$  from the Monte Carlo simulation, because of the limited simulation time.<sup>3</sup> Using this approximation, we get the free energy along the reaction coordinate

$$F_i(\gamma) = -\frac{1}{\beta} \ln P_i^{\text{bias,sim}}(\gamma) - U_i^{\text{bias}}(\gamma) + C_i. \quad (4.13)$$

At this point, we introduce the index  $i$ , because the free energy is sampled in a window of the reaction coordinate in the simulation. This window is controlled by the bias potential  $U_i^{\text{bias}}$ . The combination of multiple windows of the free energy  $F_i(\gamma)$ , which are obtained

---

<sup>3</sup>We can interpret the simulation steps of the Monte-Carlo simulation as a temporal measurement because of the applied physical moves. The time steps are the Monte-Carlo steps (MCS). We can also compute an approximate ensemble average from the simulation like introduced in the introduction 1.2.3, if the number of simulation steps between two considered configurations is high enough to consider them as independent configurations. We choose the time interpretation because it gives also access to e.g. the growth dynamics of the droplets or the droplet movement during relaxation into equilibrium.

## 4.1. Implementation of the Ternary Liquid Model in a Monte Carlo Simulation

---

by using different bias potentials  $U_i^{\text{bias}}(\gamma)$ , gives access to the complete free energy  $F(\gamma)$ . We use umbrella integration to combine these windows. In this method, the gradient of the free energy is calculated

$$\frac{\partial F_i(\gamma)}{\partial \gamma} = -\frac{1}{\beta} \frac{\partial \ln P_i^{\text{bias,sim}}(\gamma)}{\partial \gamma} - \frac{dU_i^{\text{bias}}(\gamma)}{d\gamma}. \quad (4.14)$$

By using the gradient of the free energy, we do not have to discuss or determine the constant  $C_i$ , because it is independent of  $\gamma$ . One central idea of the Umbrella integration is to use a normal distribution ansatz for the distribution of the reaction coordinate

$$P_i^{\text{bias,sim}} = \frac{1}{\sigma_i^{\text{bias,sim}} \sqrt{2\pi}} \exp\left(-\frac{1}{2} \left(\frac{\gamma - \bar{\gamma}_i^{\text{bias,sim}}}{\sigma_i^{\text{bias,sim}}}\right)^2\right), \quad (4.15)$$

with the average of the reaction coordinate  $\bar{\gamma}_i^{\text{bias,sim}}$  and the standard deviation  $\sigma_i^{\text{bias,sim}}$ . Following this logic we can say, that the distribution  $P_i^{\text{bias,sim}}(\gamma)$  is expanded in a cumulant expansion, which is truncated after the second term. This is equivalent to truncating a power series of  $F_i(\gamma)$  after the quadratic term. This treatment is well justified, because the free energy is smooth and each window covers only a small interval of  $\gamma$  [83, 82]. The normal distribution ansatz is used to evaluate the gradient of the free energy

$$\frac{\partial F_i(\gamma)}{\partial \gamma} = \frac{1}{\beta} \frac{\gamma - \bar{\gamma}_i^{\text{bias,sim}}}{\left(\sigma_i^{\text{bias,sim}}\right)^2} - \frac{dU_i^{\text{bias}}(\gamma)}{d\gamma}. \quad (4.16)$$

The only unknown parameters are the average  $\bar{\gamma}_i^{\text{bias,sim}}$  and the variance  $\left(\sigma_i^{\text{bias,sim}}\right)^2$  of the reaction coordinate, which can be sampled by Monte Carlo Simulation. In a last step, we combine the different windows to get the complete free energy along the reaction coordinate. This is done by sum up the windows weighted by  $p_i(\gamma)$ .

$$\frac{\partial F(\gamma)}{\partial \gamma} = \sum_i^{\text{windows}} p_i(\gamma) \frac{\partial F_i(\gamma)}{\partial \gamma} \quad (4.17)$$

The weights are given by

$$p_i(\gamma) = \frac{a_i}{\sum_j a_j}, \quad \text{with } a_i = n_i P_i^{\text{bias,sim}}(\gamma), \quad (4.18)$$

where  $n_i$  counts the number of steps sampled for window  $i$ . This complete gradient of the free energy can be integrated numerically to obtain the free energy profile along the the path of the reaction coordinate.

### 4.1.3 Definition of Boundary Conditions and Maintaining a Concentration Gradient

In this subsection we will discuss the boundary conditions implemented in the Monte Carlo simulation. The boundary conditions are different for the two scenarios we want to investigate with these simulations. The first scenario is an equilibrium system, in which the regulator gradient is created by an external potential. In that case, symmetric boundary

conditions are used. In the second scenario, the system is not in equilibrium, the regulator gradient is formed by diffusion with asymmetric boundary conditions. The direction of the established regulator gradient is the  $x$ -direction. The  $y$ - and  $z$ -direction is orthogonal to it. In the  $y$ - and  $z$ -direction, periodic boundary conditions are applied in both scenarios. In the case of equilibrium systems, a hard wall is used in  $x$ -direction. That means, that we consider a finite system regarding the  $x$ -direction.

In the case of a non-equilibrium system without external potential, we are using an asymmetric, semipermeable wall in the  $x$ -direction. If a regulator particle would leave the system from  $x = 0$ , it can exchange its position periodically with a  $B$ -particle at  $x = 1$ . The exchanging particles have the same  $y$ - and  $z$ -position. If a regulator particle would leave the system from  $x = 1$ , it feels a hard wall. This asymmetric, semipermeable wall leads to a passive pumping process, where the regulator is pumped from one side of the box to the opposing side (see fig. 4.1). In general, the direction of this process can be chosen arbitrary, it is determined by the implemented features of the walls.

This type of boundary conditions was introduced in section 2.3. To describe this boundary condition quantitatively, we introduce a flux of the regulator material at the boundaries  $j_{bc}$ . This flux has to be equal at  $x = 0$  and  $x = 1$  because of particle conservation. This equality is implemented in the simulation by the described coupling of the boundaries. Every particle which leaves the system on one site is immediately inserted on the other site. In general, this fluxes are a function of the regulator volume fractions at the boundaries,  $j_{bc} = j_{bc}(\phi_R(0), \phi_R(1))$ . To compute this dependency, we use the argument that the boundary fluxes and the net diffusion flux in the bulk have to be equal in the stationary state. The general solution of the diluted regulator profile in the stationary state is  $\phi_R = mx + m_0$ . Because of particle conservation, we can describe  $m_0$  in terms of  $m$  and  $\bar{\phi}_R$  (compare section 3.4). From the normalization of the regulator profile we obtain  $m_0 = \bar{\phi}_R - m/2$  with the average volume fraction of the regulator  $\bar{\phi}_R$ . According to Fick's first law of diffusion, the diffusion flux in the bulk is  $j_{diff} = -D_R \partial_x \phi_R$ , where  $D_R$  is the constant diffusion coefficient of the regulator in this system. By comparing these relations we obtain the condition

$$j_{bc}(m) = -D_R m \tag{4.19}$$

for the boundary fluxes. We use the short form  $j_{bc}(m)$  here, because  $D_R$  can be regarded as a given constant parameter, so that  $m$  is the only remaining variable of the boundary flux. From eq. (4.19) follows, that there exists exactly one well defined  $m$  which fulfills this condition, if  $j_{bc}(m)$  is bijective. This is sufficient to compute the flux in the stationary state. The detailed calculation of the boundary flux in the simulation is presented in appendix B.4.

The pumping of the regulator is illustrated in fig. 4.1. This pumping can be also interpreted as a source and a sink at the boundaries. The strict coupling of the source and the sink maintains the canonical ensemble considered in the simulation. This source-sink mechanism creates a approximately linear regulator gradient in the system (see fig. 4.2). Considering the equilibrium case, the potential can be chosen so that the regulator shows the same volume fraction profile as in the non equilibrium scenario. These two regulator profiles of different origin are compared in fig. 4.2. The proposed mapping works very well for a diluted regulator. In the later simulations, we will generate regulator gradients that are approximately equal for both cases. In fig. 4.2, the gradients obtained from the simulation

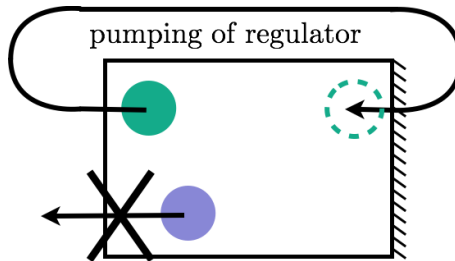


Figure 4.1 – Asymmetric boundary conditions for the regulator particles in  $x$ -direction are used. The left boundary is permeable for the regulator particles. If a regulator particle tries to pass this wall, it can periodically exchange the position with a  $B$ -particle on the other side. This exchange is accepted according to the Metropolis criterion. The right wall is not permeable. A regulator particle in the simulation box can not pass this wall. This rules lead to a passive pumping of the regulator material driven by diffusion.

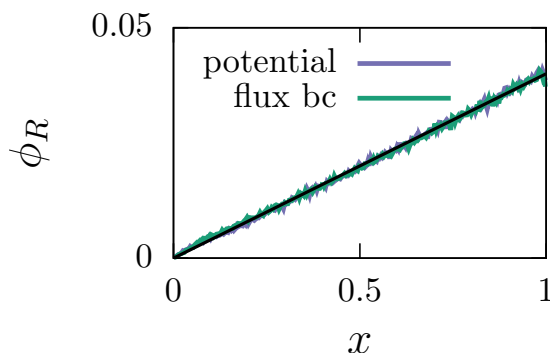


Figure 4.2 – Comparison of the regulator distributions from simulations with external potential or flux boundary conditions. This distributions are compared to the maximal constant gradient (black line), which is also the idealized solution of the regulator profile in both cases. The parameters are  $\bar{\phi}_A = 0.05$ ,  $\bar{\phi}_R = 0.02$ ,  $\chi_{AB} = 4$ ,  $\chi_{AR} = 1$ ,  $\chi_{BR} = 1$ .

data are also compared to the profile with maximal constant gradient with  $m_0 = 0$  and  $m = 2\bar{\phi}_R/L$  (we have chosen  $L = 1$ ). The distributions in the simulation show only very small deviations from this maximum constant gradient.

## 4.2 Equilibrium System without Regulator Gradient

In this section we consider the equilibrium systems in absent of an imposed regulator gradient. Of particular interest is the influence of the regulator concentration on the phase transition between the droplet state and the mixed state. This phase transition is well investigated in the literature using Monte Carlo simulation [154, 123, 10]. The purpose of this section is to give an impression of the phase separation in the lattice system. The focus of the simulations will be systems with an imposed regulator gradient and is presented in section 4.3 and section 4.4.

In the case of no imposed regulator gradient, we have performed Monte Carlo simulations in a cubic box of size  $64a$  in one direction and full periodic boundary conditions in all spatial directions if small volume fractions were considered. For high volume fractions we implemented a hard wall in one direction. This different choices were made to simplify the measurement of the volume fractions in both cases. In a first step we consider a binary

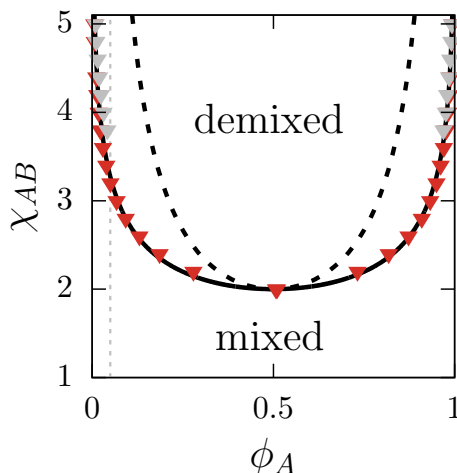


Figure 4.3 – Phase diagram of the two component system. Dependent on  $\bar{\phi}_A$  and  $\chi_{AB}$ , the system can be mixed or demixed. The solid black lines indicate the binodal lines from the mean field theory, the dashed black lines the respective spinodal lines. The red triangles show simulation results for  $\bar{\phi}_A = 0.5$ , the grey triangles for  $\bar{\phi}_A = 0.05$ . The mean field result and the simulation data are consistent in both cases. The grey dashed line indicates the average volume fraction  $\bar{\phi}_A = 0.05$  and provides a graphical solution for the phase separation behavior in that case.

system without the regulator. In equilibrium, one coherent majority phase of  $A$ -particles is formed. For periodic boundary conditions this phase is a droplet. With hard walls in one direction and high volume fractions this phase is a planar phase parallel to the hard wall. We measured the volume fraction of  $A$  inside the droplet and outside the droplet and compared these values with the mean field phase diagram. The purpose of this comparison is to get an idea if the mean field approximation works well for the considered system. The result is shown in fig. 4.3. The simulation data are consistent with the mean field predictions.

In a second step, we consider the homogeneous ternary system, no regulator gradient is imposed. The state of the system is described by an integrated order parameter. This order parameter is defined as the average number of neighbors of type  $A$  of an  $A$ -particle. Because we are using a simple cubic lattice, this parameter can take values between 0 and 6. The order parameter is 0, if all particles are isolated and no clusters exist in the configurations, it is 6, if the lattice is completely filled with droplet material particles.

Depending on the value of the interaction parameter a mixed state is observed or droplets are formed. In the second case, multiple droplets are nucleated. These small droplets grow and merge to form bigger ones (see appendix B.2). In the equilibrium state, exactly one droplet is present. The phase diagram is represented by a color code of the introduced order parameter in dependence of the average volume fractions of the regulator  $\bar{\phi}_R$  and the droplet material  $\bar{\phi}_A$ . We compare phase diagrams for different values of the Flory-Huggins parameters. In this study, the parameter  $\chi_{AB}$ , which describes the interaction between droplet material and solvent, has to be larger than 2 as a necessary condition to observe phase separation. We choose  $\chi_{AB} = 4$  to not get a too small separated region of the phase diagram.<sup>4</sup> The other parameters  $\chi_{AR}$  and  $\chi_{BR}$ , which are describing the interaction

<sup>4</sup>The value  $\chi_{AB} = 2$  is the critical value of the corresponding binary system and thus the minimum value for which phase separation occurs given the critical volume fraction  $\phi_R^c = 0.5$ .

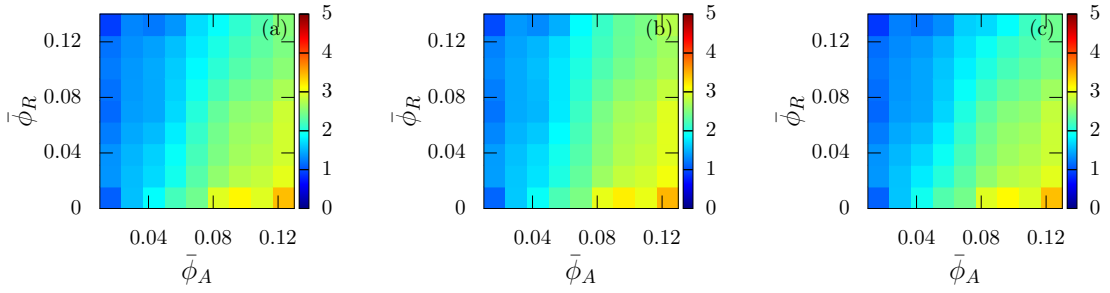


Figure 4.4 – Phase Diagrams in the  $\bar{\phi}_A$ - $\bar{\phi}_R$ -space of the system without an imposed regulator gradient for different  $\chi_{AR}$  values. The colorbar indicates the average number of  $A$ -neighbors of an  $A$ -particle. (a) In this example  $\chi_{AR} = 0$ . In this study, we consider only diluted concentrations of  $A$  and  $R$ . The mixed states are indicated by the blue color. (b) For  $\chi_{AR} = 3$ , the droplet is favored, because of the depletion of regulator particles out of the droplet. (c) Otherwise, for  $\chi_{AR} = -3$ , the mixed state is favored, because the regulator material is accumulated in the droplet. The common parameters of these phase diagrams are  $\chi_{AB} = 4$ ,  $\chi_{BR} = 0$ ,  $L = 64a$  and  $\beta = 1$

between the regulator and the droplet material or the solvent, are chosen, so that the regulator mixes with the other two components. Here, the interaction parameter  $\chi_{BR}$  is 0. The highest value of  $\chi_{AR}$  is 3. This is bigger than the critical value, but because of the very diluted regulator, segregation is not expected and not observed. This higher value was used as a compromise for a better visualization of the effects of the interaction parameter on the phase diagram. The most negative value of interaction parameter considered is  $-3$ . For very big negative interaction parameters we can also observe phase separation, because of the attractive interaction of the corresponding components. We built the phase diagram for different interaction parameters  $\chi_{AR}$  and  $\chi_{BR}$  in the region of small regulator volume fraction and small droplet material volume fraction. These volume fractions were chosen because of the biological motivation.

Results of this study are shown in fig. 4.4, where three different combinations of interaction parameters are presented. These phase diagrams show, that in general, a high regulator concentration favors the mixed solution. We explain this with the reduced number of  $A$ - $A$ -contacts inside the droplet by adding regulator particles. Consistently, the figures show, that the droplet state is favored, if the interaction parameter  $\chi_{AR}$  is positive. In that case the droplet is depleted of regulator material. As a result, the stability of the droplet is increased. In the other case, if the interaction parameter  $\chi_{AR}$  is negative, the regulator particles are accumulated inside the droplet. This supports the dissolution of the droplet.

### 4.3 Equilibrium System: Regulator Gradient by External Potential

In this section, we simulate a system with imposed regulator gradient in equilibrium. The equilibrium in such a system can be reached, if the regulator gradient is generated by an external potential, which is interacting with the regulator particles. Such a system is comparable to the system which was used in the mean field calculation presented in chapter 3. We are also using the same form of the external potential eq (2.11). The

simulation is performed in three dimensions, where the  $x$ -direction is the direction of the external potential. The external potential is constant in the other spatial directions. We present the established steady states in that ensemble and discuss the transition of the droplet position. The results are also compared to the mean field results.

### 4.3.1 Characterization of States

In the case of simulations with an imposed regulator gradient, we are using a not cubic box of the size  $256a \times 32a \times 32a$ , where the  $x$ -direction has the length  $256a$ . We discuss equilibrium states of one stable droplet. This droplet is spherical and for the chosen interaction parameters it contains about the half of the present droplet material  $A$ . Like in the mean field theory, we can observe anti-correlated droplet and correlated droplets (see section 3.2.2). In fig. 4.5 a typical example of an anti-correlated state and correlated state is shown. In both cases, we present a snapshot of the simulation and a one dimensional projection of the  $y$ - $z$ -integrated volume fractions. This integrated volume fraction should be seen as an approximate description of the system composition. There are two major limitations of this projection we have to consider. It does not distinguish if the droplet material is located inside the droplet or in the solvent phase. Each data point is a superposition of these two volume fractions. The projection does also not take into account the actual geometry of the droplet, which has an impact on the volume fraction profile. The seemingly not very sharp interface of the droplet is caused by the projection of the droplet geometry. For a detailed description of the observed equilibrium states, we use a set of different properties, which are defined in the following paragraphs.

*Energy.* The initial configuration of the simulation is defined to have 0 energy. During the simulation this energy is determined by adding up all  $\Delta E$  values that correspond to accepted moves. This observable is used as one criterion to decide, if the simulated system is in equilibrium. Because of the definition of the state of zero energy, two equilibrium energies of different simulation runs are only comparable, if the two simulations make use of the same initial configuration.

*Droplet size.* As droplet size, we define the number of particles  $N_{\text{drop}}$  of the biggest cluster in the system, with is the droplet in general. Conceptual, a cluster is identified by choosing a random non solvent particle of the system. All of the up to six neighboring non solvent particles are part of the same cluster. This process is repeated for the found neighbors until no additional particles are found. The so defined cluster is built of droplet particles and regulator particles.

*Eccentricity.* Here, the eccentricity  $e$  is the eccentricity of the shape of the droplet projection to the  $x$ - $y$  or  $x$ - $z$  plane. To this end, an ellipse is fitted to this projection shape. This eccentricity is then defined as  $e = \sqrt{1 - b^2/a^2}$ , where  $a$  and  $b$  are the semi-major axis and the semi-minor axis of the fitted ellipse [20]. It is defined in  $0 \leq e < 1$ . In the case of  $e = 0$ , the fitted ellipse is a circle and both semi axis are equal. The eccentricity is 1, if the semi-minor axis vanishes. The detailed calculation of the eccentricity is shown in appendix B.3.

*Radius of gyration.* The radius of gyration of the biggest cluster is defined as  $R_G =$

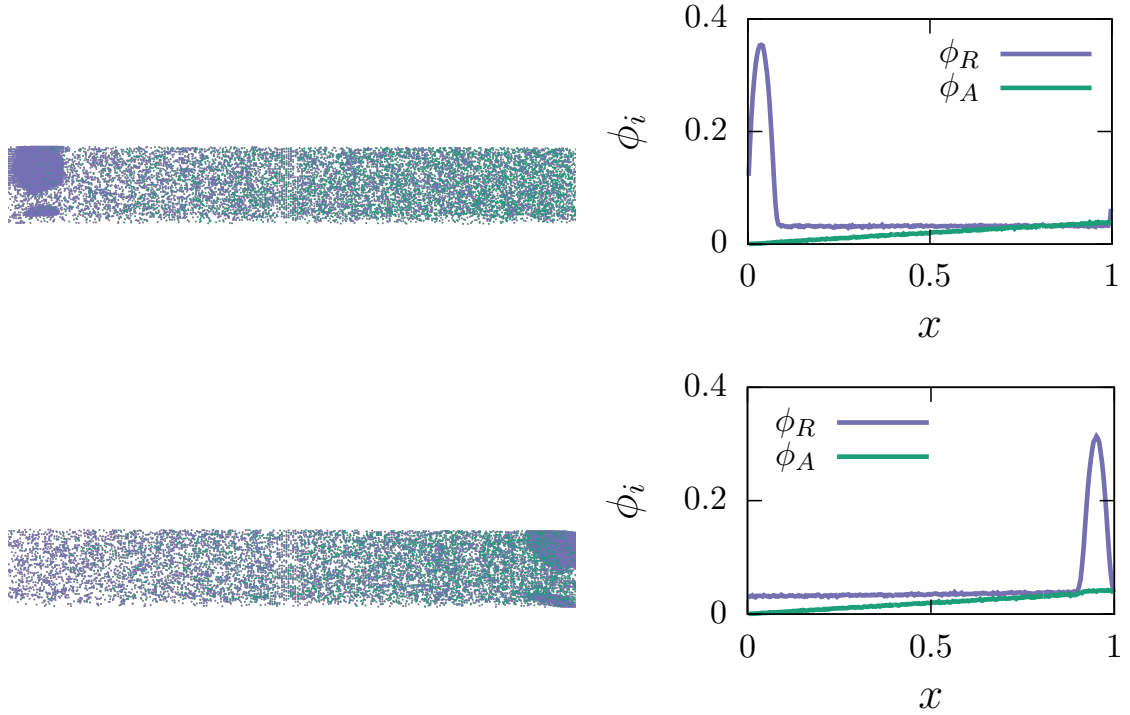


Figure 4.5 – (top left) Snapshot of an anti-correlated state from Monte-Carlo Simulation. The regulator particles are shown as green points, the  $A$ -particles are shown as purple points. The  $B$ -particles are not shown. The droplet is placed at the side of low regulator concentration. (top right) For the anti-correlated state, the volume fraction of the  $A$ - and  $R$ -particles is calculated for each  $y$ - $z$ -slice of the lattice. This property is averaged over 50 snapshots. In this  $x$ -projection, the boundaries of the droplet are smoothed out because of the geometry of the droplet. We choose  $\chi_{AR} = 2$  to visualize the anti-correlated state. (bottom left) Snapshot of a correlated state from Monte-Carlo simulation. The droplet is placed in a region of high regulator concentration. (bottom right) This profile of the volume fraction of the correlated state is also averaged over 50 snapshots. We choose  $\chi_{AR} = 0$  to visualize the correlated state. The common parameters are  $\chi_{AB} = 4$ ,  $\chi_{BR} = 0$ ,  $\bar{\phi}_R = 0.02$ ,  $\bar{\phi}_A = 0.05$ ,  $A = 0.0077$  and  $L = 256$ .

$\sqrt{\frac{1}{N_{\text{drop}}} \sum^{\text{drop}} (\mathbf{r} - \mathbf{r}_{\text{com}})^2}$ , where  $\mathbf{r}_{\text{com}}$  is the center of mass of the droplet.

*Moments of the droplet.* By measuring the  $y$ - $z$ -integrated volume fraction of the particles that are located inside the droplet, we can calculate the  $x$ -distribution of droplet particles  $P_{\text{drop}}^{\phi}(x)$ . From this distribution the first, second and third moment  $m_i^{\text{drop},x} = \int_0^L x^i P_{\text{drop}}^{\phi}(x) dx$  are obtained. The first moment can be identified as the  $x$ -component of the center of mass  $\mathbf{r}_{\text{com}}$  of the droplet. The second moment is related to a type of variance of  $P_{\text{drop}}^{\phi}(x)$  and is thus related to the width of this distribution. The third moment is the skewness and describes the asymmetric behavior of the distribution.

*Partition coefficient of the regulator material.* The partition coefficient  $p$  of the component  $R$  between the two phases  $a$  and  $b$  is defined as the fraction of the concentrations of this component in the two phases  $p = \frac{c_a^R}{c_b^R}$ . Here, we use the volume fractions of  $R$ . The phase  $a$  is the droplet (in) phase and  $b$  the surrounding solvent (out) phase. The volume fraction is proportional to the concentration in the considered ensemble, we can write  $p = \frac{\phi_R^{\text{in}}}{\phi_R^{\text{out}}}$ . The volume fraction  $\phi_R^{\text{in}}$  is approximated from the simulation data. It is the number of  $R$ -particles in a droplet  $N_R^{\text{in}}$  divided by the number of  $R$ - and  $A$ -particles  $N_A^{\text{in}}$  in that droplet. Here, we neglect the number of  $B$ -particles in the calculation, because it is not clear which  $B$ -particles are part of the droplet, especially at the boundary. Furthermore, there are very few  $B$ -particles in the droplet, neglecting them generates only a very small error. The volume fraction  $\phi_R^{\text{out}}$  is approximated by an analytic consideration. We assume that this volume fraction is governed by the external potential or the flux boundary conditions, respectively. It is  $\phi_R^{\text{out}} \approx mx_{\text{com}} + m_0$ . This linear regulator profile is the ideal profile obtained from the gradient generating mechanism, namely the external potential or the flux boundary conditions. It is evaluated at the center of mass of the droplet. This approximation is more precise, if the regulator concentration is small and the droplet contains a small amount of regulator compared to the total number of regulator particles and the size of the droplet is small compared to the system size. In section 4.1.3 we have shown that the analytic expression of the maximum constant gradient is a very good approximation for the corresponding simulation data. Finally, the partition coefficient obtained from the simulation ( $p_{\text{sim}} \approx p$ ) is  $p_{\text{sim}} = \frac{N_R^{\text{in}}}{N_R^{\text{in}} + N_A^{\text{in}}} \frac{1}{mx_{\text{com}} + m_0}$ .

The skewness and the eccentricity are 0 in very good approximation in our studies, which means that despite the anisotropic environment of the droplet, the droplet can be described as a sphere. Following this, the droplet size and the radius of gyration are of very similar meaning, because we do not observe significant shape changes of the droplet, which would effect the radius of gyration at constant droplet size. The center of mass of the droplet is important for evaluating the position of the droplet. It is also used to define the velocity of the droplet, which is the velocity of the center of mass of the droplets in the units  $a/\text{MCS}$  (lattice sites per Monte Carlo step).

### 4.3.2 Phase Transition between Equilibrium States

Now, we want to evaluate the behavior of a droplet in a regulator gradient in equilibrium. The regulator gradient is imposed by using an external potential, which affects the regulator particles. We use a not isometric simulation box of the size  $256a \times 32a \times 32a$ . The used

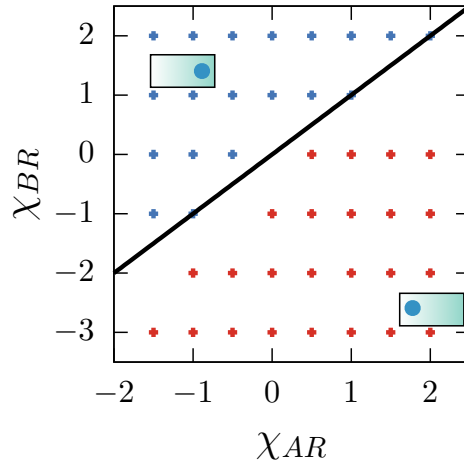


Figure 4.6 – The phase diagram of droplet states in the  $\chi_{AR}$ - $\chi_{BR}$ -plane is obtained by Monte-Carlo simulation. The blue points indicate states of a correlated droplet, the red points show the region of anti-correlated droplets. For comparison, the analytical transition line is included in this phase diagram (see section 3.4). The parameters are  $\chi_{AB} = 4$ ,  $\bar{\phi}_A = 0.05$ ,  $\bar{\phi}_R = 0.02$ ,  $A = 0.0077$  and  $L = 256$ .

boundary conditions are hard walls in  $x$ -direction, the direction of the external potential, and periodic boundary conditions in the orthogonal directions  $y$  and  $z$ . The hard wall has solvent like interactions with the particles of the neighboring layer of the lattice to prevent wetting. We will change the interactions of the regulator with the other particles  $\chi_{AR}$  and  $\chi_{BR}$  to investigate the droplet behavior. The interaction parameter  $\chi_{AB}$  has the constant value 4 in this simulations. The value is chosen considering the mean field theory, so that the droplet is stable in the whole box and does not dissolve (see section 3.2.4). In this system, we observed two types of equilibrium states, a correlated state with a droplet close to the wall at high regulator concentration and a anti-correlated state with the droplet at the wall at low regulator concentration. We can build the phase diagram by evaluating the equilibrium state of each  $\chi_{AR}$ - $\chi_{BR}$ -combination of the region of interest.

The resulting phase diagram is presented in fig. 4.6. It consists of two regions, the region of correlated states and the region of anti-correlated states. Close to the transition line between these two regions, the fluctuations of the droplet position increases significantly. At some points it was not possible to decide, which type of equilibrium state will be obtained. These cases are omitted, which is the explanation for the few missing points close to the transition line.

Now, we want to focus on the transition line. To this end, we look at a cut through the phase diagram at constant  $\chi_{AR}$ . For the different  $\chi_{BR}$ , we prepared two simulations, one starts with a droplet close to the left wall, the other starts with a droplet close to the right wall of the box. If the droplet is placed near a non stable position, the droplet starts to move to the stable region with a constant velocity. The velocity is zero, if the initial position of the droplet is already the stable position. This velocity is measured along the cut for both initial configurations. The velocities are shown in fig. 4.7. For low  $\chi_{BR}$ , the anti-correlated state is stable, indicated by the resting droplet in this states. The droplet in the correlated state moves to the left side of the box with a negative velocity. Vice versa, for higher  $\chi_{BR}$ , the correlated state is stable. Now the droplet starting in a correlated state is resting and the droplet, which was initialized in an anti-correlated state moves to

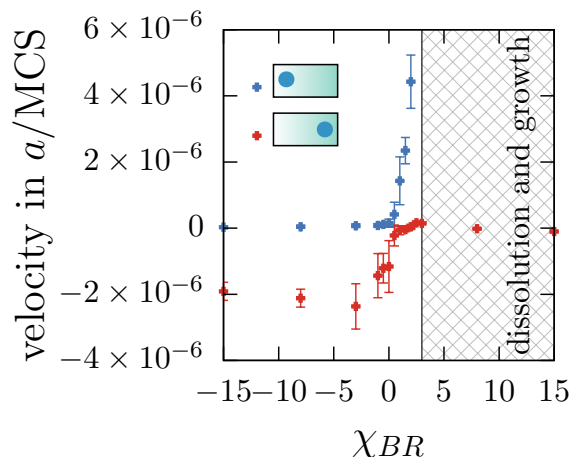


Figure 4.7 – The blue points are results of a simulations with an anti-correlated initial state, the red points indicate simulations with an correlated initial state. Both types of simulations are done along a cut at  $\chi_{AR} = 1$  through the phase diagram shown in fig. 4.6. The error bars in this plot indicate the standard deviation calculated from ten independent seeds of the simulation. The data points of moving droplets in the dissolution and growth regime are not included in this plot, because they are significantly higher than the drift data, which would make the transition region less visible. The parameters are  $\chi_{AB} = 4$ ,  $\chi_{AR} = 1$ ,  $\bar{\phi}_R = 0.02$ ,  $\bar{\phi}_A = 0.05$ ,  $A = 0.0077$  and  $L = 256$ .

the right side of the box with a positive velocity. The region, where the velocity of both types of simulation is close to zero, corresponds to the transition region and is consistent with the presented phase diagram.

Another result of this study is that we can observe two different types of droplet movement. The first process is a drift movement. In this case, the droplet is stable and the position of the whole object is moving. A typical example are the droplet which are starting at high regulator concentrations. These droplets move only if the anti-correlated state is the stable one. That means, that the droplets are also depleted of regulator material and thus of high stability considering fig. 4.4. The second process is a dissolution of the droplet and recondensation at an other place in the simulation box. This condensation is observed for the droplets starting at low regulator concentrations. These droplets move if the correlated states are stable, which also means, that they are enriched of regulator material.

This enrichment of the regulator inside the droplet is shown in fig. 4.8 using the partition coefficient  $p$  of the regulator as the measurement. In fig. 4.8, the average of  $p$  is presented for a simulation with a correlated initial state and a anti-correlated initial state. The two curves almost collapse, which is a hint, that the amount of regulator particles inside the droplet equilibrates fast compared to the droplet drift. Studying the averaged partition coefficient, we see, that for small  $\chi_{BR}$ , the fraction of regulator material in the droplet is close to zero. Around  $\chi_{BR} = 0$  this fraction growth sigmoidal and reaches its plateau around  $\chi_{BR} = 9$ . The inflection point of this growth is slightly higher than the transition value of the correlated-anti-correlated transition. The dissolution and recondensation process is observed for  $\chi_{BR} > 3$ . The corresponding regulator volume fraction  $\phi_R = 0.12$  at this point is consistent with the homogeneous phase diagram fig. 4.4, as for this value the mixed state is observed.

Within this region, we can observe two different mechanisms of dissolution and growth.

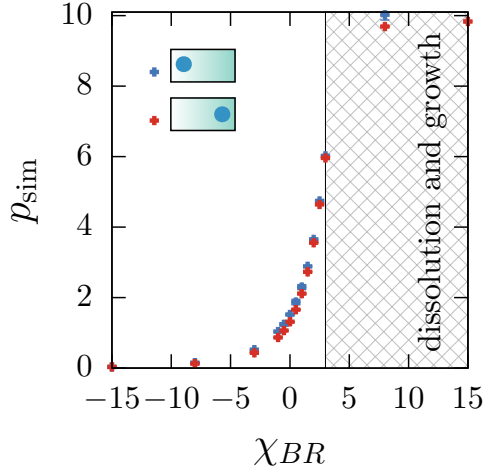


Figure 4.8 – Partition coefficient  $p$  of the regulator along the cut  $\chi_{AR} = 1$  through the phase diagram fig. 4.6. The blue points represent data from simulations with an anti-correlated initial state, the red points data from simulations with correlated initial states. Each point is an average of ten simulation runs. The error bars are representing the standard deviation from ten simulation runs, but are negligible small. There is almost no hysteresis, which suggest an absent influence of the initial conditions. The parameters are  $\chi_{AB} = 4$ ,  $\chi_{AR} = 1$ ,  $\bar{\phi}_R = 0.02$ ,  $\bar{\phi}_A = 0.05$ ,  $A = 0.0077$  and  $L = 256$ .

For very high  $\chi_{BR}$ , the droplet dissolves and many droplets condensate along the gradient. This can be explained, because the regulator material segregates strongly and can be regarded as a nucleus of the droplets. These droplets move to the stable position, driven by the external potential, and are combined there. For lower  $\chi_{BR}$ , the droplet dissolves and recondensates at the stable position, there is no drift of the new droplet observed. To summarize this subsection, we can say that dependent on the interactions of the regulator  $\chi_{AR}$  and  $\chi_{BR}$ , two types of equilibrium states can be observed, a correlated state and an anti-correlated state. A droplet, which is not placed at this stable state can reach this by two processes. For low  $\chi_{BR}$  a drift is observed, for high  $\chi_{BR}$  the droplet dissolves and recondensates. The occurrence of these processes is controlled by the fraction of regulator inside the droplet.

### 4.3.3 Regulator Distribution in the Droplet Phases and its Environment

In this subsection, we will have a closer look on the regulator accumulation or depletion inside the droplet. In section 4.3.2, we employed an integrated property, the total amount of regulator particles inside the droplet, to discuss the partition coefficient in dependence of the interaction parameter  $\chi_{BR}$ . Now, we will measure the detailed structure of the regulator distribution. To this end, we measure the radial density of the regulator with respect to the center of mass of the droplet. The calculation of the skewness and the eccentricity of the droplet has shown, that the droplet is symmetric and spherical in very good approximation. Because of that, we do not have to take into account a anisometric shape when calculating the radial distribution. To measure the radial distribution, we have divided the droplet into spherical shells of distant  $a$  and have calculated the regulator density in each shell. Fig. 4.9 shows the radial regulator density for three different conditions of the particle interactions. The dashed line indicates the radius of gyration of the droplet.

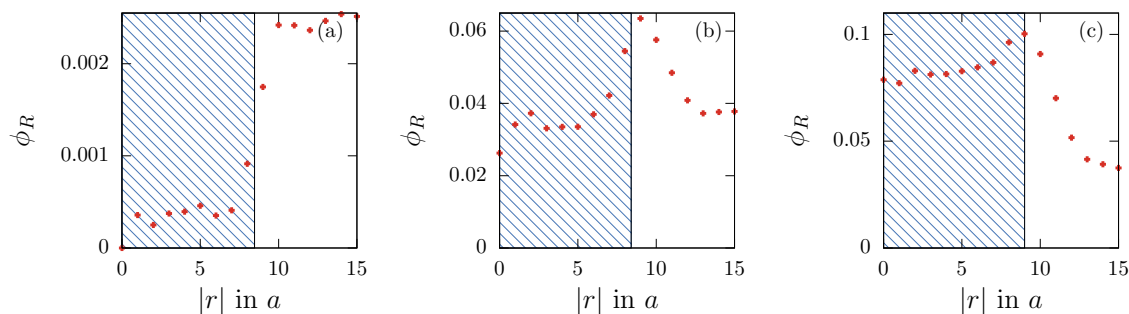


Figure 4.9 – To visualize the radial regulator distribution, the volume fraction in shells of thickness  $a$  around the center of mass of the droplet is shown. The shaded region indicates the droplet size measured by the radius of gyration. (a) In the region  $\chi_{BR} < 1$ , here  $\chi_{BR} = -1$ , the droplet is depleted of regulator material. (b) Around the transition region of the phase diagram, the regulator has no preferred phase and is accumulated at the droplet surface. We choose a correlated state to generate this figure, but the chosen state does not matter for this case of the study. It will only change the level of the regulator volume fraction but not the distribution of the regulator material. (c) For  $\chi_{BR} > 1$ , here  $\chi_{BR} = 2$ , the regulator is accumulated inside the droplet. Now, the correlated state is stable and the droplet is positioned at high regulator concentration. The parameters are  $\chi_{AB} = 4$ ,  $\chi_{AR} = 1$ ,  $\bar{\phi}_R = 0.02$ ,  $\bar{\phi}_A = 0.05$ ,  $A = 0.0077$  and  $L = 256$ .

If the net interaction between regulator and solvent becomes attractive, the droplet is depleted of the regulator particles. This scenario is shown in the first plot. The density of the regulator is very small in that case, because the droplet is in an anti-correlated state, and thus is placed on the side of low regulator concentration. The effect of the accumulation of regulator at the interface is small in comparison to the distribution of regulator inside and outside the droplet, it is not visible here. In the second figure  $\chi_{AR} = \chi_{BR} = 1$  is used, which corresponds to a simulation close to the transition line of the phase diagram fig. 4.6. In that case the regulator has no preferred phase and it shows the same volume fraction inside and outside the droplet. We observe a accumulation of regulator at the interface. This is caused by the high energetic interaction between the droplet material and the solvent,  $\chi_{AB} = 4$ . The total free energy can be decreased by placing regulator particles at the interface, so that the number of contacts between droplet material and solvent is decreased. It is also possible that the generation of the peak is supported by an entropic effect. Because we have chosen weak interactions between the regulator and the other particles compared to the  $A$ - $B$ -interaction, we can relate this to an amphiphilic character of the regulator, which leads to this tensid-like behavior. If the interaction between the regulator and the solvent becomes more repulsive, the regulator is accumulated inside the droplet as shown in the third plot. The accumulation at the interface is still visible. This effect is also obtained from the mean field results presented in appendix A.7. There we have shown that the peak is caused by an energetic effect in a simple analytic model. An entropic effect exists in this analytic model but its strength is significantly lower than the strength of the energetic effect.

The distribution of regulator in the droplet can be linked to the Phase diagram of the droplet states. In the region of anti-correlated droplets, we observe a depletion of regulator particles in the droplet. In the region of correlated droplets, the regulator particles are accumulated in the droplet. Close to the transition line, the regulator density is

approximately equal inside and outside the droplet. In this relation between regulator distribution and equilibrium states, the accumulation of regulator particles in the interface is neglected, because that is caused by other effects, like discussed earlier.

#### 4.3.4 Transition States and Signature of the Phase Transition

In this subsection we use the method of the Umbrella Sampling to explore the shape of the free energy profile between the correlated and the anti-correlated state following a chosen reaction coordinate. We use this biased sampling method because the droplet states between the correlated and the anti-correlated state are of very low probability, and thus can not be practically sampled with a direct sampling method. We have to make two choices using the Umbrella method, which are the reaction coordinate and the bias potential. The reaction coordinate has to be suitable for describing states quasi continuously from correlated to anti-correlated. Because we are using a lattice based simulation, all properties are discrete. With quasi continuous we want to say, that the reaction coordinate has a continuous limit if the spatial resolution of the lattice gets arbitrarily high. In our umbrella simulations, we use the x-coordinate of the center of mass of the biggest cluster of  $A$ - and  $R$ -particles as the reaction coordinate.

$$\gamma = \sum_{i \in \text{biggest cluster}} \frac{x_i}{N_{\text{drop}}}. \quad (4.20)$$

We have to keep in mind, that this is only a valid reaction coordinate if the same object is the biggest cluster during the complete simulation. We can not investigate parameter regions, where the identity of the biggest cluster switches between different objects at some point during the simulation. This would lead to a system out of equilibrium because the bias potential would drive different clusters depending on time.

As bias potential, the common harmonic potential is used with the analytic form

$$U_i^{\text{bias}}(\gamma) = \frac{\alpha}{2} (\gamma - \gamma_i)^2, \quad (4.21)$$

where  $\gamma$  is the reaction coordinate,  $\gamma_i$  is the reference reaction coordinate of the bias potential  $U_i^{\text{bias}}$  and  $\alpha$  is a constant parameter. The parameter  $\alpha$  determines the width of the resulting distribution of the reaction coordinate. Here we choose to produce very narrow distributions, because the assumption, that are done by applying the umbrella integration, are more accurate if small windows of the free energy are explored (see section 4.1.2). For this simulations, we will use a periodic external regulator potential. This periodic external potential is considered, because we want to avoid boundary effects (compare section 3.3). The external regulator potential is

$$U_R(x) = -\ln(1 - A \sin(2\pi(x - \omega))). \quad (4.22)$$

We use the same potential as in the mean-field calculation of the periodic system and choose  $\omega = 0$  (see eq. (3.16)). In the Boltzmann limit, this choice leads to a sinus regulator distribution, which has a minimum at  $x = L/4$  and a maximum at  $x = 3L/4$ . In the section 3.3 we have shown that the use of a periodic potential causes only a slight change of the mean field results compared to a system with linear regulator distribution. Based on this, we assume, that the intrinsic behavior of the free energy of the simulated system

with periodic or linear regulator distribution is also very similar. Because of the periodic external potential, periodic boundary conditions are used in all directions, now.

We compare two cases of the simulation, the first case is a system with a correlated equilibrium droplet position, the second case a system with a anti-correlated one. The resulting free energy profile of both cases is presented in fig. 4.10. On the left site, we present data from a simulation employing parameter values from the correlated region of the mean-field phase diagram. There is a very clear local minimum at the maximum regulator distribution, which supports the idea of a correlated equilibrium position of the droplet. We do not see a local minimum at the anti-correlated position here, like proposed considering the mean field results. At this position, a local maximum is observed. This is consistent with our observation, that the droplet is always driven to the equilibrium state in the simulation. Compared to the mean-field results the second local minimum is possibly extincted by fluctuations. This also means, that we do not expect either a first order phase transition between the correlated and the anti-correlated state or a hysteresis in the simulation. We have to mention, that there is still a chance that the phase separation can be observed for certain values of the parameters, but we did not find such a region. The right plot shows the free energy profile of the simulated system corresponding to parameter values from the anti-correlated region of the phase diagram. Again, we see a pronounced minimum at the expected anti-correlated equilibrium position, but only a local maximum at the proposed metastable state. If we compare the amplitude of the free energy of both systems, we see, that this is smaller in the correlated case. The reason is the chosen values of the  $\chi_{BR}$ -parameter. In the correlated case, we choose  $\chi_{BR} = 0$ , which is much closer to the transition line of the mean-field phase diagram than the chosen  $\chi_{BR} = -4$  in the anti-correlated case. This explains the observation, that the droplet moves slower to the equilibrium position, if the system is close to the mean field transition line.

### 4.4 Non-Equilibrium System: Regulator Gradient by Diffusion

In this section, we look at a non equilibrium system, where the regulator gradient is generated by an diffusion mechanism. We will show, that the resulting phase diagram is quantitatively dependent on the implemented dynamics. For certain dynamics, the non equilibrium phase diagram coincidences with the equilibrium phase diagram of the droplet states.

#### 4.4.1 Non Equilibrium System with Exchange Dynamics

Here, we use the classical Kawasaki dynamics, where the particles can exchange places only with neighboring particles [85, 119, 92]. In this study, we can identify two classes of steady states, a anti-correlated state and a correlated state. Now, these are not equilibrium states, because we have always a nonzero flux of the regulator material caused by the applied boundary conditions. The fluxes of an example steady state are shown in fig. 4.11. All discussed fluxes are the  $x$ -components of the actual fluxes, the  $y$ - and  $z$ -components are not considered. This figure shows detailed flux properties, that decompose the flux of the

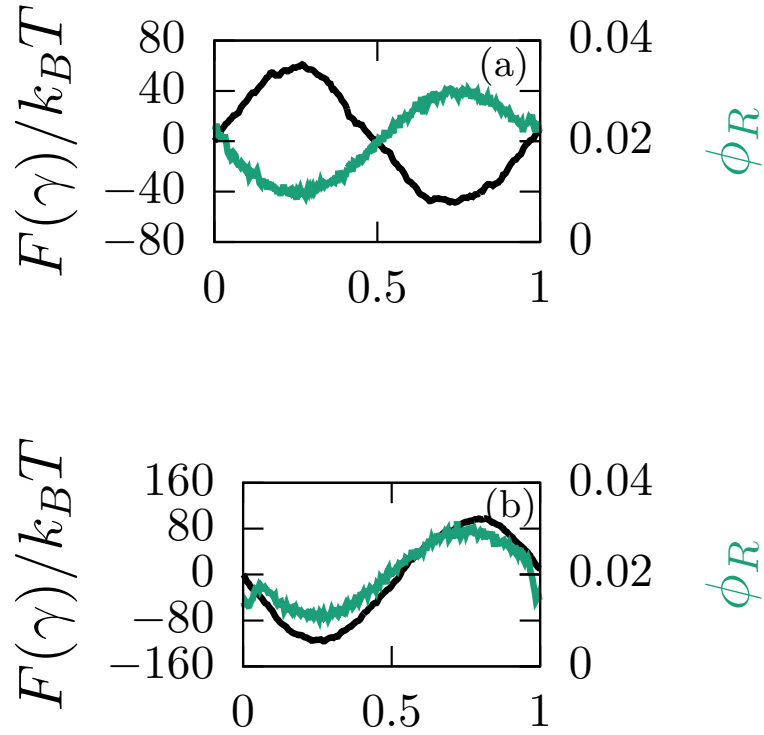


Figure 4.10 – (a) Correlated state with  $\chi_{BR} = 0$ . There is a very pronounced minimum of the free energy at the maximum of the regulator distribution (green). (b) Anti-correlated case with  $\chi_{BR} = -4$ . Here, a local minimum is visible at the maximum of the regulator distribution (green). The slightly different numbers of the free energy at the left and the right boundary are caused by integrating over the fluctuations. We did not use a correction algorithm, because this detail has no effect on the aim of the discussion. Regarding the shown regulator distribution, the corresponding droplet is located near  $x = 0$ . The droplet influences the regulator profile significantly in (b), because the attractive interaction between the regulator and the solvent leads to a depletion of regulator in the droplet. In (a), the interactions are weak and the droplet position has only minor influence on the regulator profile. The parameters fixed are  $\chi_{AB} = 4$ ,  $\chi_{AR} = 0$ ,  $\bar{\phi}_A = 0.05$ ,  $\bar{\phi}_R = 0.02$ ,  $\alpha = 20$ ,  $A = 1/2$  and  $L = 256$ .

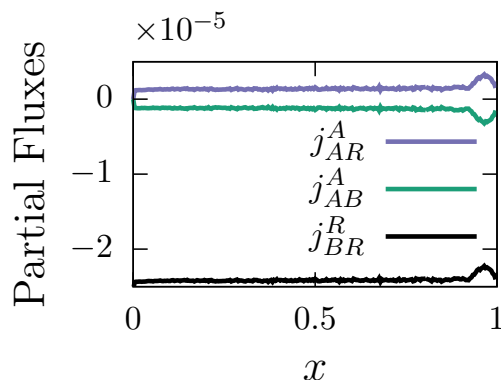


Figure 4.11 – Profile of the partial fluxes for a correlated state. The parameters are  $\chi_{AB} = 4$ ,  $\chi_{AR} = 1$ ,  $\chi_{BR} = -1$ ,  $\bar{\phi}_A = 0.05$ ,  $\bar{\phi}_R = 0.02$  and  $L = 256$ .

droplet material  $j^A$  and the flux of the regulator  $j^R$  into the contributions

$$j(x)^A = j(x)_{AB}^A + j(x)_{AR}^A, \quad (4.23)$$

$$j(x)^R = j(x)_{RB}^R + j(x)_{RA}^R. \quad (4.24)$$

The partial flux  $j_{ij}^i$  describes the part of the flux  $j^i$  corresponding to position changes of particles of type  $i$  and type  $j$ . According to the construction of these partial fluxes,  $j_{AR}^A = -j_{AR}^R$ , because they correspond to the same process using only different directions of the particle change. The partial fluxes  $j_{AB}^A$  and  $j_{AR}^A$  have to be zero at the boundary, because there are no corresponding exchanges possible through the wall. That means, that the integral of this partial flux over the boxlength  $L_x$  also has to vanish. The partial flux  $j_{RB}^R$  is directly driven by the boundary conditions. Because the regulator particles can exchange position with both, solvent particles and droplet material particles, the partial fluxes  $j_{AR}^A$  and  $j_{AB}^A$  are an indirect result of the boundary conditions. The values of the partial fluxes  $j_{AR}^A$  and  $j_{RB}^R$  are proportional to the volume fractions. They can be estimated with  $j_{AR}^A/\bar{\phi}_A = j_{RB}^R/\bar{\phi}_B$  in good approximation. The total flux of the droplet material  $j^A$  has to vanish in average in the steady state. To this end, the partial flux  $j_{AR}^A$  is compensated by the flux  $j_{AB}^A$ , which also means that both partial fluxes have the same absolute value. The reason for the high correlation between the partial fluxes is the high sampling time and the dependence of the different dynamic moves on the lattice.

The phase diagram is shown in fig. 4.12. Now, this is not a thermodynamic phase diagram like in section 4.3.2, but a compilation of the steady states of the system. If we compare the two phase diagrams, we see that the same types of steady states are observed. The slope of the transition line between the two types of states are also equal in good approximation. The main difference between the phase diagrams is the significant constant shift of the transition line. That leads to an extended region of correlated states of the phase diagram. This can be explained with the stationary fluxes in the system. The net flux of the regulator points to the place of anti-correlated steady states, because there is also the sink of the regulator material. That means, that we have a partial flux  $j_{AR}^A$  in the opposite direction (compare fig. 4.11), which transports droplet material to the region of the correlated

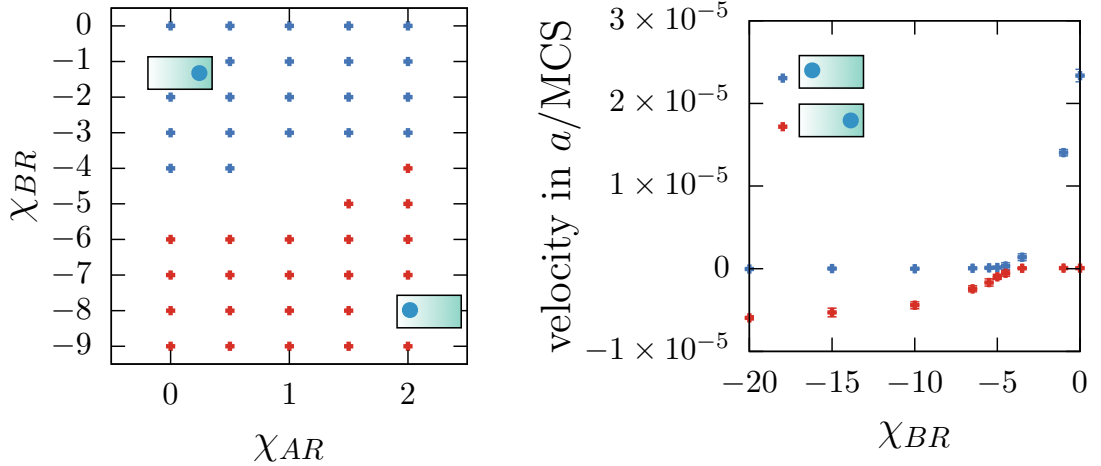


Figure 4.12 – (left) The phase diagram of the droplet states in the  $\chi_{AR}$ - $\chi_{BR}$ -plane is obtained by Monte Carlo simulation. The blue points indicate states of a correlated droplet, the red points indicate states of a correlated droplet. (right) Drift velocity of a droplet in a regulator gradient. This study is done along a cut through the phase diagram at  $\chi_{AR} = 1$ . The blue points correspond to simulations with an anti-correlated initial state, the red points to simulations with a correlated initial state. The error bars representing the standard deviation, calculated from ten independent seeds of the corresponding simulation. The parameters are  $\chi_{AB} = 4$ ,  $\bar{\phi}_A = 0.05$ ,  $\bar{\phi}_R = 0.02$  and  $L = 256$ .

stationary state. The steady state is now determined by the competition of the energetic interaction and the flux of the droplet material. The net attraction of regulator and droplet material has to be significantly stronger compared to the equilibrium system to overcome the effect of the droplet material flux.

The right plot in fig. 4.12 shows the droplet velocity of a droplet which starts in a anti-correlated position (blue) or a correlated position (red). For high negative  $\chi_{BR}$ , the anti-correlated state is stable, simulations with an anti-correlated initial state show a resting droplet. In the other case, if  $\chi_{BR}$  has a small negative value, the correlated state is stable and no droplet movement is observed in simulations with a correlated initial state. The region where both droplet velocities are close to zero corresponds to the transition region between the two states.

#### 4.4.2 Non Equilibrium System with Constrained Exchange Dynamics

In this study, we are using different dynamics than introduced in section 4.4.1. Now, the regulator particles and droplet material particles can change their position only with a neighboring solvent particle. These dynamics are still a type of Kawasaki dynamics, but with this additional rule we enforce  $j_{AR}^R = j_{AR}^A = 0$ , which leads to

$$j(x)^A = j(x)_{AB}^A, \quad (4.25)$$

$$j(x)^R = j(x)_{BR}^R. \quad (4.26)$$

We call this dynamics constrained Kawasaki dynamics. The motivation for introducing this dynamics is the assumption, that the regulator particles and droplet material particles are much bigger than the solvent particles. This idea leads to the picture that one lattice

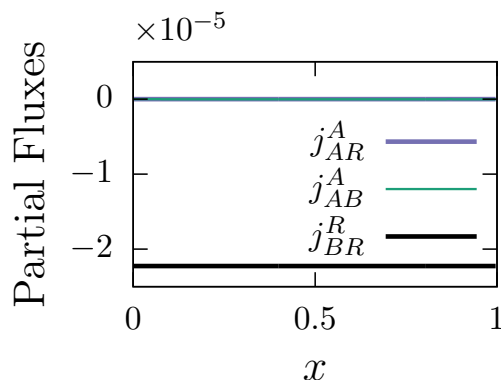


Figure 4.13 – Profile of the partial fluxes for a correlated state. The partial flux  $j_{RB}^R$  is directly driven by the boundary conditions. Although it looks constant in the plot, it shows very small fluctuations of magnitude  $10^{-9}$ . The Flux  $j_{AR}^A$  is zero by construction. The partial flux  $j_{AB}^A$  shows very small fluctuations of magnitude  $10^{-9}$ , which are not visible in the plot. The parameters are  $\chi_{AB} = 4$ ,  $\chi_{AR} = 1$ ,  $\chi_{BR} = -1$ ,  $\bar{\phi}_A = 0.05$ ,  $\bar{\phi}_R = 0.02$  and  $L = 256$ .

site is occupied by a regulator particle, a droplet material particle, or a number of solvent particles in a coarse graining sense, if the model particles are of the same size in the lattice model. In that case we expect that it is much easier to change the position of a regulator particle or a droplet material particle with solvent particles, because the solvent particles are of high mobility and can easily flow around the bigger particles. In contrast, it needs much higher effort to switch the position of a droplet material particle and a regulator particle directly, especially in crowded regions. We decided to model the limit case of an impossible direct exchange of these particles. The partial steady state fluxes are shown in fig. 4.13. As already mentioned, the only nonzero partial fluxes are  $j_{AB}^A$  and  $j_{BR}^R$ . Because of the incompressibility of the system,  $j^A = -j^R$ , which we also get from fig. 4.13. Because the walls in  $x$ -direction are hard walls for the droplet material, the flux of droplet material has to vanish in the steady state. The right plot of fig. 4.14 shows the droplet velocities of a droplet starting in a anti-correlated position (blue) or a correlated position (red). For strong attractive  $\chi_{AR}$ , the anti-correlated state is stable, the anti-correlated initial states are resting during the simulation. In the case of higher  $\chi_{AR}$ , the correlated states are stable. The region, where both types of simulation are approximately resting can be identified as the transition region and is consistent with the phase diagram presented in the left figure of fig. 4.13.

The resulting phase diagram is shown in fig. 4.14. This is very similar to the phase diagram in equilibrium. This observation is consistent to the interpretation of the phase diagram in section 4.4.1. Here, the regulator flux can not directly drive a flux of the droplet material, because of the suppressed partial flux  $j_{AR}^A$ . Thus, the stability of the steady state is only affected by the energetic interactions, there is no flux contribution to this stability. This can also be illustrated by considering the droplet material particles. From the perspective of these particles, the steady state looks like an equilibrium state, because they see the regulator gradient but experience no flux.

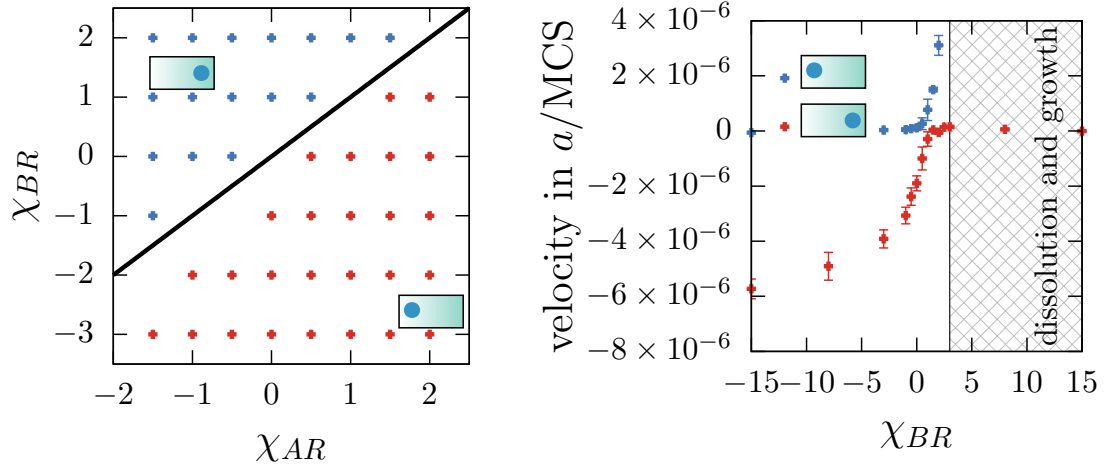


Figure 4.14 – (left) The phase diagram of droplet position in the  $\chi_{AR}$ - $\chi_{BR}$ -plane is obtained by Monte Carlo simulation. The blue points indicate states of correlated droplet positions, the red points indicate states of anti-correlated droplet positions. The analytic transition line of the simplified mean field theory is included for comparison. (right) Drift velocity of simulations with a anti-correlated initial state (blue) and a correlated initial state (red). The color bars indicate the standard deviation of ten independent seeds of the respective simulations. Moving states for  $\chi_{AR} > 3$  are not considered, because they are not drifting, the droplets are dissolve and recondensate at the stable position. The Measured velocities are a magnitude higher and the transition region would be less visible. The parameters are  $\chi_{AB} = 4$ ,  $\phi_A = 0.05$ ,  $\phi_R = 0.02$  and  $L = 256$ .

For this limit case of the Kawasaki dynamics, which allows exchanges between A-particles and solvent or regulator and solvent only, the stability of steady states can be completely understood with the knowledge of the equilibrium system. The role of the non equilibrium character of this system seems to be reduced to the creation of the regulator gradient.



# 5 Conclusions and Outlook

## 5.1 Summary of the Physical Behavior of the Inhomogeneous System

In this thesis, we investigated the positioning of droplets in an inhomogeneous environment. To this end, we employed a simple ternary model of the liquid system. Two components  $A$  and  $B$  showed a classical liquid-liquid phase separation into a  $A$ -rich phase and a  $B$ -rich phase. The third component, the regulator, mixed with both phases. This third component also defined the inhomogeneity of the environment by establishing a non zero concentration gradient in the system. We considered only chemical inhomogeneities. The concentration gradient was maintained by either an external potential, which effects only the regulator material, or a diffusion mechanism driven by specific asymmetric flux boundary conditions. In chapter 3 we introduced a mean field formulation of the inhomogeneous ternary liquid system. We used a Flory-Huggins type of free energy density, which was based on a lattice model of the system to calculate the entropic contribution to the free energy and regarded only short ranged interactions between the components. In this mean-field formulation, the gradient was maintained by an external potential on the regulator to obtain equilibrium states. This external potential caused a direct spatial dependency of the free energy density. Because of this spatial inhomogeneity, all the volume fractions, which are describing the composition of the system, were dependent on the spatial coordinate. We considered only a one dimensional system, where the external potential and the regulator gradient is dependent on the spatial coordinate  $x$ . The equilibrium states were obtained by solving the Euler-Lagrange equation corresponding to the free energy functional of the complete spatial system. The solutions showed two coexisting solutions, an anti-correlated solution, where the droplet is placed at low regulator concentration, and a correlated solution, where the droplet is placed at high regulator concentration. By changing the designated control parameter  $\chi_{BR}$ , we obtained two branches of the total free energy, one branch for each solution. These two branches intersect at one point defining the transition point  $\chi_{BR}^*$  and indicating a discontinuous phase transition between the anti-correlated and the correlated state. We also defined a order parameter measuring the correlation between two volume fraction fields. This order parameter shows a jump at the transition point, which is also consistent with a discontinuous phase transition there. To summarize the behavior of the mean field model, we built a phase diagram of the ternary system.

We repeated this studies for a system without hard wall boundary condition. We used

periodic boundary conditions and a periodic external potential to model a not finite system and exclude the effect of the walls. We obtained very similar results compared to the finite system. We concluded that the correlated-anti-correlated phase transition is an intrinsic effect of the inhomogeneous liquid system with imposed regulator gradient.

We considered also a simple analytic approach to the mean field model. In that approach we used ansatz profiles for the equilibrium volume fraction profiles that were adapted from the minimization of the free energy. With this ansatz profiles we discussed the free energy functional. This approach led to the same qualitative results as the minimization of the free energy. For  $\bar{\phi}_A = 0.5$  we obtained even quantitatively exact results. This approach showed that the correlated-anti-correlated phase transition is most likely driven by the energetic interactions between the particles.

In chapter 4 we investigated the ternary lattice model with fluctuations. To this end, we used Monte Carlo simulations to obtain the stationary states of the system. In a first scenario we used an external potential on the regulator to maintain the regulator gradient. Depending on the value of the control parameter  $\chi_{BR}$ , we observed a anti-correlated state or a correlated state. The transition between these two states occurred at the same value  $\chi_{BR}^*$  as in the mean field theory in good approximation. We were not able to give evidence if this process is also a discontinuous phase transition. The free energy along a reaction coordinate between the two states showed no signature of the existence of a metastable state. Nevertheless, the minimum of this free energy is consistent with the observed stationary state.

We also investigated the dynamics of the droplet into the stationary state. Two dynamics were observed. For small amounts of regulator particles in the droplet, the droplet performed a drift movement to its stationary state. Above a certain threshold of regulator material in the droplet, the droplet dissolved and recondensates at the stationary position. The amount of regulator particles in the droplet is mostly determined by the control parameter  $\chi_{BR}$ .

We also considered a non equilibrium system, where the regulator gradient was maintained by a diffusion mechanism and asymmetric boundary conditions. This asymmetric boundary conditions were a semipermeable wall at one side of the simulation box which can be passed by regulator particles. If a regulator particle passed this wall, it was placed on the other side of the simulation box. This mechanism allowed a one directional diffusion driven flux while keeping the number of particles strictly constant. We observed a transition between an anti-correlated state and a correlated state in this system, but the transition line was significantly shifted compared to the equilibrium studies. This shift was caused by the coupling between the regulator flux and the flux of the droplet particles. It is known, that fluxes can have quantitative influence on a phase diagram like shown for the lattice gas model in [90]. Turning off this coupling led to a transition line equal to the equilibrium case in good approximation. The origin of the regulator gradient does not have a major role for the positioning of droplets, the existence of the gradient governs the transition between the two positions.

Considering the introduced questions in chapter 1 we can summarize:

1. *In *C. elegans*' one cell stage embryo a gradient of a chemical component regulates the positioning of the *P* granules at one side of the cell. Treating the multicomponent cytoplasm as a one component solvent we can ask for the distribution of the chemical components in the system. This is closely related to the question for a minimal model*

## 5.2. Outlook and Discussion of an Proposed Experimental Realization

---

*of the liquid system, that still shows the localization of droplets.*

We have shown, that the effect of droplet positioning can be observed in a ternary liquid model. This works even for the generic interactions included in the Flory-Huggins approach, there was no need of introducing selective interactions. It became clear, that the regulator gradient itself is the key feature that makes the droplet positioning possible.

- 2. Are there stationary positions of droplets and what is the influence of the energetic interactions to these positioning? Do droplets prefer regions of high regulator concentration (correlated) or low regulator concentration (anti-correlated)? If such a stationery position exists, there are at least two qualitatively different possible dynamics of the droplet to reach this position. The droplet can simply drift to the stable position or it can dissolve and reassemble at the stationary positions. Can these dynamics be reproduced in the model and what determines the observed dynamics?*

The mean field approach showed that the correlated state and the anti-correlated state are coexisting. One of the states is stable, the other possibly metastable. The stability is governed by the interactions of the regulator with the other components. The stable states could be also confirmed by Monte-Carlo simulations. These simulations also showed, that two types of dynamics into the steady state are possible. If the droplet contains a low amount of regulator material, it was drifting to the stable state. Beyond a certain threshold of regulator material in the droplet the droplet dissolved and recondensated at the respective stationary position. The amount of regulator material inside the droplet was controlled by the interactions between the regulator and the other components.

- 3. It is possible to investigate equilibrium models or non equilibrium models of the system with a regulator gradient. What are the differences or similarities of the results from these models regarding the droplet positioning?*

Qualitatively, the equilibrium system and the non equilibrium system behave very similar regarding the stable states. In both systems correlated and the anti-correlated states are observed. The value of the Flory-Huggins parameter at the transition line between these two states changed if a coupling between the regulator flux and the flux of the droplet material were allowed. There existed one special dynamics of the particles for which this difference of the transition lines vanished and the non equilibrium phase diagram overlapped with the equilibrium phase diagram. This was observed, if regulator particles and droplet particles (A-particles) can not exchange places on the lattice during the simulation.

## 5.2 Outlook and Discussion of an Proposed Experimental Realization

*Possible experimental setup.*

An experimental investigation of the positioning of droplets can be possibly realized by employing the microfluidic framework. An abstract sketch of such a microfluidic unit is shown in Fig. 5.1. The central chamber contains the droplet material and a solvent. This

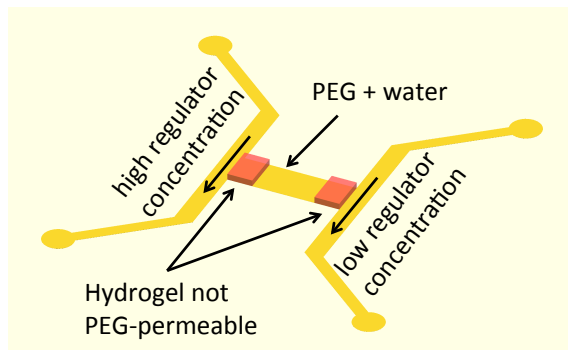


Figure 5.1 – Very abstract form of a experimental unit to investigate the positioning of droplets. The central chamber contains the droplet material and solvent. This chamber is also semipermeably connected to a reservoir of high regulator concentration and a reservoir of low regulator concentration, which will cause the gradient by diffusion. The droplet material can not pass through this semipermeable connections.

central chamber is semipermeably connected to a reservoir of high regulator concentration at one side and a reservoir of low regulator concentration on the other side. This leads to a regulator gradient by diffusion. The droplet forming material can not enter the two reservoirs. A commonly used phase separating system is PEG in water. The semipermeable membrane between the reservoirs and the central chamber can make use of the much larger size of the PEG molecules compared to the solvent molecules and regulator molecules to arrest it in the central chamber. A possible regulator for this system can be salt, it is known that salts have an effect on the PEG/water phase diagram [99, 181, 118]. The regulator reservoirs can be implemented as a flow of the respective regulator solution in contact with the semipermeable membrane. This way a constant reservoir concentration can be maintained without having the central chamber in direct contact with a very big reservoir chamber.

This setup can investigate the non equilibrium system. Experimental investigation of the equilibrium system is potentially more challenging. We propose the use of magnetic salts in the PEG/water/salt system. The corresponding external potential could then be the magnetic field of a NMR-device. With that it would be also possible to have quasi complete control over the established regulator gradient.

#### *Outlook.*

There are different points in which this project can be extended into further projects. The first important point is the dimensionality of the mean field model. The droplet character of the high concentrated A phase can be included considering a three dimensional system. This three dimensional system can be parameterized by two parameters if the system has cylinder symmetry. This is reasonable because the droplet has rotational symmetry in very good approximation and we are majorly interested in external potentials with one distinct spatial direction. For the mathematics this is a direct extension of the presented model, the same framework can be used. The major difference is, that for the 3D-model a partial differential equation has to be solved to obtain the stationary points of the functional.

Another important question is the existence of metastable states. With the computation and discussion of the second variation of the free energy it would be possible to identify

## 5.2. Outlook and Discussion of an Proposed Experimental Realization

---

metastable and not stable branches of the free energy. This could also help finding the transition state of the correlated-anti-correlated phase transition and finding the Gibbs loop of this transition.

A third point is the investigation of the dynamics in the mean field system, e.g. by a Cahn Hilliard approach. With this tool it is possible to model the equilibrium system as well as the non equilibrium system. It can give also insight to possible transient states and the dynamics to the stationary states. Furthermore, this approach provides a better connection with the Monte Carlo simulations and the proposed experiments.

Of course, it is also possible to extend the Monte Carlo simulations presented in this thesis. One important question is, if the size of the involved particles effect the positioning of the droplets. A polymer-like character of the droplet material occurs in the proposed experiments with the PEG/water/salt system and in the biological example of the *C. elegans* one cell stage embryo. It is also possible to consider more specific interaction or even competitive binding mechanisms like employed in [143]. This path would lead to simulations closer to the biological system of the *C. elegans* embryo.



# A Mean Field

## A.1 Exchange Chemical Potential in a Lattice Model

The thermodynamic definition of the chemical potential of component  $i$  using the free energy  $F(N_i, V, T)$  is

$$\mu_i^{\text{therm}} = \left. \frac{\partial F}{\partial N_i} \right|_{N_j \neq N_i, V, T}. \quad (\text{A.1})$$

The free energy is dependent on the number of particles  $N_i$ , the total volume  $V$  and the thermodynamic temperature  $T$ . This definition can not be used for an incompressible lattice model, because the number of particles and the total volume is no longer independent in that case. In detail, the total volume is

$$V = \sum_i \nu_i N_i. \quad (\text{A.2})$$

Here,  $\nu_i$  is the molecular volume of component  $i$ , which describes how many lattice sites are occupied by one particle of type  $i$ . This relation also says, that only  $M - 1$  particle numbers are independent in an  $M$ -component system. We consider the last number of particles  $N_M$  to be dependent on the other

$$N_M = \frac{1}{\nu_M} \left( V - \sum_i^{M-1} \nu_i N_i \right). \quad (\text{A.3})$$

The free energy of this lattice model is  $F(N_1, \dots, N_{M-1}, N_M(N_1, \dots, N_{M-1}), V, T)$ . Now we define a exchange chemical potential for component  $i$ . We also change the interval of the indices to  $i, j \in [1, M - 1]$

$$\mu_i = \left. \frac{\partial F}{\partial N_i} \right|_{N_j \neq N_i, V, T}. \quad (\text{A.4})$$

This exchange potential describes the energetic change, if the identity of an  $i$ -particle is changed to a  $M$ -particle and vice versa. With the definition of the lattice free energy, this exchange potential becomes

$$\mu_i = \frac{\partial F}{\partial N_i} - \frac{\nu_i}{\nu_M} \frac{\partial F}{\partial N_M}. \quad (\text{A.5})$$

## A.2 Derivation of the Flory-Huggins Free Energy of Mixing from Principles of Statistical Physics

In this section, we will derive the Flory-Huggins free energy of mixing with general principles of statistical physics. We will start with a binary system before we show the derivation of the ternary free energy of mixing. All considered systems are modeled as lattice models using a simple cubic lattice.

### A.2.1 Binary System

In the lattice model of the binary system each lattice site is occupied by an  $A$ -particle or a  $B$ -particle. There are no vacancies, the lattice is completely filled with these two components. The hamiltonian of this lattice model is

$$\begin{aligned}
 H &= \frac{1}{2} \sum_{ij} \left( J_{ij}^{AA} s_i s_j + J_{ij}^{BB} (1 - s_i)(1 - s_j) + J_{ij}^{AB} (s_i(1 - s_j) + s_j(1 - s_i)) \right) \\
 &= \frac{1}{2} \sum_{ij} \left( J_{ij} s_i (1 - s_j) + s_i J_{ij}^{AA} + (1 - s_j) J_{ij}^{BB} \right).
 \end{aligned} \tag{A.6}$$

At this point, we consider the canonical ensemble, which means, that the amount of particles of each component is constant, the number of total lattice sites, which correspond to the total volume of the system, is constant and the system is in equilibrium with a heat bath of temperature  $T$ . The indexes  $i$  and  $j$  indicate the respective single lattice site of the considered lattice. The operator  $s_i$  is 1, if the lattice site  $i$  is occupied by an  $A$ -particle, otherwise it is 0. The parameter  $J_{ij}^{\alpha\beta}$  is the interaction of an  $\alpha$ - $\beta$ -pair of particles on lattice sites  $i$  and  $j$ . Because we are considering isotropic nearest neighbor interactions,  $J_{ij}^{\alpha\beta}$  is  $J^{\alpha\beta}$  if the particles  $i$  and  $j$  are nearest neighbors and 0 otherwise. We also neglect the linear terms of the hamiltonian here, because they do not effect the phase separation. The second line of eq. (A.6) is an equivalent rearrangement of the first line with  $J_{ij} = 2J_{ij}^{AB} - J_{ij}^{AA} - J_{ij}^{BB}$ . For the derivation of the Flory-Huggins free energy we use a linearized hamiltonian applying the mean field approximation. In this approximation, the environment of a lattice site is modeled by the average of the occupation operator, which is equal to the volume fraction  $\bar{\phi}_A$  of component  $A$ , because all lattice sites are of the same volume. Applying the mean field argument, we get  $(s_j)_{\text{MF}} = \langle s_j \rangle = \bar{\phi}_A$ . Furthermore, because we consider only nearest neighbor interactions, we can use  $\sum_i \sum_{j \in NN}$  instead of the double sum  $\text{sum}_{ij}$ . Now the inner sum includes only the nearest neighbors  $NN$ . The mean field hamiltonian is

$$\begin{aligned}
 H_{\text{MF}} &= \frac{1}{2} \sum_i \sum_{j \in NN} \left( J_{ij} s_i (1 - \bar{\phi}_A) + J_{ij}^{AA} s_i + J_{ij}^{BB} (1 - \bar{\phi}_A) \right) \\
 &= \underbrace{\frac{\zeta}{2} (1 - \bar{\phi}_A) J}_{=C} \sum_i s_i + \underbrace{\frac{\zeta}{2} (J^{AA} - J^{BB})}_{=D} \sum_i s_i.
 \end{aligned} \tag{A.7}$$

The parameter  $\zeta$  is the coordination number of the lattice. The second line of eq. (A.7) uses  $J^{\alpha\beta}$  instead of  $J_{ij}^{\alpha\beta}$ , because the interaction is not spatial dependent, it is equal for each nearest neighbor pair  $\alpha$ - $\beta$ . For further calculations, we use a lattice interpretation of the great canonical ensemble, where the total number of lattice sites  $N$  is constant. The

## A.2. Derivation of the Flory-Huggins Free Energy of Mixing from Principles of Statistical Physics

---

number of A-particles  $N_A$  can be changed, which also determines the number of B-particles with  $N = N_A + N_B$ . The system is in equilibrium with a bath at temperature  $T$  and chemical potential  $\mu_A$ . This chemical potential is a relative chemical potential and related to the common chemical potential  $\tilde{\mu}_\sigma$  with  $\mu_A = \tilde{\mu}_A - \tilde{\mu}_B$  [8]. The hamiltonian of this system is

$$H_{g,\text{MF}}^f = (C + D - \mu_A) \sum_i s_i. \quad (\text{A.8})$$

We will call this ensemble grand canonical ensemble during the presented derivation. With this hamiltonian, we can compute the grand canonical partition sum, which reads

$$\begin{aligned} Z_{g,\text{MF}} &= \sum_{N_A=0}^N \sum_{\{s_k\}'} e^{-\beta(C+D-\mu_A) \sum_i s_i} \\ &= \left(1 + e^{-\beta(C+D-\mu_A)}\right)^N. \end{aligned} \quad (\text{A.9})$$

Here,  $\beta$  is the inverse temperature. The grand canonical partition sum includes all possible particle numbers  $N_A$  with their corresponding configurations  $\{s_k\}'$  on the lattice. The second line of eq. (A.9) is obtained, because all lattice sites can be regarded as independent of each other in the mean field theory. The grand canonical potential can be computed straight forward using this partition sum

$$\begin{aligned} \Omega_{\text{MF}} &= -\frac{1}{\beta} \ln Z_{g,\text{MF}}^f \\ &= -\frac{N}{\beta} \ln \left(1 + e^{-\beta(C+D-\mu_A)}\right). \end{aligned} \quad (\text{A.10})$$

To obtain the free energy of the system we compute the Legendre-transformation [161, 2] of the grand canonical potential. This transforms the chemical potential  $\mu_A$  to the volume fraction  $\bar{\phi}_A$ .

$$\begin{aligned} F_{\text{MF}} &= \Omega_{\text{MF}} - \mu_A \partial_{\mu_A} \Omega_{\text{MF}} \\ &= \Omega_{\text{MF}} + \frac{\mu_A}{\beta} \partial_{\mu_A} \ln Z_{g,\text{MF}}^f. \end{aligned} \quad (\text{A.11})$$

The partial derivative of the logarithm of the partition sum can be computed using eq. (A.9). The average of the sum of the occupation operator  $\langle \sum_i s_i \rangle = \bar{\phi}_A N$  can also be related to the derivative of the partition sum  $\langle \sum_i s_i \rangle = (1/\beta) \partial_{\mu_A} \ln Z_{g,\text{MF}}^f$ . Using this relations, the chemical potential in eq. (A.11) can be eliminated. The resulting free energy per lattice site reads

$$\frac{\beta F_{\text{MF}}}{N} = \bar{\phi}_A \ln \bar{\phi}_A + (1 - \bar{\phi}_A) \ln(1 - \bar{\phi}_A) + \underbrace{\frac{\zeta\beta}{2} J \bar{\phi}_A (1 - \bar{\phi}_A)}_{=\chi_{AB}} + \beta \bar{\phi}_A D. \quad (\text{A.12})$$

This is the total free energy. To obtain the free energy of mixing, we have to compute also the free energy of the initial state, which is the state of pure components where the particles are collected on two different lattices. One lattice is completely filled with  $A$ -particles, the other with  $B$ -particles. We use a reduced hamiltonian to describe this system neglecting

## Appendix A. Mean Field

---

all zero mixed terms.

$$H^{\text{pure}} = \frac{1}{2} \sum_{ij} \left( J_{ij}^{AA} s_i s_j + J_{ij}^{BB} (1 - s_i)(1 - s_j) \right). \quad (\text{A.13})$$

Now, the indices  $i$  and  $j$  count the lattice sites of the lattice of  $A$ -particles first, than the lattice sites on the lattice on  $B$ -particles. With this choice of counting we keep the range of  $i$  and  $j$  from 1 to  $N$ . We apply the mean field approximation also on the initial state. The mean field hamiltonian reads

$$H_{\text{MF}}^{\text{pure}} = \frac{\gamma}{2} \underbrace{\left( J^{AA} - J^{BB} \right)}_{=D} \sum_i s_i. \quad (\text{A.14})$$

We obtain the same expression  $D$  as in the complete hamiltonian eq. A.7. Because the hamiltonian is much simpler for the initial state, we can calculate the free energy directly without taking the path through the grand canonical ensemble. The canonical partition sum of the initial state is  $Z_{\text{MF}}^{\text{pure}} = \left( e^{-\beta D} \right)^{N_A}$ , which leads to the free energy  $F_{\text{MF}}^{\text{pure}} = -(1/\beta) \ln Z_{\text{MF}}^{\text{pure}} = N_A D$ . With this result, we can compute the Flory-Huggins free energy of mixing

$$\begin{aligned} f_{\text{FH}} &= \frac{\beta F_{\text{MF}}}{N} - \frac{\beta F_{\text{MF}}^{\text{pure}}}{N}, \\ &= \bar{\phi}_A \ln \bar{\phi}_A + (1 - \bar{\phi}_A) \ln(1 - \bar{\phi}_A) + \chi_{AB} \bar{\phi}_A (1 - \bar{\phi}_A). \end{aligned} \quad (\text{A.15})$$

### A.2.2 Ternary System

In this subsection, we start with the hamiltonian of a three component lattice system. With that hamiltonian, we can compute the grand canonical potential, which can be transformed to the free energy applying Legendre-transformation. We consider a thermodynamic ensemble with constant total lattice sites  $N$ . The number of  $A$ - and  $R$ -particles  $N_A$  and  $N_R$  can be changed, which determines the number of particles of the remaining component  $B$  with  $N = N_A + N_B + N_R$ . The system is in equilibrium with a heat bath of temperature  $T$  and a particle bath of chemical potential  $\tilde{\mu}_A$  and  $\tilde{\mu}_R$ . This ensemble is a lattice interpretation of the grand canonical ensemble, we will call it grand canonical ensemble during the derivation. The hamiltonian of the grand canonical three component lattice system is

$$\begin{aligned} H_g &= \frac{1}{2} \sum_{ij} \left( J_{ij}^{AA} P_i^A P_j^A + J_{ij}^{BB} P_i^B P_j^B + J_{ij}^{RR} P_i^R P_j^R \right. \\ &\quad \left. + J_{ij}^{AB} \left( P_i^A P_j^B + P_j^A P_i^B \right) + J_{ij}^{AR} \left( P_i^A P_j^R + P_j^A P_i^R \right) + J_{ij}^{BR} \left( P_i^B P_j^R + P_j^B P_i^R \right) \right) \\ &\quad + \sum_i \left( \left( \tilde{\mu}_A + \tilde{U}_A \right) P_i^A + \left( \tilde{\mu}_B + \tilde{U}_B \right) P_i^B + \left( \tilde{\mu}_R + \tilde{U}_R \right) P_i^R \right) \\ &= \frac{1}{2} \sum_{ij} \left( J_{ij}^{AA} P_i^A P_j^A + J_{ij}^{BB} P_i^B P_j^B + J_{ij}^{RR} P_i^R P_j^R \right. \\ &\quad \left. + J_{ij}^{AB} \left( P_i^A P_j^B + P_j^A P_i^B \right) + J_{ij}^{AR} \left( P_i^A P_j^R + P_j^A P_i^R \right) + J_{ij}^{BR} \left( P_i^B P_j^R + P_j^B P_i^R \right) \right) \\ &\quad + \sum_i \left( \left( \mu_A + U_A \right) P_i^A + \left( \mu_R + U_R \right) P_i^R \right). \end{aligned}$$

## A.2. Derivation of the Flory-Huggins Free Energy of Mixing from Principles of Statistical Physics

(A.16)

Because we consider only isotropic nearest neighbor interactions, the interaction parameter  $J_{ij}^{\sigma\tau}$  is  $J^{\sigma\tau}$ , if  $i$  and  $j$  are nearest neighbors and 0 otherwise. We split the linear field terms into the chemical potential  $\tilde{\mu}_\sigma$  and an external potential  $\tilde{U}_\sigma$ . In the last expression, we introduced the relative chemical potentials  $\mu_\sigma = \tilde{\mu}_\sigma - \tilde{\mu}_B$  and the relative external potentials  $U_\sigma = \tilde{U}_\sigma - \tilde{U}_B$  using  $1 = P_i^A + P_i^B + P_i^R$  and neglecting the constant terms. We introduce the external potential  $U_\tau$  here, because we consider a three component liquid systems with an external potential  $U_R$  in our studies. This hamiltonian is also discussed in [149, 150]. The operators  $P_i^\tau$  are 1, if lattice site  $i$  is occupied by an  $\tau$ -particle and 0 otherwise. This occupation operators are not independent, because each lattice site is occupied by exactly one particle. To this end, we introduce new operators, which are defined as a combination of the occupation operators:

$$\begin{aligned}\Theta_i &= P_i^A + P_i^R, \\ \Delta_i &= P_i^A - P_i^R.\end{aligned}\tag{A.17}$$

The operator  $\Theta_i$  is 0, if the lattice site  $i$  is occupied by an  $B$ -particle, otherwise it is 1. The operator  $\Delta_i$  on lattice site  $i$  is 1 for  $A$ -particle,  $-1$  for a  $R$ -particle and 0 for a  $B$ -particle. The  $B$ -occupation operator can be substituted with  $P_i^B = 1 - P_i^A - P_i^R = 1 - \Theta_i$ . With these parameters, the hamiltonian reads

$$H_g = \frac{1}{2} \sum_{ij} (K_{ij}\Theta + J_{ij}\Delta_i\Delta_j + L_{ij}(\Delta_i\Theta_j + \Delta_j\Theta_i)) + \sum_i H_i\Delta_i + \sum_i D_i\Theta_i,\tag{A.18}$$

where

$$\begin{aligned}K_{ij} &= \frac{1}{4} (J_{ij}^{AA} + J_{ij}^{RR} + 2J_{ij}^{AR}) + (J_{ij}^{BB} - J_{ij}^{AB} - J_{ij}^{BR}), \\ L_{ij} &= \frac{1}{4} (J_{ij}^{AA} - J_{ij}^{RR}) + \frac{1}{2} (J_{ij}^{BR} - J_{ij}^{AB}), \\ J_{ij} &= \frac{1}{4} (J_{ij}^{AA} + J_{ij}^{RR} - 2J_{ij}^{AR}), \\ D_i &= \frac{1}{2} (\mu_A + \mu_R + U_A + U_R) + \frac{1}{2} \sum_j (J_{ij}^{AB} + J_{ij}^{BR} - 2J_{ij}^{BB}), \\ H_i &= \frac{1}{2} (\mu_A - \mu_R + U_A - U_R) + \frac{1}{2} \sum_j (J_{ij}^{AB} - J_{ij}^{BR}).\end{aligned}\tag{A.19}$$

Now, we will apply the mean field theory to linearize the hamiltonian. To this end, we will replace the operators on position  $j$  by their homogeneous averages, explicitly  $\Theta_{j,\text{MF}} = \langle \Theta \rangle = (\bar{\phi}_A + \bar{\phi}_R)$  and  $\Delta_{j,\text{MF}} = \langle \Delta_j \rangle = (\bar{\phi}_A - \bar{\phi}_R)$ . Because we consider only nearest neighbor interactions, we can replace the inner sum with  $\sum_j = \sum_{j \in \text{NN}}$ , where NN indicates the nearest neighbors of a lattice site. We also regard the interactions as isotropic, so that we can replace  $J_{ij}^{\sigma\tau} = J^{\sigma\tau}$ , the same logic is applied to  $K_{ij}$ ,  $L_{ij}$ ,  $J_{ij}$ ,  $D_i$  and  $H_i$ . Note, that the sum in  $D_i$  and  $H_i$  is replaced by the coordination number  $\zeta$  of the lattice,

## Appendix A. Mean Field

---

because of the nearest neighbor summation. The terms of the mean-field hamiltonian are:

$$\begin{aligned}
\left( \sum_{ij} K_{ij} \Theta_i \Theta_j \right)_{\text{MF}} &= K\zeta (\bar{\phi}_A + \bar{\phi}_R) \sum_i \Theta_i, \\
\left( \sum_{ij} \Delta_i \Delta_j \right)_{\text{MF}} &= J\zeta (\bar{\phi}_A - \bar{\phi}_R) \sum_i \Delta_i, \\
\left( \sum_{ij} L_{ij} (\Delta_i \Theta_j + \Delta_j \Theta_i) \right)_{\text{MF}} &= L\zeta (\bar{\phi}_A + \bar{\phi}_R) \sum_i \Delta_i + L\zeta (\bar{\phi}_A - \bar{\phi}_R) \sum_i \Theta_i.
\end{aligned} \tag{A.20}$$

The obtained mean field hamiltonian reads

$$H_{g,\text{MF}} = B \sum_i \Delta_i + C \sum_i \Theta_i, \tag{A.21}$$

where

$$\begin{aligned}
B &= \frac{1}{2} J\zeta (\bar{\phi}_A - \bar{\phi}_R) + \frac{1}{2} L\zeta (\bar{\phi}_A + \bar{\phi}_R) + H, \\
C &= \frac{1}{2} K\zeta (\bar{\phi}_A + \bar{\phi}_R) + \frac{1}{2} L\zeta (\bar{\phi}_A - \bar{\phi}_R) + D.
\end{aligned} \tag{A.22}$$

With this hamiltonian we can compute the grand canonical partition sum of the mean-field system

$$\begin{aligned}
Z_{g,\text{MF}} &= \sum_{N_A=0}^N \sum_{N_R=0}^{N-N_A} \sum_{\{\Delta_i, \Theta_i\}'} e^{-\beta H_{g,\text{MF}}} \\
&= \sum_{\{\Delta_i, \Theta_i\}} e^{-\beta H_{g,\text{MF}}} \\
&= \prod_i \sum_{\Delta_i, \Theta_i} e^{-\beta B \Delta_i - \beta C \Theta_i} \\
&= \left( \underbrace{1}_{\Delta_i=\Theta_i=0} + \underbrace{e^{-\beta B - \beta C}}_{\Delta_i=\Theta_i=1} + \underbrace{e^{\beta B - \beta C}}_{\Delta_i=-1, \Theta_i=1} \right)^N \\
&= \underbrace{(1 + 2e^{-\beta C} \cosh(\beta B))}_{=Z_{g,\text{MF}}^1}^N
\end{aligned} \tag{A.23}$$

The expression  $\{\Delta_i, \Theta_i\}'$  counts all constrained configurations with the respective particle numbers  $N_A$  and  $N_R$ . If the dash is missing, this constrain has not to be fulfilled. To obtain the third line, we write the sum in the Hamiltonian as a product. This is possible, because all lattice sites are independent in the mean field theory. We call the quantity  $Z_{g,\text{MF}}^1$  the one particle grand canonical partition sum of the mean field system. The grand canonical potential is

$$\begin{aligned}
\Omega_{\text{MF}} &= -\frac{1}{\beta} \ln Z_{g,\text{MF}}, \\
&= -\frac{N}{\beta} \ln Z_{g,\text{MF}}^1.
\end{aligned} \tag{A.24}$$

## A.2. Derivation of the Flory-Huggins Free Energy of Mixing from Principles of Statistical Physics

---

The free energy is computed as the Legendre-transformed grand canonical potential transforming the natural variable from  $\mu_i$  to  $\bar{\phi}_i$ . The free energy is

$$\begin{aligned} F_{\text{MF}} &= \Omega_{\text{MF}} - \mu_A \partial_{\mu_A} \Omega_{\text{MF}} - \mu_R \partial_{\mu_R} \Omega_{\text{MF}}, \\ &= \Omega_{\text{MF}} + \mu_A N_A + \mu_R N_R, \\ &= \Omega_{\text{MF}} + N \left( \mu_A \bar{\phi}_A + \mu_R \bar{\phi}_R \right). \end{aligned} \quad (\text{A.25})$$

For the algebraic procedure it is convenient to calculate  $\bar{\phi}_A + \bar{\phi}_R$ ,  $\bar{\phi}_A - \bar{\phi}_R$  and  $1 - \bar{\phi}_A - \bar{\phi}_R$  obtaining

$$\begin{aligned} \bar{\phi}_A - \bar{\phi}_R &= \frac{2}{Z_{g,\text{MF}}^1} e^{-\beta C} \sinh(\beta B), \\ \bar{\phi}_A + \bar{\phi}_R &= \frac{2}{Z_{g,\text{MF}}^1} e^{-\beta C} \cosh(\beta B), \\ 1 - \bar{\phi}_A - \bar{\phi}_R &= \frac{1}{Z_{g,\text{MF}}^1}. \end{aligned} \quad (\text{A.26})$$

With this we obtain the relations

$$\begin{aligned} \beta B &= \frac{1}{2} \ln \frac{\bar{\phi}_A}{\bar{\phi}_R}, \\ \beta C &= \ln \left( 1 - \bar{\phi}_A - \bar{\phi}_R \right) - \frac{1}{2} \ln \bar{\phi}_A - \frac{1}{2} \ln \bar{\phi}_R. \end{aligned} \quad (\text{A.27})$$

We are still missing explicit expressions of the relative chemical potentials. To this end we do minor reformulations of the terms  $D$ ,  $H$ ,  $B$  and  $C$ :

$$\begin{aligned} D &\equiv \frac{1}{2} (\mu_A + \mu_R) + D', \\ H &\equiv \frac{1}{2} (\mu_A - \mu_R) + H', \\ B &\equiv B' + H' + \frac{1}{2} (\mu_A - \mu_R), \\ C &\equiv C' + D' + \frac{1}{2} (\mu_A + \mu_R). \end{aligned} \quad (\text{A.28})$$

With eq. (A.28) and eq. (A.27) we can compute the explicit expressions of the relative chemical potentials

$$\begin{aligned} \mu_A &= - (C' + D' + B' + H') - \frac{1}{\beta} \ln \left( 1 - \bar{\phi}_A - \bar{\phi}_R \right) + \frac{1}{\beta} \ln \bar{\phi}_A, \\ \mu_R &= - (C' + D' - B' - H') - \frac{1}{\beta} \ln \left( 1 - \bar{\phi}_A - \bar{\phi}_R \right) + \frac{1}{\beta} \ln \bar{\phi}_R. \end{aligned} \quad (\text{A.29})$$

With this explicit relative chemical potentials, we can compute the explicit relation of the free energy per lattice site using eq. (A.25) obtaining

$$\begin{aligned} \frac{\beta F_{\text{MF}}}{N} &= \overbrace{\bar{\phi}_A \ln \bar{\phi}_A + \bar{\phi}_R \ln \bar{\phi}_R + \left( 1 - \bar{\phi}_A - \bar{\phi}_R \right) \ln \left( 1 - \bar{\phi}_A - \bar{\phi}_R \right)}^{\text{entropic contribution}} \\ &\quad + \underbrace{E(D', C', B', H')}_{\text{energetic contribution}}, \end{aligned} \quad (\text{A.30})$$

where the energetic contribution is

$$\begin{aligned}
 E &= \chi_{AR}\bar{\phi}_A\bar{\phi}_R + \chi_{AB}\bar{\phi}_A(1 - \bar{\phi}_A - \bar{\phi}_R) + \chi_{BR}\bar{\phi}_R(1 - \bar{\phi}_A - \bar{\phi}_R) \\
 &\quad + \bar{\phi}_AU_A + \bar{\phi}_RU_R + E_{\text{mix}}, \\
 E_{\text{mix}} &= \zeta J^{AA}\bar{\phi}_A + \zeta J^{RR}\bar{\phi}_R + \zeta J^{BB}(1 - \bar{\phi}_A - \bar{\phi}_R) + \underbrace{\zeta J^{BB}}_{\text{offset}}.
 \end{aligned} \tag{A.31}$$

At this point we have introduced the Flory-Huggins interaction parameters  $\chi_{\sigma\tau} = \frac{\beta\zeta}{2}(2J^{\sigma\tau} - J^{\sigma\sigma} - J^{\tau\tau})$ . The constant contribution in  $E_{\text{mix}}$  is neglected, because it does not have a physical effect. The remaining linear contributions in  $E_{\text{mix}}$  are canceled when subtracting the energy of the pure reference states. The free energy of the pure state is  $\beta F_{\text{MF}}^{\text{pure}} = E_{\text{mix}}$ , because the purely filled lattices have zero entropy. The resulting free energy density of mixing is

$$\begin{aligned}
 f_0 &= \frac{\beta(F_{\text{MF}} - F_{\text{MF}}^{\text{pure}})}{a^3N} = \bar{\phi}_A \ln \bar{\phi}_A + \bar{\phi}_R \ln \bar{\phi}_R + (1 - \bar{\phi}_A - \bar{\phi}_R) \ln(1 - \bar{\phi}_A - \bar{\phi}_R) \\
 &\quad + \chi_{AR}\bar{\phi}_A\bar{\phi}_R + \chi_{AB}\bar{\phi}_A(1 - \bar{\phi}_A - \bar{\phi}_R) + \chi_{BR}\bar{\phi}_R(1 - \bar{\phi}_A - \bar{\phi}_R) \\
 &\quad + \bar{\phi}_AU_A + \bar{\phi}_RU_R.
 \end{aligned} \tag{A.32}$$

### A.3 Relation Between the Interfacial Parameter and the Flory-Huggins Interaction Parameter for a Three Component System

To derive the relation between the Flory-Huggins interaction parameters and the gradient parameters, we start from the local mean field free energy on the lattice and calculate the continuum limit of this free energy as shown in reference [142] for a binary system. The local free energy density of the three component system is derived in [149, 150] using a mean-field approximation:

$$\begin{aligned} \beta F = & \sum_i \left( \phi_i^A \ln \phi_i^A + \phi_i^R \ln \phi_i^R + (1 - \phi_i^A - \phi_i^R) \ln (1 - \phi_i^A - \phi_i^R) \right) \\ & + \frac{1}{2} \sum_{i,j \text{ with } i \neq j} \left( J_{ij}^{AB} \phi_i^A (1 - \phi_j^A - \phi_j^R) + J_{ij}^{BR} \phi_i^R (1 - \phi_j^A - \phi_j^R) + J_{ij}^{AR} \phi_i^A \phi_j^R \right). \end{aligned} \quad (\text{A.33})$$

The indices  $i$  and  $j$  indicate the positions on the lattice. The first line describes the entropy of the mixture, the second line contains the energetic part of the free energy. It describes the non-local interactions between neighboring lattice sites. Each contribution is local. In the next steps we compute the continuum limit. In case of the entropic contribution, we can simply replace  $\phi_i^\tau \rightarrow \phi_R(x)$ . In case of the energetic contributions, we rearrange the terms leading to:

$$\begin{aligned} \beta F = & \sum_i \left( \phi_i^A \ln \phi_i^A + \phi_i^R \ln \phi_i^R + (1 - \phi_i^A - \phi_i^R) \ln (1 - \phi_i^A - \phi_i^R) \right) \\ & + \frac{1}{2} \sum_{i,j \text{ with } i \neq j} \left( J_{ij}^{AB} \phi_i^A (1 - \phi_j^A) + J_{ij}^{BR} \phi_i^R (1 - \phi_j^R) \right) \\ & + \left( J_{ij}^{AR} - J_{ij}^{AB} - J_{ij}^{BR} \right) \phi_i^A \phi_j^R. \end{aligned} \quad (\text{A.34})$$

Each contribution can be written as:

$$J_{ij}^{AB} \phi_i^A (1 - \phi_j^A) = \frac{1}{2} J_{ij}^{AB} \left( (\phi_i^A - \phi_j^A)^2 - (\phi_i^A)^2 - (\phi_j^A)^2 + 2\phi_i^A \right) \quad (\text{A.35})$$

$$J_{ij}^{BR} \phi_i^R (1 - \phi_j^R) = \frac{1}{2} J_{ij}^{BR} \left( (\phi_i^R - \phi_j^R)^2 - (\phi_i^R)^2 - (\phi_j^R)^2 + 2\phi_i^R \right) \quad (\text{A.36})$$

$$\begin{aligned} \left( J_{ij}^{AR} - J_{ij}^{AB} - J_{ij}^{BR} \right) \phi_i^A \phi_j^R = & \frac{1}{2} \left( J_{ij}^{AR} - J_{ij}^{AB} - J_{ij}^{BR} \right) \left( \phi_i^A \phi_i^R + \phi_j^A \phi_j^R \right) \\ & - \left( \phi_i^A - \phi_j^A \right) \left( \phi_i^R - \phi_j^R \right). \end{aligned} \quad (\text{A.37})$$

We can identify the Flory-Huggins interaction parameter as  $\chi_{\tau\sigma} = \frac{1}{2} \sum_j J_{ij}^{\tau\sigma}$ . In the continuum limit the differences of neighboring volume fractions can be mapped to the gradient of the respective volume fraction  $(\phi_i^\sigma - \phi_j^\sigma) \rightarrow a \nabla \phi_\sigma$ . The replacement of the interaction parameters and the simple limit of the gradient of the volume fraction is obtained by considering only nearest neighbor interactions. We finally obtain the free

## Appendix A. Mean Field

---

energy

$$F = \int dr \left( f_0(r)/a^3 + \frac{\kappa_A}{2} |\nabla \phi_A(r)|^2 + \frac{\kappa_R}{2} |\nabla \phi_R(r)|^2 + \frac{\kappa}{2} \nabla \phi_A(r) \nabla \phi_R(r) \right), \quad (\text{A.38})$$

where

$$\begin{aligned} f_0 = & \phi_A(r) \ln \phi_A(r) + \phi_R(r) \ln \phi_R(r) \\ & + (1 - \phi_A(r) - \phi_R(r)) \ln (1 - \phi_A(r) - \phi_R(r)) \\ & + \chi_{AR} \phi_A(r) \phi_R(r) + \chi_{AB} \phi_A(r) (1 - \phi_A(r) - \phi_R(r)) \\ & + \chi_{BR} \phi_R(r) (1 - \phi_A(r) - \phi_R(r)), \end{aligned} \quad (\text{A.39})$$

The gradient coefficients are  $\kappa_\sigma = \chi_{\sigma B}/a$  and  $\kappa = (\chi_{AR} - \chi_{AB} - \chi_{BR})/a$ .

## A.4 First Order Form of the Euler-Lagrange equation

The matrix form of the Euler-Lagrange equations is

$$\vec{\phi}'' = M^{-1}\vec{h} = \begin{pmatrix} \tilde{h}_R \\ \tilde{h}_A \end{pmatrix}. \quad (\text{A.40})$$

for the numeric analysis of this system, we use the inbuilt MATLAB solver `bvp4c`, which is able to solve first order systems of differential equations. To this end, we will rewrite the second order system into a first order system. Furthermore, we will include the Lagrange multipliers as additional functions to the system to not have to deal with unknown parameters in the numeric calculation. All this is done by defining a new set of eight functions, which are

$$\begin{aligned} y_1 &= \phi_R \\ y_2 &= \phi'_R \\ y_3 &= \phi_A \\ y_4 &= \phi'_A \\ y_5 &= \lambda_R \\ y_6 &= \int_0^x \phi_R dx' \\ y_7 &= \lambda_A \\ y_8 &= \int_0^x \phi_A dx'. \end{aligned} \quad (\text{A.41})$$

By differentiating this system of equation once, we obtain

$$\begin{aligned} y'_1 &= y_2 & 0 &= w_R - \left. \frac{\partial f}{\partial \phi'_R} \right|_{x=0} \\ y'_2 &= \tilde{h}_R & 0 &= w_R + \left. \frac{\partial f}{\partial \phi'_R} \right|_{x=1} \\ y'_3 &= y_4 & 0 &= w_A - \left. \frac{\partial f}{\partial \phi'_A} \right|_{x=0} \\ y'_4 &= \tilde{h}_A & 0 &= w_A + \left. \frac{\partial f}{\partial \phi'_A} \right|_{x=1} \\ y'_5 &= 0 & 0 &= y_6(0) \\ y'_6 &= y_1 & 0 &= y_6(1) - \bar{\phi}_R \\ y'_7 &= 0 & 0 &= y_8(0) \\ y'_8 &= y_3 & 0 &= y_8(1) - \bar{\phi}_A. \end{aligned} \quad (\text{A.42})$$

The first four boundary conditions are derived from the minimization of the free energy functional, the remaining four boundary conditions can be obtained from the normalization of the volume fraction profiles. Mathematically, the Lagrange multiplier is a constant parameter for each problem, which makes the derivative of  $y_5$  and  $y_7$  trivial. This first order problem contains exactly the same information as the constrained second order problem, they are physically equivalent.

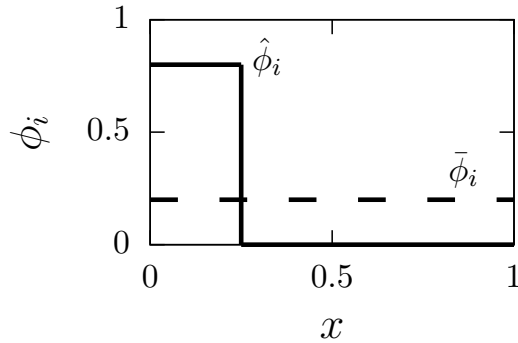


Figure A.1 – Simple sketch for illustrating the procedure of finding the reference profile used for the normalization of the order parameter  $\rho_{ij}$ . The dashed line indicates the level of the average volume fraction of the component  $i$ . The solid black line shows an example profile of the considered class, which is a step function and jumps from some constant value to zero. The calculation shows, that the profile that jumps from 1 to 0 possesses the maximal variance within this class and is thus considered as the reference profile.

## A.5 Normalization of the Order Parameters

Our aim is to define a normalization, that provides the highest absolute values of the order parameter for profiles that are perfectly demixed. The order parameter reads

$$\rho_{ij} = \mathcal{N}_{|j|} \int_0^L (\phi_i - \bar{\phi}_i) (\phi_j - \bar{\phi}_j) dx, \quad (\text{A.43})$$

where  $\mathcal{N}_{|j|}$  is the normalization of the respective order parameter. We have already identified this order parameter as a kind of a covariance. One established way to normalize the covariance is the normalization by the variances of the variables, obtaining the correlation factor [135]. This normalization is not beneficial in our case, because it reaches the maximum value, if the two variables are linearly dependent. In general, this is not the case in the demixed region of the phase diagram. Furthermore, an approximately linear dependency is observed for mixed equilibrium states, because the regulator profile is linear in that case and the droplet material aligns to this gradient. The introduction of the correlation factor would highlight mixed states, while demixed states are of low absolute value and hardly distinguishable in the color-coded phase diagram. Instead of using the actual variance for normalization, we will use a maximum variance corresponding to an ideally demixed profile comparable to the resulting volume fraction profiles.

The reference profile is illustrated in fig. A.1. For obtaining the reference profile we considered a class of profiles that is comparable to the profiles obtained from the free energy minimization. That means, that the minority  $A$ -phase has a volume fraction of 0 and the majority  $A$ -phase of 1. The position of the jump varies. If we do not consider this constraint of the minimum and maximum volume fraction, we obtain a maximum variance for a jumps at  $x = L/2$  from 0 to  $2\bar{\phi}_i$ . This is not related to the profiles we obtain generally from the numeric calculation, which motivates us to apply the additional

constraint. Because the average volume fraction is given, the parameters are connected by  $\epsilon \hat{\phi}_i = L \bar{\phi}_i$ , where  $\epsilon \in [L \bar{\phi}_i, L]$  to maintain  $\bar{\phi}_i < 1$ . The variance of this profile is

$$\sigma_i^2 = \frac{1}{L} \int_0^L (\phi_i - \bar{\phi}_i)^2 dx = \bar{\phi}_i \left( \frac{L}{\epsilon} - 1 \right). \quad (\text{A.44})$$

This variance has a monotonic behavior and thus no local minimum. The global minimum of this expression is obtained for the minimum value of  $\epsilon$

$$\sigma_{i,\max}^2 = \bar{\phi}_i (1 - \bar{\phi}_i). \quad (\text{A.45})$$

Because we are already mentioned, that the reference profile should jump from 0 to 1, this calculation should only verify, that such a profile is consistent with a maximum of the variance. This result is used to calculate the normalization

$$\mathcal{N}_{ij} = \frac{1}{\sigma_{i,\max} \sigma_{j,\max}} = \frac{1}{\sqrt{\bar{\phi}_i (1 - \bar{\phi}_i)} \sqrt{\bar{\phi}_j (1 - \bar{\phi}_j)}}. \quad (\text{A.46})$$

## A.6 Influence of the Shape of the Regulator Gradient on the Transition Point

In this section we will shortly discuss the influence of the potential strength  $s$  on the transition between the correlated and the anti-correlated equilibrium states. Fig. A.2(a) shows the transition point in dependency of  $s$  for three different  $\bar{\phi}_A$ . This transition point is observed for all values of  $s$  with exception  $s = 0$ . The data suggest, that a nonzero external potential is essential for the transition. There is no evidence, that there exists a critical value of  $s$ , which has to be overcome first to observe the transition. In Fig. A.2(b), the jump of the order parameter at the transition point is measured varying  $s$  for different  $\bar{\phi}_A$ . The jump height is linearly dependent of  $s$  is very good approximation.

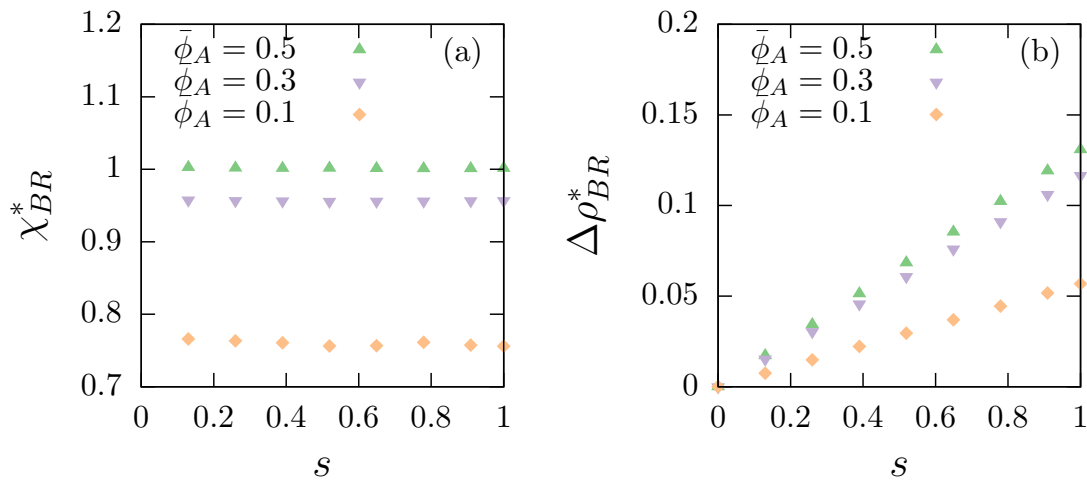


Figure A.2 – (a) The transition point is independent of the slope of the regulator gradient  $s$ . (b) The jump of the order parameter at the transition point linearly increases with the slope of the gradient  $s$ . The slope of this linear dependence is influenced by  $\bar{\phi}_A$ . The fixed parameters are  $\chi_{AB} = 4$ ,  $\chi_{AR} = 1$ ,  $\bar{\phi}_R = 0.02$ ,  $\kappa_R/L^2 = 7.63 \cdot 10^{-5}$ ,  $\kappa_A/L^2 = 6.10 \cdot 10^{-5}$ ,  $\kappa/L^2 = 6.10 \cdot 10^{-5}$ .

## A.7 Regulator Peak at the Droplet Interface

*Influence of selected parameters on the regulator peak.*

Two examples of regulator peaks at the droplet interface are presented in fig. A.3. We use the height and the area of the peak to describe it. Both are calculated by subtracting the approximately linear background of the regulator profile. The area of the peak is defined as the integral over the remaining profile and the height of the peak as the maximum of this profile. The height of the peak is a measure of the equilibrium volume fraction of the regulator at the  $A$ -interface. The peak area measures, which amount of regulator material is collected at the  $A$ -interface. We will consider two scenarios to study the behavior of the peak. In the first case, we will change the  $\kappa$ -parameters simultaneously, so that always  $\kappa_A = \kappa_R = \kappa$ . This case is of interest, because we used the  $\kappa_A = \kappa_R = \kappa = 0$  limit to make analytic arguments on the transition between correlated and anti-correlated states. The data of this case are compiled in fig. A.4. The peak height is constant in good approximation for all considered  $\kappa$ -values, the  $\kappa$ -parameters have a negligible effect on the equilibrium volume fraction of the regulator at the droplet interface. On the other side, they have a significant effect on the amount of regulator material, which is stored at the interface. If the  $\kappa$ -parameters go to zero, the peak area vanishes. One explanation is, that the droplet interface becomes much more narrow, if the  $\kappa$ -parameters are decreasing. Thus, there is also much less space to store the regulator material. Another effect is, that the profiles can establish much steeper gradients for smaller  $\kappa$ -parameters, so that the equilibrium volume fraction at the interface can be reached within a smaller characteristic length. The observed effects of the  $\kappa$ -parameters on the peak height and area are also visible in the example profiles of fig. A.3, in which two different  $\kappa$ -values are compared. In the second case, the influence of the interaction parameters is investigated. We choose a constant  $\chi_{AB}$ , because the  $A$ -profile should not be majorly influenced during this study. Furthermore, we consider  $\chi_{AR} = \chi_{BR}$  in a system with  $\bar{\phi}_A = 0.5$  to follow the binodal line between the correlated and the anti-correlated states. We follow this binodal line, because the background profile of the regulator is linear in very good approximation there. Profiles of significant distance from the binodal line show step-like behavior and nonlinearities, which makes it hard to subtract the background analytically. It is also possible that the peak is not visible if the system is far from the binodal line. The results are presented in fig. A.5. The points are obtained from the numerical solution of the Euler-Lagrange equation, the solid black line shows the result of a simple analytic model. The analytic model will be introduced in the next paragraph of this section. The equilibrium volume fraction of the regulator at the interface is increased for more repulsive interactions of the regulator with the other components. A hand-waving explanation for this behavior is that the interfacial region is already of higher energy than the bulk phases because of the repulsive interaction  $\chi_{AB}$ . in a particle picture, it is easier to destroy  $A$ - $B$ -bonds and generating  $A$ - $R$ - and  $B$ - $R$ -bonds, than generating these bonds and keeping the  $A$ - $B$ -bonds.

*Simple analytic model of the peak.*

A simple analytic model to describe the behavior of the peak separates the system into three different spatial regions: Region (I) in  $0 \leq x < (1 - \epsilon)/2$  with the volume fractions  $\phi_A^I = \phi_{A,\text{in}}$  and  $\phi_R^I = \phi_{R,\text{bulk}}$  is the region of the bulk phase of high  $A$  volume fraction. Region (II) is in  $(1 + \epsilon)/2 \leq x \leq 1$ , has the volume fractions  $\phi_A^{\text{II}} = \phi_{A,\text{out}}$  and  $\phi_R^{\text{II}} = \phi_{R,\text{bulk}}$ ,

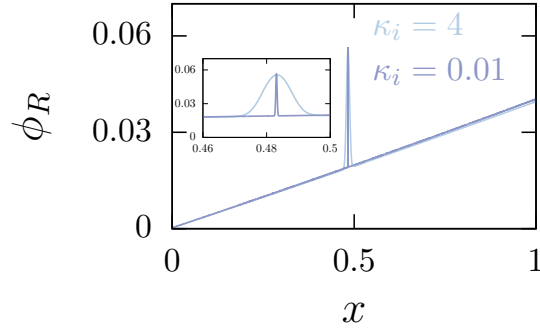


Figure A.3 – Two example profiles for regulator peaks at the droplet interface. The two presented cases are of different  $\kappa$ -parameters with  $\kappa_A = \kappa_R = \kappa$ . Both peaks show very similar heights but differ significantly in their area, because of their widths. The peak width decreases, if the  $\kappa$ -parameters are decreasing. The applied parameters are  $\chi_{AB} = 4$ ,  $\chi_{AR} = \chi_{BR} = 1$ ,  $\bar{\phi}_R = 0.02$ ,  $\bar{\phi}_A = 0.5$ ,  $Ls = 0.99$ .

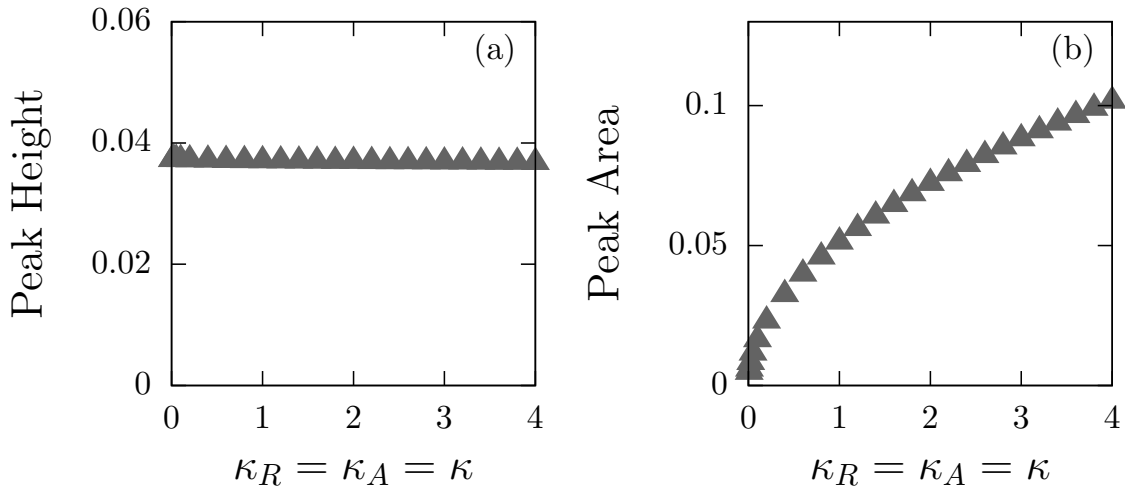


Figure A.4 – Characterization of the peak for different  $\kappa$ -parameters, while  $\kappa_A = \kappa_R = \kappa$ . (a) The peak height is constant in good approximation, the equilibrium regulator volume fraction at the  $A$ -interface is almost not affected by the  $\kappa$ -parameters. (b) The Peak goes to zero for vanishing  $\kappa$ -parameters. The applied parameters are  $\chi_{AB} = 4$ ,  $\chi_{AR} = \chi_{BR} = 1$ ,  $\bar{\phi}_R = 0.02$ ,  $\bar{\phi}_A = 0.5$ ,  $Ls = 0.99$ .

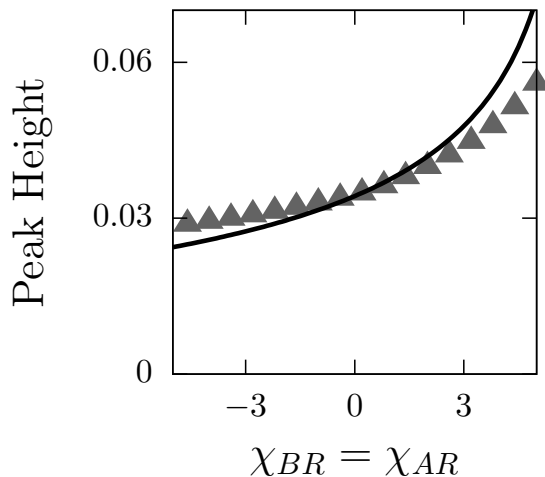


Figure A.5 – Measured peak height for different interaction parameters  $\chi_{AR} = \chi_{BR}$ . The points are data obtained from the numerical solution of the Euler-Lagrange equation, the solid black line shows the result of the simple analytic model of the peak presented in this section. The chosen parameters for the numeric points are  $\chi_{AB} = 4$ ,  $\bar{\phi}_A = 0.5$ ,  $\bar{\phi}_R = 0.02$ ,  $\kappa_R/L^2 = 7.63 \cdot 10^{-5}$ ,  $\kappa_A/L^2 = 6.10 \cdot 10^{-5}$ ,  $\kappa/L^2 = 6.10 \cdot 10^{-5}$  and  $Ls = 0.99$ . The chosen parameters in the analytic model are  $\chi_{AB} = 4$ ,  $\bar{\phi}_R = 0.02$ ,  $\bar{\phi}_A = 0.5$ ,  $\phi_{A,\text{out},\text{bin}} = 0.02332$ ,  $\epsilon = 0.05$ .

and is the region of the bulk phase of low  $A$  volume fraction. The remaining region (III) is located at  $(1 - \epsilon)/2 \leq x < (1 + \epsilon)/2$ . The volume fractions are  $\phi_A^{\text{III}} = \phi_{A,\text{peak}}$  and  $\phi_R^{\text{III}} = \phi_{R,\text{peak}}$ . This region models the interface between the droplet and the surrounding phase, it is also the region where the peak lives. The modeled peak width and thus the width of region (III) is  $\epsilon$ . In this simple model,  $\phi_{A,\text{out}}$  is modeled as the volume fraction of the  $A$  depleted phase of the binary  $A$ - $B$ -system of equal  $\chi_{AB}$ ,  $\phi_{A,\text{bin},\text{out}}$ . We use the average volume fraction  $\bar{\phi}_A = 0.5$  to be consistent with our previous choice of this parameter while solving the Euler-Lagrange equation. The average volume fraction of the regulator is  $\bar{\phi}_R = 0.02$ . The exact number is not very important, we choose the value we commonly do in this thesis. From particle conservation we get

$$\begin{aligned} \phi_{R,\text{bulk}} &= \frac{\bar{\phi}_R - \epsilon \phi_{R,\text{peak}}}{1 - \epsilon}, \\ \phi_{A,\text{in}} &= \frac{2\bar{\phi}_A - \phi_{A,\text{bin},\text{out}} + \epsilon(\phi_{A,\text{bin},\text{out}} + \phi_{R,\text{peak}} - 1)}{1 - \epsilon} \end{aligned} \quad (\text{A.47})$$

for the other volume fraction values of this model. The free energy of this system will be minimized with respect to  $\phi_{R,\text{peak}}$  to obtain the equilibrium volume fraction of the regulator at the interface. All other parameters are constant parameters in this model. The only unknown parameter is  $\epsilon$ . We want to highlight, that this model does not include a regulator gradient, which also means, that there is also no transition between correlated and anti-correlated states included. This model is only constructed to give a explanation to the peak, but the existence of the peak does not need the imposed regulator gradient. It is an effect intrinsic to the interface and the ternary nature of the system.

Using this ansatzes, we can calculate the free energy of the system  $\tilde{F}_{\text{IM}}(\phi_{R,\text{peak}})$  applying eq. (3.1) and integrating the free energy density. The discussed free energy is  $F_{\text{IM}}(\phi_{R,\text{peak}}) =$

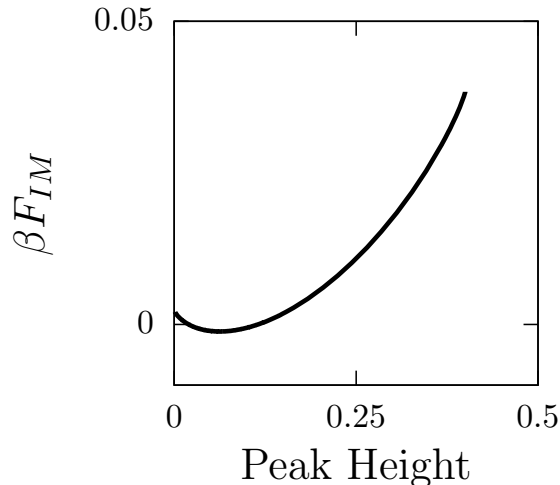


Figure A.6 – Free energy of the analytic interval model of the peak. The free energy shows a minimum at a certain value of the peak height, which corresponds to the equilibrium peak height of the model. For each set of parameters, there is an equilibrium maximum peak height as long as the model free energy is well defined. For higher peak heights there exists a conflict of the chosen parameters, which leads to volume fractions larger than 1 or smaller than 0 and a not defined value of the free energy. For the applied high value of the peak width  $\epsilon = 0.05$ , this maximum peak height is smaller than 1 and thus visible in the plot. The applied parameters are  $\chi_{AB} = 4$ ,  $\chi = 1$ ,  $\bar{\phi}_R = 0.02$ ,  $\bar{\phi}_A = 0.5$ ,  $\phi_{A,\text{out,bin}} = 0.02332$ ,  $\epsilon = 0.05$ .

$\tilde{F}_{\text{IM}}(\phi_{R,\text{peak}}) - \tilde{F}_{\text{IM}}(\phi_{R,\text{peak}} = \phi_{R,\text{bulk}})$ , which sets the reference point to a system without peak. For simplicity, we neglect the gradient terms in the free energy and assume, that the effect of the  $\kappa$ -parameters can be modeled by the thickness  $\epsilon$  of region (III). This free energy is shown in fig. A.6. This free energy is defined up to a maximum peak width for each set of parameters. For higher peak heights, certain volume fractions will get larger than 1 or smaller than 0 and the value of the free energy is no more defined. For the chosen large peak width of  $\epsilon = 0.05$ , this maximum peak height is smaller than 1 and visible in fig. A.6. The free energy has one local minimum at a certain peak height, which is the equilibrium peak height of this model. If the entropic contributions and the energetic contributions are computed separately, it can be shown, that the entropic contribution can explain the maximum peak height. But furthermore, the energetic contributions have a similar effect and are significantly larger than the entropic contributions. Thus the peak can be regarded as an energetic effect. Now, we can calculate the equilibrium peak height for different interaction parameters  $\chi_{AR} = \chi_{BR}$  numerically. The result is shown in fig. A.5. The analytic model shows a similar trend as the results obtained from the solutions of the Euler-Lagrange equation. The parameter  $\epsilon$  is chosen, so that the difference between the two curves at  $\chi_{AR} = 0$  is close to 0. That leads to  $\epsilon = 0.05$ , which is a high value but not unreasonable. The analytic model and the solution of the Euler-Lagrange equation show good agreement considering the strong simplifications applied to the analytic model.

## A.8 Hysteresis of the Order Parameter

In this section the hysteresis of the order parameter  $\rho_{BR}$  around the transition point between correlated and anti-correlated states is investigated in more detail. This hysteresis is shown in fig. A.7(a), it consists of the correlated branch and the anti-correlated branch. For comparison, the behavior of the order parameter in a system without external potential is included. In this case without an external potential only one curve is present, because both solutions are energetically degenerate. Regarding to the hysteresis in the anisotropic system, we did not find a point, for which a hysteresis branch becomes unstable. We observe a asymptotic approach of the two branches. We consider this hysteresis as quasi infinite, because we are also not completely sure, if the points of instability we have found for some more extreme interaction values are of physical or numeric origin. Furthermore, the hysteresis loop is asymmetric and the asymptotic approach of the two branches is slower for negative interaction parameters. The asymptotic approach of the two branches is also the aim of fig. A.7(b). Here, the absolute value of the difference between the branches is plotted for two different strengths of the external potential. This difference is presented in dependency of the distant from the transition point to give a better visualization of the asymmetry of the hysteresis. Because the value of the order parameter is linearly dependent on the strength of the external potential in good approximation (see fig. A.2(b)), we decide to present a scaled value of the order parameter difference. The scaling factor is  $s_{\max}/s$ . The parameter  $s_{\max}$  is the maximum strength, at which the external potential is no more well defined, in the chosen units  $s = 1$ . The data suggest, that the hysteresis loop and the asymmetry are also relatively smaller for weaker external potential. The black line in fig. A.7(b) indicates, that a change of sign of the difference occurred for  $s = 0.99$ . This visual indication was introduced to keep this information by the use of the absolute value of the presented difference. In general, this change of sign is connected to a intersection of the two hysteresis branches. This should not be possible in the hysteresis process. Taking the numbers of the difference at this sign change into account it is very likely that the origin of this observation is the accuracy of the numeric solution.

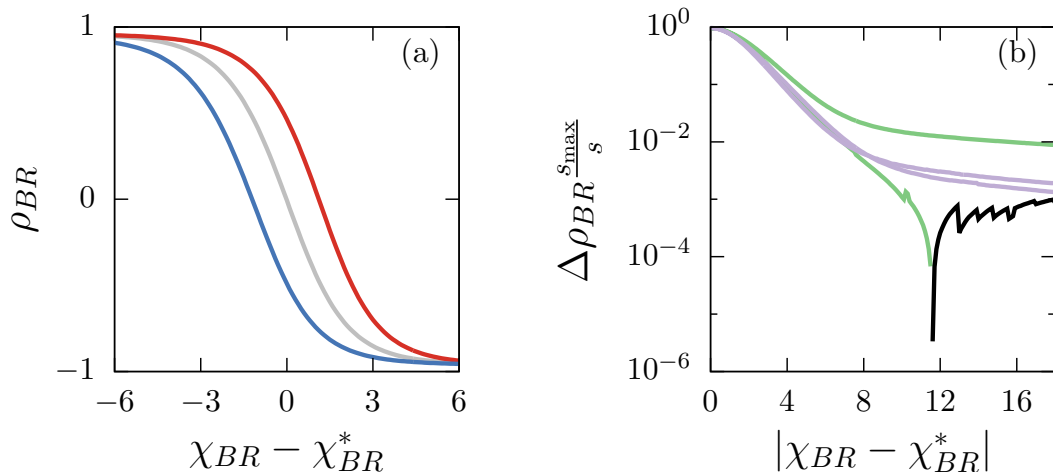


Figure A.7 – Asymmetric behavior of the hysteresis of the order parameter  $\rho_{BR}$  around the transition point. (a) Asymmetric hysteresis of the order parameter around the transition point. Besides the two states correlated (blue) and anti-correlated (red), there is also the system without external potential (grey) included for comparison. On the left side, the hysteresis loop is still not closed, on the right side a asymptotic approach is observed. (b) Difference between the two branches of the hysteresis curves for two different values of the potential strength  $s = 0.99$  (lime green) and  $s = 0.13$  (grayish violet). The black line indicates a negative measured difference of the two branches. Here, only the difference in dependency of the distance from the transition point is shown, to give a better visualization of the asymmetric behavior. The fixed parameters are  $\chi_{AB} = 4$ ,  $\chi_{AR} = 1$ ,  $\bar{\phi}_A = 0.5$ ,  $\bar{\phi}_R = 0.02$ ,  $\kappa_R/L^2 = 7.63 \cdot 10^{-5}$ ,  $\kappa_A/L^2 = 6.10 \cdot 10^{-5}$ ,  $\kappa/L^2 = 6.10 \cdot 10^{-5}$ .

## A.9 Ensemble with Constant Regulator Distribution

### A.9.1 Conditions for the Stationary Points of the Free Energy

In this section we will consider an ensemble, where the regulator distribution  $\phi_R(x)$  is imposed and strictly constant. This can be seen as the conjugate problem to the previously considered ensembles with external potential. Now, the regulator distribution is known and we can define a conjugate regulator potential, which is the conjugate potential to the field  $\phi_R(x)$ . The conjugate potential can be obtained by the functional derivative

$$U_R = -\delta_{\phi_R} \left( \min_{\phi_A} F[\phi_A | \phi_R] \right). \quad (\text{A.48})$$

This expression is the functional derivative with respect to  $\phi_R$  of the minimum of the free energy  $F$  with respect to  $\phi_A$  given a certain regulator distribution  $\phi_R$ . Eq. (A.48) describes the relation between the constant potential ensemble and the constant distribution ensemble. Here, we will not compute this potential.

The free energy density of this system is

$$\underbrace{\beta \nu \tilde{f}}_{=f} = \underbrace{\phi_A \ln \phi_A + \phi_R \ln \phi_R + \phi_B \ln \phi_B + \chi_{AB} \phi_A \phi_B + \chi_{AR} \phi_A \phi_R + \chi_{BR} \phi_A \phi_R}_{=f_0} + \frac{\kappa_A}{2} (\partial_x)^2 + \frac{\kappa_R}{2} (\partial_x \phi_R)^2 + \frac{\kappa}{2} \partial_x \phi_A \partial_x \phi_R. \quad (\text{A.49})$$

## A.9. Ensemble with Constant Regulator Distribution

---

Here, the field  $\phi_B$  is used as an abbreviation, because an incompressible system is considered. It is given by  $\phi_B = 1 - \phi_A - \phi_R$ . The fields  $\phi_A(x)$  and  $\phi_R(x)$  are functions of the spatial coordinate  $x$ . The spatial coordinate  $x$  is defined between 0 and 1. The free energy density  $\tilde{f}$  is the free energy per volume. By multiplying it with the molecular volume  $\nu$  we define the free energy per lattice site  $f$ . Because the system is densely packed and are particles are of the same size, these two densities are connected by this simple scalar multiplication. The total free energy of the bulk region is

$$F_{\text{bulk}} = \int_0^1 f dx, \text{ with } \bar{\phi}_A = \int_0^1 \phi_A dx. \quad (\text{A.50})$$

The additional condition implements the constraint of a fixed average volume fraction of component  $A$ . The total free energy of the bulk region considering this constraint is given by

$$F_{\text{bulk}}^{\text{cons}}[\phi_A] = F_{\text{bulk}} + \lambda \int_0^1 (\phi_A - \bar{\phi}_A) dx. \quad (\text{A.51})$$

Now, we have to define the effect of the boundary on the system. here, we assume a very short ranged interaction of the walls with component  $A$ . Only the particles at the boundary will contribute to this interaction. Such a potential can be described as

$$W = w (\phi_A(0) + \phi_A(1)). \quad (\text{A.52})$$

The total free energy of the system is the sum of the boundary potential and the constraint free energy of the bulk region

$$F[\phi_A] = F_{\text{bulk}}^{\text{cons}} + W. \quad (\text{A.53})$$

The stationary points of the are the profiles for which the first functional derivative of the free energy vanishes

$$0 = \delta_{\phi_A} F[\phi_A]. \quad (\text{A.54})$$

With eq. (A.50), eq. (A.51), eq. (A.52) and eq. (A.53), this becomes

$$\begin{aligned} 0 = & \int_0^1 \left( \frac{\partial f_0}{\partial \phi_A} + \lambda - \kappa_A \partial_x^2 \phi_A - \frac{\kappa}{2} \partial_x^2 \phi_R \right) \delta \phi_A dx \\ & + \left( w - \kappa_A \partial_x \phi_A|_{x=0} - \frac{\kappa}{2} \partial_x \phi_R|_{x=0} \right) \delta \phi_A|_{x=0} \\ & + \left( w + \kappa_A \partial_x \phi_A|_{x=1} + \frac{\kappa}{2} \partial_x \phi_R|_{x=1} \right) \delta \phi_A|_{x=1}. \end{aligned} \quad (\text{A.55})$$

Because  $\delta \phi_A$  is a quasi arbitrary function, the first functional derivative vanishes, if the integral kernel is zero and the brackets outside the integral become zero. From the integral kernel we obtain the Euler-Lagrange equation, the boundary terms define the natural boundary conditions of the system. The stationary points of the free energy functional are

the solutions of the differential equation

$$0 = \frac{\partial f_0}{\partial \phi_A} + \lambda - \kappa_A \partial_x^2 \phi_A - \frac{\kappa}{2} \partial_x^2 \phi_R, \quad (\text{A.56})$$

$$0 = w - \kappa_A \partial_x \phi_A|_{x=0} - \frac{\kappa}{2} \partial_x \phi_R|_{x=0}, \quad (\text{A.57})$$

$$0 = w + \kappa_A \partial_x \phi_A|_{x=1} + \frac{\kappa}{2} \partial_x \phi_R|_{x=1}. \quad (\text{A.58})$$

### A.9.2 Linear Regulator Profile

In this section, we will consider only a linear regulator profile  $\phi_R = mx + m_0$ . With the constrain  $\bar{\phi}_R = \int_0^1 \phi_R dx$ , we can write the offset of the regulator profile in terms of the slope of the profile and the average volume fraction of the regulator

$$\phi_R = mx + \bar{\phi}_R - \frac{m}{2}. \quad (\text{A.59})$$

Given this profile, the first derivative of the regulator profile is  $\partial \phi_R = m$ , the second derivative vanishes  $\partial_x^2 \phi_R = 0$ . We also choose  $w = 0$ , the walls have no interactions with the  $A$ -particles.

The Euler-Lagrange equation was solved using the MATLAB solver `bvp4c`. Four example profiles are plotted in fig. A.8. The also plotted regulator profile is not part of the solution, but is included to present the complete system.

Now, we choose  $\chi_{BR}$  to be the control parameter and compute the stationary solutions for different  $\chi_{BR}$ . For each  $\chi_{BR}$  we find two coexisting solutions, one anti-correlated solution and one correlated solution. Knowing the volume fraction profiles, we can compute the corresponding free energy. The result are shown in fig. A.9. The solid lines show the free energy of the equilibrium solutions. The dashed lines correspond to the not stable solutions. Following the path of the lowest free energy we observe a kink of the free energy at  $\chi_{BR}^*$ . This indicates a discontinuous phase transition at this point. This result shows, that this phase transition is not caused by the detailed adaption of the regulator profile to the  $A$ -profile or the  $A$ -profile to the regulator profile. The existence of a regulator gradient seems sufficient to cause this phase transition.

Related to this, we can look at the difference of the free energy  $\Delta F = F^l - F^r$ . This property is shown in fig. A.10. The dashed line shows the difference of the free energy obtained from the solutions of the Euler-Lagrange equation, the solid black line shows the result from the analytic model introduced in section 3.4. Both lines show very good agreement. The main reason for that is most likely that the analytic model also considers a constant linear regulator distribution. Both lines intersect at  $\chi_{BR} = 0$ , which is also the transition point.

This transition can also be characterized using the order parameter  $\rho_{BR}$  of the solution with the lowest free energy. The observed behavior of the order parameter is shown in fig. A.11. Looking only at one solution, the value of the order parameter is independent of  $\chi_{BR}$  in good approximation. This is consistent with the observed linear behavior of the free energy. At the transition point  $\chi_{BR}^*$  the the value of the order parameter jumps between the two branches.

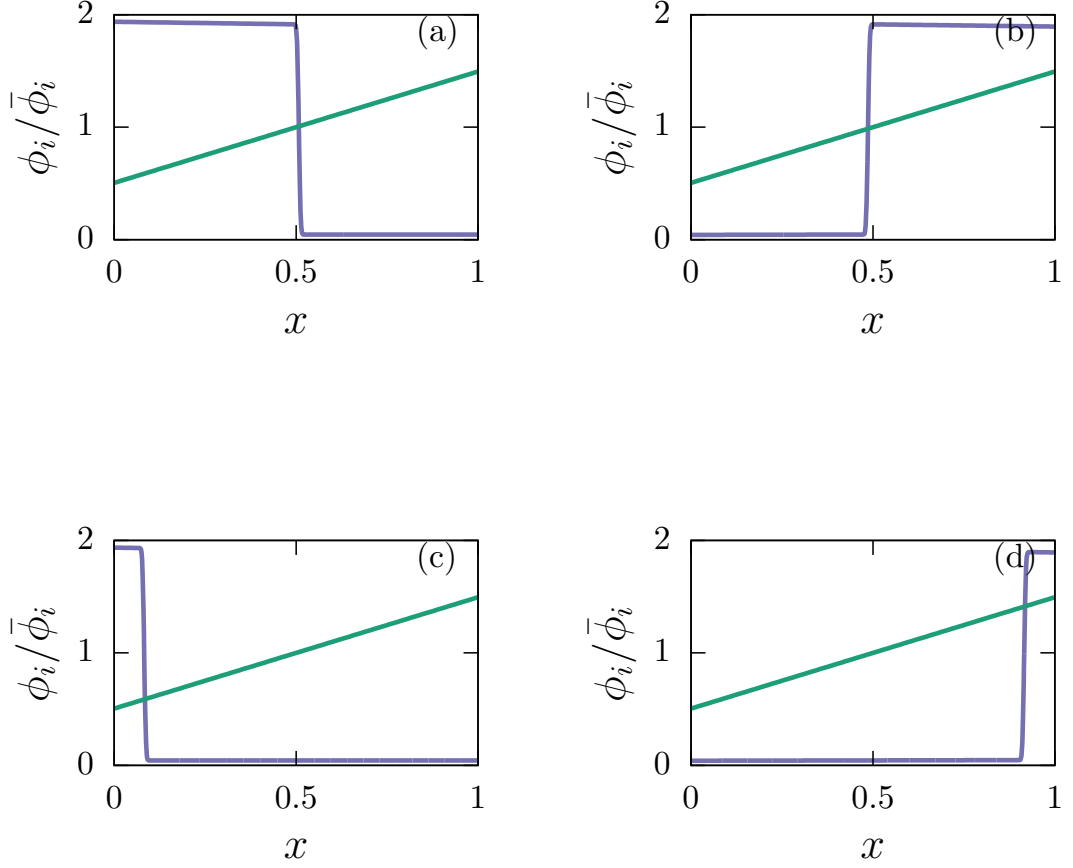


Figure A.8 – The top line shows the anti-correlated state (a) and the correlated state (b) for an average volume fraction of  $\bar{\phi}_A = 0.5$ . The bottom line shows the anti-correlated state (c) and the correlated state (d) for  $\bar{\phi}_A = 0.1$ . The chosen parameters are  $\chi_{AB} = 4$ ,  $\chi_{AR} = 0$ ,  $\bar{\phi}_R = 0.02$ ,  $\kappa_R/L^2 = 7.63 \cdot 10^{-5}$ ,  $\kappa_A/L^2 = 6.10 \cdot 10^{-5}$ ,  $\kappa/L^2 = 6.10 \cdot 10^{-5}$  and  $m/\bar{\phi}_R = 0.99$ . For the anti-correlated states  $\chi_{BR} = -3$ , for the correlated states  $\chi_{BR} = 3$ .

### A.9.3 Periodic Regulator Profile

At this point it is still possible, that the phase transition is supported by the interaction of  $A$ -particles with the wall. To clarify this we consider a periodic system without walls. In that case the Euler-Lagrange equation is unchanged, but the boundary conditions are now periodic boundary conditions

$$\begin{aligned} 0 &= \phi_A(0) - \phi_A(1), \\ 0 &= \partial_x \phi_A(0) - \partial_x \phi_A(1). \end{aligned} \tag{A.60}$$

The imposed periodic regulator field is

$$\phi_R = m\bar{\phi}_R \cos(2\pi x) + \bar{\phi}_R. \tag{A.61}$$

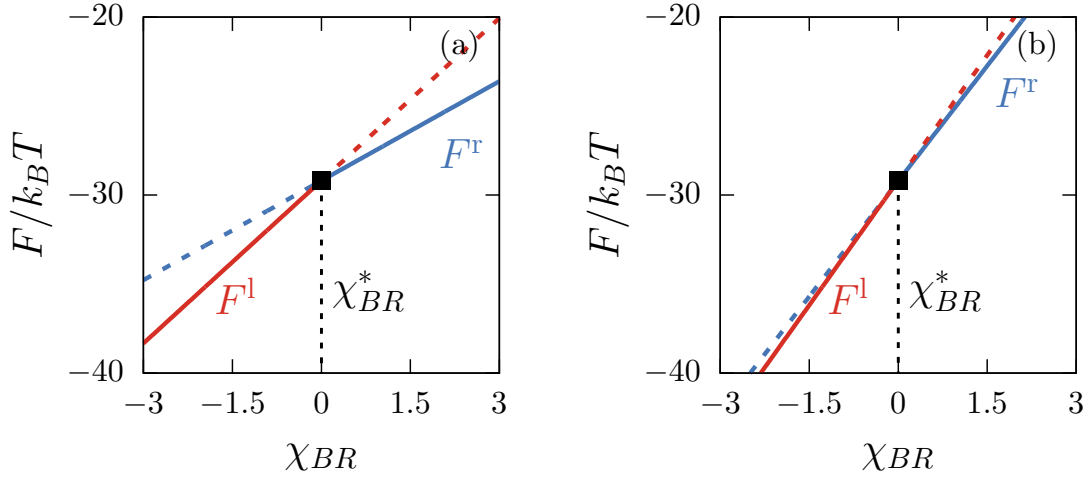


Figure A.9 – Free energy of the anti-correlated solution ( $F^l$ ) and the correlated solution ( $F^r$ ). (a)  $\phi_A = 0.5$ . (b)  $\phi_A = 0.1$ . The two free energy branches intersect at  $\chi_{BR}^*$ . Following the path of the lowest free energy, which corresponds to the equilibrium solutions, we observe a kink of the free energy at  $\chi_{BR}^*$ . The chosen parameters are  $\chi_{AB} = 4$ ,  $\chi_{AR} = 0$ ,  $\bar{\phi}_R = 0.02$ ,  $\kappa_R/L^2 = 7.63 \cdot 10^{-5}$ ,  $\kappa_A/L^2 = 6.10 \cdot 10^{-5}$ ,  $\kappa/L^2 = 6.10 \cdot 10^{-5}$  and  $m/\bar{\phi}_R = 0.99$ .

Now, the second derivative of the regulator profile does not vanish and adds a inhomogeneous contribution to the Euler-Lagrange equation. The profile  $\phi_A$  is again obtained as the solution of the Euler-Lagrange equation. Two typical profiles are shown in fig A.12. We found two different types of solutions, a anti-correlated solution where the droplet is placed at the minimum of the regulator profile, and a correlated solution where the droplet is placed at the maximum of the regulator profile. We can calculate the free energy corresponding to the two solutions. The two branches of the free energy in dependence of the control parameter  $\chi_{BR}$  are shown in fig. A.13. The two branches of the free energy intersect at one point, which leads to a kink of the path of the minimum free energy at this point. This indicates a discontinuous phase transition and the position of its transition point. Consistently, if we compute the order parameter  $\rho_{BR}$  in dependence of the control parameter  $\chi_{BR}$ , a jump of the order parameter is observed at the transition point (see fig. A.13).

The existence of the discontinuous phase transition in the periodic ensemble shows, that the correlated-anti-correlated phase transition is intrinsic in the inhomogeneous system and not enabled by the boundary conditions.

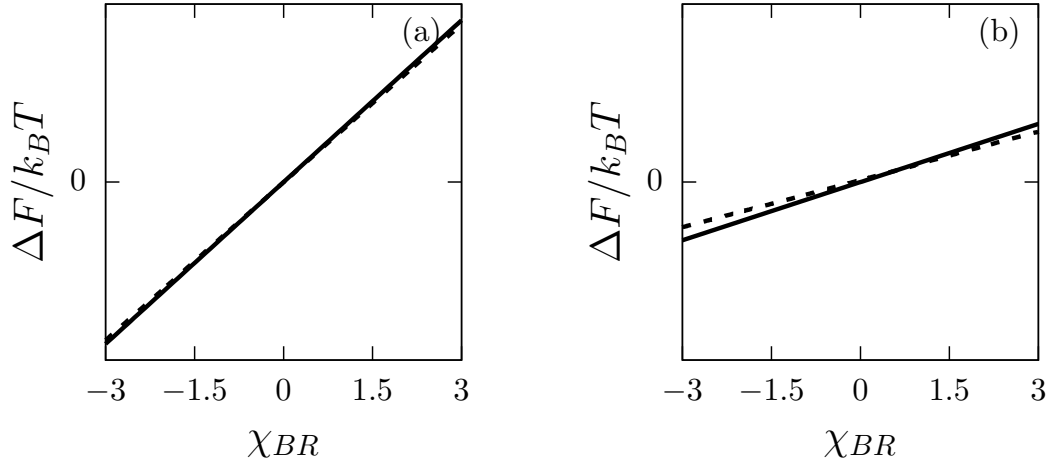


Figure A.10 – Difference of the free energy  $\Delta F = F^l - F^r$ . The solid lines show the results from the analytic model, the dashed lines are obtained from the solutions of the Euler-Lagrange equation. (a)  $\bar{\phi}_A = 0.5$ . (b)  $\bar{\phi}_A = 0.1$ . Both lines intersect at  $\chi_{BR} = 0$ . The chosen parameters are  $\chi_{AB} = 4$ ,  $\chi_{AR} = 0$ ,  $\bar{\phi}_R = 0.02$ ,  $\kappa_R/L^2 = 7.63 \cdot 10^{-5}$ ,  $\kappa_A/L^2 = 6.10 \cdot 10^{-5}$ ,  $\kappa/L^2 = 6.10 \cdot 10^{-5}$  and  $m/\bar{\phi}_R = 0.99$ .

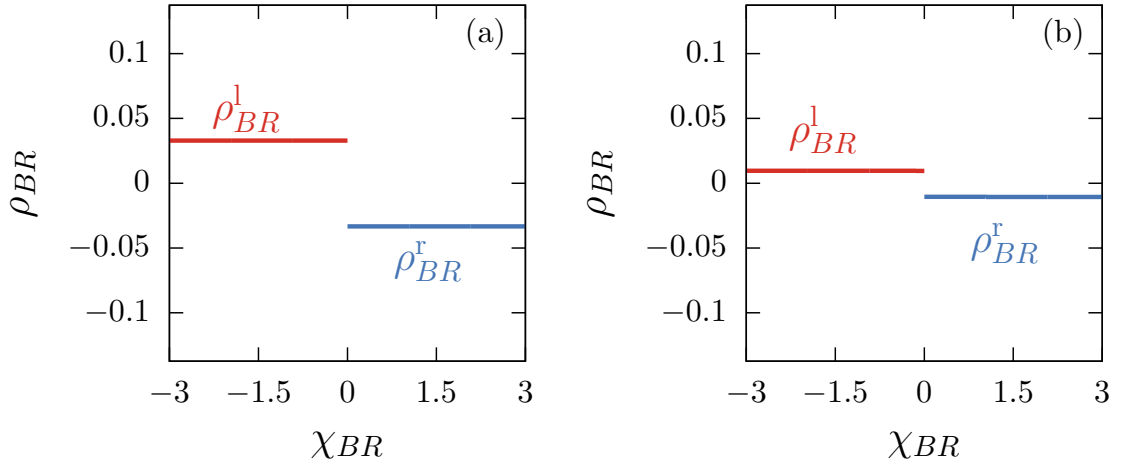


Figure A.11 – Behavior of the order parameter  $\rho_{BR}$ . (a)  $\bar{\phi}_A = 0.5$ . (b)  $\bar{\phi}_A = 0.1$ . The value of the order parameter jumps at  $\chi_{BR} = 0$ . For each branch, the value of the order parameter is constant in good approximation. The chosen parameters are  $\chi_{AB} = 4$ ,  $\chi_{AR} = 0$ ,  $\bar{\phi}_R = 0.02$ ,  $\kappa_R/L^2 = 7.63 \cdot 10^{-5}$ ,  $\kappa_A/L^2 = 6.10 \cdot 10^{-5}$ ,  $\kappa/L^2 = 6.10 \cdot 10^{-5}$  and  $m/\bar{\phi}_R = 0.99$ .

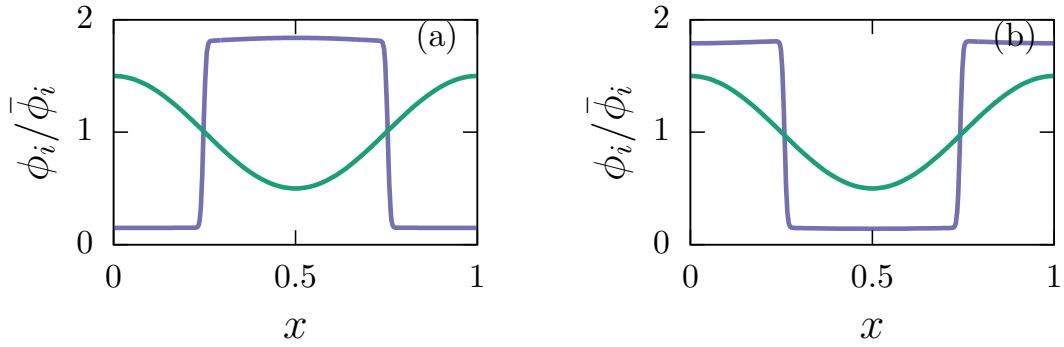


Figure A.12 – Anti-correlated state (a) and the correlated state (b) for an average volume fraction of  $\bar{\phi}_A = 0.5$ . The chosen parameters are  $\chi_{AB} = 3$ ,  $\chi_{AR} = 1$ ,  $\bar{\phi}_R = 0.02$ ,  $\kappa_R/L^2 = 7.63 \cdot 10^{-5}$ ,  $\kappa_A/L^2 = 6.10 \cdot 10^{-5}$ ,  $\kappa/L^2 = 6.10 \cdot 10^{-5}$  and  $m = 0.5$ . For the anti-correlated states  $\chi_{BR} = -1$ , for the correlated states  $\chi_{BR} = 3$

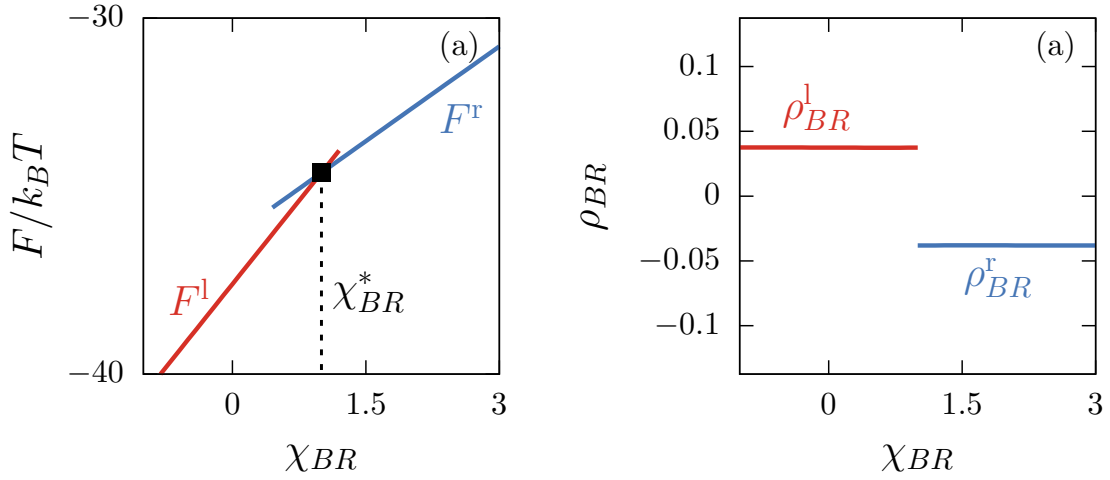


Figure A.13 – (a) Free energy of the obtained anti-correlated and correlated solutions. The two branches intersect at one point, the path of the lowest free energy possess a kink there. (b) Equilibrium order parameter  $\rho_{BR}$  of anti-correlated solution and the correlated solution. This order parameter shows a jump at the transition point. The chosen parameters are  $\chi_{AB} = 3$ ,  $\chi_{AR} = 1$ ,  $\bar{\phi}_R = 0.02$ ,  $\kappa_R/L^2 = 7.63 \cdot 10^{-5}$ ,  $\kappa_A/L^2 = 6.10 \cdot 10^{-5}$ ,  $\kappa/L^2 = 6.10 \cdot 10^{-5}$  and  $m = 0.5$ .

# B Simulation

## B.1 Computation of the Energy Difference between Succeeding Configurations

New configurations are generated by exchanging the position of a particle with one of its neighboring particle. There are three different cases, a  $A$ -particle can change position with a vacancy ( $B$ -particle), a  $R$ -particle can change positions with a vacancy, or an  $A$ -particle can change positions with a  $R$ -particle. The reverse process of a  $R$ -particle changes position with an  $A$ -particle only changes the sign of the energetic difference.

*Exchange of A and R.* To calculate the energetic difference between two succeeding configurations 1 and 2, we add up the pair interactions of the exchanging particles with their nearest neighbors. we are only considering nearest neighbor interactions in our model. The interaction between two neighboring particles  $i$  and  $j$  is  $\epsilon_{ij}$ . The numbers of neighbors are counted by the parameter  $\gamma_{1,2}^i$ . This gives the number of  $i$  neighbors of a particle at position 1 or 2, where 1 is the original position of the  $A$ -particle (configuration 1) and 2 the new position of the  $A$ -particle (configuration 2). The total interaction energy of the pair of particles in the original configuration is

$$\begin{aligned} E_1^{AR} &= \gamma_1^A \epsilon_{AA} + \gamma_1^R \epsilon_{AR} + \gamma_2^A \epsilon_{AR} + \gamma_2^R \epsilon_{RR} \\ &+ \left( \zeta - \gamma_1^A - \gamma_1^R - \gamma_1^W - 1 \right) \epsilon_{AB} + \left( \zeta - \gamma_2^A - \gamma_2^R - \gamma_2^W - 1 \right) \epsilon_{BR} \\ &+ \gamma_1^W w_A + \gamma_2^W w_R. \end{aligned} \quad (\text{B.1})$$

The coordination number of the lattice is  $\zeta$ . The parameter  $\gamma_{1,2}^W$  counts the number of wall particles next to position 1 or 2. In general, the wall particles possess a individual interaction  $w_A$  and  $w_R$  with the bulk particles, which is the reason to consider them explicitly at this point. The parameter  $\gamma_{1,2}^W$  is 1, if the respective position is next to the wall and 0 if it is a bulk position. Because we consider an incompressible lattice system, the number of  $B$ -particles is given by  $\zeta - \gamma_{1,2}^A - \gamma_{1,2}^R - \gamma_{1,2}^W - 1$ . In this counting 1 is subtracted because the interaction of the exchanging particles is not taken into account. This interaction is present in both configurations and cancels out when calculating the energetic difference

## Appendix B. Simulation

---

between them. The interaction energy of the new configuration is

$$\begin{aligned}
E_2^{AR} &= \gamma_1^A \epsilon_{AR} + \gamma_1^R \epsilon_{RR} + \gamma_2^A \epsilon_{AA} + \gamma_2^R \epsilon_{AR} \\
&+ \left( \zeta - \gamma_1^A - \gamma_1^R - \gamma_1^W - 1 \right) \epsilon_{BR} + \left( \zeta - \gamma_2^A - \gamma_2^R - \gamma_2^W - 1 \right) \epsilon_{AB} \\
&+ \gamma_1^W w_R + \gamma_2^W w_A.
\end{aligned} \tag{B.2}$$

Accordingly, the energetic difference between the configurations is

$$\begin{aligned}
\Delta E^{AR} &= E_2^{AR} - E_1^{AR} \\
&= \left( \gamma_2^A - \gamma_1^A \right) \left( \epsilon_{AA} - \epsilon_{AR} + \epsilon_{BR} - \epsilon_{AB} \right) + \left( \gamma_2^R - \gamma_1^R \right) \left( \epsilon_{AR} - \epsilon_{RR} + \epsilon_{BR} - \epsilon_{AB} \right) \\
&+ \left( \gamma_2^W - \gamma_1^W \right) \left( \epsilon_{BR} - \epsilon_{AB} + w_A - w_R \right).
\end{aligned} \tag{B.3}$$

The last term, which is the only term including the wall interactions, vanishes, if the wall particles have the same interactions as the B-particles. This is the default choice for most of the simulations presented in this thesis. The wall term also vanishes for this choice in the further cases.

With the definition of the Flory-Huggins interaction parameter  $\chi_{ij} = \beta\zeta/2(2\epsilon_{ij} - \epsilon_{ii} - \epsilon_{jj})$ , we can replace the combinations of the microscopic interaction parameters with combinations of the Flory-Huggins parameters.

$$\begin{aligned}
\chi_{BR} - \chi_{AB} - \chi_{AR} &= \beta\zeta \left( \epsilon_{AA} - \epsilon_{AR} + \epsilon_{BR} - \epsilon_{AB} \right), \\
\chi_{BR} + \chi_{AR} - \chi_{AB} &= \beta\zeta \left( \epsilon_{AR} - \epsilon_{RR} + \epsilon_{BR} - \epsilon_{AB} \right), \\
\chi_{BR} - \chi_{AB} + \chi_{AW} - \chi_{BW} &= \beta\zeta \left( \epsilon_{BR} - \epsilon_{AB} + w_A - w_R \right).
\end{aligned} \tag{B.4}$$

The energetic change between the two configurations in terms of the Flory-Huggins parameters is

$$\begin{aligned}
\beta\Delta E^{AR} &= \frac{\gamma_2^A - \gamma_1^A}{\zeta} \left( \chi_{BR} - \chi_{AB} - \chi_{AR} \right) + \frac{\gamma_2^R - \gamma_1^R}{\zeta} \left( \chi_{BR} + \chi_{AR} - \chi_{AB} \right) \\
&+ \frac{\gamma_2^W - \gamma_1^W}{\zeta} \left( \chi_{BR} - \chi_{AB} + \chi_{AW} - \chi_{RW} \right).
\end{aligned} \tag{B.5}$$

*Exchange of A and B.* Analogous to the previous case, the energy change caused by an exchange of an A- with a B-particle can be computed. Again, the formulation with the Flory-Huggins parameters is used.

$$\begin{aligned}
\beta\Delta E^{AB} &= -\frac{2\left(\gamma_2^A - \gamma_1^A\right)}{\zeta} \chi_{AB} + \frac{\gamma_2^R - \gamma_1^R}{\zeta} \left( \chi_{AR} - \chi_{BR} - \chi_{AB} \right) \\
&+ \frac{\gamma_2^W - \gamma_1^W}{\zeta} \left( \chi_{AW} - \chi_{BW} - \chi_{AB} \right).
\end{aligned} \tag{B.6}$$

## B.1. Computation of the Energy Difference between Succeeding Configurations

---

*Exchange of R and B.* The energetic difference of a exchange of a  $R$ - and a  $B$ -particle is

$$\begin{aligned} \beta\Delta E^{RB} = & \frac{\gamma_2^A - \gamma_1^A}{\zeta} (\chi_{AR} - \chi_{AB} - \chi_{BR}) - \frac{2(\gamma_2^R - \gamma_1^R)}{\zeta} \chi_{BR} \\ & + \frac{\gamma_2^W - \gamma_1^W}{\zeta} (\chi_{RW} - \chi_{BW} - \chi_{BR}). \end{aligned} \quad (\text{B.7})$$

The use of the Flory-Huggins parameters simplifies the evaluation of the simulation, because the parameter space is reduced. Considering the ternary system with a solvent-like wall, there are six microscopic interaction parameters. From the formulation in terms of the Flory-Huggins parameters we see, that only three independent parameters effect the system. If the system with a not solvent-like wall is considered, we also reduce the number of parameters by three (from nine to six) applying this mapping.<sup>1</sup> The mapping is possible, because the number of particles of each component is strictly conserved in the canonical simulation. Even in the simulation with flux boundary conditions, the boundary conditions are constructed in a way that this conservation is fulfilled in each simulation step. In the case of a grand canonical simulation, this conservation is not considered during the generation of new configurations and this mapping could not be applied. Even if the averaged properties of the system in equilibrium are still governed by the Flory-Huggins parameters, the energetic change between configurations is effected by all six microscopic interaction parameters.

---

<sup>1</sup>The parameter  $\epsilon_{WW}$  does not appear in the expression of the energetic difference, because the number of W-W neighbors can not be changed during this simulation.

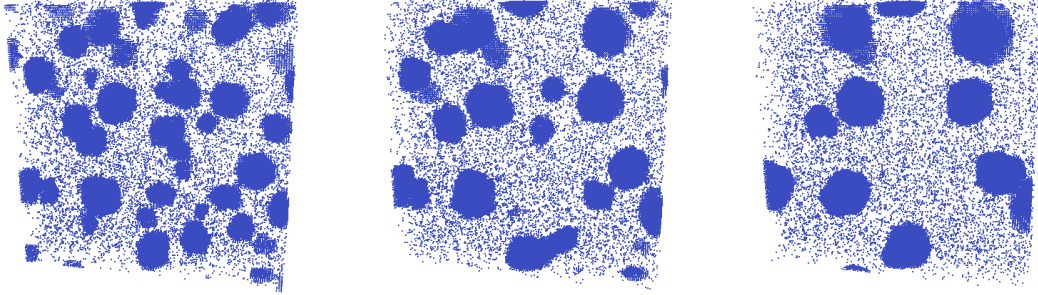


Figure B.1 – Snapshots at different times of the simulation illustrate the droplet growth. From left to right these snapshots were taken after  $10^5$  MCS,  $2.5 \cdot 10^5$  MCS and  $5 \cdot 10^5$  MCS. The used parameter values are  $\bar{\phi}_A = 0.05$ ,  $\chi_{AB} = 4$  and  $L_x = L_y = L_z = 64a$ .

## B.2 Monte Carlo Simulation without Regulator Gradient - Growth dynamics

The growth dynamics are measured for a binary system without regulator to check the consistency of the simulation. For the binary system, a cubic simulation box was used. Given the homogeneous character of this system, periodic boundary conditions are applied in all three directions. The initial state is well mixed with  $\bar{\phi}_A = 0.05$ . The Flory-Huggins parameter is  $\chi_{AB} = 4$  and thus deep in the separating region of the corresponding mean field phase diagram. This consistency checks are done for the short time of  $5 \cdot 10^5$  MCS. The simulation shows the formation and the growth of droplets. Some snapshots are shown in fig. B.1

To quantify this process, we calculated the characteristic length scale of a droplet  $\langle L(s) \rangle_{xyz}$ . The length  $L$  measures the continuous length inside a droplet following a linear path  $s$ . We measured this property in the  $x$ -,  $y$ - and  $z$ -direction and calculated its distribution to obtain the averaged length scale. This characteristic length scale is related to the average radius  $\langle R \rangle$  of the droplets assuming they have spherical shape

$$\langle L(s) \rangle_{x,y,z} = \frac{\pi^2}{8} \langle R \rangle. \quad (\text{B.8})$$

The development of the characteristic length scale in time is shown in fig. B.2. For comparison a line with a slope of  $1/3$  is also included in this figure. the simulation data show good agreement with this expected theoretical slope [103, 109].

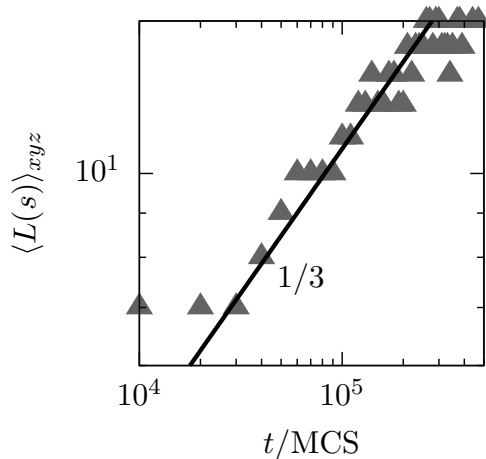


Figure B.2 – Characteristic length during the growth of the droplets (triangles) and a line with a slope of  $1/3$  for comparison. The used parameter values are  $\bar{\phi}_A = 0.05$ ,  $\chi_{AB} = 4$  and  $L_x = L_y = L_z = 64a$ .

### B.3 Calculation of the Eccentricity from Configuration Data

*Eccentricity of a region of a binary image.* For the calculation of the eccentricity, a moment based method, commonly used in image processing, is applied here. It is explained in [20]. We assume, that the picture is provided in the form of a two dimensional lattice, parameterized by the parameters  $u$  and  $v$ . The  $pq$ -moment of a chosen region  $\mathcal{R}$  is defined as

$$m_{pq} = \sum_{(u,v) \in \mathcal{R}} I(u,v) u^p v^q. \quad (\text{B.9})$$

The function  $I(u,v)$  gives the weight of each lattice point. For the evaluation of the simulation data, we use only binary images. In binary images  $I(u,v) = 1$  for  $(u,v) \in \mathcal{R}$  and 0 otherwise. For the case of a binary image, the moment  $m_{00}$  is the area  $|\mathcal{R}|$  of the region  $\mathcal{R}$ . With the first moments, we can compute the centroid  $(\bar{x}, \bar{y})$  of the region  $\mathcal{R}$ .

$$\begin{aligned} \bar{x} &= \frac{1}{|\mathcal{R}|} \sum_{(u,v) \in \mathcal{R}} u^1 v^0 = \frac{m_{10}}{m_{00}}, \\ \bar{y} &= \frac{1}{|\mathcal{R}|} \sum_{(u,v) \in \mathcal{R}} u^0 v^1 = \frac{m_{01}}{m_{00}}. \end{aligned} \quad (\text{B.10})$$

To calculate transition invariant properties of the region  $\mathcal{R}$ , we place the origin of the coordinate system to the center of the region  $\mathcal{R}$  using the calculated centroid. With that, we obtain the central moments of the region  $\mathcal{R}$

$$\mu_{pq} = \sum_{(u,v) \in \mathcal{R}} I(u,v) \cdot (u - \bar{x})^p \cdot (v - \bar{y})^q. \quad (\text{B.11})$$

## Appendix B. Simulation

---

In this thesis, the eccentricity is defined as

$$\epsilon = \sqrt{1 - \frac{b^2}{a^2}}, \quad (\text{B.12})$$

where  $a$  and  $b$  are the ellipse's major and minor axis. This eccentricity is 0, if the evaluated shape possess radial symmetry and 1, if the shape is infinitely elongated in one direction and finite in the other directions.<sup>2</sup> The major and minor axis are computed using the matrix of the quadratic moments

$$\mathbf{A} = \begin{bmatrix} \mu_{20} & \mu_{11} \\ \mu_{11} & \mu_{02} \end{bmatrix}. \quad (\text{B.13})$$

The values of a  $a$  and  $b$  are related to the eigenvalues of this matrix

$$\lambda_{1,2} = \frac{\text{tr}(\mathbf{A}) \pm \sqrt{\text{tr}^2(\mathbf{A}) - 4\det(\mathbf{A})}}{2}. \quad (\text{B.14})$$

Their values are

$$\begin{aligned} a &= 2\sqrt{\frac{\lambda_1}{|\mathcal{R}|}}, \\ b &= 2\sqrt{\frac{\lambda_2}{|\mathcal{R}|}}. \end{aligned} \quad (\text{B.15})$$

We can use eq. (B.14) to calculate the eccentricity directly from the matrix  $\mathbf{A}$

$$\epsilon = \sqrt{1 - \frac{4\det(\mathbf{A})}{\left(\text{tr}(\mathbf{A}) + \sqrt{\text{tr}^2(\mathbf{A}) - 4\det(\mathbf{A})}\right)^2}}. \quad (\text{B.16})$$

*Computation of the eccentricity from the 3D simulation data.* All presented simulation are done in three dimensions. We calculate eccentricities by projecting the droplet to a chosen observation plane. Because of the underlying lattice, we use projections orthogonal to the  $x$ - and parallel to  $y$ - or  $z$ -axis. The projections are interpreted as a binary image, each lattice point of the projection plane, where at least one droplet particle is projected has the value 1, otherwise it has the value 0. Because the eccentricities measured on the  $xz$ - and the  $xz$ -plane are very similar (not shown), we assume that the droplet is radial symmetric around the  $x$ -axis. We use the eccentricities to have a quick check of the anisotropic shape of the droplet, which is the reason to apply this simple method.

---

<sup>2</sup>Even the discrete rotational symmetry of shapes with at least a 3-fold symmetry axis lead to a vanishing eccentricity.

## B.4 Mastercurve of the Regulator Flux through Boundary Conditions

In the introduced simulation, the particles move only by diffusion. To describe this process in the dilute regime, we can employ Fick's second law

$$\partial_t c_R = D_R \partial_x^2 c_R, \quad (\text{B.17})$$

where  $c_R = \phi_R/a^3$  is the particle concentration of the regulator and  $D_R$  is its one-dimensional isotropic diffusion coefficient. In the steady state the left side vanishes and the steady state profile is a linear function  $c_R^s = mx + c_0$ . The total amount of regulator material is normalized by  $\int_0^{L_x} c_R dx = \frac{N_R}{A}$ , where  $A = L_y L_z$  is the area perpendicular to the  $x$ -direction. Using the normalization, we can identify  $c_0 = \bar{c}_R$  as the average concentration of the regulator. The flux in the diffusion process is related to the concentration profile by  $j_x = -D_R \partial_x c_R$ , which obtains

$$c_R^s = -\frac{j_x}{D_R} x + \bar{c}_R \quad (\text{B.18})$$

in the steady state. In the steady state the flux has to be constant, especially  $j_x = j_x(0) = j_x(L)$ . Later, we will use  $j_x(L)$  in the calculation. Although this choice is mathematically arbitrary, it is a kind of natural choice to observe  $j_x(L)$  or  $j_x(0)$ , because the regulator material is pumped at this position. In the discrete simulation the flux is measured by

$$j_x(L) = \frac{\Delta N_R}{A \Delta t}. \quad (\text{B.19})$$

Here,  $\Delta N_R$  counts the number of particles crossing the plane at  $x = L$  in the observed time interval  $\Delta t$ . A particle moving in positive direction contributes +1. Remember, that a moving in negative direction through  $x = L$  is not possible because of the boundary conditions. The crossing particles  $\Delta N_R$  per Monte Carlo step can be estimated as

$$\Delta N_R = P(L-1) \frac{N_R w}{z}. \quad (\text{B.20})$$

Because we choose to observe one Monte Carlo step, we introduced the factor  $N_R$ , the factor  $1/\zeta$  takes into account that only one of the six possible moving directions of the particle leads to a crossing of the observed plane. The parameter  $w$  is a simulation parameter, which adjusts the permeability of the observed wall,  $w = 0$  means a hard wall,  $w = 1$  means that each particle, which passes the metropolis criterion, passes the boundary. The function  $P(x)$  measures the probability, that a particle at position  $x$  is picked during one simulation step. Here, we use a simple linear estimation for  $\Delta N_R$ , because particles that move more than one lattice site during a Monte Carlo step are neglected. The results will show, that in average this approximation is sufficient. The probability  $P$  is given as  $P(x) = N_R(x)/N_R$ , with  $N_R(x) \phi_R(x) A a$  and  $N_R = \bar{\phi}_R A L_x$ . With this, the flux can be written as

$$j_x = \frac{\phi(L-1)w}{\zeta a^3 \Delta t}. \quad (\text{B.21})$$

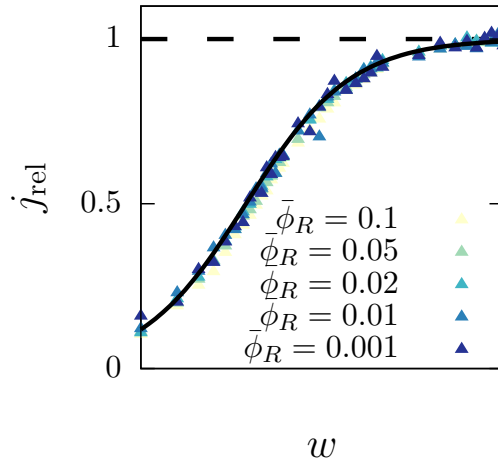


Figure B.3 – Relative fluxes  $j_{\text{rel}}$  in dependency of the permeability parameter  $w$  for different average volume fractions  $\bar{\phi}_R$ . The different curves can be combined to one mastercurve in very good approximation. Furthermore, the theoretic approximation, shown as black line, is consistent with the simulation results. The diffusion constant  $D_R$  is the only parameter in the theoretic approximation, which is not a input parameter of the simulation or a arbitrary choice. The diffusion coefficient was measured by the mean square displacement as  $D_R^{\text{MSD}} = 0.158a^2/\text{MCS}$ .

Also, from the steady state profile eq. (B.18) we get the flux relation

$$j_x = \frac{2D_R(\phi_R(L-1) - \bar{\phi}_R)}{a^3L}. \quad (\text{B.22})$$

Combining eq. (B.21) and eq. (B.22), we can eliminate the volume fraction close to the observed plane  $\phi_R(L-1)$  and get

$$j_x = \frac{2D_R w \bar{\phi}_R}{a^2(aLw + 2D_R \zeta \Delta t)}. \quad (\text{B.23})$$

To construct a mastercurve, we aim to relate the regulator flux to a maximum regulator flux. Within the used framework, the maximum regulator flux  $j_{\text{max}} = -D_R m_{\text{max}}$  is achieved for the maximum regulator gradient  $m_{\text{max}}$  and can be estimated as

$$j_{\text{max}} = \frac{2D_R \bar{\phi}_R}{a^3L}. \quad (\text{B.24})$$

Combined with the flux eq. (B.23), we define the relative flux

$$j_{\text{rel}} = \frac{j_x}{j_{\text{max}}} = \frac{aLw}{aLw + 2D_R \zeta \Delta t}. \quad (\text{B.25})$$

This function is shown in fig. B.3. The results of the simulation collapse to one mastercurve and show very good agreement with eq. (B.25).

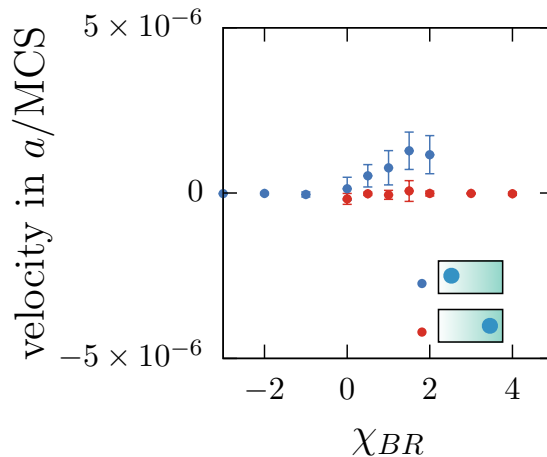


Figure B.4 – Initial velocity of a droplet in a correlated initial state and a droplet in a correlated initial state. The parameters are  $\chi_{AB} = 4$ ,  $\chi_{AR} = 1$ ,  $\bar{\phi}_A = 0.05$ ,  $\bar{\phi}_R = 0.02$  and  $L = 256$ .

## B.5 Positioning of Droplets with Immobile Regulator Particles

The Simulations of this section are inspired by the results of section A.9. There, we have shown, that the correlated-anti-correlated phase transition is also observed if the the regulator profile is imposed directly. The perfectly constant regulator profile shows very similar qualitative results as presented in chapter 3. Nevertheless, the mapping of the constant regulator distribution to the particle based simulation is not straight forward. We modeled this by using immobile regulator particles. This particle were distributed in  $x$ -direction according to the linear distribution eq. (A.59). At each slice of constant  $x$ -coordinate, the particles are distributed randomly in the  $y$ - $z$ -plane. This procedure leads to a quasi perfect linear regulator distribution considering the  $x$ -projection.<sup>3</sup> We studied the position of the transition point by measuring the initial velocities of a droplet placed in a correlated state and a droplet placed in anti-correlated state (see fig. B.4). If the droplets are close to the equilibrium state, the velocity vanishes. Close to the transition point both velocities are nonzero. We observe a very clear signature for the droplet in the anti-correlated initial condition, which is consistent with the mean-field transition point  $\chi_{BR}^* = 1$ . For the droplet in the correlated state, this signature is not clearly observed. The velocity vanishes for high  $\chi_{BR}$ , but no clear movement is observed like for the other droplet. Maybe it is possible to interpret a very slow movement towards the correlated state for  $\chi_{BR=0}$ . This problem is caused by the chosen process of generation of the gradient. If the regulator particles are distributed randomly in each slice, a local accumulation of regulator material can occur. This can effect the movement of droplets in the  $x$ -direction by "gluing" them to certain points.

If this ensemble is of further interest and shall be studied in more detail, a different method of synthesizing the gradient is strongly recommended.

<sup>3</sup>The regulator distribution is only quasi linear because of the discrete character of the simulation model. In each slice an error of up to one particle can occur when calculating the amount of regulator particles in that slice. In a last step of generating the regulator gradient, the total difference of particles is randomly added to the lattice. This leads to very minor fluctuations of the regulator distribution.



# Bibliography

- [1] A. Aharoni, A. D. Griffiths, and D. S. Tawfik. *Current Opinion in Chemical Biology*, 9:210, 2005.
- [2] R. A. Alberty. *Chemical Reviews*, 94(6):1457, 1994.
- [3] M. A. Amin, S. Matsunaga, and S. Uchiyama. *Biochemical Journal*, 415:345, 2008.
- [4] J. S. Andersen, Y. W. Lam, A. K. L. Leung, S.-E. Ong, C. E. Lyon, A. I. Lamond, and M. Mann. *Nature*, 433:77, 2005.
- [5] P. Anderson, N. Kadersha, and P. Ivanov. *Biochimica et Biophysica Acta*, 1849:861, 2015.
- [6] T. Baumgart, A. T. Hammond, P. Sengupta, S. T. Hess, D. A. Holowka, B. A. Baird, and W. W. Webb. *Proceedings of the National Academy of Sciences of the United States of America*, 104(9):3165, 2007.
- [7] J. Beisson and M. Jerka-Dziadosz. *Biology of the Cell*, 91:367, 1999.
- [8] L. S. Bennethum, J. H. Cushman, and M. A. Murad. *International Journal of Engineering Science*, 34(14):1611, 1996.
- [9] J. Berry, S. C. Weber, N. Vaidya, M. Haataja, and C. P. Brangwynne. *Proceedings of the National Academy of Science of the United States of America*, 112:E5237, 2015.
- [10] K. Binder. *Reports on Progress in Physics*, 50:683, 1987.
- [11] K. Binder and D. Heermann. *Monte Carlo Simulations in Statistical Physics*. Springer-Verlag, 1986.
- [12] D. Bonn and D. Ross. *Reports on Progress in Physics*, 64:1085, 2001.
- [13] M. Bornens. *Nature Reviews*, 9:874, 2008.
- [14] T. Boublik. *Journal of Chemical Physics*, 53:471, 1970.
- [15] C. P. Brangwynne, C. R. Eckmann, D. S. Courson, A. Rybarska, C. Hoegel, J. Gharakhani, F. Jülicher, and A. A. Hyman. *Science*, 324:1729, 2009.
- [16] C. P. Brangwynne, T. J. Mitchison, and A. A. Hyman. *Proceedings of the National Academy of Science of the United States of America*, 108:4334, 2011.
- [17] A. J. Bray. *Advances in Physics*, 43:357, 1994.

## Bibliography

---

- [18] G. Brugerolle and J.-P. Mignot. *Protoplasma*, 222(1-2):13, 2003.
- [19] J. R. Buchan, D. Muhlrاد, and R. Parker. *Journal of Cell Biology*, 183:441, 2008.
- [20] W. Burger and M. J. Burge. *Principles of Digital Image Processing*. Springer-Verlag, 2009.
- [21] K. A. Burke, A. M. Janke, C. L. Rhine, and N. L. Fawzi. *Molecular Cell*, 60:231, 2015.
- [22] M. A. Burns, B. N. Johnson, S. N. Brahma Sandra, K. Handique, J. R. Webster, M. Krishnan, T. S. Sammarco, P. M. Man, D. Jones, D. Heldsinger, C. H. Mastrangelo, and D. T. Burke. *Science*, 282:484, 1998.
- [23] J. C. Butcher. *Numerical Methods for Ordinary Differential Equations*. John Wiley & Sons, 2003.
- [24] J. W. Cahn. *Acta Metallurgica*, 9:795, 1961.
- [25] J. W. Cahn. *Journal of Chemical Physics*, 42:93, 1965.
- [26] J. W. Cahn and J. E. Hilliard. *Journal of Chemical Physics*, 28:258, 1958.
- [27] X. Chen, D. Cui, C. Liu, H. Li, and J. Chen. *Analytica Chimica Acta*, 584:237, 2007.
- [28] M. Cioce and A. I. Lamond. *Annual Reviews*, 21:105, 2005.
- [29] E. M. Courchaine, A. Lu, and K. M. Neugebauer. *The EMBO Journal*, 35:1603, 2016.
- [30] C. R. Cowan and A. A. Hyman. *Nature*, 431:92, 2004.
- [31] W. A. Curtin. *Physical Review B*, 39:6775, 1989.
- [32] W. A. Curtin and N. W. Ashcroft. *Physical Review A*, 32:2909, 1985.
- [33] W. A. Curtin and N. W. Ashcroft. *Physical Review Letters*, 56:2775, 1986.
- [34] Z. T. Cygan, J. T. Cabral, K. L. Beers, and E. J. Amis. *Langmuir*, 21:3629, 2005.
- [35] B. R. Daniels, T. M. Dobrowsky, E. M Perkins, S. X. Sun, and D. Wirtz. *Development*, 137:2579, 2013.
- [36] A. R. Denton and N. W. Ashcroft. *Physical Review A*, 39:4701, 1989.
- [37] P. S. Dittrich, M. Jahnz, and P. Swille. *ChemBioChema*, 6:811, 2005.
- [38] P. S. Dittrich and A. Manz. *Nature Reviews Drug Discovery*, 5:210, 2006.
- [39] D. G. Drubin and W. J. Nelson. *Cell*, 84:335, 1996.
- [40] C. Ebner, W. F. Saam, and D. Stroud. *Physical Review A*, 14:2264, 1976.
- [41] S. Elbaum-Garfinkle, Y. Kim, K. Szczepaniak, C. C.-H. Chen, C. R. Eckmann, S. Myong, and C. P. Brangwynne. *Proceedings of the National Academy of Sciences of the United States of America*, 112:7189, 2015.

- 
- [42] M. Elstner and A. Schiller. *Center for Advancing Electronics Dresden Interim Report 2012-2016*, page 30.
- [43] D. J. Evans and G. P. Morris. *Chemical Physics*, 77:63, 1983.
- [44] R. Evans. *Fundamentals of Inhomogeneous Fluids*. Wiley, 1992.
- [45] J. Feder, K. C. Russell, J. Lothe, and G. M. Pound. *Advances in Physics*, 15:111, 1966.
- [46] A. Fick. *Annalen der Physik*, 170:59, 1855.
- [47] P. J. Flory. *Journal of Chemical Physics*, 10:51, 1942.
- [48] A. H. Fox, Y. W. Lam, A. K. L. Leung, C. E. Lyon, J. Andersen, M. Mann, and A. I. Lamond. *Current Biology*, 12:13, 2002.
- [49] A. H. Fox and A. I. Lamond. *Cold Spring Harbor Perspectives in Biology*, 2:a000687, 2010.
- [50] D. Frenkel and B. Smit. *Understanding Molecular Simulation*. Academic Press, 2002.
- [51] S. Frey, R. P. Richter, and D. Görlich. *Science*, 314:815, 2006.
- [52] Z. R. Gagnon. *Electrophoresis*, 32:2466, 2011.
- [53] C. M. Gallo, J. T. Wang, F. Motegi, and G. Seydoux. *Science*, 330:1685, 2010.
- [54] P. R. C. Gascoyne and J. Vykoukal. *Electrophoresis*, 23:1973, 2002.
- [55] I. M. Gelfand and S. V. Fomin. *Calculus of Variations*. Dover Publications, inc., 2000.
- [56] J. Gharakhani. *Cell Cytoplasm Compartmentalization: Localization Through Gradients*. PhD thesis, Technische Universität Dresden, 2012.
- [57] V. L. Ginzburg and L. D. Landau. *Journal of Experimental and Theoretical Physics (USSR)*, 20:1064, 1950.
- [58] D. R. Gossett, W. M. Weaver, A. J. Mach, S. C. Hur, H. T. K. Tse, W. Lee, H. Amini, and D. Di Carlo. *Analytical and Bioanalytical Chemistry*, 397:3249, 2010.
- [59] E. E. Griffin, D. J. Odde, and G. Seydoux. *Cell*, 146:955, 2011.
- [60] P. M. Günther, F. Möller, T. Henkel, J. M. Köhler, and G. A. Groß. *Chemical Engineering and Technology*, 28:520, 2005.
- [61] S. Guo and K. J. Kemphues. *Current OPinion in genetics and Development*, 6:408, 1996.
- [62] S. Haeberle and R. Zengerle. *Lab on a Chip*, 7:1094, 2007.
- [63] M. Hanazawa, M. Yonetani, and A. Sugimoto. *Journal of Cell Biology*, 192:929, 2011.

## Bibliography

---

- [64] C. L. Hansen, S. Classen, J. M. Berger, and S. R. Quake. *Journal of the American Chemical Society*, 128:3142, 2006.
- [65] C. L. Hansen, E. Skordalakes, J. M. Berger, and S. R. Quake. *Proceedings of the National Academy of Science of the United States of America*, 99:16531, 2002.
- [66] C. L. Hansen, M. O. A. Sommer, and S. R. Quake. *Proceedings of the National Academy of Science of the United States of America*, 101:14431, 2004.
- [67] J.-P. Hansen and I. R. McDonald. *Theory of Simple Liquids*. Elsevier, 1990.
- [68] W. K. Hastings. *Biometrika*, 57(1):97, 1970.
- [69] D. Hernandez-Verdun. *Nucleus*, 2:189, 2011.
- [70] D. Hildebrandt and D. Glasser. *The Chemical Engineering Journal*, 54:187, 1994.
- [71] S. N. Hird, J. E. Paulson, and S. Strome. *Development*, 122:1303, 1996.
- [72] C. Hoege and A. A. Hyman. *Nature Reviews Molecular Cell Biology*, 14:315, 2013.
- [73] P. Hohenberg and W. Kohn. *Physical Review*, 136:B865, 1964.
- [74] W. G. Hoover. *Physical Reviews A*, 31:1695, 1985.
- [75] M. L. Huggins. *Journal of Chemical Physics*, 9:440, 1941.
- [76] L. Ionov, A. Sidorenko, M. Stamm, S. Minko, B. Zdyrko, V. Klep, and I. Luzinov. *Macromolecules*, 37:7421, 2004.
- [77] K. Jähnisch, V. Hessel, H. Löwe, and M. Baerns. *Angewandte Chemie International Edition*, 43:406, 2004.
- [78] S. Jain and R. Parker. *Advances in Experimental Medicine and Biology*, 768:23, 2013.
- [79] M. E. Janson, R. Loughlin, I. Loïodice, C. Fu, D. Brunner, F. J. Nédélec, and P. T. Tran. *Cell*, 128(2):357, 2007.
- [80] N. Kadersha, M. R. Cho, W. Li, P. W. Yacono, S. Chen, L. Gilks, D. E. Golan, and P. Anderson. *Journal of Cell Biology*, 151:1257, 2000.
- [81] E. Karsenti, F. J. Nédélec, and T. Surrey. *Nature Cell Biology*, 8(11):1204, 2006.
- [82] J. Kästner. *Advanced Review*, 1:932, 2011.
- [83] J. Kästner and W. Thiel. *Journal of Chemical Physics*, 123:144104, 2005.
- [84] M. Kato, T. W. Han, S. Xie, K. Shi, X. Du, L. C. Wu, H. Mirzaei, E. J. Goldsmith, J. Longgood, J. Pei, N. V. Grishin, D. E. Frantz, J. W. Schneider, S. Chen, L. Li, M. R. Sawaya, D. Eisenberg, R. Tycko, and S. L. McKnight. *Cell*, 149:753, 2012.
- [85] K. Kawasaki. *Physical Review*, 145(1):224, 1966.
- [86] S. A. Khan, A. Günther, M. A. Schmidt, and K. F. Jensen. *Langmuir*, 20:8604, 2004.
- [87] J. Kierzenka and L. F. Shampine. *ACM TOMS*, 27:299, 2001.

- 
- [88] P. J. Kitson, M. H. Rosnes, V. Sans, V. Dragone, and L. Cronin. *Lab on a Chip*, 12:3267, 2012.
- [89] W. Kohn and L. J. Sham. *Physical Review*, 140:A1133, 1965.
- [90] A. B. Kolomeisky, G. M. Schütz, E. B. Kolomeisky, and J. P. Straley. *Journal of Physics A: Mathematical and General*, 31:6911, 1998.
- [91] R. Koningsveld, W. H. Stockmayer, and E. Nies. *Polymer Phase Diagrams: A Textbook*. Oxford University Press 2001, 1994.
- [92] P. L. Krapivsky, S. Redner, and E. Ben-Naim. *A Kinetic View of Statistical Physics*. Cambridge University Press, 2010.
- [93] S. Kumar, D. Bouzida, R. H. Swendsen, P. A. Kollmana, and J. M. Rosenberg. *Journal of Computational Chemistry*, 13(8):1011, 1992.
- [94] S. Kumar and J. M. Rosenberg. *Journal of Computational Chemistry*, 16(11):1339, 1995.
- [95] I. Kwon, M. Kato, S. Xiang, L. Wu, . Theodoropoulos, H. Mirzaei, T. Han, S. Xie, J. L. Corden, and S. L. McKnight. *Cell*, 155:1049, 2013.
- [96] A. I. Lamond and D. L. Spector. *Nature Reviews Molecular Cell Biology*, 4:605, 2003.
- [97] L. Landau and E. Lifshitz. *Physikalsche Zeitschrift der Sowjetunion*, 8:153, 1935.
- [98] C. F. Lee, C. P. Brangwynne, J. Gharakani, A. A. Hyman, and F. Jülicher. *Physical Review Letters*, 111:088101, 2013.
- [99] X. Lei, A. D. Diamond, and J. T. Hsu. *Journal of Chemical and Engineering Data*, 35:420, 1990.
- [100] J. E. Lennard-Jones. *Proceedings of the Royal Society of London A*, 106:738, 1924.
- [101] P. Li, S. Banjade, H.-C. Cheng, S. Kim, B. Chen, L. Guo, M. Llaguno, J. V. Hollingsworth, D. S. King, S. F. Banani, P. S. Russo, Q.-X. Jiang, B. T. Nixon, and M. K. Rosen. *Nature*, 483:336, 2012.
- [102] Z. Li, D. Cao, and J. Wu. *Journal of Chemical Physics*, 122:174708, 2005.
- [103] I. M. Lifshitz and V. V. Slyozov. *Journal of Physics and Chemistry of Solids*, 19:35, 1961.
- [104] Y. Lin, D. S. W. Protter, M. K. Rosen, and R. Parker. *Molecular Cell*, 60:208, 2015.
- [105] J. Lippincott-Schwartz, L. C. Yuan, S. Bonifacino, and R. D. Klausner. *Cell*, 56(5):801, 1989.
- [106] C. J. Malone, L. Misner, N. Le Bot, M.-C. Tsai, J. M. Campbell, J. Ahringer, and J. G. White. *Cell*, 115(7):825, 2003.
- [107] G. A. Mansoori, . F. Carnahan, K. E. Starling, and T. W. Leland Jr. *Journal of Chemical Physics*, 54:1523, 1971.

## Bibliography

---

- [108] E. Marco, R. Wedlich-Soldner, R. Li, S. J. Altschuler, and L. F. Wu. *Cell*, 129(2):411, 2007.
- [109] J. A. Marqusee and J. Ross. *Journal of Chemical Physics*, 80:536, 1984.
- [110] A. Marsh, B. J. Clark, and K. D. Altria. *Journal of Separation Science*, 28:2023, 2005.
- [111] D. A. McQuarrie. *Statistical Mechanics*. Harper and Collins, 1976.
- [112] N. D. Mermin. *Physical Review*, 137:A1441, 1965.
- [113] N. Metropolis, A. W. Rosenbluth, M. N. Rosenbluth, A. H. Teller, and E. Teller. *Journal of Chemical Physics*, 21(6):1087, 1953.
- [114] A. Michelot, J. Berro, C. Guérin, R. Boujemaa-Paterski, C. J. Staiger, J.-L. Martiel, and L. Blanchoin. *Current Biology*, 17(10):825, 2007.
- [115] M. K. Miller, J. M. Hyde, M. G. Hetherington, A. Cerezo, G. D. W. Smith, and C. M. Elliott. *Acta Metallurgica*, 43:3385, 1995.
- [116] D. M. Mitrea and R. W. Kriwacki. *Cell Communication and Signalling*, 14:1, 2016.
- [117] A. Molliex, J. Temirov, J. Lee, M. Coughlin, A. P. Kanagaraj, H. J. Kim, T. Mittag, and J. P. Taylor. *Cell*, 163:123, 2015.
- [118] T. Murugesan and M. Perumalsamy. *Journal of Chemical and Engineering Data*, 50:1392, 2005.
- [119] T. Nagai and K. Kawasaki. *Physica A*, 134(3):483, 1986.
- [120] F. J. Nédélec, T. Surrey, A. C. Maggs, and S. Leibler. *Nature*, 389:305, 1997.
- [121] S. Nosé. *Journal of Chemical Physics*, 81:511, 1984.
- [122] T. J. Nott, E. Petsalaki, P. Farber, D. Jarvis, E. Fussner, A. Plochowietz, T. D. Craggs, D. P. Bazett-Jones, T. Pawson, J. D. Forman-Kay, and A. J. Baldwin. *Molecular Cell*, 57:936, 2015.
- [123] A. Nußbaumer, E. Bittner, T. Neuhaus, and W. Janke1. *Europhysics Letters*, 75(5):716, 2006.
- [124] J. Oakey, J. Allely, and D. W. M. Marr. *Biotechnology Progress*, 18:1439, 2002.
- [125] L. Onsager. *Physical Review*, 37:405, 1931.
- [126] L. Onsager. *Annals of the New York Academy of Science*, 51:627, 1949.
- [127] D. W. Oxtoby. *Annual Review of Material Research*, 32:39, 2002.
- [128] E. M. Ozbudak, A. Becskei, and A. van Oudenaarden. *Developmental Cell*, 9(4):565, 2005.
- [129] J. M. Pagano, B. M. Farley, L. M. McCoig, and S. P. Ryder. *Journal of Biological Chemistry*, 282:8883, 2007.

- 
- [130] N. Pamme. *Lab on a Chip*, 7:1644, 2007.
- [131] A. Z. Panagiotopoulos. *Molecular Physics*, 61:813, 1987.
- [132] A. Patel, H. O. Lee, L. Jawerth, S. Maharana, M. Jahnel, M. Y. Hein, S. Stoykov, J. Mahamid, S. Saha, T. M. Franzmann, A. Pozniakovski, I. Poser, N. Maghelli, L. A. Royer, M. Weigert, E. W. Myers, S. Grill, D. Drechsel, A. A. Hyman, and S. Alberti. *Cell*, 162:1066, 2015.
- [133] J. K. Percus and G. J. Yevick. *Physical Review*, 110:1, 1958.
- [134] H. Reiss, H. L. Frisch, and J. L. Lebowitz. *Journal of Chemical Physics*, 110:1, 1959.
- [135] J. A. Rice. *Mathematical Statistics and Data Analysis*. Thompson/Brooks/Cole, 2007.
- [136] J.-L. Rivail. *Eléments de Chimie Quantique à l'usage des chimistes*. InterEditions/CNRS Editions, 1994.
- [137] Y. Rosenfeld. *Physical Review Letters*, 63:980, 1989.
- [138] Y. Rosenfeld. *Molecular Physics*, 86:637, 1995.
- [139] A. Roux, D. Cuvelier, P. Nassoy, J. Prost, P. Bassereau, and B. Goud. *The EMBO Journal*, 24:1537, 2005.
- [140] M. Rubinstein and R. H. Colby. *Polymer Physics*. Oxford University Press, 2003.
- [141] S. Saeki, N. Kuwahara, M. Nakata, and M. Kaneko. *Polymer*, 8:685, 1976.
- [142] S. A. Safran. *Statistical Thermodynamics of Surfaces, Interfaces, and Membranes*. Addison-Wesley Publishing Company, 1994.
- [143] S. Saha, C. A. Weber, M. Nusch, O. Adame-Arana, C. Hoegge, M. Y. Hein, E. Osborne-Nishimura, J. Mahamid, M. Jahnel, L. Jawerth, A. Pozniakovski, C. R. Eckmann, F. Jülicher, and A. A. Hyman. *Cell*, 166:1572, 2016.
- [144] P. Sajeesh and A. K. Sen. *Microfluid Nanofluid*, 17:1, 2014.
- [145] M. L. Schlossman. *Current Opinion in Colloid and Interface Science*, 7:235, 2002.
- [146] C. M. Schubert, R. Lin, C. J. de Vries, R. H. Plasterk, and J. R. Priess. *Molecular Cell*, 5:671, 2000.
- [147] J. C. Schwartz, X. Wang, E. R. Podell, and T. R. Cech. *Cell Reports*, 5:918, 2013.
- [148] Y. Shav-Tal, J. Blechmann, X. Darzacq, C. Montagna, B. T. Dye, J. G. Patton, R. H. Singer, and D. Zipori. *Molecular Biology of the Cell*, 16:2395, 2005.
- [149] J. Sivardière and J. Lajzerowicz. *Physical Review A*, 11:2090, 1975.
- [150] J. Sivardière and J. Lajzerowicz. *Physical Review A*, 11:2101, 1975.
- [151] H. Song, D. L. Chen, and R. F. Ismagilov. *Angewandte Chemie International Edition*, 45:7336, 2006.

## Bibliography

---

- [152] D. L. Spector and A. I. Lamond. *Cold Spring Harbor Perspectives in Biology*, 3:a000646, 2011.
- [153] C. P. Stanners and H. Becker. *Journal of Cellular Physiology*, 77:31, 1971.
- [154] D. Stauffer, A. Coniglio, and D. W. Heermann. *Physical Review Letters*, 49(18):1299, 1982.
- [155] S. Strome and W. B. Wood. *Proceedings of the National Academy of Science of the United States of America*, 79:1558, 1982.
- [156] M. Strzlecka, S. Trowitzsch, G. Weber, R. Lühmann, A. C. Oates, and K. M. Neugebauer. *Nature Structural and Molecular Biology*, 17:403, 2010.
- [157] S. Takeuchi, P. Garstecki, D. B. Weibel, and G. M. Whitesides. *Advanced Materials*, 17:1067, 2005.
- [158] Y. Tang and B. C.-Y. Lu. *Journal of Chemical Physics*, 99:9828, 1993.
- [159] Y. Tang and J. Wu. *Physical Review E*, 70:011201, 2004.
- [160] J. R. Tenlen, J. N. Molk, N. London, B. D. Page, and J. R. Priess. *Development*, 135:3665, 2008.
- [161] L. Tisza. *Annals of Physics*, 13(1):1, 1961.
- [162] G. M. Torrie and J. P. Valleau. *Journal of Computational Physics*, 23:187, 1977.
- [163] I. Ugrinova, K. Monier, C. Ivaldi, M. Thiry, S. Storck, F. Mongelard, and P. Bouvet. *BMC Molecular Biology*, 8:66, 2007.
- [164] P. Ungerer, C. Nieto-Draghi, B. Rousseau, G. Ahunbay, and V. Lachet. *Journal of Molecular Liquids*, 134:71, 2007.
- [165] D. L. Updike, A. K. Knutson, T. A. Egelhofer, A. C. Campbell, and S. Strome. *Current Biology*, 24:970, 2014.
- [166] D. L. Updike and S. Strome. *Journal of Andrology*, 31:53, 2010.
- [167] J. van der Gucht, E. Paluch, J. Plastino, and C. Sykes. *Proceedings of the National Academy of Sciences of the United States of America*, 102(22):7847, 2005.
- [168] J. D. van der Waals. *Verh K Akad Wet Amsterdam*, 1:8, 1893.
- [169] A. van Oudenaarden and J. A. Theriot. *Nature Cell Biology*, 1:493, 1999.
- [170] F. Varnik, P. Truman, B. Wu, P. Uhlmann, D. Raabe, and M. Stamm. *Physics of Fluids*, 20:072104, 2008.
- [171] L. Verlet. *Physical Review*, 159:98, 1967.
- [172] E. Voronina, G. Seydoux, P. Sassone-Corsi, and I. Nagamori. *Cold Spring Harbor Perspectives in Biology*, 3:a002774, 2011.
- [173] G. Wan, B. D. Fields, G. Spracklin, A. Shukla, C. M. Phillips, and S. Kennedy. *Nature*, 557:679, 2018.

- 
- [174] J. T. Wang, J. Smith, B.-C. Chen, H. Schmidt, D. Rasoloson, A. Paix, B. G. Lambrus, D. Calidas, E. Betzig, and G. Seydoux. *eLife*, 3:e04591, 2014.
- [175] X. Wang, J. C. Schwartz, and T. R. Cech. *Nucleic Acids Research*, 43:7535, 2015.
- [176] P. Watts and S. J. Haswell. *Current Opinion in Chemical Biology*, 7:380, 2003.
- [177] P. Watts and S. J. Haswell. *Chemical Society Reviews*, 34:235, 2005.
- [178] R. Wedlich-Soldner, S. Altschuler, L. Wu, and R. Li. *Science*, 299(5610):1231, 2003.
- [179] F. Wippich, B. Bodenmiller, M. G. Trajkovska, S. Wanka, R. Aeberlold, and L. Pelkmans. *Cell*, 152:791, 2013.
- [180] J. Wu. *American Institute of Chemical Engineers*, 52:1169, 2005.
- [181] M. T. Zafarani-Moattar and A. A. Hamidi. *Journal of Chemical and Engineering Data*, 48:262, 2003.
- [182] H. Zhang, S. Elbaum-Garfinkle, E. M. Langdon, N. Taylor, P. Occhipinti, A. A. Bridges, C. P. Brangwynne, and A. S. Gladfelter. *Molecular Cell*, 60:220, 2015.
- [183] D. Zwicker, R. Seyboldt, C. A. Weber, A. A. Hyman, and F. Jülicher. *Nature Physics*, 13:408, 2017.



# Versicherung

schriftliche Erklärung gemäß § 5 Abs. 1 Punkt 5 der Promotionsordnung

Hiermit versichere ich, Samuel Krüger, dass ich die vorliegende Arbeit ohne unzulässige Hilfe Dritter und ohne Benutzung anderer als der angegebenen Hilfsmittel angefertigt habe; die aus fremden Quellen direkt oder indirekt übernommenen Gedanken sind als solche kenntlich gemacht. Die Arbeit wurde bisher weder im Inland noch im Ausland in gleicher oder ähnlicher Form einer anderen Prüfungsbehörde vorgelegt. Die Arbeit wurde in Dresden am Leibniz-Institut für Polymerforschung und am Max-Planck-Institut für Physik komplexer Systeme unter der Betreuung von Professor Jens-Uwe Sommer und Professor Frank Jülicher angefertigt. Ich erkenne hiermit die Promotionsordnung des Bereichs Mathematik und Naturwissenschaften der Technische Universität Dresden vom 23.02.2011 an.

Dresden, 27. September 2018

Samuel Krüger